UNIVERSITÀ DELLA CALABRIA

Dipartimento di Ingegneria per l'Ambiente ed il Territorio ed Ingegneria Chimica

Scuola di Dottorato in Scienza Ingegneristiche "Pitagora"

Dottorato di Ricerca in
INGEGNERIA IDRAULICA PER L'AMBIENTE ED IL TERRITORIO
XXVIII CICLO

WEAKLY-COMPRESSIBLE SPH MODELING OF FLUID-STRUCTURE INTERACTION PROBLEMS

SSD ICAR/02

Supervisori:
Prof. Ing. Paolo Veltri

Prof. Ing. Roberto G. Tomasicchio

Ing. Francesco Aristodemo

Ing. Salvatore Marrone

Coordinatore:
Prof. Ing. Francesco Macchione

Dissertazione di Dottorato di:
Domenico Davide Meringolo

– Novembre 2015 –

in memoria di
Nonno Nicola,

cui devo tanto.

Ringraziamenti

Diverse persone mi hanno seguito, appoggiato e supportato durante il percorso che mi ha portato a completare questo lavoro di tesi. Tra queste, *in primis*, desidero ringraziare Francesco Aristodemo, con il quale sicuramente ho trascorso la maggior parte del tempo, per la sensibilità, il supporto e la costante presenza. Ringrazio il Prof. Paolo Veltri per la fiducia fornitami, l'onnipresente disponibilità e la capacita di trovare sempre una soluzione ad ogni difficoltà. Un altro ringraziamento va al Prof. Roberto Tomasicchio, per gli input fornitemi nello sviluppo di diverse analisi riguardanti parte degli argomenti investigati nella tesi.

Durante il periodo trascorso in Olanda ho avuto la piacevole esperienza di poter collaborare con una persona autenticamente genuina, Paul Groenenboom. Il mio ringraziamento non va solo alle dritte scientifiche, ma soprattutto ai diversi consigli ed al supporto datomi in svariate circostanze. *Thank you Paul*.

L'ultimo periodo del dottorato di ricerca è stato sicuramente quello in cui ho imparato di più e sono arrivati anche i risultati più interessanti. Questo è stato possibile grazie alla supervisione di Andrea Colagrossi e Salvatore Marrone, dell'Istituto INSEAN-CNR di Roma. Sono estremamente lieto di aver avuto la possibilità di questa collaborazione, di fare loro più profonda conoscenza e di rimanere stupefatto del loro approccio alla ricerca, che sconfina dal campo scientifico. A loro va un mio profondo e sincero ringraziamento.

Dal mio primo lavoro di tesi triennale su frattali e turbolenza sono ormai passati diversi anni e le tematiche di ricerca sono da allora cambiate. Eppure, sebbene molte cose cambino nel corso degli anni, alcune persone rimangono sempre. Ringrazio il Prof. Massimo Veltri per la guida ed il costante riferimento e Samuele De Bartolo per avermi seguito durante diversi anni della mia formazione.

Il mio ringraziamento più grande va infine a mio padre, a mia madre, a mia sorella, ai miei familiari ed agli amici più cari, che sono come sempre il mio fulcro.

Rende, 30 Novembre 2015 *Davide Meringolo*

Sommario

I RISULTATI scientifici presentati nella tesi di dottorato riguardano la modellazione numerica, attraverso la tecnica lagrangiana SPH debolmente compressibile, di problemi di interazione fluido-struttura. Diversi aspetti, sia di natura puramente modellistico fisica che di natura ingegneristica ed applicativa, vengono investigati nella tesi.

Nello specifico, parte dei risultati presentati ha come primo obiettivo la validazione del modello numerico, ottenuta attraverso diversi test preliminari: in primis la conservazione della soluzione idrostatica in un serbatoio d'acqua, dopodiché diversi test dinamici in cui viene presentata la conservazione dell'energia, dimostrando come l'energia meccanica dissipata dal sistema venga esattamente trasformata in energia termica. Alcuni aspetti legati all'ipotesi di debole compressibilità adottata alla base del modello SPH considerato, riguardanti l'istantaneo accumulo di energia elastica durante impatti, vengono già messi in luce in questa parte della tesi. I test dinamici svolti riguardano dunque l'evoluzione nel tempo di una massa d'acqua di forma circolare sottoposta ad un campo di forze centrale che periodicamente evolve in forme ellittiche, l'analisi dell'evoluzione di diversi casi di dam-break e l'evoluzione nel tempo di un fenomeno di tracimazione di un ostacolo orizzontale investito dal moto ondoso.

Uno degli argomenti centrali della tesi di dottorato riguarda l'analisi dell'interazione di onde con strutture costiere come cassoni forati. I cassoni forati sono strutture marittime ampiamente utilizzate nelle zone portuali con l'obiettivo di minimizzare dell'energia riflessa del moto ondoso al fine di limitare oscillazioni di grande ampiezza dovute alla sovrapposizione di onde incidenti e riflesse, garantendo quindi, durante le mareggiate, condizioni di sicurezza per la navigazione. Suddette strutture sono state studiate, fino ad ora, essenzialmente attraverso modelli approssimati ed analisi sperimentali, mentre l'utilizzo di un modello numerico di dettaglio è stato raramente impiegato per il loro dimensionamento. In questo contesto, il modello SPH è stato implementato per studiarne nel dettaglio il comportamento idraulico e di stabilità strutturale. In particolare, durante le analisi numeriche si è andati incontro a difficoltà sia di natura computazionale che di natura modellistica nella loro simulazione. Una prima difficoltà è consistita nella riproduzione numerica dei muri verticali forati che costituiscono la parete frontale di queste strutture in quanto, essendo spesso caratterizzati da

spessori sottili, rendono la simulazione computazionalmente onerosa nel contesto numerico SPH. In questo contesto vengono introdotte le *multi-node fixed ghost particles*, che consentono di poter utilizzare un numero totale di particelle pari ad $(1/2)^D$, in cui D è il numero di dimensioni spaziali del problema, il numero totale di particelle altrimenti necessario. Nelle analisi effettuate relative a cassoni pienamente e parzialmente forati, in cui $D = 2$, il risparmio in termini di tempo di calcolo è stato rispettivamente del 79,5$\%$ e del 77.7 $\%$.

Un altro aspetto modellistico cui si è andati incontro nella simulazione dei problemi considerati è legato alla presenza di rumore nel campo di pressione ottenuto dalla soluzione SPH, che porta in molti casi a risultati difficilmente utilizzabili ai fini ingegneristici. Questo aspetto, che viene investigato in dettaglio nell'ultima parte del lavoro di tesi, è legato alla componente acustica della soluzione fornita dai modelli in cui il fluido è supposto essere debolmente compressibile. Nel tentativo di limitare tali oscillazioni in alta frequenza del campo di pressione, negli ultimi anni diversi autori hanno introdotto diversi termini diffusivi che agiscono all'interno dell'equazione di continuità. In generale questi modelli possono essere raggruppati in due formulazioni: la prima è costituita da termini che fanno riferimento alla formula di Morris; la seconda, nota come δ-SPH differisce dalla prima essenzialmente per l'aggiunta di gradienti renormalizzati del campo di densità. La prima famiglia di modelli è caratterizzata dall'introduzione di errori numerici in prossimità della superficie libera ed, inoltre, l'azione di "smoothing" deteriora la soluzione idrostatica nel tempo. In presenza invece di impatti l'azione diffusiva svolta da questi modelli risulta essere efficace nell'attenuazione di onde di shock non fisiche successive all'impatto. Il modello δ-SPH, essendo invece un operatore più accurato, non introduce alcun errore vicino alla superficie libera e conserva la soluzione idrostatica nel tempo. Nel caso invece di impatti, questo modello risulta essere meno efficace nell'azione di attenuazione delle onde di shock.

Al fine di avere un modello che conservi le proprietà del fluido quando questo è caratterizzato da fenomeni di dinamica lenta e che agisca al meglio nel processo di attenuazione delle onde di shock conseguenti a dinamiche di impatto, o veloci, viene introdotto un *modello diffusivo ibrido* che permette di passare da una formulazione all'altra, a seconda delle condizioni presenti nella massa fluida, grazie all'introduzione di un parametro, β, che attiva o disattiva i gradienti renormalizzati di densità.

La modellazione dei contorni solidi sottili ed i termini diffusivi ibridi presentati vengono implementati per la simulazione numerica SPH dell'interazione onda-cassone forato. I risultati analizzati riguardano sia l'aspetto di stabilità dell'opera, riguardante in questo caso la valutazione delle pressioni dinamiche agenti sulle pareti della struttura, sia l'aspetto idraulico, riguardante la valutazione dei coefficienti di riflessione. Per quanto concerne le distribuzioni di pressione, i risultati numerici ottenuti dimostrano la presenza di cadute di pressione in prossimità dei fori della struttura legati all'effetto Bernoulli. Questo risultato numerico richiede, ad ogni modo, una più profonda investigazione dal punto di vista sperimentale, attraverso l'osservazione del comportamento del campo di moto in prossimità dei fori della parete. Per quanto concerne invece le analisi idrauliche, i coefficienti di riflessione sono stati valutati attraverso un metodo classico, considerando diversi valori del rapporto tra la larghezza della camera di assorbimento e la lunghezza d'onda.

Nell'ultima parte del lavoro di tesi viene investigato il problema del rumore acustico nelle soluzioni ottenute dal presente modello SPH (e che riguarda, in generale, tutti i modelli debolmente compressibili) e viene presentata una procedura per il filtraggio corretto di tale componente basata sulla trasformata wavelet. L'idea che sta alla base della procedura di filtraggio presentata si basa sul fatto che la soluzione debolmente compressibile può essere scritta, per piccoli valori del numero di Mach, come la sovrapposizione di una soluzione incompressibile più una perturbazione acustica. Le equazioni di Navier-Stokes debolmente compressibili vengono dunque analizzate mettendo in evidenza la presenza di perturbazioni acustiche. Tale componente acustica è risolta analiticamente per un caso circolare, per cui viene dimostrato come i modi di vibrare ottenuti analiticamente corrispondano esattamente alle frequenze di vibrazione ottenute dal segnale di pressione simulando lo stesso problema con SPH. L'analisi successiva è effettuata considerando il problema della massa d'acqua sottoposta ad un campo di forze centrale. In questo caso, si osserva come la procedura presentata attraverso le wavelet consenta di filtrare correttamente la componente acustica, ottenendo esattamente la soluzione analitica. Questo risultato, essendo infatti caratterizzato da dinamiche non di impatto, è caratterizzato da un definito disaccoppiamento delle componenti acustica ed incompressibile, facendo si che il processo di filtraggio consenta di eliminare esattamente la componente acustica.

I casi analizzati successivamente riguardano invece dinamiche più complesse, in cui avvengono impatti fluidi, caratterizzati quindi da singolarità nel campo di pressione. In questi casi si osserva come, al crescere dell'impulsività del fenomeno, la componente acustica ed incompressibile risultino sempre più accoppiate tra loro, per cui la procedura di filtraggio inevitabilmente elimina insieme alla componente acustica anche parte della soluzione incompressibile del problema, ovvero quella fisicamente basata. Tali risultati vengono analizzati considerando un cuneo d'acqua che impatta su una parete verticale e prendendo in esame un caso di sloshing in cui si osservano fenomeni di frangimento delle onde.

Abstract

THE present thesis deals with the numerical modeling of fluid-structure interaction problems through the Lagrangian weakly-compressible Smoothed Particles Hydrodynamics (SPH) method. Different aspects, embracing computational enhancements, investigation on physical issues of weakly-compressible solutions and applications to engineering problems, are investigated. In particular, the initial investigations aim to validate the numerical model through several preliminary tests: a first one dealing with the conservation of the hydrostatic solution for a still water tank, then various test cases in dynamic conditions in which the conservation of energy is analyzed, showing the dissipation process of mechanical energy into thermal energy during the flow evolution. Some aspects related with the weakly-compressibility assumption in SPH, regarding the instantaneous accumulation of elastic energy during impacts, are highlighted in this part of the thesis. Preliminary tests in dynamic conditions refers to the time evolution of a water drop subjected to a central force field, dam-break flows and a wave overtopping a horizontal deck placed above the still water level.

A central argument of investigation is the wave interaction with coastal structures, such as perforated breakwaters. In this context, the SPH method is used to analyze the performances of these structures in terms of wave pressures at the walls and reflection coefficients. Some difficulties have been encountered for their numerical modeling. In particular, since the slotted front walls of the caissons are often characterized by a small thickness, the result is that, for a correct numerical treatment of thin solid elements, a high spatial resolution is required, resulting in an expensive computational cost for the simulation. The fixed ghost particles technique to model the solid boundary is here extended through the adoption of more interpolation nodes for the same solid particle, resulting in a multi-node approach. In the proposed multi-nodes fixed ghost particles approach allow for a reduction of the total number of particles to $(1/2)^D$, in which D is the number of dimensions of the problem, the total number of particles otherwise needed with a classical approach.

Another aspects analyzed in the thesis is the presence of noise in the pressure solution related to the acoustic component of the weakly-compressible SPH solvers. In order to limit the occurrence of pressure disturbances, several authors have introduced

different diffusive corrections acting within the continuity equation to stabilize the solution. Synthetically, these models can be grouped into two families. The former refers to the terms approximated through the Morris formula, while the latter refers to the δ-SPH model, that differs for the addition of renormalized density gradients. For the cases characterized by water impacts the Morris-like formulations result to be more effective in the smoothing of unphysical shock waves consequent the impacts, while the δ-SPH is more suitable in slow dynamics problems in which it results to be more conservative for the flow properties. In this context, a hybrid diffusive formulation between these two diffusive terms is introduced in order to deal with problems characterized by phenomena in which both slow and fast dynamics occur.

The simulation of wave interaction with perforated breakwater are performed by implementing the mentioned improvements. Regarding the wave pressure distribution, the numerical results have shown the presence of pressure drops close to the holes of the structures. This fact is related with the Bernoulli effect's and is due to the pressure gradients encountered between the holes of the breakwater. Regarding the hydraulic analysis, the reflection coefficient is evaluated through the method of Goda and Suzuki considering time series of surface elevations for different values of the ratio between chamber width B and wave length L.

In the last part of the thesis, the drawback of the noise in the pressure field is deeply investigated. Indeed, the use of the diffusive formulations allow for a smoothing only of the high frequency noise related with the scale length of the support kernel where the diffusive term operates. However pressure perturbations still persist in the numerical solution. The result is that often the SPH pressure solutions have to be filtered in order to obtain a practical result for engineering applications and this procedure is often arbitrarily performed. In this context a precise filtering algorithm, based on the wavelet transform, is introduced. The basic assumption for the methodology is that the weakly-compressible solution can be expressed, under certain conditions, as a superposition of an incompressible solution and an acoustic perturbation. The wavelet transform allows therefore to identify the frequencies related with the acoustic perturbations and recover the incompressible solution by filtering the acoustic component. This method is applied considering different test cases. In particular, it is highly efficient for cases in which violent fluid impacts do not occur and therefore the incompressible and acoustic components can be decoupled. When the impulsiveness of the flow dynamic increases the incompressible and acoustic perturbation result to be coupled resulting in difficulties for the application of the filtering procedure. The analyzed cases regard a water wedge impacting a vertical wall and a sloshing process with the formation of breaking waves during the flow evolution.

Contents

CHAPTER 1

Introduction

1.1 Outline of the thesis

A topic of relevant interest in a broad range of applied sciences is the interaction between fluids and structures. Hydraulic engineers invest enormous efforts in the study of various phenomena dealing with water dynamics in presence of solid bodies, especially when impulsive situations like water impacts or slamming on perforated/solid walls take place. These studies prove to be fundamental for the support of the design process in terms of knowledge of the efficiency, performances and also durability of the analyzed structure. In coastal engineering field, these issues find applications in different research subjects. Among them it is possible to mention the understanding of the water dynamics through slotted structures such as perforated breakwaters, the comprehension of complex flow dynamics such as wave overtopping, reflection and transmission, sloshing processes and the knowledge of the actions exerted by waves on rigid elements in breaking and non-breaking situations. The present thesis deals with the numerical modeling of the interaction between fluid and structures.

One of the most affirmed and reliable approach in solving complex fluid dynamic problems is furnished by the numerical analysis. Nowadays grid-based numerical methods are widely applied to various areas of computational fluid mechanics and represent the dominant approach to solve fluid dynamic problems. In grid-based models a prerequisite for the numerical simulation is the mesh generation for the problem domain. Since different phenomena studied in this thesis are characterized by violent dynamics with large fluid deformations, their analysis result to be a quite difficult matter when a conventional method is employed. Situations characterized by strong deformations, such as breaking waves, splashing and fragmentation, contain intrinsic difficulties for standard methods. Indeed, in Eulerian grid methods, the construction of a regular grid for irregular or complex geometries requires additional computations that can be, in

some cases, even more expensive than solving the problem itself. Despite the great success, grid-based numerical methods still suffer from some difficulties in different aspects, which limit their applicability in many problems.

In this context, the Smoothed Particle Hydrodynamics (SPH) model, because of its meshless nature, represents a good alternative. In SPH the flow evolution is described following the motion of a set of fluid particles, resulting in a Lagrangian representation of the fluid. The SPH particles, being both approximation points and material components, allow for a simple tracking of the fluid evolution for problems in which large deformations occur. It has to be also underlined that some theoretical aspects of the SPH related with the accuracy of the method are elusive when dealing with a set of disordered particles. This aspect induced a general mistrust from the scientific community with respect to the reliability of the method. However, the insights and enhancements obtained in the last decades from different researchers allowed for a deeper understanding of the SPH nature and resulted in improvements in terms of its stability and applicability. These achievements lead to the implementation of SPH to a wider number of hydraulic problems, resulting therefore in an increasing number of practitioners. Moreover, the development of the computational capability of the calculators allowed to perform simulations of detail for problems whose study is practically impossible to achieve employing another approach. Today, in fact, it is customary to see SPH simulations performed with the order of a billion or even more number of particles to reproduce full-scale dynamic problems.

The SPH has been already largely applied for analyzing offshore and coastal engineering problems. In recent years the study of different coastal structures found a wide interest for their construction in harbors and marine areas. Among them it is possible to mention the perforated breakwaters. The aim of these structures regards the dissipation of the incident wave energy, allowing for safe navigation conditions during sea storms. The dissipation process that occurs in the non-reflective cells of the perforated breakwater, depends on the geometrical configuration of the caisson chamber. Their configurations, as it is possible to see in Fig. 1.1, can be even complicated in order to maximize the dissipation process. In this context, the mechanics of the dissipation is not yet well understood. The water dynamics inside the chamber of the caisson, induced from the wave action, is a complex phenomenon in which the pressure gradients between the outside and the inside of the structure regulates the flow evolution. The hydraulic efficiency of the breakwater is measured in terms of reflection coefficient, generally defined as the ratio between the reflected and incident wave amplitudes. This parameter, at a first approximation, is dependent on the incident wave length, L, and on chamber width, B. For this reason it is usual to study their performances by varying the ratio B/L.

The dimensioning of perforated breakwaters is essentially based on approximated formulas. Classical methods to predict wave forces on dikes and slotted walls are based on empirical formulations, obtained from laboratory observations. The use of numerical methods to simulate their performances has been rarely adopted to support their design. In this context, the present thesis aims to furnish an insight to understand the wave dynamics into the chamber, the actions exerted by the waves at the walls of the structure and the hydraulic properties regarding the reflection coefficient.

When the fluid-structure interaction becomes more violent, the actions exerted on

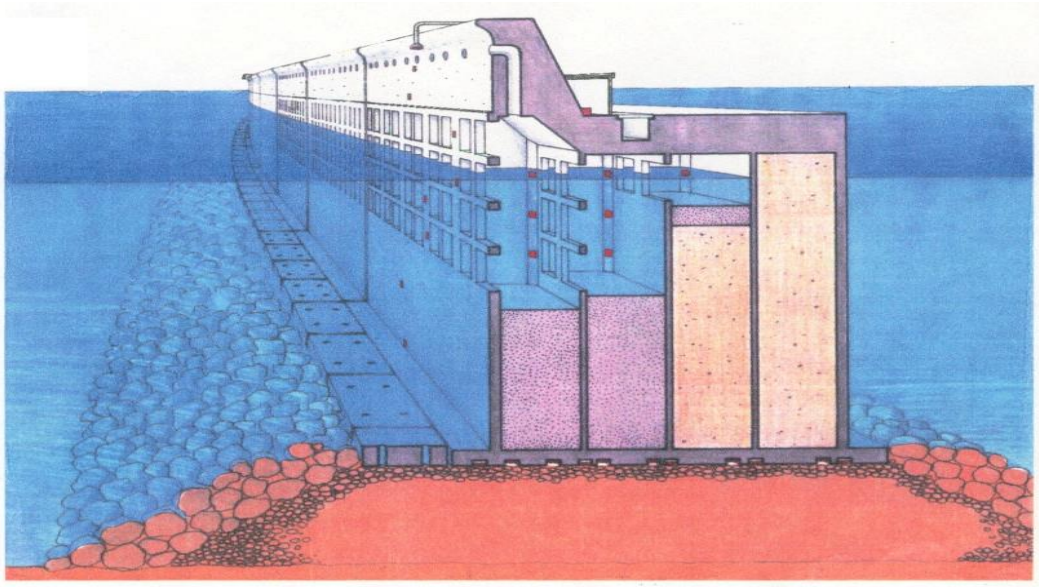

Figure 1.1: *Perforated breakwater made by cellular concrete caissons, crown walls and anti-reflective cells in Porto Torres, Italy (De Girolamo [41]).*

the solid elements become more severe and their knowledge is essential for engineering purposes. Indeed, protective structures like sea walls and their slender components such as crown walls, need to be sufficiently robust to withstand the most violent wave impacts. Fig. 1.2 shows a wave breaking on a vertical wall and represents a situation often encountered in case of sea storms. The complexity of these phenomena is far to be completely understood resulting, also in this case, in the use of simplified models for their characterization. The size and duration of water-wave impact pressure are relatively well investigated in literature. Blackmore and Hewson [14] found that for a wave with a height of about 1 m the maximum pressure can be of the order of 10^5 N/m^2. The remarkable evidence is that, during these events, the pressure rises and falls in a time window of the order of 10^{-3} s. The study of phenomena characterized by violent fluid interaction with solid structures is today investigated through both experimental and numerical analyses. Regarding the former, the accuracy of the measurements is fundamental for a correct evaluation of the pressure peaks and experimental sensors with high frequency sampling and spatial resolution are necessary to capture these rapid dynamic changes and the spatial occurrence. These instrumentation are often expansive and require for their installation a troublesome procedure, particularly at the edges of the structures and along curved boundaries.

On the other hand, the numerical analysis offers another approach to study the problem. Also in this case there are some shortcomings in modeling these events. In computational fluid mechanics, especially when the interaction between fluid and structure becomes more impulsive, it is fundamental to know the features of the numerical scheme adopted and the hypothesis made for the fluid, or for the mixture of fluids, in order to obtain results related with the real physics of the problem. For example, the fluid in SPH is generally modeled as a weakly-compressible medium. Though convenient form a computational point of view, this assumption sometimes leads to the appearance

of high frequency noise in the pressure field. The presence of these pressure oscillations in the SPH solution makes the result unpractical for engineering applications if the data are not post-processed. For this reason, the pressure results are usually filtered and the choice of the type and magnitude of the filter is often made in a arbitrary way. In this context, the thesis presents a deeper study of the acoustic component in weakly-compressible solutions and a rigorous approach for their filtering based on the individuation of the acoustic frequencies. The filtering of the acoustic component in

Figure 1.2: *Snapshot of a wave impacting a vertical wall (photograph D.H.Peregrine).*

weakly-compressible schemes allows therefore to recover the incompressible solution of the problem. Generally, most of the problems characterized by impulsive fluid dynamic can be simulated with this approach. Fig. 1.3 presents a simplified scheme of a wave breaking on a vertical wall, with a particular focusing on the contact area of the

impact. As it is possible to see, the wave configuration at the wall can be schematized as a water wedge characterized by a *deadrise angle*, α, defined as the angle between the wall and the approaching water mass. In this case the dynamic of the impact is highly dependent on the value of the deadrise angle. As pointed out by Zhao and Faltinsen [159], only when $\alpha > 4°$ the compressibility effects of the fluid are negligible and an incompressible description of the dynamic is physically correct. In this case, moreover, if the fluid is modeled as weakly-compressible the filtering of the acoustic component allows to recover the incompressible solution, under the condition that acoustic and incompressible components are decoupled.

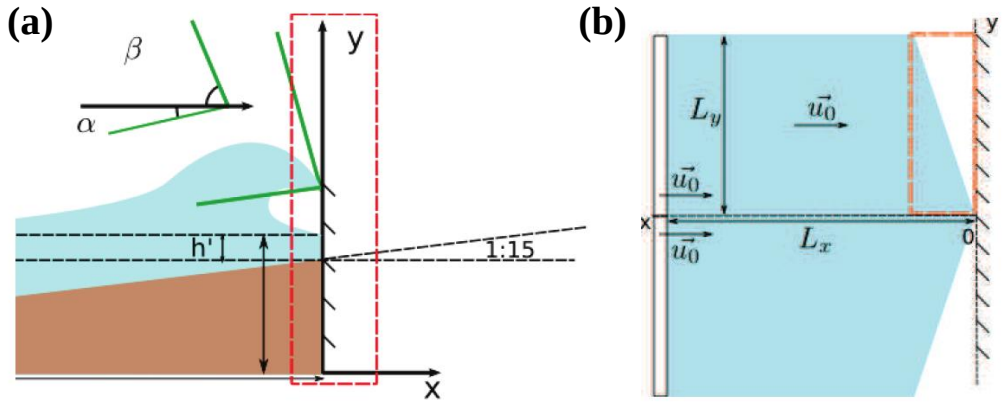

Figure 1.3: *Wave breaking onto a vertical wall; in (a) is the wave configuration at the wall, while in (b) is a schematized description of the impact (Lu et al. [90]).*

A different situation is encountered in the limit condition of a flat impact, *i.e.* when $\alpha \to 0$, in which the water hammer (acoustic) effect related with the real compressibility of the medium defines the magnitude of the exerted actions. In this case, if the fluid is modeled as incompressible the effects related with the water compressibility are not contemplated in the numerical solution missing to capture the acoustic shocks. In this case, the incompressible pressure field solution instantaneously "adapts" to the new configuration after the impact. As it is possible to see in Fig. 1.4 (a), in presence of a flat impact, modeled with a mono-phase incompressible model, the pressure field is dependent on the time-step adopted. In this case, indeed, when the numerical solution tends to the original differential problem, *i.e.* $\Delta t \to 0$, the pressure solution becomes singular, $P^{Inc}_{MAX} \to \infty$. In singular conditions therefore the incompressible solution could not be representative for the problem.

A different situation is encountered when the fluid is modeled as weakly-compressible. In this case, as described before, the pressure peak is determined by the acoustic shock and is therefore dependent on adopted speed of sound for the simulation, c. As it is possible to observe in Fig. 1.4 (b), for a flat impact modeled with a mono-phase weakly-compressible model, the pressure peak assumes a value $P^{Comp}_{MAX} = \rho_0 c U$. This quantity is indeed the pressure of the water-hammer (acoustic) effect, in which, however the entity of the peak depends on the artificial compressibility given to the fluid through the speed of sound adopted in the simulation. The pressure wave generated at the impact propagates along the fluid domain, reflecting when arrives at the boundaries. In this case, if the boundary is the free surface a negative wave pressure is reflected back,

while if the boundary is a solid one, a positive wave pressure is reflected back. As described in Marrone et al. [100], the wave reflection process continue until its energy is dissipated.

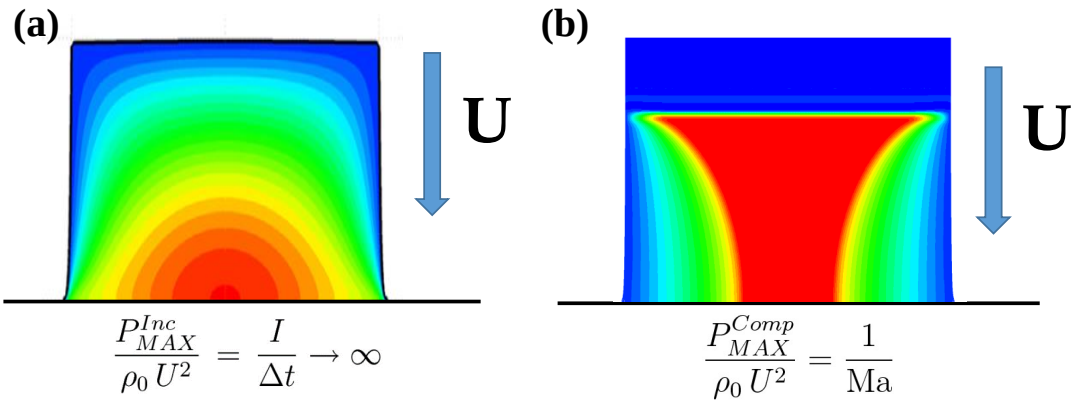

Figure 1.4: *Flat impact of a rectangular water patch to a horizontal wall; in (a) is the incompressible solution, while in (b) is the compressible solution. (Colagrossi and Souto-Iglesias [31]).*

As pointed out by Cooker and Peregrine [32], when describing the large brief pressures of wave impact, the effects of compressibility of the fluid may play a role in this case. Considering pure water at atmospheric pressure condition and temperature 20 °C, the resulting speed of sound is $c = 1484$ m/s. This value however, is not representative of the fluid phase encountered at the impact interface, in which the trapped air bubbles play a crucial role. As highlighted by Peregrine [124], for laboratory waves, the compressibility of the air can give rise to two important features: an increase in the duration of the pressure peak, with related reduction of peak pressure, and oscillations of pressure following the peak. The effect of even a small volume fraction of air in water greatly increases its compressibility. At atmospheric pressure, just 1% of air gives a velocity of sound of 120 m/s, and velocities as low as 30 m/s for 20% of air. High air percentages are characteristic of situation in which the wave breaking occurs before the impact with the wall. In these cases the speed of sound of the mixture air-water serendipitously assumes values in the range of those assumed for the artificial speed of sound adopted in the weakly-compressible SPH simulations. The result however obtained from a weakly-compressible solution with the mentioned values of speed of sound can not be considered for a comprehensive analysis of the phenomenon, if a mono-phase approach is used. In these cases indeed, the problem needs to be modeled, for an effective evaluation of the wave actions, by taking into account the presence of air, using a double-phase model.

Since the analysis developed in the thesis are based on a mono-phase model, the hydraulic applications analyzed all refers to problems in which the presence of air does not play an effective role in the dynamic evolution.

1.2 Brief overview on meshless methods

Numerical methods are based on the fundamental idea of discretize the computational domain into a finite number of nodes in and solve the governing partial differential equations with respects of these nodes. Classical methods need an *a priori* definition of the connectivity between these points, resulting in the creation of a fixed mesh for the considered problem. Following this strategy, the fluid results to be described with a Eulerian approach: the observer keeps a fixed position in space resulting in a spatial description of the flow quantities. The most well-known members of these widely developed mesh-based methods are the Finite Element Method (FEM), the Finite Volume Method (FVM) and the Finite Difference Method (FDM).

A different approach is obtained when the partial differential equations are only written on a set of nodes without the need for an additional mesh. This relatively new class of numerical solvers are often referred as *meshless*, *gridless*, *element-free* or *particle* methods. In this case, the fluid is described with a Lagrangian approach: the observer follow the fluid trajectory by keeping a velocity identical to the fluid element, resulting in a material description of the flow quantities. A multitude of meshless methods has been presented during the last decades and a comprehensive classification of these approaches has been presented by Fries and Matthies [57].

One of the first particle methods was the Particle In Cell (PIC) model, introduced in 1964 by Harlow [70]. Smoothed Particle Hydrodynamics was born in 1977 with the works of Lucy [91] and Gingold and Monaghan [61], who presented a modified version of PIC in which a pure particle treatment was also introduced for the pressure term. Successively many other approaches have been developed. Among them it is possible to mention the Diffuse Element Method (DEM) introduced by Nayroles et al. [122], based on a Moving Least Square (MLS) approximation within a Galerkin method. This approach resulted to be consistent and quite stable but more expensive than the original SPH. Belytschko et al. [11] further developed this method and renamed it Element Free Galerkin (EFG). Belytschko et al. [10] pointed out that all the methods based on MLS approximation belong to a bigger class of meshless methods named Partition of Unity. More recently the Meshfree Local Petrov-Galerkin (MLPG) and Local Boundary Integral Equation (LBIE) have been developed and a description of these methods is furnished by Atluri and Zhu [8].

Another family of meshless solvers is represented by the Vortex Methods. In this case the fluid dynamic equations are written in terms of the vorticity field, being this quantity the computational variable. Since the vorticity is defined as the curl of the velocity field, this last variable is obtained through a spatial integral of the vorticity field. Through this approach, moreover, the pressure field is not explicitly solved. A practical introduction to this family of methods has been presented by Cottet and Koumoutsakos [33]. By contrast with the SPH, in which it is more difficult to model vorticity and in general turbulence, Vortex methods result to be very efficient for problems characterized by high vorticity fields.

Among the mentioned meshless methods, SPH results to be one of the most used and developed schemes for engineering applications. The versatility of the method is one of the key point for the success of SPH and for these reasons it has been chosen for the analysis in the present thesis.

1.3 SPH: a state of art

SPH was firstly applied in astrophysical field to simulate the interaction of boundless fluid masses in vacuum (see *e.g.* [91], [61]). For many years this technique has been applied only to astrophysical problems. The method has been successively extended to other contexts, with the aim to solve various engineering problems, from solid to fluid mechanics and multiphase flows. Several researchers have recently devoted their activity to improve this method. Therefore, the state of art about all the aspects of SPH embrace many disciplines and for a more exhaustive description the reader should refer to Monaghan [110]. In this section, the most remarkable contributes, related to the outline of the thesis, are illustrated.

1.3.1 Stability issues and their enhancements

The properties of the continuous SPH interpolation are well known. When implementing the method in computational mechanics, the integral interpolations becomes a summation over the total particles, N_p, used to discretize the domain. Di Lisio et al. [43] proved the convergence of the SPH discrete equation to the regularized Euler equation for a generic polytropic fluid in the case of $N_p \to \infty$, when the number of interacting particles $N_{int} \to \infty$. Successively this result was also confirmed by Rasio [127] using an analysis based on acoustic wave propagation. From these results it became clear that the SPH method is always convergent when the fluid is discretized with an infinite number of particles each of them having an infinite number of interacting particles. This result however gave no idea about what happens in practical situations, *i.e.* when N_p and N_{int} are not infinite. In this case indeed it has been demonstrated that the solution is strictly depended on the level of disorder assumed by the particles. In the case of particles collocated on a regular mesh with N_{int} constant and large enough, Colagrossi [26] has shown that the integral interpolation inside the fluid domain presents a second order accuracy, as in the case of the continuous formulation. A different situation is encountered when dealing with a set of disordered particles. In this case, only more recently the behavior of the interpolation became clear. One of the first analysis on the disorder in the SPH scheme has been presented by Quinlan et al. [126], where the analysis has been conducted by a one-dimensional approach. In their work it is shown that, while increasing the number of points, the second-order convergence is retained only up to a certain threshold refinement. After that increasing the resolution does not reduce the error interpolation. In the work by Antuono et al. [3] the analysis has been extended disregarding the number of spatial dimensions, through the introduction of a parameter defining the level of disorder. From these results it is possible to observe a degradation of the accuracy, as the particle disorder increases.

Stability represents a crucial topic for the SPH method. One of the major issue when dealing with a discrete SPH model is known as *tension instability* and represents the major drawback of the method. When the particles are subjected to negative stresses their resultant action becomes attractive, resulting in the introduction of unphysical forces. As a consequence of the negative pressures an unphysical cavitation is observed in the SPH solution. This situation is often encountered instantaneously after fluid impacts, as a consequence of the negative shock waves generated in the collisions. A first attempt to control this effect was presented by Monaghan and Gingold [112], with

the introduction of an artificial viscosity into the momentum equation in order to damp the oscillations appearing in shock waves. Successively Morris et al. [119] presented another version for the artificial viscous term. The artificial viscosity presents the same aspect of a real viscosity, but it differs from the latter because is a function of the adopted resolution, *i.e.* it vanishes when $N_p \rightarrow \infty$. Even if the use of the artificial viscosity do not allows to get rid of the SPH instabilities, it provides an improvement on the numerical stability. Indeed, nowadays the use of an artificial viscosity is a tool of common practice in SPH solvers. Another approach to the problem has been presented by Moussa et al. [120] with the introduction of a Riemann solver to avoid the use of artificial viscosity and regularize the pressure field.

Monaghan [107] presented an anticlumping term to introduce in the momentum equation in order to avoid the clustering of the particles. This correction acts as a repulsive force only when the pressure of the particles becomes negative and their mutual distance is smaller than the spatial resolution. This term introduces a force that, even if it acts slightly and only in certain situations, is not motivated by physical reasons. The anticlumping term allows to avoid the occurrence of tensile instability but, when violent dynamics occurs, some instabilities still persist in the solution.

Another evidence observed in the SPH model, is the reassessment of the fluid particles in the domain during the simulation. Concerning this aspect, Le Touzé et al. [81] noticed that it is strictly dependent on the adopted resolution. Indeed, when refining, the effect of the self-redistribution is quickly attenuated and it is almost hidden within other "regular" errors. This result is consistent with the fact previously presented that when the number of particles used for the simulation is big enough, the SPH discrete solution behaves as in the continuous formulation. In order to find a solution to this problem, Colagrossi et al. [29] introduced a packing algorithm that allows to encounter the configuration of minimal energy for the fluid particles, avoiding self-redistribution effects. It is noticed also that, in the case of the use of a corrected scheme, such as a MLS operator, the self-redistribution mechanism is not present. In these case however some other complications are introduced in the numerical solution.

A crucial aspect of the weakly-compressible SPH is the presence of noise in the pressure solution. In order to obtain a more regular solution a first solution has been presented by Colagrossi and Landrini [30], through the use of a periodic re-initialization of the density field. While this approach yields good pressure results, it does not conserve the total volume of the fluid system for long time simulations, because the hydrostatic component is improperly filtered (Antuono et al. [4]). In the last years another practice to control these fluctuations and also enhance the stability of the model has been presented through the introduction of diffusive corrections. The diffusive term acts in the continuity equation as a numerical mass diffusion and presents a similar mathematical structure of the operator used for the artificial viscosity. The first diffusive schemes have been presented by Molteni and Colagrossi [104], Ferrari et al. [56] and successively by Groenenboom and Cartwright [68]. A slightly different approach has been introduced with the δ-SPH by Antuono et al. [6]. This formulation has been successfully applied to several hydrodynamics problems proving to be stable and accurate (see *e.g.* [96], [5], [98], [7]). The δ-SPH recently has become a quite popular variant of the standard SPH, being used in several engineering applications (see *e.g.* [16], [40], [90]).

1.3.2 Treatments of solid boundaries

The boundary conditions enforcement is a crucial topic when simulating the interaction of fluid with solid structures and represents a central topic of the thesis. When SPH was first applied to astronomical problems, since the all studied phenomena occurred in open space, there was no need to enforce solid boundary conditions. After the first application of SPH to free surface flows, introduced by Monaghan [106], solid boundary enforcement becomes an important issue for SPH simulations.

The free surface boundary condition results to be intrinsically verified in the SPH model. A different situation is encountered when dealing with a solid boundary, in which it is necessary to represent the solid components interacting with the fluid mass. A classical approach to set solid boundary conditions in hydrodynamic simulations was introduced by Monaghan [106], by considering an intermolecular repulsive force. A drawback of this approach is that the pressure field resulted as being noisy near the solid boundaries. This technique was subsequently improved by Monaghan and Kajtar [113] to treat solid shapes more effectively. As pointed out by Colagrossi [26], the main drawbacks of such technique are the pressure wave disturbances at the beginning of the numerical simulation and the inadequacy in calculating accurately the local hydrodynamic loads induced on the structures.

Another approach to model solid boundaries is the *ghost particles* technique, first introduced by Libersky et al. [85] and developed by Colagrossi and Landrini [30] to exactly enforce boundary conditions in inviscid free-surface incompressible flows. In the ghost particles technique, the fluid particles approaching the solid boundary are mirrored with the respect of the body profile, in a layer with size equal to the adopted kernel radius. This method can be easily applied to straight profiles and right angles, but it becomes more complicated when a generic solid shape is considered. Marrone et al. [96] proposed an enhanced version of this method, introducing the *fixed* ghost particles. In this case, the ghost particles are fixed in the frame of reference of the body and the values attributed to these particles are calculated at their interpolation nodes located inside the fluid domain. The values associated to them are obtained from a MLS interpolation over the fluid particles, within the range of influence. The main advantage of using fixed ghost particles instead of standard ghost ones is that their distribution is always uniform because it does not depend on the fluid particle positions. In the work by De Leffe et al. [42] the ghost type particles are characterized by different treatment when dealing with hyperbolic and elliptic parts of the Navier-Stokes equations to enforce boundary conditions. In particular, the free slip condition is used to compute the pressure gradient and velocity divergence, whereas the no-slip condition is enforced for calculating Laplacian velocity, resulting in different values of velocity associated to the same solid particle. The fixed ghost particle technique has been successfully applied to a wide range of fluid dynamic contexts such as the study of free-surface open-channel flows (see *e.g.* [55]), wave patterns induced by ships (see *e.g.* [99]), flows past square or circular cylinders (see *e.g.* [150], [98]) and flow separation at bends (see *e.g.* [71]).

1.3.3 Hydraulic applications

Applications of SPH to hydraulic problems started in 1994, after the work of Monaghan [106] about a simple bam-break flow. As expressed by the same author, the possibility of treating the fluid as incompressible seemed too difficult to be practiced in the SPH framework. In this context, a weakly-compressible approach appeared to be more promising, on the condition that the density fluctuations remained confined in the order of 1% the incompressible density. This approach began to be extended to a wide class of problems like wave breaking on beaches. Monaghan [114] studied the dynamics of a solitary waves breaking on a beach, while Monaghan and Kos [115] the waves produced by rigid bodies sliding down a ramp. A detailed study of wave breaking processes has been presented by Dalrymple and Rogers [37] and Landrini et al. [79]. Another phenomenon investigated by many authors in literature through the SPH is the sloshing process (see *e.g.* [26], [144], [143], [101]). Other studies related with water wave problems investigated in literature are the green water overtopping (see *e.g.* [65], [60]), solitary waves (see *e.g.* [83]), bow waves generated by ships (see *e.g.* [99], [80]), non-linear periodic waves (see *e.g.* [67]) and tsunami waves (see *e.g.* [77]). Rodriguez-Paz and Bonet [129] presented a corrected SPH formulation of the shallow-water equations, while De Chowdhury and Sannasiraj [39] studied the wave propagation in shallow water conditions. The dynamics of water impacts has been also extensively studied by different authors from the slamming of a hull on a free surface (see *e.g.* [151]), wave breaking on a vertical wall (see *e.g.* [90]), to the study of more critical phenomena, such as flat impacts (see *e.g.* [100]). The interaction between regular waves and vertical breakwaters or rubble mound breakwaters have been studied in coastal engineering field (see *e.g.* [130] [2]). Perforated breakwaters have been recently studied by Jiang et al. [76], in which the relationship between the ratio of total horizontal force acting on caisson under regular waves and its influence factors is examined. In fluvial hydraulic context, Federico et al. [54] proposed an algorithm to simulate open-channel flows and applied it to the analysis of uniform, non-uniform and unsteady flows.

An alternative approach to simulate incompressible flows has been presented by Cummins and Rudman [35] with the introduction of the Incompressible SPH (ISPH). This approach is based on a two-step projection method, in which the divergence-free velocity field is obtained by solving the Poisson pressure equation. Other methods to model the fluid as exactly incompressible have been then developed by Shao and Edmond [138] and Ellero et al. [49]. The ISPH has been also successively applied to solve various hydraulic problems, such as wave overtopping (see *e.g.* [140]), wave breaking and overtopping with turbulence modeling (see *e.g.* [139]). Lind et al. [86] presented a generalized diffusion-based algorithm for stability and validations for impulsive flows and propagating waves in Incompressible SPH. Even if the weakly-compressible approach has higher computational potential, the incompressible approach presents also some advantages and are discussed by Lee et al. [82].

1.4 Structure of the thesis

The thesis embraces different aspects, from the description of the fluid dynamic equations to the corresponding numerical method developed for the application to the problems of interest. Specifically, chapter 2 presents the equation governing the dynamics of fluid and the SPH method. Here it is shown moreover how these equations are discretized in the SPH framework to be adopted for the simulations, together with the numerical corrections to improve the calculation.

In chapter 3 the computational strategies adopted for the SPH solver are presented. The different diffusive corrections are shown and two *hybrid formulations* are introduced to deal with phenomena characterized by both slow and fast dynamics. The fixed ghost particle treatment is extended to model solid boundaries in which the thickness of the body is small and the fluid ambient surrounds the wall from more than one side, as in the case of objects immersed in water. In this context *multi-node* fixed ghost particles are introduced to overcome this drawback. Attention is also devoted to the time integration schemes and to the procedure adopted to evaluate dynamic pressures at the body profile in the simulations.

Preliminary analyses are shown in chapter 4. These results are presented for the conservation of energy in different situations, regarding a simple hydrostatic tank, a prototype problem of an oscillating drop under the action of a central force field and dam-break problems. In the last part of the chapter the multi-node fixed ghost particles treatment is validated in a hydrostatic case, regarding the conservation of the solution and a hydrodynamic test, regarding a wave hitting a thin horizontal deck.

The analysis of wave interaction with perforated breakwaters is presented in chapter 5. The simulations are firstly performed for a vertical wall with a successive application to different types of perforated wall caissons. The numerical results are in this case compared with experimental data. A successive analysis regards the simulation of perforated breakwaters with thin front wall. In this case the multi-nodes fixed ghost particles are employed for the simulation. The analysis are performed for both pressure distributions at the walls and for the evaluation of the reflection coefficient.

In chapter 6 the post-processing of the pressure signals obtained from a weakly-compressible SPH solution is presented. The filtering approach is exploited through the wavelet analysis, which allows for the analysis of non stationary signals, as in the case of classical fluid dynamic problems. The case of the oscillating drop is firstly analyzed. Successive analyses regards a water wedge impacting a vertical wall and a sloshing dynamic.

CHAPTER 2

Fluid dynamic equations and SPH

2.1 Governing equations

The equations governing fluid dynamics problems are expressed by a scalar equation representing the conservation of mass and a vectorial equation representing the conservation of momentum. In situations in which also the internal energy is a quantity of interest for the problem, a third scalar equation representing the conservation of energy, is introduced. These equation, known as Navier-Stokes equations, read as:

$$\begin{cases} \dfrac{D\rho}{Dt} = -\rho \nabla \cdot \boldsymbol{u} \\ \dfrac{D\boldsymbol{u}}{Dt} = \boldsymbol{g} + \dfrac{1}{\rho} \nabla \cdot \mathbb{T} \\ \dfrac{De}{Dt} = \dfrac{1}{\rho} \mathbb{T} : \mathbb{D} - \nabla \cdot \boldsymbol{q} \end{cases} \tag{2.1}$$

In system 2.1, ρ, $\boldsymbol{g}$ and $\boldsymbol{u}$ represent the density, the external volume forces and the velocity vectors, respectively. The terms e and $\boldsymbol{q}$ are the specific internal energy and the heat flux. The quantity $\mathbb{T}$ represents the stress tensor, while $\mathbb{D}$ is the strain rate tensor, $\mathbb{D} = (\nabla \boldsymbol{u} + \nabla \boldsymbol{u}^T)/2$. From the stress tensor is possible to define the pressure at a point in a moving fluid, p, as the mean normal stress with reversed sign:

$$p = -\text{tr}(\mathbb{T})/3 \tag{2.2}$$

It is convenient to rewrite the stress tensor as the sum of an isotropic part, $-p\mathbb{I}$, where the quantity $\mathbb{I}$ represents the Kronecker tensor, and a remaining non-isotropic (deviatoric) part, $\mathbb{V}$, representing the viscous contribution, entirely due to the motion of the

fluid [9]:

$$\mathbb{T} = -p\mathbb{I} + \mathbb{V} \tag{2.3}$$

In the case of a Newtonian fluid, the viscous stress tensor can be rewritten in terms of the strain rate tensor:

$$\mathbb{V} = \lambda \text{tr}(\mathbb{D})\mathbb{I} + 2\mu\mathbb{D}, \tag{2.4}$$

where μ and λ are the dynamic and the bulk viscosity coefficients, respectively. From Eq. 2.4 it can be observed that $\mathbb{V}$, and therefore $\mathbb{T}$, are symmetric tensors, property that will be successively recalled. From Eqs. 2.3 and 2.4 the stress tensor can be expressed as:

$$\mathbb{T} = (-p + \lambda \text{tr}(\mathbb{D}))\mathbb{I} + 2\mu\mathbb{D}, \tag{2.5}$$

In this way the divergence of the stress tensor results to be equal to:

$$\nabla \cdot \mathbb{T} = -\nabla p + \nabla \cdot \mathbb{V} = -\nabla p + (\lambda + \mu)\nabla(\nabla \cdot \boldsymbol{u}) + \mu\nabla^2\boldsymbol{u} \tag{2.6}$$

When dealing with system 2.1, a common approach is to consider the fluid to be inviscid, so that the divergence of the viscous stress tensor 2.4 is considered equal to zero. In this way from the original Navier-Stokes equations 2.1, the inviscid formulation, known as Euler equations, is recovered.

2.1.1 Incompressible vs weakly-compressible

Another hypothesis on the nature of the fluid to make is to consider the fluid either compressible or incompressible. For fluids like water, where the sound speed $c \propto 10^3$m/s, the Mach number, $Ma = U/c$, for classical fluid dynamic problems results to be extremely small, so it is customary to approximate the fluid by an artificial fluid which is exactly incompressible [106]. When a fluid is considered to be incompressible the continuity equation in system 2.1 becomes:

$$\nabla \cdot \boldsymbol{u} = 0 \tag{2.7}$$

Taking the divergence of the momentum equation in System 2.1 and introducing Eq. 2.7, leads to write the Navier-Stokes equations in terms of a Poisson equation for the pressure field:

$$\nabla^2 p = \rho L(\boldsymbol{u}, \nabla\boldsymbol{u}) \tag{2.8}$$

in which L is a defined function. Under this assumption the Navier-Stokes equations become, as it is possible to see, elliptic equations. The solution in this case does not presents acoustic perturbations and instantaneous energy loss is encountered during impacts.

A different approach is obtained when the fluid is consider as "artificially compressible". In this case, the compressibility adopted for the fluid is not the real one, but results to be increased from its real value. The real fluid is therefore approximated with another artificial fluid that is, in this case, more compressible than the real one. The artificial compressibility method was originally introduced by Chorin [23], with the objective of solving the steady state incompressible Navier-Stokes equations. With the introduction of an artificial compressibility, the elliptic incompressible equations becomes an hyperbolic compressible system, which can be solved by standard, implicit, time-marching methods. Peyret and Taylor [125] and successively Merkle and

Athavale [103] extended this approach to solve unsteady Navier-Stokes equations, with the introduction of a dual time stepping. In this approach a pseudo time-stepping is introduced within each physical time step, with the objective to lead the unsteady solution towards a quasi-steady state solution. A similar approach has also been applied to solve incompressible oceanographic flows (see *e.g.* Jensen [75]). A discussion on the use of artificial compressibility in fluid dynamic problems is presented by Madsen and Schäffer [92].

The use of an artificial compressibility, with a non-iterative approach and therefore a slight different scheme of the mentioned cases, is also the basic hypothesis for most of the SPH solvers and it is known as weakly-compressible assumption. In this framework, the artificial sound speed is chosen to be much lower than that of the real fluid, but much faster than the bulk velocity and therefore it presents negligible effects on the fluid dynamics. In this case the pressure field is related to the density and the internal energy, through a state equation, $p = p(\rho, e)$. This approach avoids the resolution of the Poisson equation for the pressure field and, although the evolution equations are coupled, the continuity and momentum equations can be evaluated independently and without solving an algebraic system. The hyperbolic nature of the weakly-compressible Navier-Stokes equations has also specific issues on the numerical solution, characterized, in this case, by acoustic perturbations in the pressure field. The acoustic component of the solution is therefore related with the artificial compressibility of the fluid, rather then the real acoustic, resulting in a spurious contribution.

From a computational point of view the main difference between the weakly compressible and incompressible approaches is that the former requires small time steps constrained by the speed of sound, while the latter needs the solution of an algebraic system with a sparse matrix, permitting larger time steps but quite complex for an efficient code parallelization. Moreover, the incompressible approach requires the explicit detection of the free surface in order to assign the dynamic boundary condition. Unfortunately, this is not easily performed, especially in the case of violent free-surface flows. Furthermore, the solution of the Poisson equation is highly dependent on the free surface configuration and, consequently, small errors in the free-surface detection may lead to different flow evolutions. When modeling a fluid with the SPH method, the most followed approach is the weakly- compressible one, rather than incompressible. The incompressible approach is also practiced but it does not leads to the same computational potential and applicability. The approach adopted here is to consider the fluid as weakly-compressible.

2.1.2 State equation

In general, fluids whose density varies weakly with pressure or temperature, can be treated as barotropic fluids, meaning that both pressure and internal energy are single-valued functions of density. This assumption is generally adoptable for liquids, while it is not for gases, in which the entropy, S, plays an important role. When dealing with fluids like water, it is therefore possible to adopt a state equation that is only a function of density, $p = p(\rho)$. A common choice for the state equation [106] is:

$$p = B\left[\left(\frac{\rho}{\rho_0}\right)^{\gamma} - 1\right], \tag{2.9}$$

where ρ_0 is the density when $p = 0$, γ is the polytropic index of fluid set equal to 7 for water, while B is related to the speed of sound of the media. The speed of sound is defined as:

$$c^2 = \frac{\partial p}{\partial \rho}\Big|_{S=const} \tag{2.10}$$

Introducing Eq. 2.9 into Eq. 2.10:

$$c^2 = \frac{B\gamma}{\rho_0}\left(\frac{\rho}{\rho_0}\right)^{\gamma-1} = c_0^2\left(\frac{\rho}{\rho_0}\right)^{\gamma-1} \tag{2.11}$$

where $c_0 = B\gamma/\rho_0$ is the initial speed of sound. A different version of state equation can be obtained linearising Eq. 2.9. This variation is motivated by the fact that in the weakly-compressible regime only small fluctuation of density occurs, leading to negligible differences from the original formulation [95]:

$$p = B\left[\left(\frac{\rho_0+\Delta\rho}{\rho_0}\right)^{\gamma} - 1\right] \tag{2.12}$$

$$= B\left\{1 + \gamma\frac{\Delta\rho}{\rho_0} + O\left[\left(\frac{\Delta\rho}{\rho_0}\right)^2\right] - 1\right\} \tag{2.13}$$

$$\cong \frac{B\gamma}{\rho_0}\Delta\rho = c_0^2(\rho-\rho_0) \tag{2.14}$$

Under the same conditions is possible to linearise the equation for the speed of sound, Eq. 2.11:

$$c^2 = c_0^2\left(\frac{\rho_0+\Delta\rho}{\rho_0}\right)^{\gamma-1} \tag{2.15}$$

$$= c_0^2\left\{1 + (\gamma-1)\frac{\Delta\rho}{\rho_0} + O\left[\left(\frac{\Delta\rho}{\rho_0}\right)^2\right]\right\}, \tag{2.16}$$

that leads to the following expression:

$$c \cong c_0 + \frac{\gamma-1}{2}\frac{\Delta\rho}{\rho_0} \tag{2.17}$$

The parameter γ induces small perturbation on the speed of sound through fluctuations of the density field, while, from Eq. 2.14, it does not affect the pressure field. The result is that, under weakly-compressible assumption, the linearized version of the state equation can be adopted and the speed of sound can be practically considered constant, $c = c_0$, since the small variation given by Eq. 2.17 are in practice negligible (see Marrone [95]).

The value of the celerity adopted to model the fluid defines its compressibility. From Eq. 2.14, the higher the celerity the lower it results the compressibility of the fluid, for a given pressure impulse. To guarantee a weakly-compressible regime the density fluctuations have to be smaller than $1\%\rho_0$ [106]. This condition can be expressed directly after using the linear state Eq. 2.14 as pointed out by Antuono et al. [7]:

$$c_0 \geq 10\sqrt{\frac{p_{max}}{\rho_0}} \tag{2.18}$$

where p_{max} is the maximum expected pressure in the fluid domain. As expressed by Marrone et al. [100], to correctly enforce the sound speed value, different pressure scales have to be taken into account, among: the static pressure scale due the gravity force, $p = \rho g H$, where H is the water depth, the stagnation pressure scale related to the kinetic energy, $p = \rho U^2$, the acoustic pressure scale, $p = \rho c U$, due to compressibility, produced during impacts. From these three conditions, Eq. 2.18 is rewritten as:

$$\begin{cases} c_0 \geq 10 \max\limits_t \left[\max\limits_\Omega \sqrt{gH}\right] \\ \\ c_0 \geq 10 \max\limits_t \left[\max\limits_\Omega (|\boldsymbol{u}|)\right] \\ \\ c_0 \geq 100 \max\limits_t \left[\max\limits_\Omega (|\boldsymbol{u}|)\right] \end{cases} \tag{2.19}$$

The result obtained in Eq. 2.19 have to be used according with the simulated problem. For example, in the case of free surface flows in which violent fluid impacts do not occur in the fluid domain, the acoustic pressure limit is rarely attained, therefore the correspondent constraint can be disregarded from the evaluation. In the other hand, when a phenomenon is characterized by violent fluid impacts, the condition related to acoustic pressure constraint is dominant and therefore has to be considered as constraint for the problem.

2.1.3 Boundary conditions

The set of equations presented in System 2.1, with Eq. 2.14, requires the knowledge of some information at the boundaries of the domain to be solved. In particular, these information are furnished through the knowledge of the derivative of the function, known as Neumann boundary conditions, or through the knowledge of the function itself, known as Dirichlet boundary conditions.

In classical fluid dynamic problems, the domain, Ω, is usually bounded by solid surfaces, $\partial\Omega_B$, and by a free surface, $\partial\Omega_F$. Regarding the free surface, there are two types of boundary conditions to consider, namely *kinematic* and *dynamic* boundary conditions. The kinematic boundary condition defines that a volume of fluid belonging to the free surface remains on the free surface during the time evolution. As shown by Colagrossi et al. [27], in SPH it is not necessary to enforce kinematic boundary condition explicitly, being intrinsically verified in the lagrangian flow description. The dynamic boundary condition defines instead the continuity of stresses across the free-surface. Assuming that the surface tension is negligible, the fluid will present both normal and tangential shear stresses equal to zero. In the case of Newtonian fluids the dynamic boundary condition reads as:

$$\boldsymbol{t} = \mathbb{T} \cdot \boldsymbol{n} = (-p\mathbb{I} + \mathbb{V}) \cdot \boldsymbol{n} = (-p + \lambda \text{tr}(\mathbb{D}))\boldsymbol{n} + 2\mu\mathbb{D} \cdot \boldsymbol{n} = \boldsymbol{0}, \tag{2.20}$$

where $\boldsymbol{t}$ is the stress vector, while $\boldsymbol{n}$ is the free-surface normal unit vector. If the viscous coefficients are really small in Eq. 2.20, the pressure can be considered continuous across $\partial\Omega_F$. Therefore the pressure on the free surface of the fluid is equal to the external pressure, p_{ex}. As a consequence, because of the barotropic assumption, also

the density has to be constant on the free surface, resulting in:

$$\nabla \cdot \boldsymbol{u} = 0 \qquad \forall \boldsymbol{r} \in \partial\Omega_F, \tag{2.21}$$

in which $\boldsymbol{r}$ is the position vector. Regarding the boundary conditions at the solid walls, the no-penetration condition and the adherence condition can be enforced, resulting respectively in:

$$\boldsymbol{u} \cdot \boldsymbol{n}_B = \boldsymbol{u}_B \cdot \boldsymbol{n}_B \tag{2.22}$$

$$\boldsymbol{u} \cdot \boldsymbol{\tau}_B = \boldsymbol{u}_B \cdot \boldsymbol{\tau}_B \tag{2.23}$$

in which $\boldsymbol{n}_B$ and $\boldsymbol{\tau}_B$ are the normal and the tangential unit vectors at the walls, while $\boldsymbol{u}_B$ is the boundary velocity. When considering *free-slip* boundary conditions, only Eq. 2.22 is enforced, while *no-slip* boundary condition are obtained enforcing both Eqs. 2.22 and 2.23.

Regarding the assignment of the pressure field along the solid boundaries, the Neumann boundary condition have to be enforced, that is:

$$\frac{\partial p}{\partial n} = -\rho \left[\frac{d\boldsymbol{u}_B}{dt} \cdot \boldsymbol{n} + (\boldsymbol{u}_B - \boldsymbol{u}) \cdot \frac{d\boldsymbol{n}}{dt} - \boldsymbol{g} \cdot \boldsymbol{n} \right] \tag{2.24}$$

Eq. 2.24 is obtained after introducing the free slip condition, Eq. 2.22, in the momentum equation.

2.1.4 Considerations on energy conservation

In this section, the different forms of energy that characterize the fluid mass are taken into account, and the relationship among them is presented. The fluid mass is characterized by a kinetic energy, E_K, and, in presence of a conservative force field, by a potential energy, E_P, only related to the mass location in the domain. From the potential and kinetic energy the mechanical energy of the system, E_M, is defined as:

$$E_M = E_P + E_K \tag{2.25}$$

Assuming that no external non-conservative forces are present, the expression of mechanical energy reads as (see Marrone et al. [100]):

$$\frac{DE_M}{Dt} = \int_\Omega (\nabla \cdot \mathbb{T}) \cdot \boldsymbol{u} dV \tag{2.26}$$

Through the divergence theorem is possible to write:

$$\begin{aligned} \int_{\partial\Omega} (\boldsymbol{n} \cdot \mathbb{T}) \cdot \boldsymbol{u} dS &= \int_\Omega \nabla \cdot (\mathbb{T} \cdot \boldsymbol{u}) dV \\ &= \int_\Omega \nabla \cdot (\mathbb{T}) \cdot \boldsymbol{u} dV + \int_\Omega (\mathbb{T} : \nabla \boldsymbol{u}) dV \end{aligned} \tag{2.27}$$

This surface integral is equal to zero on the free surface, because the stress vector, $\boldsymbol{t} = \boldsymbol{n} \cdot \mathbb{T}$ (=$\mathbb{T} \cdot \boldsymbol{n}$, because of the symmetry of $\mathbb{T}$) is zero from the dynamic boundary condition, Eq. 2.20. In the case of a solid boundary it is also equal to zero because the

velocity of the boundary is assumed, in this case, to be null. Considering the symmetry of the stress tensor, is possible to rewrite Eq. 2.26, through Eq. 2.27:

$$\frac{DE_M}{Dt} = -\int_\Omega (\mathbb{T} : \mathbb{D}) dV \tag{2.28}$$

When the fluid is Newtonian, Eq. 2.28 can be rewritten as:

$$\frac{DE_M}{Dt} = \int_\Omega p\nabla \cdot \boldsymbol{u} dV - \lambda \int_\Omega (\nabla \cdot \boldsymbol{u})^2 dV - 2\mu \int_\Omega (\mathbb{D} : \mathbb{D}) dV \tag{2.29}$$

From Eq. 2.29 is possible to see that in the case of incompressible flows, because of Eq. 2.7, only the last term in the right hand side equation is different from zero. This quantity in fact is the energy dissipated by the fluid viscosity, that is transformed into heat. From this term it is possible to define the power dissipated:

$$\frac{DE_D}{Dt} = -2\mu \int_\Omega (\mathbb{D} : \mathbb{D}) dV \tag{2.30}$$

When going to a weakly-compressible fluid, from Eq. 2.29, two supplemental terms have to be taken into account. The second term on the right hand side of the equation is negligible compared to the first one, fact that has been also verified numerically by Marrone et al. [100]. The first term represents, instead, a pure reversible term associated to the energy stored by the fluid when compressed:

$$\frac{DE_C}{Dt} = -\int_\Omega p\nabla \cdot \boldsymbol{u} dV \tag{2.31}$$

Through the use of continuity equation and the state equation, Eq. 2.31 can be expressed as the time variation of the elastic energy. In the case of a linear state Eq. 2.14, Eq. 2.31 becomes:

$$E_C = E_C(\rho_0) + c^2 \int_\Omega \left[\log \frac{\rho}{\rho_0} + \frac{\rho_0}{\rho} - 1 \right] \rho dV \tag{2.32}$$

where $E_C(\rho_0)$ is the elastic energy at rest conditions. Eq. 2.28, with Eqs. 2.30 and 2.31 becomes:

$$\frac{DE_M}{Dt} = \frac{DE_D}{Dt} - \frac{DE_C}{Dt} \tag{2.33}$$

In the case of an incompressible medium, the elastic energy E_C is null. Under the hypothesis of inviscid fluid, also the term related to the viscous dissipation is null, resulting, in the case of fluid impacts, in an instantaneous energy loss, as shown by Rogers and Szymczak [131] and by Marrone et al. [100]. In this case, in fact, the energy balance has to be rewritten as:

$$\frac{DE_M}{Dt} = \frac{DE_\Delta}{Dt}, \tag{2.34}$$

in which $E_\Delta = K\delta(t - t^*)$, with δ the delta Dirac function (being $t = t^*$ the instant of time in which the collision occurs) and K an unknown constant, defining the intensity of the energy loss.

In the case of a weakly-compressible model, instead, no energy losses are encountered and, during impacts, as it will be shown in section 4.2, there is an instantaneous accumulation of elastic energy. The energy is therefore continuously transferred between the mechanical and the elastic ones, at a velocity of conversion proportional to the speed of sound of the fluid. As pointed out by Marrone et al. [100], increasing the speed of sound, *i.e.* vanishing the Mach number, the mechanical energy transformed into elastic energy, results to be equal to E_Δ. The energy introduced into the fluid mass after the impact, in the case of viscous flows, is then dissipated by the viscosity. After the mechanical energy is dissipated, the residual mechanical energy is close to the incompressible solution. Indeed, Seo and Moon [137] demonstrated that in the weakly-compressible regime the compressible solution is equal to a superposition of an acoustic component over an incompressible solution. This aspect has been confirmed numerically by Marrone et al. [100] and will be further investigated in chapter 6.

2.2 Fundamentals of SPH

In a Lagrangian meshless approach the fluid mass is modeled as a finite number of particles, each one carrying information about its mass, density and other physical properties. In this framework, the partial differential equation governing the problem are solved with respect to these points, by using their information to reconstruct the fluid properties everywhere in the domain.

2.2.1 SPH interpolation

In the continuous formulation, the field of a generic function, f, is interpolated through a convolution integral over the domain Ω, of the form:

$$\langle f(\boldsymbol{r})\rangle = \int_\Omega f(\boldsymbol{r'})W(\boldsymbol{r}-\boldsymbol{r'};h)dV', \tag{2.35}$$

where $\langle\cdot\rangle$ represent a quantity approximated through the SPH interpolation, $\boldsymbol{r}$ is the position where the field value is interpolated from its known values in $\boldsymbol{r'}$. The term $W(\boldsymbol{r}-\boldsymbol{r'};h)$ is the interpolating function, also called *smoothing* or *kernel function*, while h is the *smoothing length*, representative of the domain of influence $\Omega_{\boldsymbol{r'}}$ of $\boldsymbol{r'}$, *i.e.* the sub-domain where the kernel differs from zero. From the integral interpolation $\langle f(\boldsymbol{r})\rangle$ of Eq. 2.35 it comes also the name "Smoothed" in SPH, since this object can be seen as a smoothed version of the original function $f(\boldsymbol{r})$. Hereafter the notation $W(\boldsymbol{r}-\boldsymbol{r'})$ for the kernel function is adopted, implicitly assuming its dependence on the smoothing length. A generic function, to be adopted as a kernel function, has to satisfy the following requirements [87]:

- $W(\boldsymbol{r}-\boldsymbol{r'}) \geq 0$ for $\boldsymbol{r} \in \Omega_{\boldsymbol{r'}} \subset \Omega$ and zero otherwise, so that the kernel has a compact support;
- $W(\boldsymbol{r}-\boldsymbol{r'})$ decrease monotonously as $\|\boldsymbol{r}-\boldsymbol{r'}\|$ increases;
- $\int_\Omega W(\boldsymbol{r}-\boldsymbol{r'})$ =1, partition of unity or normalization condition;
- $\lim_{h\to 0} W(\boldsymbol{r}-\boldsymbol{r'}) = \delta(\boldsymbol{r}-\boldsymbol{r'})$, delta function limit condition;

- $\nabla W(\boldsymbol{r}-\boldsymbol{r'}) = -\nabla' W(\boldsymbol{r}-\boldsymbol{r'})$, where ∇' means that the derivative is computed on the $\boldsymbol{r'}$ variable. This symmetric property implies that the kernel is an even function.

The same operator can be applied to the derivatives of f:

$$\langle \nabla f(\boldsymbol{r}) \rangle = \int_{\Omega} \nabla' f(\boldsymbol{r'}) W(\boldsymbol{r}-\boldsymbol{r'}) dV' \tag{2.36}$$

Integrating by parts, Eq. 2.36 becomes:

$$\langle \nabla f(\boldsymbol{r}) \rangle = \int_{\partial\Omega} f(\boldsymbol{r'}) W(\boldsymbol{r}-\boldsymbol{r'}) \boldsymbol{n'} dS' - \int_{\Omega} f(\boldsymbol{r'}) \nabla' W(\boldsymbol{r}-\boldsymbol{r'}) dV' \tag{2.37}$$

where the surface integral of Eq. 2.37 is obtained after applying the divergence theorem. This last term is equal to zero inside the fluid domain. Using the symmetry property of the kernel $\nabla' W(\boldsymbol{r}-\boldsymbol{r'}) = -\nabla W(\boldsymbol{r}-\boldsymbol{r'})$ and neglecting the surface term, the approximation of the gradient of a function, f, can be written only through the gradient of the kernel:

$$\langle \nabla f(\boldsymbol{r}) \rangle = \int_{\Omega} f(\boldsymbol{r'}) \nabla W(\boldsymbol{r}-\boldsymbol{r'}) dV' \tag{2.38}$$

Even if near the free surface it provides just a poor approximation, due to the non-zero surface integral, this formulation is usually used to solve gradient of functions in SPH models.

When going to discrete level, the relationships presented so far can be expressed in different forms. A direct discretized version for the smoothed function presented in Eq. 2.35 can be written as:

$$\langle f(\boldsymbol{r}_i) \rangle = \sum_j f_j W_j(\boldsymbol{r}_i) dV_j, \tag{2.39}$$

while a discrete formulation for the gradient presented in Eq. 2.38 is:

$$\langle \nabla f(\boldsymbol{r}_i) \rangle = \sum_j f_j \nabla W_j(\boldsymbol{r}_i) dV_j \tag{2.40}$$

In the case of the gradient of functions, Eq. 2.40 is practically never implemented in SPH solvers, because it does not correctly reproduce gradients of constant fields, resulting in spurious contribution and numerical errors.

It is noticed indeed that, when approximating functions on data arbitrarily scattered, the above approximations do not allow to correctly reproduce constant or bi-linear functions. This fact, that will be further discussed in section 2.2.3, is related to the impossibility to satisfy the following requirements (see Colagrossi [26]), for a function:

$$\sum_j W_j(\boldsymbol{r}_i) dV_j = 1, \tag{2.41}$$

$$\sum_j \boldsymbol{r}_j W_j(\boldsymbol{r}_i) dV_j = \boldsymbol{r}_i \tag{2.42}$$

and for gradients:

$$\sum_j \nabla W_j(\boldsymbol{r}_i) dV_j = \mathbf{0}, \tag{2.43}$$

$$\sum_j \boldsymbol{r}_j \otimes \nabla W_j(\boldsymbol{r}_i) dV_j = \mathbb{I} \tag{2.44}$$

Therefore the result is the introduction of spurious contribution that generate numerical errors. In literature, different approaches have been presented in order to find a solution to this inconvenient, by introducing corrections in the kernel evaluation. In particular, a simple corrected formulation has been presented by Shepard [141]:

$$\langle f(\boldsymbol{r}_i) \rangle = \sum_j f_j W_j^{\mathrm{S}}(\boldsymbol{r}_i) dV_j, \tag{2.45}$$

where:

$$W_j^{\mathrm{S}}(\boldsymbol{r}_i) = \frac{W_j(\boldsymbol{r}_i)}{\sum_k W_k(\boldsymbol{r}_i) dV_k} \tag{2.46}$$

Another approach, known as Corrected SPH (CSPH), has been introduced by Bonet and Kulasegaram [15], by considering:

$$W_j^{\mathrm{C}}(\boldsymbol{r}_i) = W_j(\boldsymbol{r}_i) \alpha(\boldsymbol{r}_i) \left[1 + \beta(\boldsymbol{r}_i)(\boldsymbol{r}_i - \boldsymbol{r}_j)\right] \tag{2.47}$$

where α and β are obtained by enforcing consistency conditions. The corrections presented in Eqs. 2.45 and 2.47 both allow to correctly reproduce uniform functions, expressed by Eq. 2.41 and the gradient of uniform functions, expressed by Eq. 2.43.

The kernel can be corrected also with a higher operator, as presented with the Moving Least Square SPH (MLSPH), by Dilts [44]:

$$W_j^{\mathrm{MLS}}(\boldsymbol{r}_i) = (\mathbb{A}^{-1} \cdot \boldsymbol{e}_1) \cdot \boldsymbol{b}\ W_j(\boldsymbol{r}_i), \tag{2.48}$$

where:

$$\begin{cases} \boldsymbol{b}^T = \left[1, (x_j - x_i), (y_j - y_i), (z_j - z_i)\right], \\ \boldsymbol{e}_1^T = [1, 0, 0, 0], \\ \mathbb{A} = \sum_i (\boldsymbol{b} \otimes \boldsymbol{b})\ W_j(\boldsymbol{r}_i) dV_i \end{cases} \tag{2.49}$$

This approach ensures that both uniform and linear functions are reproduced correctly, represented by Eqs. 2.41 and 2.42, respectively. In this case, moreover, also the correct evaluation of gradients of constant functions, Eq. 2.43, is recovered. To satisfy the last equality in Eq. 2.44, a supplemental MLS correction for the evaluation of the kernel derivatives have to be introduced (see Colagrossi [26]).

The introduction of kernel corrections allows to recover consistency in the discrete SPH formulation. Moreover corrected kernel avoids particles self-redistribution mechanism (see section 4.1). The consequence is that, regions with high velocity gradient

can experience anisotropic particle distributions. In those region, matrices $\mathbb{A}$ in Eq. 2.49 become ill-conditioned and their inversion causes strong numerical instabilities. As pointed out by Le Touzé et al. [81], to overcome this drawback, a periodic "remeshing", which consists in redistributing particles uniformly in the domain, is necessary for the higher order SPH scheme. Then, particle data are interpolated at these points, which become the new set of particles for the next time-step. This simple remeshing procedure does not, however, preserve the linear and angular momenta, resulting for the corrected kernel do the rise of physical inadequacy, related to the conservation properties. Corrected kernel, indeed, do not guarantee an equal and opposite reaction between the interacting particles. Moreover, the use of a corrected SPH model results in an increasing of the resulting CPU costs. On this considerations it is preferable to find an expression that is conservative, even if it introduce small numerical errors. Even if the formulation presented in Eq. 2.48 is not used to compute the SPH integrals, it is implemented for the solid boundary conditions enforcement (see section 3.2) and to evaluate field values (see section 3.4).

Another way to obtain a simple and effective correction, and achieve higher accuracy, can be acquired by rewriting the gradient of f in the following form [106]:

$$\nabla f = \frac{1}{\Phi}(\nabla(\Phi f) - f\nabla\Phi) \tag{2.50}$$

where Φ represents any differentiable function. When Φ is set equal to 1, the SPH discrete version of Eq. 2.50 becomes:

$$\langle \nabla f(\boldsymbol{r}_i) \rangle = \sum_j (f_j - f_i)\nabla W_j(\boldsymbol{r}_i) dV_j, \tag{2.51}$$

This formulation, used for the continuity equation (see section 2.3.1), vanishes when f is constant, so it allows to recover the equalities expressed in Eqs. 2.41 and 2.43. The advantage of using this expressions, compared with kernel corrections, is that it is computationally inexpensive and also easy to implement. This formula however, as for kernel corrections, also results not to be conservative, therefore for the momentum equation, as it will be shown in section 2.3.1, another expression have to be found.

2.2.2 Kernel choice

Different mathematical expressions for the kernel function can be adopted for SPH. Among them, one of the most used is the Gaussian kernel, expressed as:

$$W_{\mathrm{G}}(s) = \begin{cases} \dfrac{1}{\pi h^2} e^{-(\frac{s}{h})^2} & \text{if} \quad s < \gamma h \\ \\ 0 & \text{otherwise} \end{cases} \tag{2.52}$$

where $s = \|\boldsymbol{r} - \boldsymbol{r'}\|$, while γ represents, in this context, the cut-off radius coefficient, often set equal to 3. An important property of the Gaussian kernel is that its derivatives can be evaluated directly from the value of the function:

$$\frac{\partial W}{\partial r}\Big|_i = -2\frac{r - r_i}{h^2} W_i \tag{2.53}$$

It is easy to see that the expression of the Gaussian kernel in Eq. 2.52 is truncated in correspondence of the cut-off radius, resulting for the normalization condition not to be satisfied. This inaccuracy is negligible in the case γ =3 (in which it results in an error equal to 0.012%), while it becomes greater in the case γ =2 (in which it would result in an error equal to 1.234%). For this reason, a renormalized kernel is introduced to match the property of the unit integral. Moreover, the renormalized kernel goes to zero when the interacting distance approaches the support radius γh. The renormalized Gaussian kernel is defined as [104]:

$$W_{\mathrm{RG}}(s) = \begin{cases} \dfrac{e^{-(s/h)^2} - C_0}{2\pi C_1} & \text{if} \quad s < \gamma h \\ \\ 0 & \text{otherwise} \end{cases} \tag{2.54}$$

where $C_0 = e^{-\gamma^2}$ and C_1 is evaluated as follows:

$$C_1 = \int_0^{\gamma h} s \left[e^{-(s/h)^2} - e^{-\gamma^2} \right] ds \tag{2.55}$$

For the case $\gamma = 2$ it results $C_0 = 0.018316$ and $C_1 = 0.4542h^2$, while for $\gamma = 3$ it results $C_0 = 1.23 \cdot 10^{-4}$ and $C_1 = 0.49938h^2$. As it has been shown by Morris [118] the kernel functions presents the best stability properties and the largest code efficiency compared with other kernel functions.

Another expression for the kernel is obtained from the Wendland [155] functions. In this case the mathematical expression is chosen from a class of univariate polynomial functions characterized by exhibiting a minimal degree for a given smoothness. Among them, one of the expression proposed by Wendland [155] reads as:

$$W_{\mathrm{W}}(s) = \begin{cases} \dfrac{1}{2\pi C} \left(1 - \dfrac{s}{\gamma h} \right)^3 \left(\dfrac{3s}{\gamma h} + 1 \right) & \text{if} \quad s < \gamma h \\ \\ 0 & \text{otherwise} \end{cases} \tag{2.56}$$

The value of the normalization constant C is obtained as:

$$C = \int_0^{\gamma h} s \left[\left(1 - \frac{s}{\gamma h} \right)^3 \left(\frac{3s}{\gamma h} + 1 \right) \right] ds \tag{2.57}$$

In the case $\gamma = 2$ it results $C = 2/5h^2$, while for $\gamma = 3$ is $C = 9/10h^2$. Fig. 2.1 illustrates the longitudinal sections of 2D kernel functions presented in Eqs. 2.54 and 2.56, for $\gamma = 2$ and $\gamma = 3$.

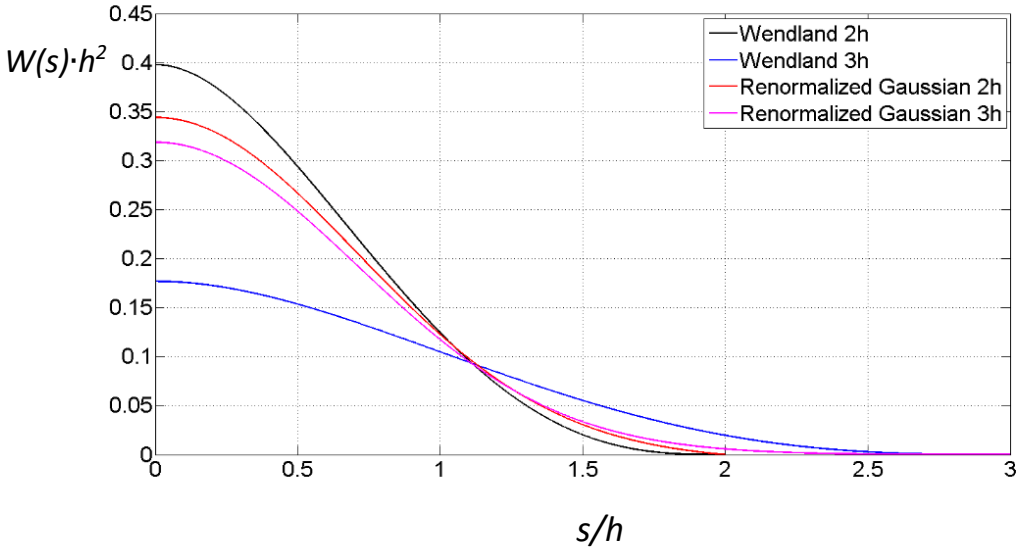

Figure 2.1: *Longitudinal sections of 2D-kernel functions presented in Eqs. 2.54 and 2.56 with support radius equal to 2h and 3h.*

2.2.3 Convergence of SPH

The error introduced by the SPH interpolation can be estimated using a Taylor expansion of $f(\boldsymbol{r'})$ around $\boldsymbol{r}$, where $f(\boldsymbol{r})$ is differentiable [87]:

$$\begin{aligned}\langle f(\boldsymbol{r})\rangle &= \int_\Omega f(\boldsymbol{r'})W(\boldsymbol{r}-\boldsymbol{r'})dV' \\ &= \int_\Omega \left[f(\boldsymbol{r}) + f'(\boldsymbol{r})(\boldsymbol{r'}-\boldsymbol{r}) + O(\boldsymbol{r'}-\boldsymbol{r})^2\right] W(\boldsymbol{r}-\boldsymbol{r'})dV' \\ &= f(\boldsymbol{r})\int_\Omega W(\boldsymbol{r}-\boldsymbol{r'})dV' + f'(\boldsymbol{r})\int_\Omega (\boldsymbol{r'}-\boldsymbol{r})W(\boldsymbol{r}-\boldsymbol{r'})dV' + O(h^2)\end{aligned} \tag{2.58}$$

Since the kernel is a even function, the quantity $(\boldsymbol{r'}-\boldsymbol{r})W(\boldsymbol{r}-\boldsymbol{r'})$ is a odd one, resulting in:

$$\int_\Omega (\boldsymbol{r'}-\boldsymbol{r})W(\boldsymbol{r}-\boldsymbol{r'})dV' = 0 \tag{2.59}$$

Using Eq. 2.59 and the unity condition, Eq. 2.58 becomes

$$\langle f(\boldsymbol{r})\rangle = f(\boldsymbol{r}) + O(h^2) \tag{2.60}$$

From this result, a quantity continuously interpolated with the SPH converge to the solution with h^2, when the support kernel is not truncated by the solid boundary. A different situation is encountered in presence of a boundary, where consistency cannot be reached since the partition of unity is not satisfied, as shown in Fig. 2.2. When dealing with this drawback in a computational framework, as it will be presented in section 3.2, a numerical solution is obtained through the implementation of ghost particles to represent the solid boundary. In the case of a free surface this inaccuracy persists.

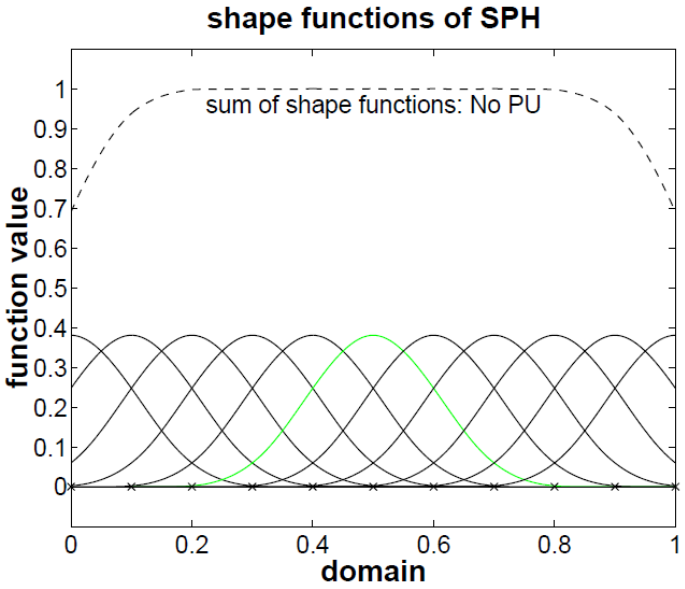

Figure 2.2: *Kernel function sum representation in the domain. The partition of unity is not respected near the boundaries (Fries and Matthies [57]).*

In the discrete version of the SPH interpolation an additional error is introduced in the solution, resulting in the following accuracy:

$$h^2 + h^{-n}\left(\frac{\Delta x}{h}\right)^2 \tag{2.61}$$

in which n is the order of the derivative and Δx is the spatial resolution. From this result the discrete interpolation error does not converge to the zero-th order, while it diverges for its derivatives. This inaccuracy however can be controlled by assuming a small value of the ratio $\Delta x/h$, that results in taking a large number of neighbor interacting particles. Eq. 2.61, directly related to the impossibility to satisfy Eq. 2.41, is shown in terms of kernel sum in Fig. 2.3, where is possible to see oscillations around the partition of unity. As shown by Dilts [44], this effect is directly related to the appearance of the tension instability in SPH, previously presented. The tension instability is a consequence of using Eulerian kernels in a Lagrangian scheme.

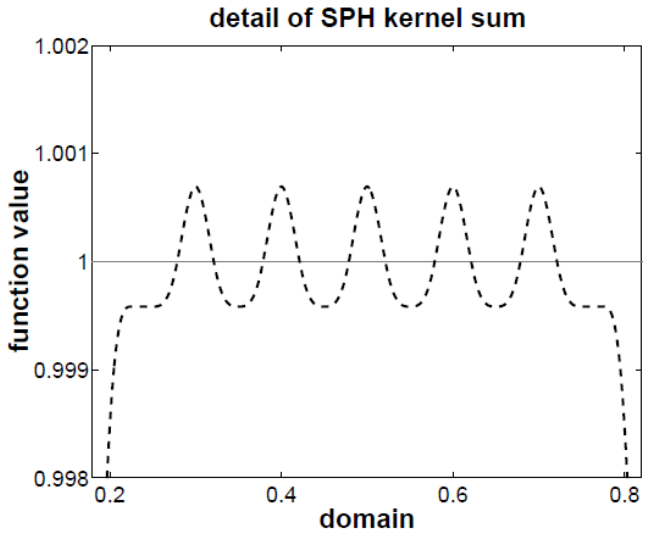

Figure 2.3: *Detail of kernel sum in a discrete framework, where oscillation around the partition of unity are encountered (Fries and Matthies [57]).*

2.3 Regularized Navier-Stokes equations

The equations implemented in the SPH model, for the simulation of fluid dynamic problems, are the continuity, momentum and energy equations, presented in System 2.1 and the linear state equation, Eq. 2.14:

$$\begin{cases} \dfrac{D\rho}{Dt} = -\rho \langle \nabla \cdot \boldsymbol{u} \rangle \\ \dfrac{D\boldsymbol{u}}{Dt} = \boldsymbol{g} - \dfrac{1}{\rho} \langle \nabla p \rangle + \dfrac{1}{\rho} \langle \nabla \cdot \mathbb{V} \rangle \\ \dfrac{De}{Dt} = -\dfrac{p}{\rho} \langle \nabla \cdot \boldsymbol{u} \rangle + 2\dfrac{\mu}{\rho} \langle \mathbb{D} : \mathbb{D} \rangle \\ p = c^2(\rho - \rho_0) \end{cases} \tag{2.62}$$

The equation for the conservation of energy is written after taking into account Eqs. 2.28 and 2.29, and considering no heat flux involved in the problem. System 2.62 has to be considered together with the equation that relates the velocity vector, $\boldsymbol{u}$, to its spatial position, $\boldsymbol{r}$:

$$\frac{D\boldsymbol{r}}{Dt} = \boldsymbol{u} \tag{2.63}$$

In this section it is shown how the smoothed terms in System 2.62 are discretized to become employable for computational mechanics.

2.3.1 Gradients and divergences

In the case of the divergence of velocity field, the approach presented in Eq. 2.50 is followed:

$$\nabla \cdot \boldsymbol{u} = \frac{\nabla \cdot (\rho \boldsymbol{u}) - \boldsymbol{u} \cdot \nabla \rho}{\rho} \tag{2.64}$$

Discretizing Eq. 2.64 it leads to:

$$\begin{aligned} \langle \nabla \cdot \boldsymbol{u} \rangle &= \sum_j \frac{\rho_j \boldsymbol{u}_j}{\rho_i} \cdot \nabla_i W_j(\boldsymbol{r}_i) \frac{m_j}{\rho_j} - \sum_j \frac{\rho_j \boldsymbol{u}_i}{\rho_i} \cdot \nabla_i W_j(\boldsymbol{r}_i) \frac{m_j}{\rho_j} \\ &= \sum_j \frac{m_j}{\rho_i} (\boldsymbol{u}_j - \boldsymbol{u}_i) \cdot \nabla_i W_j(\boldsymbol{r}_i), \end{aligned} \tag{2.65}$$

where $\boldsymbol{u}_i$, ρ_i, m_i represent the vector velocity, the density and the mass of the considered i-th particle, respectively. In the case of the gradient of pressure, as already mentioned in section 2.2.1, the same approach as Eq. 2.64 results to be non-conservative. In this case the equation is rewritten in a symmetric form [106]:

$$\nabla p = \frac{\nabla (p/\rho) - p \nabla (1/\rho)}{1/\rho} = \rho \nabla \left(\frac{p}{\rho} \right) + p \frac{\nabla \rho}{\rho} \tag{2.66}$$

Using this form, the approximate formula for the gradient becomes:

$$\begin{aligned} \langle \nabla p \rangle &= \rho_i \sum_j \frac{p_j}{\rho_j} \nabla_i W_j(\boldsymbol{r}_i) \frac{m_j}{\rho_j} + \sum_j \frac{p_i \rho_j}{\rho_i} \nabla_i W_j(\boldsymbol{r}_i) \frac{m_j}{\rho_j} \\ &= \sum_j \rho_i^2 \left(\frac{p_j}{\rho_j^2} + \frac{p_i}{\rho_i^2} \right) \nabla_i W_j(\boldsymbol{r}_i) \frac{m_j}{\rho_i} \end{aligned} \tag{2.67}$$

From the point of view of the accuracy, Eq. 2.67 is equivalent to Eq. 2.40, resulting in the introduction of the inaccuracy described in the previous section. Eqs. 2.65 and 2.67 are used to solve continuity and momentum equations, respectively.

2.3.2 Viscous approximation

In the SPH formalism the divergence of the viscous stress tensor can be expressed in different ways (see *e.g.* Monaghan and Gingold [112], Morris et al. [119]). Here, among the different formulations, the expression furnished by Monaghan and Gingold [112], that, because of its symmetry, preserves both linear and angular momenta, is taken into account:

$$\langle \nabla \cdot \mathbb{V} \rangle = \mu \sum_j \pi_{ij} \nabla_i W_j(\boldsymbol{r}_i) \frac{m_j}{\rho_j}, \tag{2.68}$$

where:

$$\pi_{ij} = 2(k+2) \frac{(\boldsymbol{u}_j - \boldsymbol{u}_i) \cdot (\boldsymbol{r}_j - \boldsymbol{r}_i)}{\|\boldsymbol{r}_j - \boldsymbol{r}_i\|^2}, \tag{2.69}$$

in which k is the number of the spatial dimensions of the considered problem.
Usually, in SPH application, the real viscosity of the fluid is replaced by an artificial one, that is related with the real viscosity but is designed to allow shock phenomena to be simulated, or simply to stabilize the numerical algorithm. The artificial viscosity

formulation is essentially identical to Eq. 2.68, in which the real viscosity, μ, is set equal to:

$$\mu = \frac{\alpha c_0 \rho h}{2(k+2)} \tag{2.70}$$

where α represents the artificial viscosity coefficient. In the case of a 2D problem the artificial viscosity is $\alpha = 8\mu/c_0\rho h$. The parameter α is dependent on the type of simulation and it usually assumes, in hydraulic application [106], values in the range [0.01 - 0.05], in order to enhance the stability of the computational scheme.

2.3.3 SPH discrete formulation

On the basis of the mentioned approximations, the discrete version of the System 2.62 reads as [13]:

$$\begin{cases} \dfrac{D\rho_i}{Dt} = -\displaystyle\sum_j m_j(\boldsymbol{u}_j - \boldsymbol{u}_i)\cdot\nabla_i W_j(\boldsymbol{r}_i), \\ \dfrac{D\boldsymbol{u}_i}{Dt} = \boldsymbol{g}_i - \displaystyle\sum_j m_j\left(\frac{p_j}{\rho_j^2}+\frac{p_i}{\rho_i^2}\right)\nabla_i W_j(\boldsymbol{r}_i) + \mu\sum_j \frac{m_j}{\rho_i\rho_j}\pi_{ij}\nabla_i W_j(\boldsymbol{r}_i), \\ \dfrac{De_i}{Dt} = -\displaystyle\sum_j \frac{p_i}{\rho_i^2} m_j(\boldsymbol{u}_j - \boldsymbol{u}_i)\cdot\nabla_i W_j(\boldsymbol{r}_i) + \frac{\mu}{2}\sum_j \frac{m_j}{\rho_i\rho_j}\pi_{ij}(\boldsymbol{u}_j - \boldsymbol{u}_i)\cdot\nabla_i W_j(\boldsymbol{r}_i), \\ \dfrac{D\boldsymbol{r}_i}{Dt} = \boldsymbol{u}_i, \qquad\qquad p_i = c_0^2(\rho_i - \rho_0) \end{cases} \tag{2.71}$$

A slightly different formulation is obtained through the use of m_j/ρ_j instead of m_j/ρ_i. This approach has been successfully applied to a broad range of phenomena and fluid-structure interaction processes (*e.g.* Colagrossi and Landrini [30], Antuono et al. [6], Cherfils et al. [22], Marrone et al. [100], etc.). The corresponding discretized version of governing equations reads as:

$$\begin{cases} \dfrac{D\rho_i}{Dt} = -\rho_i\displaystyle\sum_j \frac{m_j}{\rho_j}(\boldsymbol{u}_j - \boldsymbol{u}_i)\cdot\nabla_i W_j(\boldsymbol{r}_i), \\ \dfrac{D\boldsymbol{u}_i}{Dt} = \boldsymbol{g}_i - \displaystyle\sum_j \frac{m_j}{\rho_i\rho_j}(p_j + p_i)\nabla_i W_j(\boldsymbol{r}_i) + \mu\sum_j \frac{m_j}{\rho_i\rho_j}\pi_{ij}\nabla_i W_j(\boldsymbol{r}_i), \\ \dfrac{De_i}{Dt} = -p_i\displaystyle\sum_j \frac{m_j}{\rho_i\rho_j}(\boldsymbol{u}_j - \boldsymbol{u}_i)\cdot\nabla_i W_j(\boldsymbol{r}_i) + \frac{\mu}{2}\sum_j \frac{m_j}{\rho_i\rho_j}\pi_{ij}(\boldsymbol{u}_j - \boldsymbol{u}_i)\cdot\nabla_i W_j(\boldsymbol{r}_i), \\ \dfrac{D\boldsymbol{r}_i}{Dt} = \boldsymbol{u}_i, \qquad\qquad p_i = c_0^2(\rho_i - \rho_0) \end{cases} \tag{2.72}$$

As shown by Colagrossi et al. [28], for $h \to 0$ and $\Delta x/h \to 0$, where $\Delta x = (m_i/\rho_i)^{1/k}$, Systems 2.71 and 2.72 converge to the Navier-Stokes equations.

In discretized form, the kinetic energy associated to the fluid mass, in a generic instant of time, is given by:

$$E_K = \sum_j \frac{1}{2} m_j \left\| \boldsymbol{u}_j \right\|^2, \tag{2.73}$$

where the sum is extended to all the fluid particles. Regarding the potential energy, E_P, its expression is dependent on the force field that characterizes the specific problem. For hydraulic problems subjected to the gravitational force near the surface of the earth, the potential energy is approximated with:

$$E_P = E_{P0} + \sum_j m_j g z_j, \tag{2.74}$$

while in the case of fluid mass subjected to central conservative force field the potential energy is given by:

$$E_P = E_{P0} + \sum_j \frac{1}{2} m_j B^2 \left\| \boldsymbol{r}_j \right\|^2, \tag{2.75}$$

where B is a dimensional parameter, representing the intensity of the force field. In Eqs. 2.74 and 2.75 the term E_{P0} represents the reference potential energy.

The internal energy of the system, E_I, is given by the sum of the irreversible, or dissipated energy, E_D, plus the reversible, or elastic energy, E_C. Regarding the irreversible energy, it can be evaluated through the second term of the specific internal energy expressed in the third equation of Systems 2.71 or 2.72 as follows [100]:

$$E_D = \sum_i m_i \frac{\mu}{2} \sum_j \frac{m_j}{\rho_i \rho_j} \pi_{ij} (\boldsymbol{u}_j - \boldsymbol{u}_i) \cdot \nabla_i W_j(\boldsymbol{r}_i), \tag{2.76}$$

The reversible energy, is instead furnished by the first term of the specific internal energy. If a linear state equation is taken into account the elastic internal energy, E_C, is given by discretization of Eq. 2.32:

$$E_C = E_C(\rho_0) + c^2 \sum_j m_j \left[\log\left(\frac{\rho_j}{\rho_0}\right) + \frac{\rho_0}{\rho_j} - 1 \right], \tag{2.77}$$

in which, as mentioned before, $E_C(\rho_0)$ is the elastic energy at rest conditions.

2.3.4 Numerical corrections for code efficiency

In addition to the above discretized equations, some supplementary corrections are usually introduced to enhance the numerical stability. Among them the most used refer to:

- *Anticlumping term.*
  Monaghan [107] presented an anticlumping term with the aim to avoid tensile instability and consequent unphysical cavitation phenomena with generation of voids. This correction is presented as a small repulsive force to introduce in the momentum equation, that acts effectively only when the distance between the interacting particles becomes smaller than the initial spatial resolution. Introducing

the anticlumping correction, the terms for the momentum equation in System 2.71 become [107]:

$$\frac{p_j}{\rho_j^2} + \frac{p_i}{\rho_i^2} + Rf_{ij}^{\nu}, \tag{2.78}$$

in which the interparticle force f_{ij} is expressed as the ratio between the kernel evaluated in different distances :

$$f_{ij} = \frac{W_j(\boldsymbol{r}_i)}{W(\Delta x)} \tag{2.79}$$

The exponent ν of f_{ij} is usually set equal to 4, while the factor R = R_i + R_j. If $p_i < 0$ or if $p_j < 0$, the values of R_i and R_j are evaluated respectively by means of the following equations [107]:

$$R_i = \epsilon\frac{|p_i|}{\rho_i^2}, \qquad R_j = \epsilon\frac{|p_j|}{\rho_j^2} \tag{2.80}$$

where the coefficient ϵ is empirically set equal to 0.2. In the SPH solution there is slight tendency for the particles to form local linear structures. These can be removed if a small artificial pressure is included even if the pressure is positive. In the case of $p_i > 0$ and if $p_j > 0$, therefore:

$$R = 0.01\left(\frac{p_i}{\rho_i^2} + \frac{p_j}{\rho_j^2}\right) \tag{2.81}$$

It is noticed that an alternative manner to limit tensile instability refers to the use of an empirical background pressure in the linearized state equation (see *e.g.* Marrone et al. [98], Grenier et al. [66]).

- *X-SPH Correction*.
  The XSPH correction has been introduced by Monaghan [105], with the idea to move particles with "smoothed" velocity gradients. It consists in adding a numerical filter to the motion equation as follows:

$$\frac{D\boldsymbol{r}_i}{Dt} = \boldsymbol{u}_i + \epsilon_X \sum_j (\boldsymbol{u}_j - \boldsymbol{u}_i) W_j(\boldsymbol{r}_i)\frac{m_i}{\rho_i} \tag{2.82}$$

  where ϵ_X is a coefficient that defines the magnitude of the smoothing, and it is usually chosen in the range $[0, 1]$. The correction introduced by the XSPH does not change the total linear or angular momentum. However, in the case in which the particles are moving with the smoothed velocity, energy is not conserved.

- *Density reinitialization*.
  The weakly-compressible SPH model is characterized by the occurrence of high frequency noise in the pressure field. This problem was firstly prevented by a periodic re-initialization of the density field in order to obtain a more regular solution. This correction, introduced by Colagrossi and Landrini [30], is performed through a first order approximation based on a MLS corrected kernel (see Eq. 2.48):

$$\langle\rho_i\rangle = \sum_j \rho_j W_j^{\text{MLS}}(\boldsymbol{r}_i)V_j = \sum_j m_j W_j^{\text{MLS}}(\boldsymbol{r}_i), \tag{2.83}$$

being V_j the volume of the j-th particle, $V_j = m_j/\rho_j$.
In any case, in recent years diffusive corrections have been introduced in the continuity equation in order to smooth the pressure field, and therefore this approach is generally no longer practiced. The diffusive formulations will be exhaustively discussed in section 3.1.

For the hydraulic problems simulated in this thesis, different formulations, with different corrections, are taken into account. The set-up of the adopted model to solve the problem at hand will be therefore presented in the introduction of the considered test.

CHAPTER 3

Computational aspects

3.1 Diffusive formulations

Standard weakly-compressible SPH formulations have the drawback of generating spurious high frequency numerical oscillations in the pressure field. In recent years, different authors have proposed several diffusive corrections to stabilize the solution and attain more reliable results. From the governing equations presented in System 2.71 (and identically form System 2.72), these diffusive formulations are obtained through the introduction of a diffusive term, D_i, in the continuity equation, resulting in:

$$\frac{D\rho_i}{Dt} = -\sum_j m_j(\boldsymbol{u}_j - \boldsymbol{u}_i) \cdot \nabla_i W_j(\boldsymbol{r}_i) \; + D_i \tag{3.1}$$

The diffusive term, D_i, can be expressed in the following general form:

$$D_i = 2\delta h c_0 \sum_j \psi_{ij} \frac{(\boldsymbol{r}_j - \boldsymbol{r}_i) \cdot \nabla_i W_j(\boldsymbol{r}_i)}{\|\boldsymbol{r}_j - \boldsymbol{r}_i\|^2} V_j \tag{3.2}$$

in which δ is a parameter that defines the magnitude of the diffusive term, while the term ψ_{ij} is evaluated in accordance with the specific formulation. Molteni and Colagrossi [104] expressed the term ψ_{ij} as the density difference between the considered fluid particles:

$$\psi_{ij}^{\text{Mol}} = \rho_j - \rho_i \tag{3.3}$$

Another formulation was proposed by Ferrari et al. [56] on the basis of a monotone upwind flux and it presents a similar mathematical structure of Eq. 3.3. In this case the expression for ψ reads:

$$\psi_{ij}^{\text{Fe}} = \frac{\rho_j - \rho_i}{2h} \|\boldsymbol{r}_j - \boldsymbol{r}_i\| \tag{3.4}$$

This formulation presents a slightly different form of the Molteni and Colagrossi [104] formulation, but it assumes the same smoothing magnitude when $\delta^{\text{Mo}} = 0.5$.

Groenenboom and Cartwright [68] derived a diffusive formulation by inspecting the time-discretized version of the momentum equations for an inviscid fluid without external forces and analyzing the backward Euler finite difference formulation. Also in this case, as noticed by the authors, this formulation is similar to that proposed by Molteni and Colagrossi, if the linearized state equation is assumed. Specifically, a direct connection between the two formulations can be found when the acoustic time step restriction referred to the weakly-compressibility assumption is adopted:

$$\Delta t = \text{CFL}\frac{h}{c_0 + \lambda} \tag{3.5}$$

in which $\lambda = \max\{\|\boldsymbol{u}_i\| + \pi_{ij}\}$. For the considered fluid problems, the constraint expressed in Eq. 3.5 is usually the most restrictive condition, ensuring the temporal stability with respect to other conditions linked to the particle acceleration, the artificial viscosity and the diffusive term. In this way, it is possible to write a relationship between the parameter δ^{Gr} of Groenenboom and Cartwright [68] model and the parameter δ^{Mo} of Molteni and Colagrossi [104] model:

$$\delta^{\text{Gr}} = \frac{1}{\text{CFL}}\frac{c_0 + \lambda}{c_0}\delta^{\text{Mo}} \tag{3.6}$$

The parameter δ^{Gr} is thus a function of the integration scheme since the Courant Friedrichs Lewy (CFL) number is involved in its evaluation. Moreover, in this formulation it is not necessary to impose any other constraints on the time step related to the diffusive term, since it is intrinsically satisfied by the time step being explicitly present in this diffusive scheme.

In the mentioned formulations, the diffusive term is approximated by the Morris formula [119] that represents the Laplacian in SPH schemes:

$$\Lambda_i = 2\sum_j (f_j - f_i)\frac{(\boldsymbol{r}_j - \boldsymbol{r}_i)\cdot\nabla_i W_j(\boldsymbol{r}_i)}{\|\boldsymbol{r}_j - \boldsymbol{r}_i\|^2}V_j \tag{3.7}$$

where f is a scalar quantity. To investigate the behavior of this operator, Antuono et al. [6] studied the convergence of the Laplacian in SPH context and they noticed that this last formula is singular near the free surface. In particular, they found that, for kernels in the form $W = W(-|\boldsymbol{r}_{ji}|^2/h^2)$, such as Gaussian ones, the following expression holds:

$$\nabla^2\langle f\rangle|_i = \Lambda_i - 2\nabla f|_i \cdot \nabla S|_i + O((1 - S|_i)) + O(h^2) \tag{3.8}$$

in which $S|_i = \sum_j W_j(\boldsymbol{r}_i)V_j$. From Eq. 3.8 the Morris formula (Eq. 3.7) converges to the Laplacian of f only if $\nabla S = 0$ and $S = 1$. This condition is verified inside the fluid domain, but not near the free surface, where ∇S diverges as h^{-1} introducing errors in the numerical solution [27].

To find an expression that always converges in the fluid domain, Antuono et al. [6] proposed a modified diffusive term to better approximate Eq. 3.8. The improvement of the model comes from the introduction of renormalized density gradients, inside the

diffusive term, in order to assure the convergence over the fluid domain and preserve the conservation of mass. In this formulation, called δ-SPH, the term ψ_{ij} reads as:

$$\psi_{ij}^{\text{An}} = (\rho_j - \rho_i) - 1/2[\langle\nabla\rho\rangle_i^L + \langle\nabla\rho\rangle_j^L] \cdot (\boldsymbol{r}_j - \boldsymbol{r}_i) \tag{3.9}$$

The quantity $\langle\nabla\rho\rangle_i^L$ represents the renormalized density gradient, defined as:

$$\langle\nabla\rho\rangle_i^L = \sum_j (\rho_j - \rho_i)\boldsymbol{L}_i \nabla_i W_j(\boldsymbol{r}_i) V_j \tag{3.10}$$

$$\boldsymbol{L}_i = \left[\sum_j (\boldsymbol{r}_j - \boldsymbol{r}_i) \otimes \nabla_i W_j(\boldsymbol{r}_i) V_j\right]^{-1}$$

The range of variation of δ^{An} parameter has been found by Antuono et al. [4] through a linear stability analysis and, in case of a Gaussian kernel, it results in:

$$\frac{\alpha^3}{27} < \delta^{\text{An}} < \frac{9}{2\pi^2}\left(\frac{\alpha}{2} + \frac{3}{2\pi}\right). \tag{3.11}$$

The limit of δ^{An} parameter is therefore related to the magnitude of the artificial viscosity adopted. In the typical range of α used in hydraulic applications, δ^{An} is smaller than about 0.22.

Antuono et al. [4] presented a detailed analysis of the diffusive terms, putting particular attention to Morris-like models (see [104], [56], [68]), and δ-SPH [6] formulation. In particular, because of the inaccuracy near the free surface, the Morris-like models show an unphysical upwards displacement of the fluid particles near the free surface. This inaccuracy is no longer encountered in the δ-SPH scheme, as a result of the presence of the renormalized density gradients. Another issue related to the former models is the loss of potential energy, also noticed for purely hydrostatic simulations. Conversely, the latter model preserves the hydrostatic solution. A different situation is encountered when high velocities and rapid changes in the fluid domain occur. In these cases, the δ-SPH model presents a lower efficiency in smoothing the traveling sound waves after violent fluid-fluid or fluid-solid impacts.

3.1.1 Hybrid diffusive term

In order to find an expression for the diffusive term that is effective when dealing with situation of slow and fast dynamics, a small modification to the diffusive term proposed by Antuono et al. [6] is introduced, by considering a tuning parameter, $\beta(\boldsymbol{r})$, that activates or deactivates the renormalized density gradients as a function of the position of the particles inside the fluid domain. Considering Eq. 3.9, the expression for ψ_{ij} becomes:

$$\psi_{ij}^{\text{Hy}} = (\rho_j - \rho_i) - 1/2[\beta(\boldsymbol{r}_i)\langle\nabla\rho\rangle_i^L + \beta(\boldsymbol{r}_j)\langle\nabla\rho\rangle_j^L] \cdot (\boldsymbol{r}_j - \boldsymbol{r}_i) \tag{3.12}$$

in which $\beta(\boldsymbol{r}) \in [0, 1]$. In the case that $\beta(\boldsymbol{r}) = 0$, the Molteni and Colagrossi [104] formulation is recovered, while the Antuono et al. [6] formulation is recovered when $\beta(\boldsymbol{r}) = 1$. For values in the range $0 < \beta(\boldsymbol{r}) < 1$, a transition (or hybrid zone) between the two formulations is obtained. This last condition is introduced in order to give a

gradual transition between the two models, instead of a step function. A variation law for the parameter β is defined for the transition zone, that is considered here as simple linear variation, although smoother functions can be taken into account. Referring to Eq. 3.8, the introduction of this parameter acts on the second term of the right hand side of the equation, hence the transition from the involved two models can be regarded as a gradual introduction of a higher approximation of the diffusive term.

The use of the hybrid diffusive term implies that in the fluid domain away from rapid fluid dynamics (absence of fluid-fluid and fluid-solid impacts) the δ-SPH formulation is applied, while in the area characterized by faster dynamics (violent impacts) the Molteni and Colagrossi term is enforced. In this way, the 4th order diffusive formulation conserves the fluid properties in the majority of the fluid domain and, in presence of fluid impacts, the 2nd order diffusive term better smooths the spurious oscillations, limiting the generation of spurious shock waves.

The use of the hybrid diffusive formulation is implemented for a test case dealing with wave interaction with perforated breakwater. As it will be presented in section 5.2, the β-parameter is modeled according with the distance from the walls of the breakwaters, where fluid-structure interaction occurs.

3.1.2 Automatic hybrid term

In the hybrid formulation presented in Eq. 3.12, if a certain part of the domain is expected to be characterized by violent impacts would be implemented with $\beta(\boldsymbol{r}) = 0$, recovering therefore the [104] formulation, while for the remaining parts of the fluid domain it would be $\beta(\boldsymbol{r}) = 1$, recovering the [6] formulation. The result is that the portions of the fluid domain in which the specific diffusive formulation is acting have to be defined *a priori* and does not take into account for the instantaneous variation of the field values.

In this context, an improvement of the model is introduced by considering a tuning parameter that detects the occurrence of fluid impacts and automatically switches between the two formulations. In the weakly-compressible context, the occurrence of fluid-fluid or fluid-solid impacts implies a spatial variation of pressure or, equivalently, density between the involved interacting particles. Since $\Delta\rho < 1\%\rho_0$, it results to be more convenient to consider the β-parameter as a function of the differences in density between the two interacting fluid particles, $\beta(\Delta\rho_{ij})$. Therefore, the automatic hybrid diffusive term for ψ_{ij} becomes:

$$\psi_{ij}^{\mathrm{HyA}} = (\rho_j - \rho_i) - 1/2\,\beta(\Delta\rho_{ij})[\langle\nabla\rho\rangle_i^L + \langle\nabla\rho\rangle_j^L] \cdot (\boldsymbol{r}_j - \boldsymbol{r}_i) \tag{3.13}$$

in which $\beta(\Delta\rho_{ij}) \in [0, 1]$. Also in the case, when $\beta(\Delta\rho_{ij}) = 0$, the [104] formulation is recovered, while the [6] formulation is recovered when $\beta(\Delta\rho_{ij}) = 1$. In the range $0 < \beta(\Delta\rho_{ij}) < 1$, an hybrid zone between the two formulations is obtained.

It is noticed that, in the case of free surface flows, and when fluid particles are located at different heights, there is a difference in density only due to the hydrostatic compression of the particles. This static quantity has to be subtracted because it does not count in hydrodynamic contribute. For a particle located at a water depth d_i and considering the linearized state equation, the value of the density in hydrostatic conditions results to be:

$$\rho_{is} = \rho_0 + \frac{\rho_0 g}{c_0^2} d_i \tag{3.14}$$

The variation of density between the two interacting particle only due to the hydrodynamic contribution results, therefore, to be:

$$\Delta\rho_i = \rho_i - \rho_{is} = \rho_i - \rho_0 - \frac{\rho_0 g}{c_0^2} d_i \tag{3.15}$$

If the water depth is $d_i = z_{max} - z_i$, with z_{max} the dynamic free surface level, assumed to be the same for the two particles, the differences in density between two particles only due to hydrodynamic contribute (water impacts) is:

$$\Delta\rho_{ij} = |\rho_i - \rho_j + \frac{\rho_0 g}{c_0^2}(z_i - z_j)| \tag{3.16}$$

where the absolute value is used to incorporate the conditions $\Delta\rho_i > \Delta\rho_j$ and $\Delta\rho_j > \Delta\rho_i$. The most extreme condition under weakly compressible assumption is that the i-th particle shows a value $\rho_i = \rho_0 + 1\%\rho_0$ while the j-th particle a value $\rho_j = \rho_0 - 1\%\rho_0$. The maximum difference in particles density is therefore equal to $\Delta\rho_{ij} = 2\%\rho_0$ and a dependence for $\beta(\Delta\rho_{ij})$ has to be defined in the range $\Delta\rho_{ij} \in [0, 2\%\rho_0]$. Referring to Fig. 3.1, for small differences of density between the particles, the value of β is equal to 1 and the δ-SPH formulation is enforced. In this case, these variations of density are only associated to slow dynamics phenomena. The upper limit of this range is defined by the value $\Delta\rho_A$, in which the acoustic component starts to appear in the flow field. In the second range, the hybrid formulation takes place, in which the β-parameter assumes a linear variation between 1, in correspondence to $\Delta\rho_A$, and 0, in correspondence to $\Delta\rho_M$. In this range, high frequency noise starts to rise in the pressure field

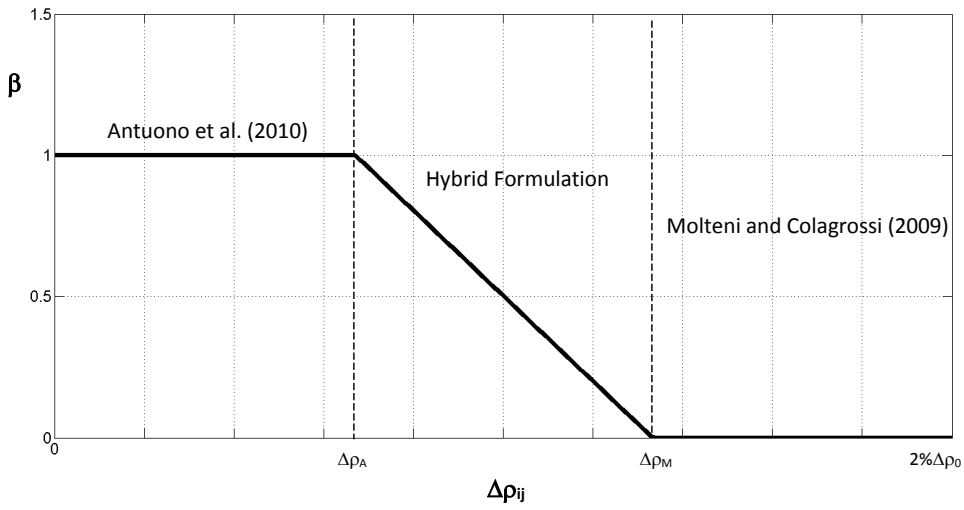

Figure 3.1: *Variation of β-parameter as a function of the dynamic density difference between the fluid particles.*

but it is still not yet relevant. For values higher than $\Delta\rho_M$, the parameter β is set equal to 0 and the Molteni and Colagrossi formulation is enforced. In this case, significant variations in the density field due to the presence of fast dynamics and water impacts are encountered in the pressure field.

It have to be noticed that, in the case of a suspended fluid mass (like for example the splash after an impact or in the case of a breaking wave) even if there is no hy-

drostatic compression contribution, the static term is also subtracted. This situation represents, in any case, only a minor issue of the formulation. The values of $\Delta\rho_{ij}$ in which the transition between the different formulations occurs are here heuristically fixed to $\Delta\rho_A = 0.3\%\rho_0$ and $\Delta\rho_M = 0.6\%\rho_0$. A test case in which the automatic hybrid formulation is applied regards the analysis of waves-perforated breakwaters, presented in section 5.3.1.

3.2 Enforcing solid boundary conditions

The enforcing of solid boundary condition is a crucial topic for several SPH applications and, for some aspects, it is still an open problem. Over the years many different approaches have been presented, which have therefore resulted in a lack of a universal technique. One of the major issues related with the particle approaching a solid boundary is the truncation of the kernel function by the body profile, resulting in a rapid decrease of the interpolation accuracy (see section 2.2.3). For this reason, most of these techniques have been addressed to overcome this drawback.

Among the different approaches, the most used in literature are the repulsive-type particle [106] and the ghost-type particle [26] treatments. In the case of the repulsive forces, the no-penetration boundary condition is enforced by introducing "repellent" particles along the region where the solid body is located. In this case the interacting force is given by a defined expression, derived from physical considerations on the nature of the solid-fluid interaction. Conversely, in the ghost particles framework, all the fluid particles, within a layer with thickness equal to the kernel radius from the considered wall, are mirrored inside the solid body. In this way, the field values associated to the ghost particle are those obtained from the correspondent mirrored one in the fluid mass, where the normal component of velocity is reversed. This approach, that allows to exactly enforce free slip boundary conditions, is adopted in this thesis. Therefore a detailed presentation of an enhancement of this method is here illustrated.

3.2.1 Fixed ghost particles

The fixed ghost particles treatment, introduced by Marrone et al. [96], is an enhancement of the ghost particles technique. In this framework the ghost particles are fixed in the frame of reference of the solid and are created once at the beginning of the simulation with a regular distribution. The fixed ghost particles cover a body region with size equal to the width of the kernel support radius. An interpolation point is associated to every solid particle, obtained by mirroring the position of the fixed ghost particle in the fluid domain, with the respect of the body profile. The interpolation procedure of the field values around the interpolation node, to associate to the fixed particles is obtained through a MLS corrected kernel, Eq. 2.48, at each time step of the simulation. For the properties previously mentioned the MLS interpolation ensures an accurate mirroring of the flow quantities. A scheme of the implementation of fixed ghost particles is presented in Fig. 3.2. In the fixed ghost particles approach, the distribution of ghost particles is always uniform and does not depend on the positions of the fluid particles, allowing for modeling more complicated shapes of boundaries. When implementing

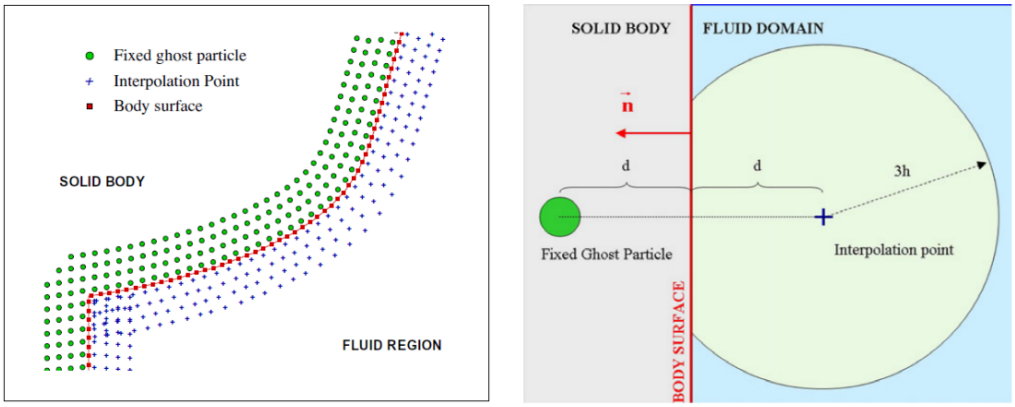

Figure 3.2: *Left: sketch of fixed ghost particles with interpolation nodes. Right: sketch of the interpolation procedure (Marrone et al. [96]).*

the free-slip boundary condition, Eq. 2.22 and Eq. 2.23 become:

$$u_{nG} = 2u_{nB} - u_{nI} \tag{3.17}$$
$$u_{\tau G} = u_{\tau I} \tag{3.18}$$

where u_{nG} and $u_{\tau G}$ are the normal and tangential component of velocity enforced to the fixed ghost particle, u_{nB} is the velocity of the boundary (in the case of a moving contour) and u_{nI} and $u_{\tau I}$ are the normal and tangential velocity interpolated in the fluid domain:

$$u_{nI} = \sum_{j \epsilon fluid} u_{nj} W_i^{\text{MLS}}(\boldsymbol{r}_j)\, dV_j, \qquad u_{\tau I} = \sum_{j \epsilon fluid} u_{\tau j} W_i^{\text{MLS}}(\boldsymbol{r}_j)\, dV_j \tag{3.19}$$

in which u_{nj} and $u_{\tau j}$ are the normal and tangential velocity components of the considered j-th fluid particle. Following this approach is also possible to implement no-slip conditions, by reversing the interpolated tangential velocity:

$$u_{nG} = 2u_{nB} - u_{nI} \tag{3.20}$$
$$u_{\tau G} = -u_{\tau I} \tag{3.21}$$

Regarding the value of the pressure, p_G, to associate to the solid particles, this quantity is calculated as:

$$p_G = \sum_{j \epsilon fluid} p_j W_i^{\text{MLS}}(\boldsymbol{r}_j)\, dV_j + 2d_s \frac{\partial p}{\partial n} \tag{3.22}$$

The second term on the right hand side of the equation, as expressed in Eq. 2.24, is introduced to take into account differences on the hydrostatic pressure due to the position of the solid particle compared to its interpolation node and, in case of a moving boundary condition, to account for the linear and angular acceleration effects of the solid boundary. The quantity d_s is the distance between the ghost particle (or the interpolation point inside the fluid) and the body profile and it proves to be dependent on the value of Δx.

Here some details about the enforcing of a moving-boundary condition in the case of a wave generator are presented. For a piston-type wavemaker, that will be successively

adopted in different hydraulic applications, all solid points are subjected to a translation motion, resulting for the angular velocity, in Eq. 2.24, to be $d\boldsymbol{n}/dt = \mathbf{0}$. The values of $\boldsymbol{u}_B$ are calculated deriving the time variation of the horizontal displacement, $e(t)$, at the wavemaker section. For regular waves, the horizontal displacement is:

$$e(t) = \frac{S_0}{2}\sin(\omega t) \tag{3.23}$$

where S_0 is defined as the stroke of the paddle, ω (wave frequency) = $2\pi/T$ and T is the wave period. Eq. 3.23 is expressed by a sinusoidal motion law which gives in the channel a periodic wave train with a degree of non-linearity quantified by the combination of wave height, H, wave period and water depth and expressed by the number of wave harmonics occurring in the spectral density of the surface elevation. The stroke is related to the wave characteristics along the channel by the help of Biésel transfer function, B. For a piston-type wavemaker, the value of B is given by:

$$B = \frac{H}{S_0} = \frac{2\sinh(kd)^2}{\sinh(kd)\cosh(kd) + kd} \tag{3.24}$$

where k (wave number) = $2\pi/L$ and L is the wave length. For a given water depth, the values of H and T are calculated by the zero-up crossing statistical method from the numerical results of the time records of the surface elevations, η.

To avoid impulsive phenomena in the numerical wave channel which could perturb the flow field, the time series of horizontal displacements are modified with a ramp function, $R(t)$, associated to an initial time window:

$$R(t) = \frac{1}{2}\left[1 - \cos\left(\frac{\pi}{\tau_r}t\right)\right] \tag{3.25}$$

where τ_r represents the ramp duration which is here set equal to T.

3.2.2 Multi-node fixed ghost particles

In the fixed ghost particles approach, as described in the previous section, it is necessary to cover a distance equal to the length of the kernel radius. In this way, as particles of the fluid domain approach the solid boundary, they will always find neighboring interacting particles and the accuracy related to kernel truncation is not compromised. For a support kernel with a radius equal to $3h$ this would result in a layer formed by four lines of fixed ghost particles, equispaced with the initial resolution Δx, since $h = 4/3\Delta x$.

For a problem in which the fluid mass is present at both sides of a solid boundary, to correctly enforce boundary conditions, four lines of fixed ghost particles interacting with fluid particles in the left side and four lines of fixed ghost particles interacting with fluid particles in the right side are necessary. This approach results in a layer consisting of eight lines of fixed ghost particles (case of kernel $3h$). This situation does not represent any difficulty if the width of the solid body is big enough, but problems may arise if the structure is thin. Since the adopted initial spatial resolution is driven, in this case, by the presence of thin solid elements, a high resolution is necessary even if it leads to disadvantages in terms of the computational time of the simulation. Specifically, the

numerical simulation of a thin structure leads to choose a small initial spatial resolution for the considered problem, resulting in an increase of the computational cost. This situation often occurs in the numerical reproduction of small-scale laboratory experiments. Indeed, physical models of structures are often made by slender elements such as the decks of offshore platforms or ships [34], or in the case of perforated wall-caisson breakwaters where timber [12], Perspex [78] or plastic plates [52] are used.

To overcome the problem, the CPU time can be reduced through the use of MPI-OpenMP programming models (*e.g.* Marrone et al. [97]) or Graphics Processing Units (*e.g.* Domínguez et al. [47], [48]) or, alternatively, by using a variable resolution (*e.g.* Vacondio et al. [150]). The mentioned solutions could result in efforts in the implementation of the SPH code.

A different solution can be obtained if, at every fixed ghost particle representing a thin structure, more interpolation nodes are associated resulting in a multi-node fixed ghost particle approach. Thus the fluid domain is divided into sub-areas Ω_k and an interpolation node for the reference solid particle is associated to every sub-area. Consequently, the fixed ghost particles present an array of values interpolated at different sub-areas for the same physical quantity. When a fluid particle located in a region Ω_k interacts with a multi-node fixed ghost particle, the last assumes the field values interpolated in the reference area Ω_k through the k-th node. In Fig. 3.3, a general case of the use of the multi-node approach is sketched, where the limits between the sub-regions are represented by dashed lines. For a correct modeling, the solid particles located away from the ends of the slender structure are characterized by only two nodes since the interaction with fluid particles occurs only from two sides, while the solid particles located on the ends, being surrounded by the fluid mass, are characterized by three interpolation nodes, with a resulting subdivision into three regions.

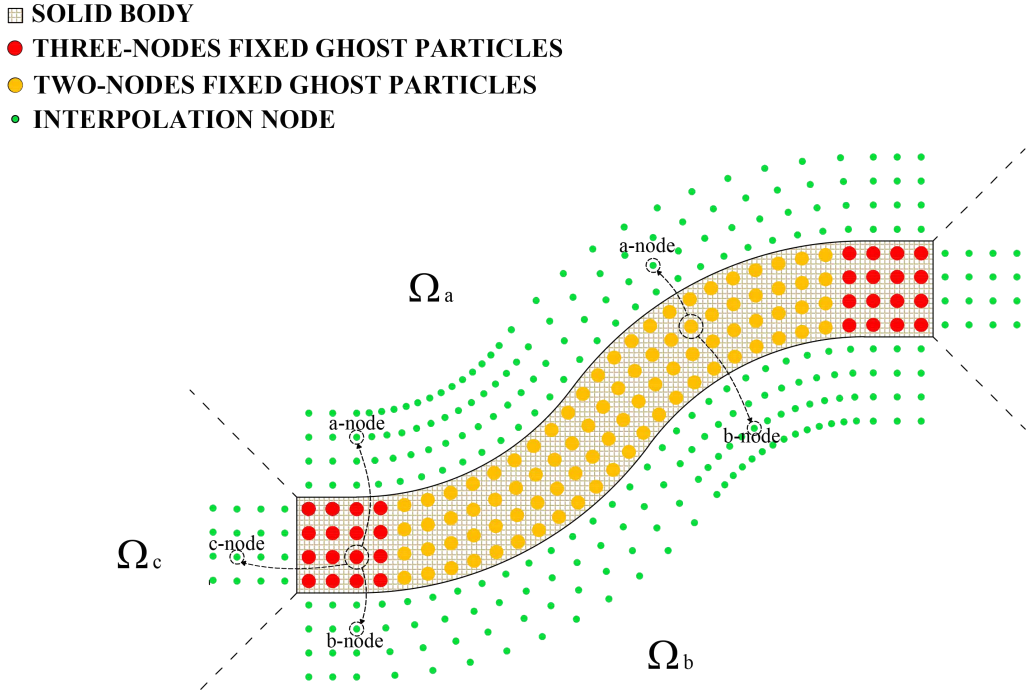

Figure 3.3: *Sketch of multi-node fixed ghost particles with interpolation nodes for a solid body.*

In Fig. 3.4 the differences in modeling a solid object with fixed ghost particles and multi-node fixed ghost particles are illustrated. With reference to the example in the right sketch in Fig. 3.4, the coordinates of the k-th node (x_{kn}, z_{kn}) of the fixed ghost particles with coordinates (x_i, z_i) are determined as follows:

$$\begin{cases} a_{node}: & x_{an} = x_l - (x_i - x_l), & z_{an} = z_i \\ b_{node}: & x_{bn} = x_r + (x_r - x_i), & z_{bn} = z_i \\ c_{node}: & x_{cn} = x_i, & z_{cn} = z_o + (z_o - z_i) \end{cases} \tag{3.26}$$

Moreover, it is possible to observe that the interpolation nodes of the solid particles located on the bisectors of the edges of the body are mirrored along the projection of the bisectors in the fluid domain using the classical fixed ghost particles framework (see left sketch in Fig. 3.4). In the multi-node approach, the node is instead always mirrored with the respect of the body profile. The transition between sub-areas occurs along the projection of the bisectors characterized by different interpolation nodes.

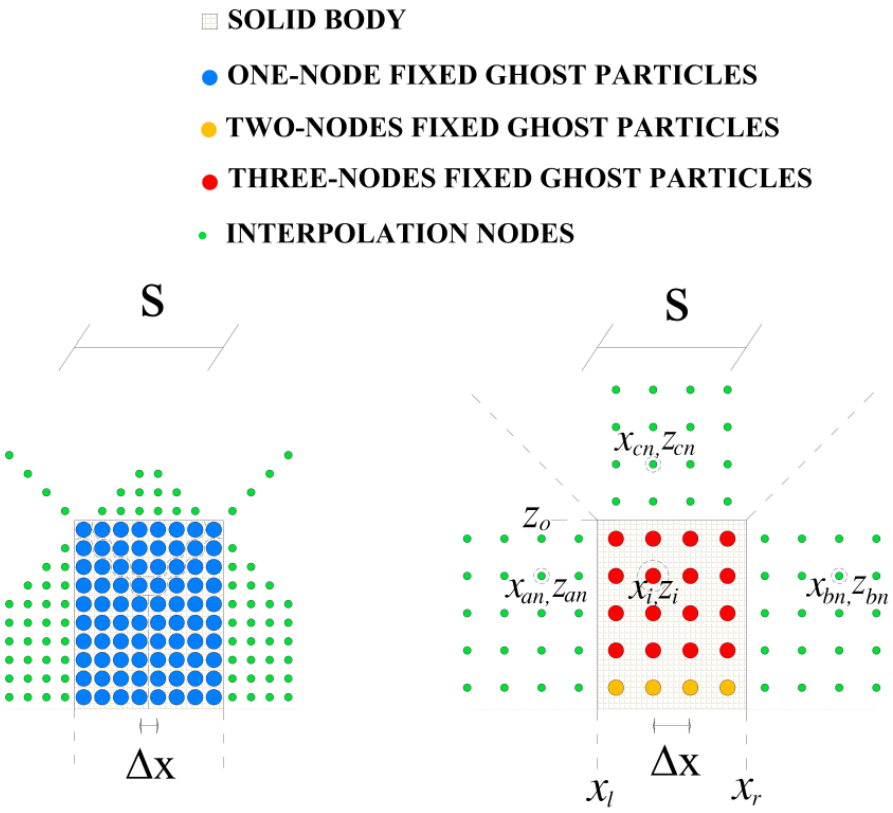

Figure 3.4: *Differences between classical fixed ghost particles approach (left sketch) and multi-node approach (right sketch) in modelling a solid boundary (the value of Δx represents the minimal resolution necessary to model the body characterized by a width s).*

The multi-node method is direct and easy to implement in the case of flat surfaces and well defined corners, while some difficulties may arise when dealing with a more complicated shape. In this case, the difficulties would be to find the right location for

the fixed ghost particles with related nodes and then to determine the domain subdivision into sub-areas with their transitions. Regarding the former problem, it is recommendable to use a method based on a spline interpolation which has been successfully employed for the case of fixed ghost particles by Marrone et al. [96] and applied to more complex shapes (*e.g.* Bouscasse et al. [17]). For the latter one, the individuation of the sub-domains is dependent on the geometrical shape of the thin object. An object with one dimension prevalent on the other one (long-limbed) would require a subdivision in three sub-domains near the ends and two away from them, as in the case of the slotted wall. In the case of small square objects, a different solution would be the adoption of four sub-domains division with corresponding interpolation nodes.

For 2D problems, the number of total particles required by the proposed multi-node technique is, in the case of a thin object driving the resolution, $N_p \propto (1/2)^2 = 1/4$ the number of total particles requested by the use of the fixed ghost particles. It is interesting to notice that, in the case of extension to 3D simulations, the multi-node approach would result in a number of total particles that is $N_p \propto (1/2)^3 = 1/8$ the number of total particles needed with the classical approach. For 3D problems, the computational time saving would be quite higher than that obtained in the 2D cases.

3.3 Time integration schemes

Since the SPH method reduces the original continuum partial differential equations into a set of ordinary differential equations, any stable time-stepping algorithm to integrate ordinary differential equations can be taken into account [108]. In this section the time integration schemes implemented for the present SPH solver are shown, with considerations on the time step length.

For the considered fluid problem, *i.e.* viscous flow modeled by a weakly-compressible diffusive SPH scheme, the time-step Δt is calculated through the following restrictive conditions:

$$\Delta t \leq \min(\Delta t_v, \Delta t_\delta, \Delta t_c), \tag{3.27}$$

where Δt_v is the time-step referred to the artificial viscosity:

$$\Delta t_v = \text{CFL}_v \frac{h^2}{\nu} \tag{3.28}$$

and ν is the kinematic viscosity. The term Δt_δ is the time-step referred to the presence of the diffusive term:

$$\Delta t_\delta = \text{CFL}_\delta \frac{h}{\delta c_0}, \tag{3.29}$$

meaning that the time-step should decrease when the diffusive coefficient, δ, increases. Finally, the advective/acoustic component time-step restriction is expressed by:

$$\Delta t_c = \text{CFL}_c \min_i \left(\frac{h}{c_0 + \|\boldsymbol{u}_i\| + h \max_j \pi_{ij}} \right) \tag{3.30}$$

In Eqs. 3.28, 3.29 and 3.30 the quantities CFL_v, CFL_δ and CFL_c represents dimensionless parameters heuristically fixed according with the accuracy of the involved integration scheme. In particular, the higher the accuracy of the scheme, the larger the values of these coefficients, allowing for a wider time-step.

3.3.1 Modified Verlet

The *modified Verlet* time-stepping scheme conserves linear and angular momenta and also furnish suitable results for integrations which involve a large number of time-steps [109]. As observed by Molteni and Colagrossi [104], the modified Verlet scheme, being a 2nd-order scheme, makes possible to assume a larger time step with respect to other time integration schemes adopted in SPH context, such as modified Euler scheme (see *e.g.* [108]). The variables of interest are evaluated at the first step as follows:

$$\begin{cases} \boldsymbol{r}_i^{(1)} = \boldsymbol{r}_i^{(n)} + \dfrac{1}{2}\Delta t \boldsymbol{u}_i^{(n)} \\ \\ \rho_i^{(1)} = \rho_i^{(n)} + \dfrac{1}{2}\Delta t \left(\dfrac{D\rho}{Dt}\right)_i^{(n)} \end{cases} \tag{3.31}$$

The field values are then evaluated in a second (final) time-step as follows:

$$\begin{cases} \boldsymbol{u}_i^{(n+1)} = \boldsymbol{u}_i^{(n)} + \Delta t \left(\dfrac{D\boldsymbol{u}}{Dt}\right)_i^{(1)} \\ \\ \boldsymbol{r}_i^{(n+1)} = \boldsymbol{r}_i^{(1)} + \dfrac{1}{2}\Delta t \boldsymbol{u}_i^{(n+1)} \\ \\ \rho_i^{(n+1)} = \rho_i^{(1)} + \dfrac{1}{2}\Delta t \left(\dfrac{D\rho}{Dt}\right)_i^{(1)} \end{cases} \tag{3.32}$$

where the indices (n), (1) and $(n+1)$ denote the values at the initial step, halfway and at the end of a step, respectively. In the case of a modified Verlet scheme, the time-step coefficients are heuristically set equal to $\text{CFL}_v = 0.125$, $\text{CFL}_\delta = 0.44$ and $\text{CFL}_c = 1.2$.

3.3.2 Runge-Kutta

Since diffusive weakly-compressible SPH schemes are used for different analysis in this thesis, the evaluation of the diffusive term in the continuity equation can be, in some case, computationally demanding. Consequently, the choice of an appropriate integration scheme can reduce the run time of the simulations. Considering the governing System 2.62 in the following general form:

$$\frac{D\boldsymbol{w}}{Dt} = \boldsymbol{F}(\boldsymbol{w}) \tag{3.33}$$

the generic quantity can be split as $\boldsymbol{F} = \boldsymbol{M} + \boldsymbol{D}$, in which $\boldsymbol{D}$ contains only the diffusive term. Operating this manipulation, the Eq. 3.33 is solved with a 4th-order *Runge-Kutta*

integration scheme through a frozen diffusive approach (see Jameson et al. [73]):

$$\begin{cases} \boldsymbol{w}^{(0)} = \boldsymbol{w}^{(n)} \\ \boldsymbol{w}^{(1)} = \boldsymbol{w}^{(0)} + \boldsymbol{M}(\boldsymbol{w}^{(0)})\Delta t/2 + \boldsymbol{D}(\boldsymbol{w}^{(0)})\Delta t/2 \\ \boldsymbol{w}^{(2)} = \boldsymbol{w}^{(0)} + \boldsymbol{M}(\boldsymbol{w}^{(1)})\Delta t/2 + \boldsymbol{D}(\boldsymbol{w}^{(0)})\Delta t/2 \\ \boldsymbol{w}^{(3)} = \boldsymbol{w}^{(0)} + \boldsymbol{M}(\boldsymbol{w}^{(2)})\Delta t + \boldsymbol{D}(\boldsymbol{w}^{(0)})\Delta t \\ \boldsymbol{w}^{(4)} = \boldsymbol{w}^{(0)} + [\boldsymbol{M}(\boldsymbol{w}^{(0)}) + 2\boldsymbol{M}(\boldsymbol{w}^{(1)}) + \\ \quad 2\boldsymbol{M}(\boldsymbol{w}^{(2)}) + \boldsymbol{M}(\boldsymbol{w}^{(3)})]\Delta t/6 + \boldsymbol{D}(\boldsymbol{w}^{(0)})\Delta t \\ \boldsymbol{w}^{(n+1)} = \boldsymbol{w}^{(4)} \end{cases} \tag{3.34}$$

in which the indices (1), (2), (3) and (4) represents the intermediate time-steps, while (n) and $(n+1)$ the initial and final time-steps. The scheme 3.34 differs from the original Runge-Kutta scheme by taking the diffusive term to be evaluated once within each time-step [4].

In the case of a mobile solid boundary, as successively adopted in different hydraulic applications involving wave generation, the movement of the solid vertical wall representing a wavemaker is updated at each sub-time step of the Runge-Kutta integration scheme. Consequently, its position, $\boldsymbol{r}_B$, is:

$$\begin{cases} \boldsymbol{r}_B^{(0)} = \boldsymbol{r}_B^{(n)} \\ \boldsymbol{r}_B^{(1)} = \boldsymbol{r}_B^{(0)} + \boldsymbol{u}_B^{(1)}\Delta t/4 \\ \boldsymbol{r}_B^{(2)} = \boldsymbol{r}_B^{(1)} + \boldsymbol{u}_B^{(2)}\Delta t/4 \\ \boldsymbol{r}_B^{(3)} = \boldsymbol{r}_B^{(2)} + \boldsymbol{u}_B^{(3)}\Delta t/4 \\ \boldsymbol{r}_B^{(4)} = \boldsymbol{r}_B^{(3)} + \boldsymbol{u}_B^{(4)}\Delta t/4 \\ \boldsymbol{r}_B^{(n+1)} = \boldsymbol{r}_B^{(4)} \end{cases} \tag{3.35}$$

where $\boldsymbol{u}_B$ is the velocity of the moving boundary. Also in the case of a Runge-Kutta integration scheme, the time-steps referred to the artificial viscosity, Eq. 3.28, to the diffusive term, Eq. 3.29 and to the advective/acoustic condition, Eq. 3.30, have to be satisfied. It can be noticed that the considered integration scheme gives greater values of CFL number in comparison with the modified Verlet scheme or a 3rd-order TVD Runge-Kutta scheme [4]. The values for the time-step coefficients have been heuristically fixed, in Antuono et al. [4], equal to $\text{CFL}_v = 0.125$, $\text{CFL}_\delta = 0.44$ and $\text{CFL}_c = 2.2$.

3.4 Dynamic pressures at body profiles

In the analysis that will be presented in chapter 5 regarding the wave interaction with perforated breakwater, the assessment of dynamic pressures, Δp, acting on specific points of a body profile proves to be fundamental in evaluating the hydrodynamic forces.

Regarding the evaluation of the dynamic pressures, the general continuous formulation for the relationship between the total pressure, p, its static component, p_s, and Δp,

for a 2D problem, reads as:

$$\int_{\Gamma} p(\boldsymbol{r'}) W^{\mathrm{MLS}}(\boldsymbol{r} - \boldsymbol{r'}) d\Gamma' = \int_{\Gamma} [p_s(\boldsymbol{r'}) + \Delta p(\boldsymbol{r'})] W^{\mathrm{MLS}}(\boldsymbol{r} - \boldsymbol{r'}) d\Gamma' \tag{3.36}$$

in which, in this context, $\boldsymbol{r}$ represents here the position of the numerical pressure gauge, $\boldsymbol{r'}$ the position of the considered fluid particle and Γ is the specific support area. In Eq. 3.36 the evaluation is performed considering a weighting function with MLS correction, as expressed in Eq. 2.48.

Since $p_s = \rho g(d - z)$, where z is the vertical coordinate starting from the flume bottom, the expression for the dynamic pressure becomes:

$$\Delta p(d - z) = \int_{\Gamma} p W^{\mathrm{MLS}}(\boldsymbol{r} - \boldsymbol{r'}) d\Gamma' - \int_{\Gamma} \rho g(d - z) W^{\mathrm{MLS}}(\boldsymbol{r} - \boldsymbol{r'}) d\Gamma' \tag{3.37}$$

From Eq. 3.37 the second integral of the right side of the equation is equal to the value of the hydrostatic pressure evaluated in the barycenter depth, h_G, of the weighting function over the support area Γ. It can be noticed that subtracting directly the hydrostatic component of the numerical gauge depth from the integrated total pressure may lead to an error in estimation of the dynamic component. In this case, only when the barycenter of the supporting area coincides with the location of the measuring point, is the evaluation of the dynamical pressure correct. In the continuous formulation, this condition is always satisfied when the support area is symmetrical with respect to the measuring point. In the presence of non straight contours such as the edges of a perforated breakwater, this condition is no longer satisfied, resulting in an overestimation or underestimation of the dynamic pressures (see Fig. 3.5).

To prevent this, a correct procedure for the evaluation of dynamic pressure in a discrete formulation is considering the dynamic pressures for each involved particle and afterward operating with the interpolation technique. For the i-th measuring point, it reads as:

$$\Delta p_i = \sum_{j \epsilon \Gamma} \left[p_j - (d - z_j) \rho_0 g \right] W_j^{\mathrm{MLS}}(\boldsymbol{r}_i) V_j. \tag{3.38}$$

Eq. 3.38 is referred to all the particles below the Still Water Level (SWL), while for the particles above the still water level the dynamic pressure is equal to the total pressure. The evaluation of the pressure with Eq. 3.38 is determined for all the points located along the body profile of the breakwaters and equispaced by the adopted value of Δx. Particular attention should be paid to the measuring points near the free surface and, in particular, within the wave run-up and run-down. As sketched in Fig. 3.6, water particles are located inside the support area of the interpolating function even if there is no contact between the fluid mass and the measuring point. To avoid improper measurements, the pressure gauges are activated only when the free-surface level is higher than the position of the gauge point and are otherwise inactivated.

Regarding the evaluation of an optimal support area to weight the neighbor fluid particles in order to assess the wave pressures well, different formulations and radius of influence are tested. For instance, Gao et al. [60] have calibrated rectangular control area with support radius $2h$ and $3h$ through a spatial average of the involved fluid particles, while Ren et al. [128] have adopted a circular area using a spline kernel.

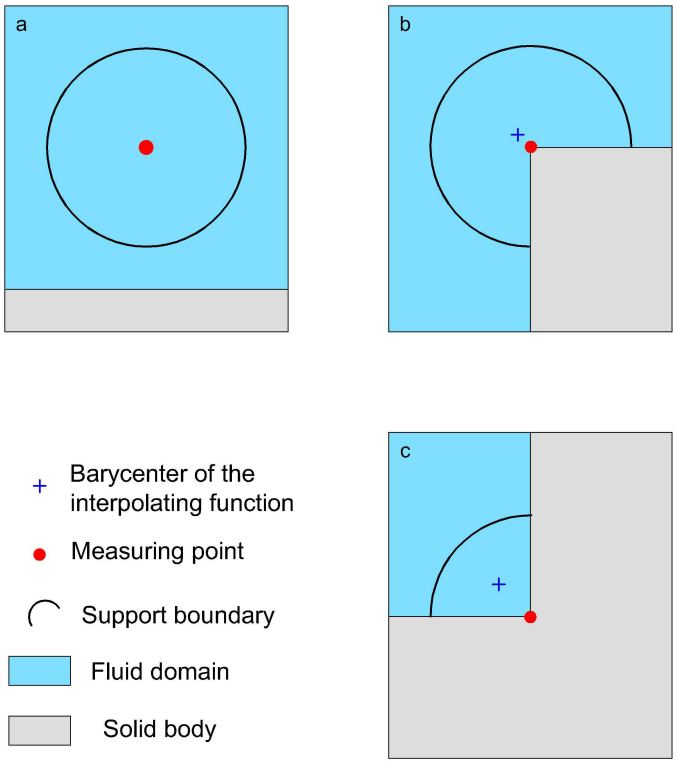

Figure 3.5: *Support area for a pressure gauge; in a) the area is not truncated by the solid boundary, therefore the measuring point and the barycenter of the interpolating function correspond; in b) and c) the truncation of the support area leads to a displacement between the measuring point and the barycenter of the interpolating function.*

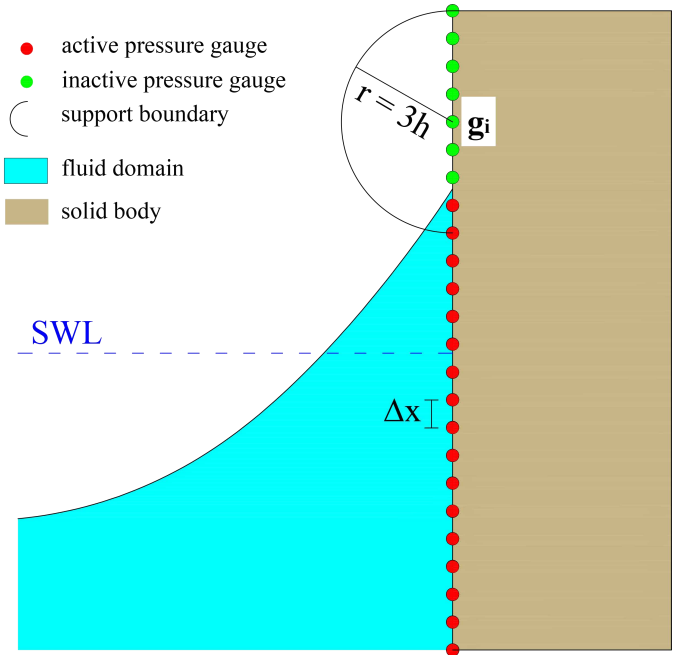

Figure 3.6: *Sketch of dynamic pressure interpolation for the gauges near the free surface (the pressure gauge g_i is inactivated even if the fluid mass reaches the area of the support radius).*

CHAPTER 4

Preliminary analysis

4.1 Still water tank

The simplest test case to validate the stability of the present computational scheme is the conservation of the hydrostatic solution. With this purpose, a still water tank initialized with a hydrostatic pressure distribution is presented. The governing equations expressed by System 2.72 are used, while classical ghost particles are implemented for the modeling of the solid boundary. In this case a Runge-Kutta integration scheme with no diffusive correction is taken into account, while for the artificial viscosity a coefficient $\alpha = 0.01$ is enforced. The initial configuration of the problem is shown in Fig. 4.1 (a), where the fluid particles are located in a regular grid, equispaced with an initial resolution $\Delta x = 0.004$ m. The height of the water tank is $H = 0.4$ m, while its width is $L = 0.6$ m. The final configuration, at $t = 30$ s, is shown in Fig. 4.1 (b), where the particles assumes a different spatial location from the initial configuration.

Even if the solution results to be stable in time, a small variation on the locations of the fluid particles occurs during the simulation, until their equilibrium position is not reached. To better understand this fact, and to also have a deeper insight on some aspects of the SPH, the conservation of energy is presented. In particular, in Fig. 4.2 the evolution of kinetic (Eq. 2.73), potential (Eq. 2.74), dissipated (Eq. 2.76) and elastic (Eq. 2.77) energies are displayed. For convenience, the initial potential energy, E_{P0}, is set equal to zero, resulting in an initial mechanical energy to be also equal to zero, being null the initial kinetic energy.

Fig. 4.3 is a detail of Fig. 4.2, in which the first 3 s of simulation are shown. As it is possible to see, in the first part of the simulation, until the initial regular grid locations of the particles is not broken, oscillation between different form of energy are observed. In particular, the dissipated internal energy energy result to be null, meaning that no dissipation processes are involved in this initial part of the simulation, and the only

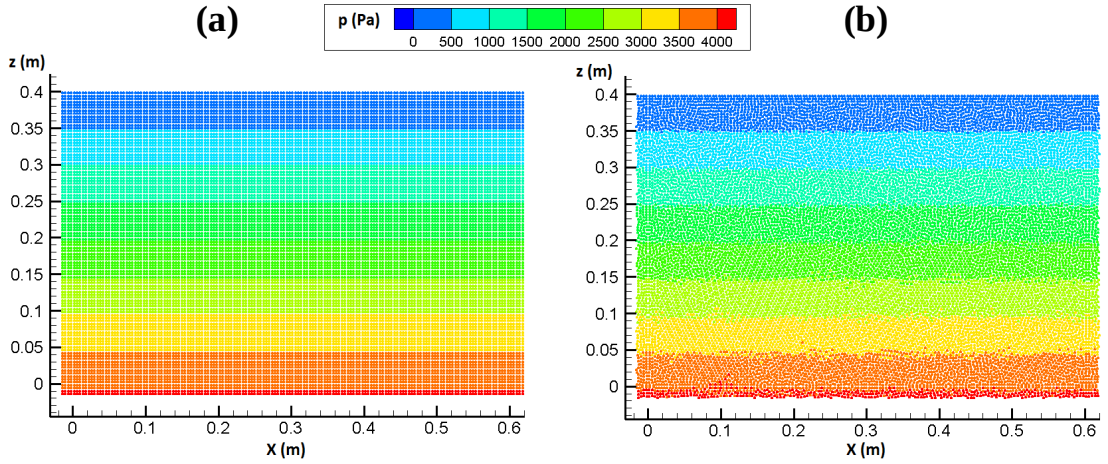

Figure 4.1: *Frames of the simulation with pressure distribution for the hydrostatic problem; (a) initial configuration of the particles; (b) final configuration at $t = 30$ s.*

variations of internal energy are due to the reversible energy. On the other hand, since the particles are not moving, their kinetic energy is equal to zero and the oscillations of internal energy are exactly balanced by oscillations of potential energy.

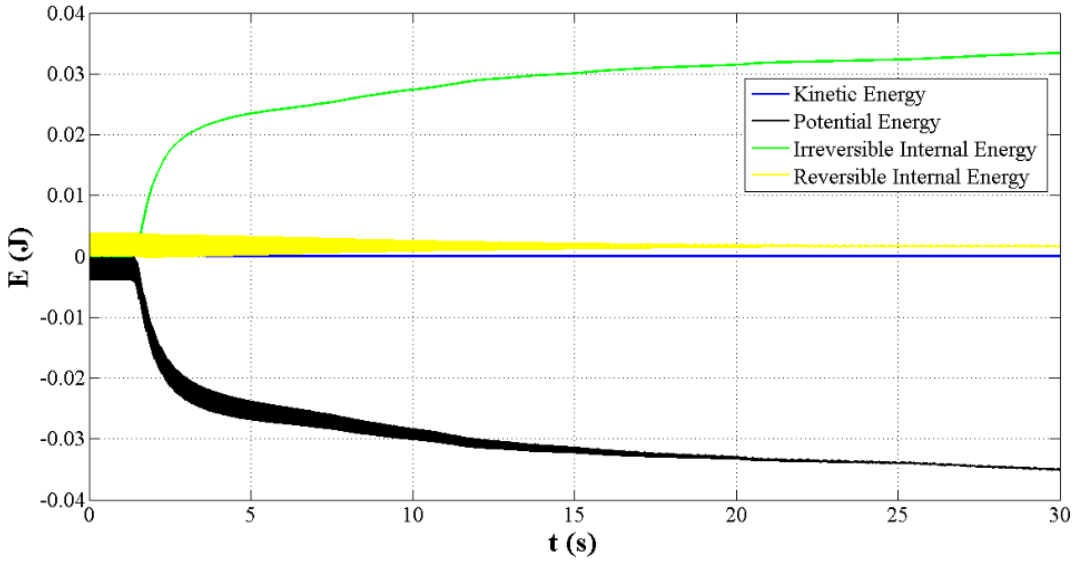

Figure 4.2: *Time evolution of the different forms of energy for the hydrostatic problem.*

When the unstable initial location of the particles is broken (at $t \cong 1.3$ s, see Fig. 4.3), the potential energy of the particles decrease with time, according with the fact that the particles move to a lower energy level (more stable positions). Conversely the total internal energy increase with time, allowing for the conservation of the total energy, as shown in Fig. 4.4. The reassessment of the particles after the breaking of the initial configuration, results therefore, as shown in Fig. 4.3, in a slight increment in the kinetic energy, related with the motion of the particles. This quantity however goes

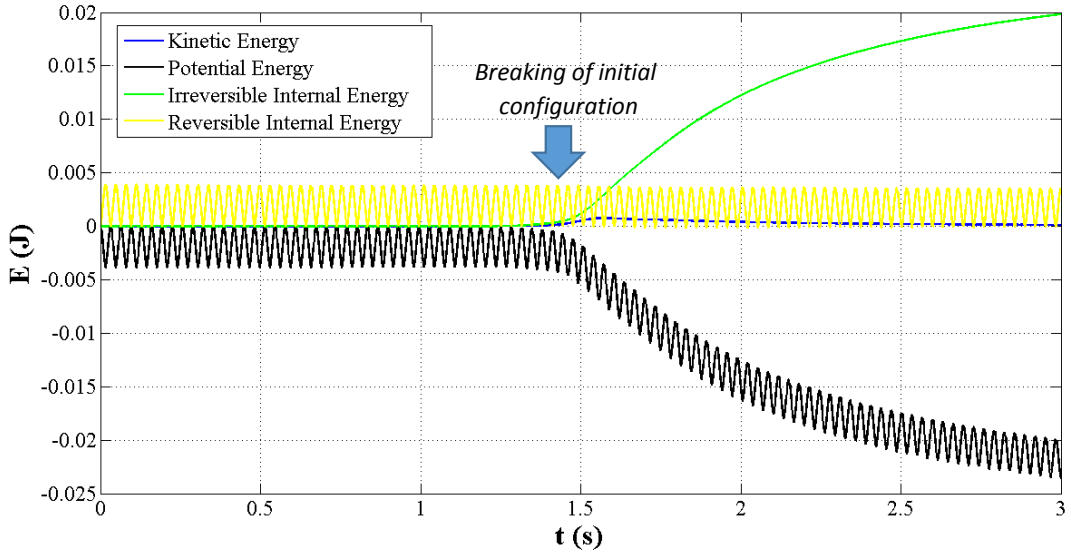

Figure 4.3: *Detail of Fig. 4.2 for the first 3 s of simulation, highlighting the time instant when the breaking of the initial configuration occurs.*

to zero for long time evolution, since the system tends to a stable solution of minimal potential energy and an increased internal energy. The sum of mechanical and internal energies, *i.e.* total energy, proves the conservativeness of the SPH scheme.

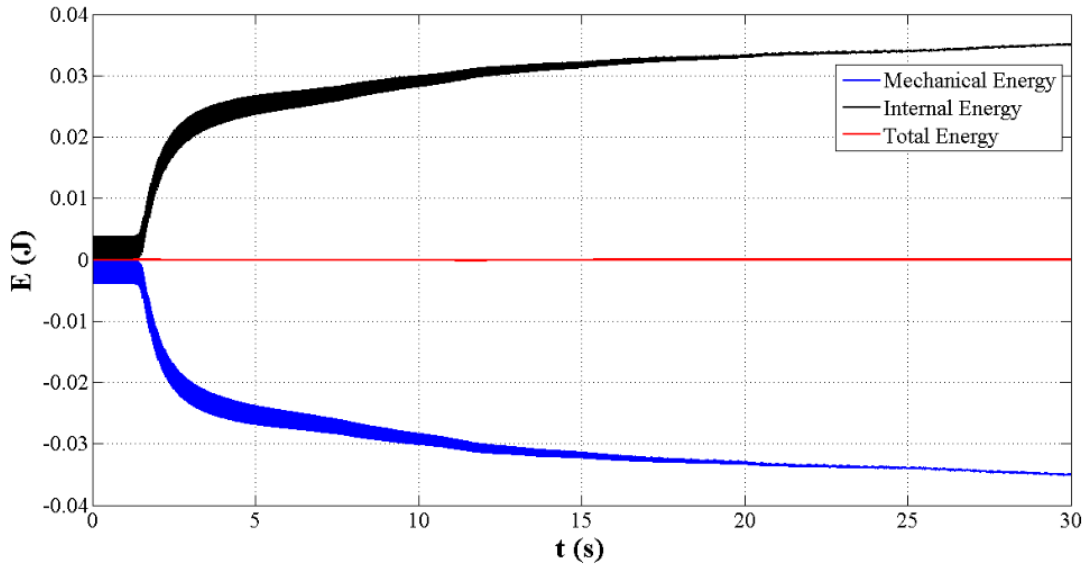

Figure 4.4: *Time evolution of internal and mechanical energies. The total energy, sum of E_I and E_M energies, is conserved in time.*

It is interesting to notice that, since the irreversible internal energy (energy dissipated into heat) is furnished by the viscous contribution, in the case of an inviscid SPH solution, *i.e.* artificial viscosity $\alpha = 0$, the potential energy due to the initial configuration of the particles is never dissipated. The result is that, after the breaking of the initial

configuration, the equilibrium configuration of the fluid particles is never attained, resulting in a continuous spurious motion of the fluid particles. This is the reason why in SPH solvers the artificial viscosity is used to enhance the stability of the model.

Anyhow, the problem of the initial configuration of the fluid particles is a relevant topic in SPH since, for particular geometries of the domain, it could result in the impossibility of attainment the equilibrium position, resulting in a destruction of the numerical solution. Colagrossi et al. [29] have shown that these spurious contribution are essentially due to the deviation of the pressure gradient operator from the exact differential operators. To propose a solution to this problem, the same authors presented the packing algorithm for the fluid particles that allows to recover, for every geometry of the domain, the spatial configuration of minimal energy for the particles, avoiding the introduction of spurious contribution related to particles location.

4.2 Oscillating drop under a central force field

In this section the dynamic of a two-dimensional fluid drop subjected to a central conservative force field is taken into account. This prototype test is often used in SPH context to evaluate the capabilities of the numerical model for a simple problem in which a characteristic physical phenomenon take place. In this case indeed the analytical solution is known, resulting for this case in a valuable benchmark for the model.

The force field is expressed by $-B^2\boldsymbol{r}$, where B is a dimensional parameter, while the drop at rest presents a circular shape with radius R. The drop periodically evolves as an oscillating fluid ellipse, according to the following law:

$$\begin{cases} u(t) = A(t)x \\ v(t) = -A(t)y \end{cases} \tag{4.1}$$

where the solution for $A(t)$ is given in Monaghan and Rafiee [111]. The drop is initialized with a velocity field given by $A(t=0) = A_0$. The global evolution of the drop depends on the ratio A_0/B.

In this case, the governing equations expressed by System 2.72 are taken into account. The problem is solved with a Runge-Kutta integration scheme, in which standard SPH and δ-SPH are compared. The artificial viscosity is tuned with a coefficient $\alpha = 0.01$.

4.2.1 Energy conservation during the drop evolution

This test case deals with the energy conservation during the evolution of the drop. In this case only standard SPH is taken into account. The initial configuration of the problem is shown in Fig. 4.5, where the initial pressure field and velocity vectors are represented. The radius of the drop is $R = 1$ m, while the adopted resolution is $\Delta x = 0.01$ m. A value for the ratio $A_0/B = 1/5$ is here considered.

The drop periodically evolves into ellipses as shown in Fig. 4.6 at the time instants of maximum elongations. In Fig. 4.7 the evolution of kinetic (Eq. 2.73), potential (Eq. 2.75), dissipated (Eq. 2.76) and elastic (Eq. 2.77) energies are displayed. The initial potential energy, E_{P0}, is set equal to the initial kinetic energy reversed in sign, so that the initial mechanical energy of the system is equal to zero. In this case is possible to

observe a periodic oscillation between kinetic and potential energy. When the drop is at its maximum elongation the potential energy is maximal and the kinetic energy is null, while a reversed situation is encountered when the drop is in a circular form.

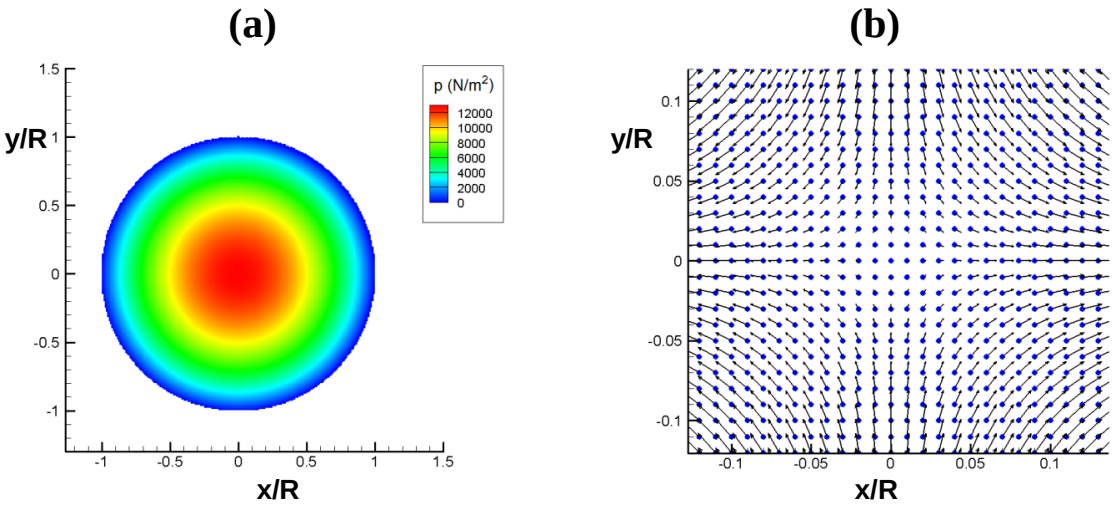

Figure 4.5: *Initial condition for the drop; (a) pressure field; (b) detail of the center of the drop in which the velocity vectors are represented.*

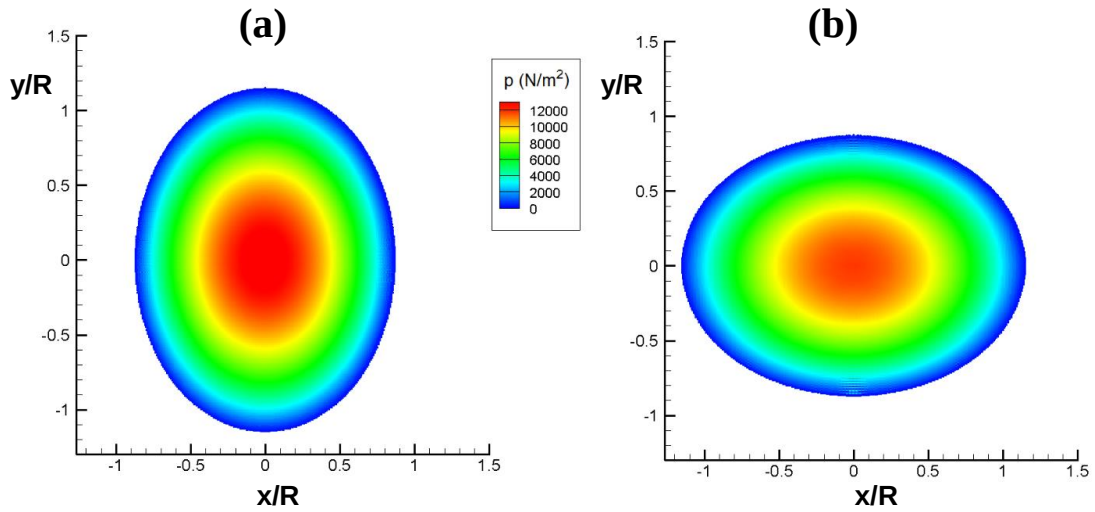

Figure 4.6: *Drop configuration at its maximal elongations for the first period of the evolution, in (a) along the y direction, while in (b) along the x direction.*

As the drop evolves in time, the oscillation of potential and kinetic energies are damped by the viscosity. This fact results in a decreasing of mechanical energy and an increasing in internal energy in time. As shown in Fig. 4.8, the mechanical energy dissipated is exactly balanced by the gained internal energy. For long time evolution the solution tends to a static configuration in which the drop assumes a circular shape, where the mechanical energy is completely dissipated into heat.

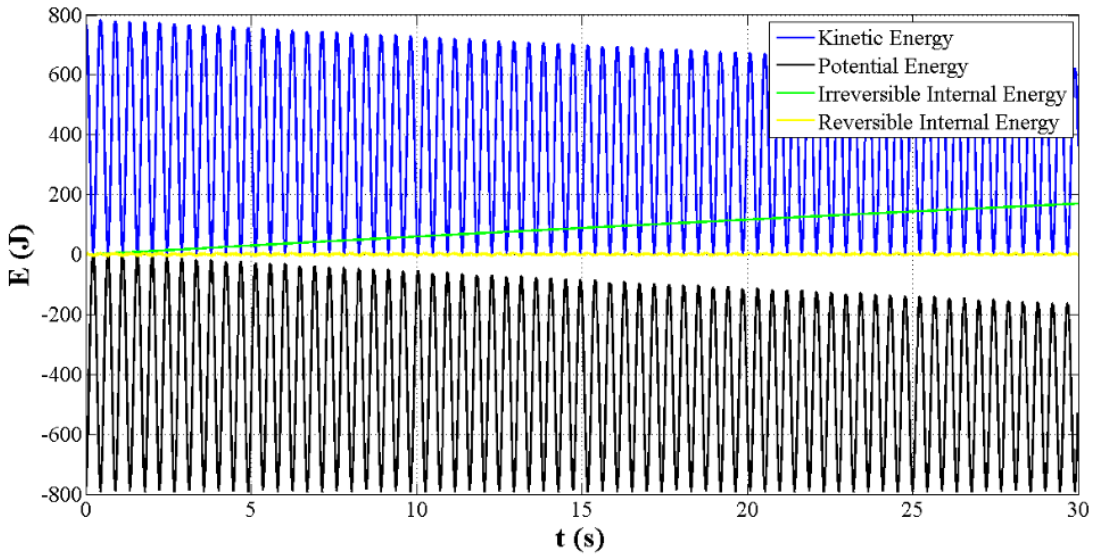

Figure 4.7: *Time evolution of the different forms of energy for the fluid drop.*

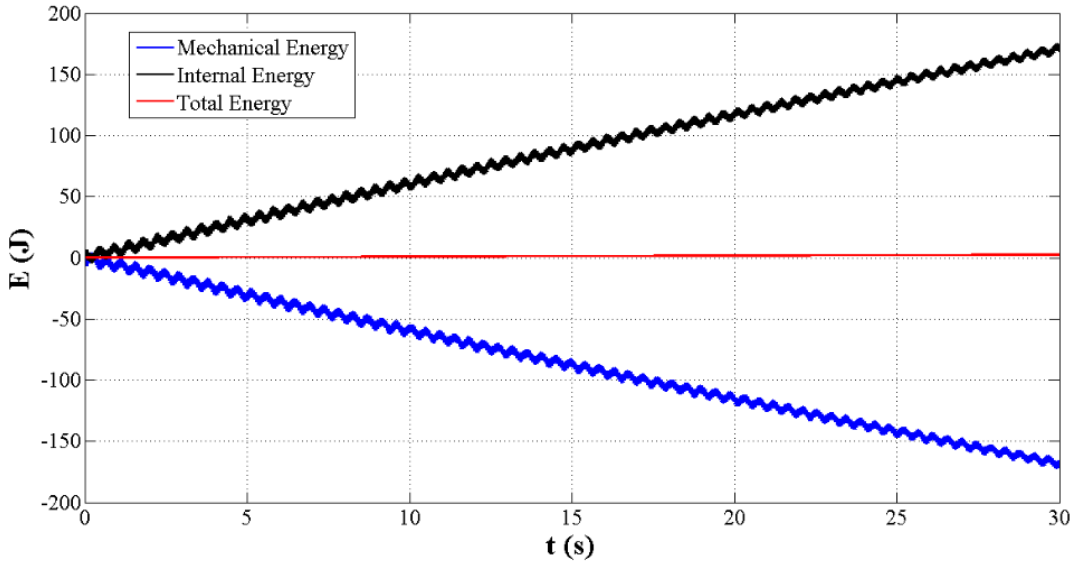

Figure 4.8: *Time evolution of internal and mechanical energies. The total energy, sum of E_I and E_M energies, is conserved in time.*

4.2.2 Analysis of the pressure noise

In this test case, the analysis of the pressure evolution at the center of the drop is presented. A value of the ratio $A_0/B = 1$ is taken into account, resulting in higher oscillations of the drop with respect of the previous case. Fig. 4.9 shows the result obtained for the drop at the maximum elongations after 8 oscillations, in which it is possible to observe a noisy pressure field. The solution results indeed to be affected by acoustic disturbances that increases with time as the drop evolves.

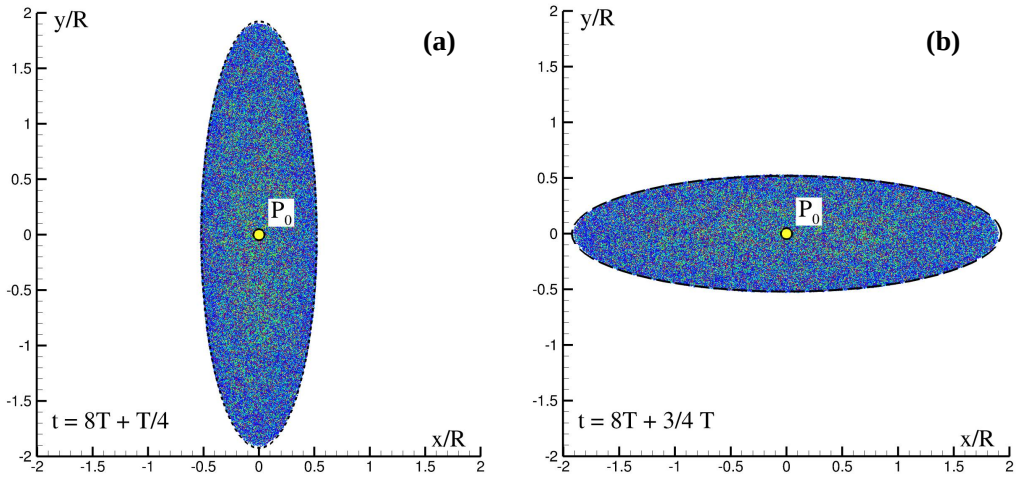

Figure 4.9: *Pressure field of the drop configuration at the maximum elongation, in (a) along the y direction, while in (b) along the x direction, obtained with standard SPH with $R/\Delta x = 200$.*

This fact is highlighted in Fig. 4.10, in which the evolutions of the pressure signal evaluated at the center of the drop, P_0, is displayed for different values of spatial resolution. To investigate the effects of the diffusive correction, both SPH without diffusive corrections and δ-SPH, are taken into account. The standard SPH model shows a level of noise that progressively increases with time. In this case, the effect of the adopted resolution result to be more relevant, since the numerical solution converge to the analytic solution only for high values of the ratio $R/\Delta x$. In the case of the δ-SPH, instead, the solution result to be much more stable in time, with a smaller effect of the adopted resolution to the numerical result. Only in correspondence of the first trough of the evolution of the drop is possible to see considerable localized noise, due in this case, to the spatial rearrangement of the fluid particles.

To analyze the effects of the adopted resolution to the pressure noise, the analysis in the frequency domain is presented. In this case, because of the periodicity of the signal, a simple Fourier analysis results to be suitable for this investigation. Fig. 4.11 presents the Fast Fourier Transform (FFT) of the signals presented in Fig. 4.10. In the frequency domain the analytic peaks, multiples of the fundamental harmonic related with the harmonics of the oscillations, are contained in the low frequency range of the spectrum. For high frequencies, the energy content is entirely due to the acoustic noise. As it is possible to observe, the range of frequencies analyzed varies according with the spatial resolution adopted, because the time resolution is related to the spatial one by the Courant-Friedrichs-Lewy time step condition: for higher spatial resolution it results a higher maximal frequency, because the time step is smaller.

A slight difference for the same resolution is encountered between the Standard and the δ-SPH: the latter, being more stable, shows a smaller maximal frequency compared with the former.

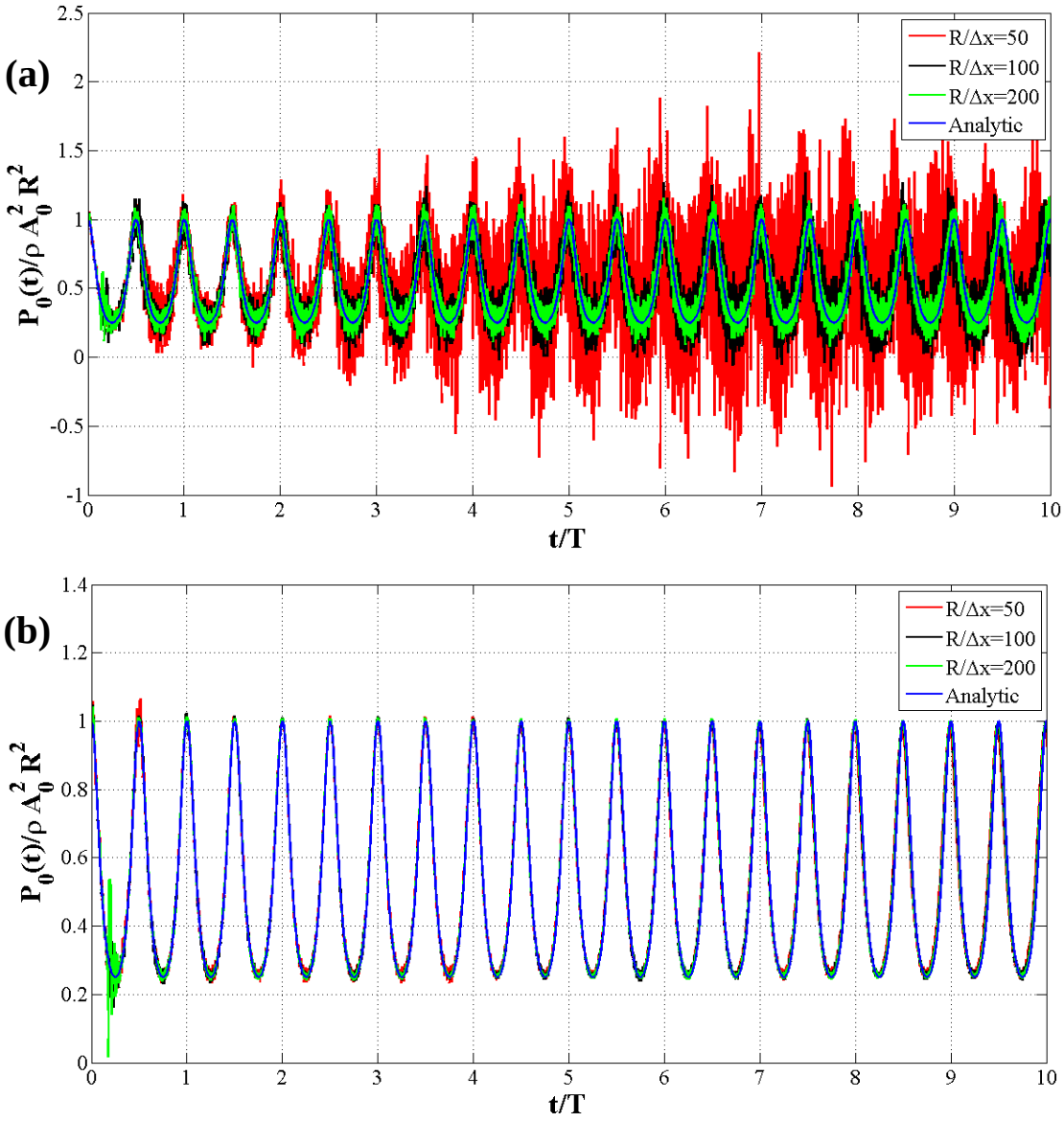

Figure 4.10: *Time evolution of pressure signal for three different resolutions $R/\Delta x$=50, 100, 200, compared with the analytic solution; (a) SPH without diffusive correction; (b) δ-SPH.*

From the results obtained from the Standard SPH, shown in Fig. 4.11, is possible to see that as the resolution increases the acoustic noise goes to higher frequencies, presenting curves of the noise with a smaller maximum peak, while for low resolution all the acoustic noise is concentrated in the low frequencies region. In the case of the δ-SPH is possible to see that the energy content of the high frequencies area of the spectrum result to be really diminished, being the diffusive term operating at the scale of the smoothing length.

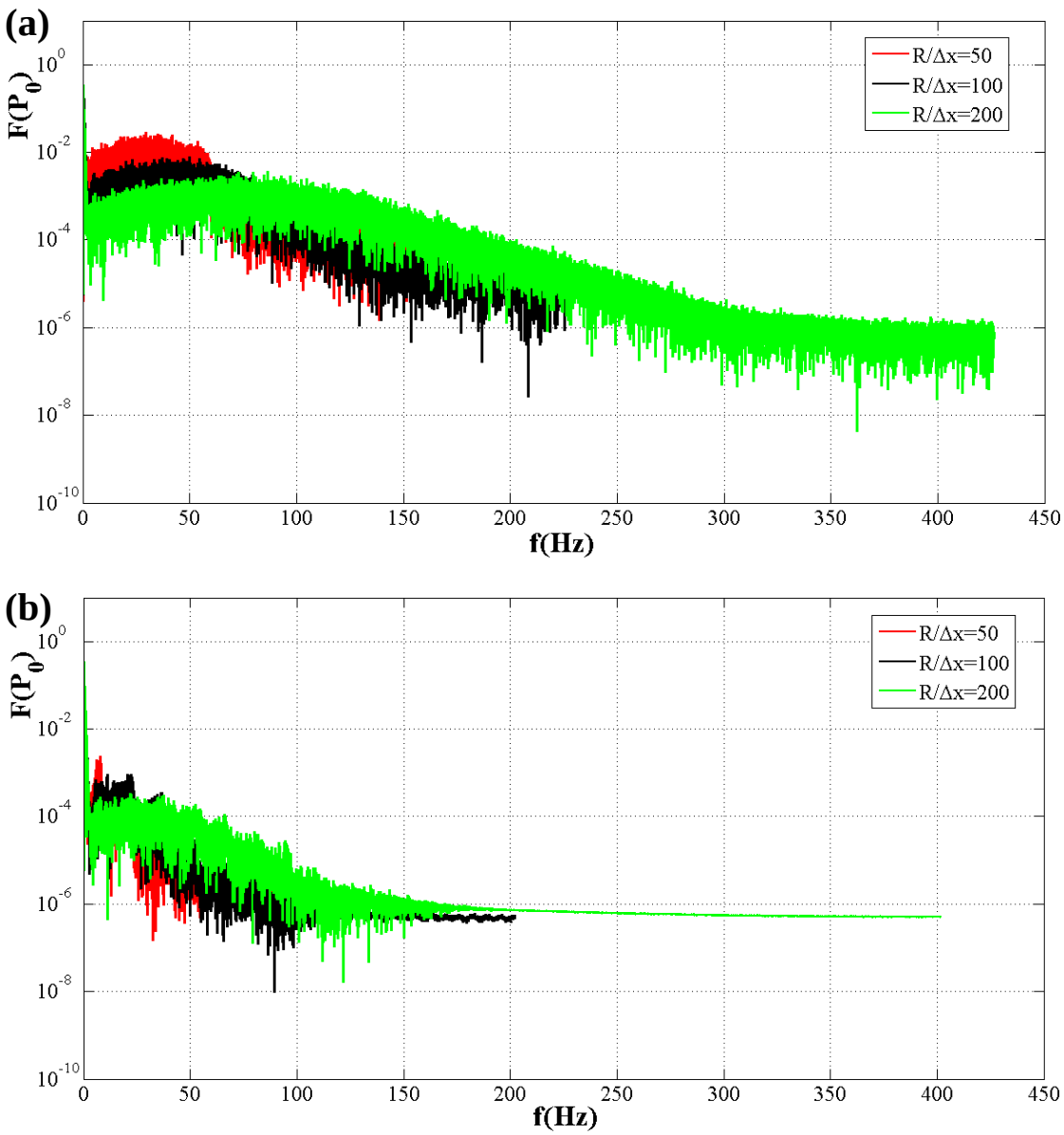

Figure 4.11: *FFT of the pressure signals presented in Fig. 4.10 for the three resolutions $R/\Delta x$=50, 100, 200; (a) SPH without diffusive correction; (b) δ-SPH.*

4.3 Dam-breaks

In this section different dam-break cases are taken into account. The set up of the problem is given by placing a mass of water in an initial rectangular configuration and instantaneously releasing one of the containing walls. To furnish the correct initial condition for the pressure field is important to impose null pressure all over the boundary in contact with the free surface. In particular, the initial condition for the pressure field has to satisfy [104]:

$$\begin{cases} \nabla^2 p(t=0) = 0 \\ \\ p = 0, \quad \text{on the free surface} \\ \\ \dfrac{\partial p}{\partial n} = 0, \quad \text{on the solid walls} \end{cases} \tag{4.2}$$

A first analysis is carried out considering the energy evolution of a simple dam-break and considerations on the transformation of energy are presented. A second test case deals with the impact of a dam-break on a rectangular obstacle, in which the pressure evolution measured at three different locations of the domain are presented by considering different diffusive formulations.

4.3.1 Energy conservation during a dam-break

The first test case deals with the analysis of a simple dam-break. For this problem, the governing equations expressed by System 2.72 are taken into account and classical ghost particles are implemented for the modeling of the solid boundaries. The problem is solved with a Runge-Kutta integration scheme, without diffusive correction. The artificial viscosity is implemented with a coefficient $\alpha = 0.01$. The initial configuration of the problem is presented in Fig. 4.12, where water height is $h_w = 0.6$ m, while the water length is $L_w = 2h_w$. The lenght of the channel is $L_c = 5.3667h_w$. In this case the adopted resolution is $\Delta x = 0.00316$ m. In Fig. 4.13 the evolution of kinetic (Eq. 2.73), potential (Eq. 2.74), dissipated (Eq. 2.76) and elastic (Eq. 2.77) energies are displayed and some crucial instants of time on the fluid dynamics are marked. The correspondent frame of the fluid simulation showing the pressure distribution are presented in Figs. 4.15 and 4.16.

Since the initial kinetic energy is zero (the particles are initialized with zero velocities) also the initial potential energy, E_{P0}, is set equal to zero in order to have null initial mechanical energy. As the mass of water starts to move it is possible to notice a decrease in potential and an increase on kinetic energies, due to the unsteady flow motion. This process continues until the fluid impacts the right wall, where the system gain again potential energy and lose kinetic one, due to the jet created after the impact along the vertical direction. The first relative minimum/maximum in potential/kinetic energy is encountered at $t \cong 0.76$ s, as shown in Fig. 4.13 and displayed in the relative frame in Fig. 4.15. The vertical water jet created after the impact increase/decrease again potential/kinetic energy until $t \cong 1.34$ s where, as shown in Fig. 4.15, a plunging wave occurs. The potential energy is again transformed into kinetic one, during the

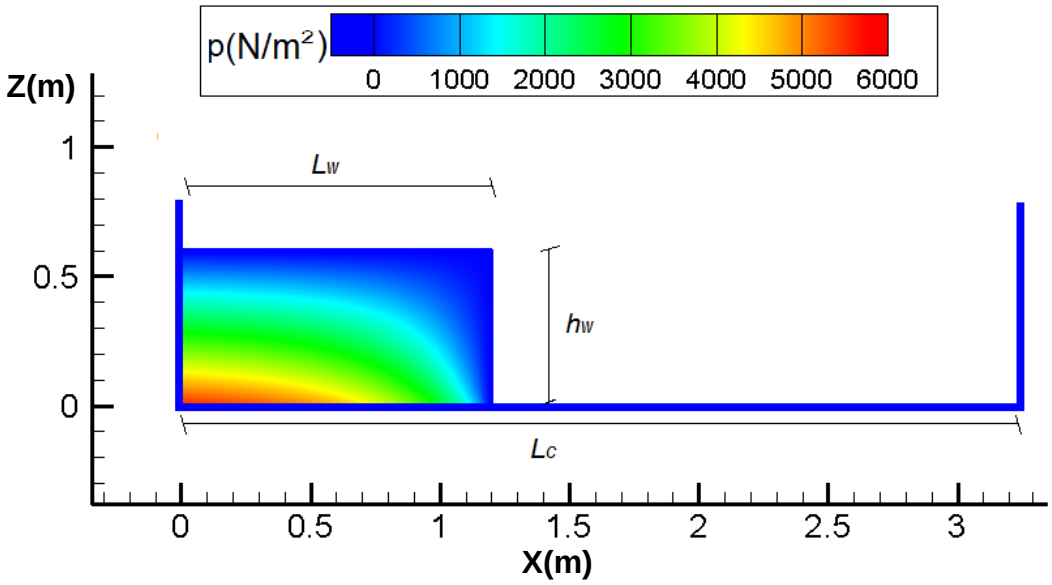

Figure 4.12: *Initial configuration with pressure distribution of the dam-break.*

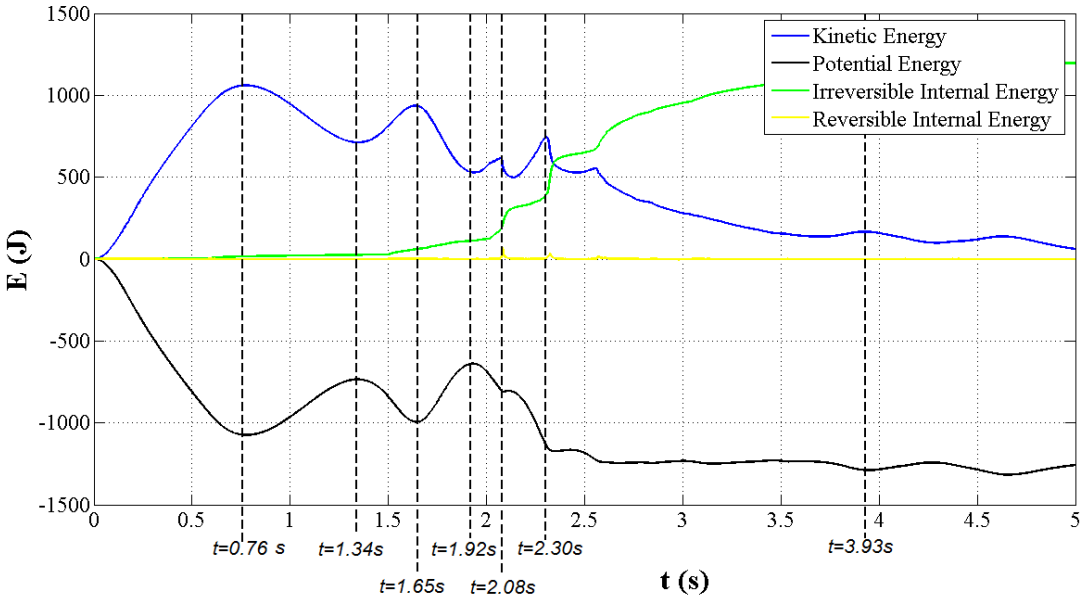

Figure 4.13: *Time evolution of the various form of energy for the dam-break. In the plot are marked some significant instant of time, whose frames of simulation, with the pressure field, are displayed in Figs. 4.15 and 4.16.*

process of falling of the fluid mass and consequent wave breaking. A second relative minimum/maximum of potential/kinetic energy is therefore encountered at $t \cong 1.65$ s, as shown in Fig. 4.13, and displayed in the frame of Fig. 4.15.

The wave breaking generates a second jet that again leads to an increase/decrease in potential/kinetic energy, as shown in Fig. 4.13, and reachs another relative maximum/minimum at $t \cong 1.92$ s, as displayed in Fig. 4.16. A really interesting phenomenon is encountered at $t \cong 2.08$ s, as displayed in Fig. 4.16, where the cavity generated after the wave breaking process collapses on the fluid mass, with a consequent fluid-fluid impact. This rapid process creates an instantaneous compression of the fluid particles, that results in the peak in the elastic energy, as shown in Fig. 4.13. During these rapid dynamics of the fluid mass, the mechanical energy is dissipated by the viscosity, resulting therefore in an increase of the internal energy.

A second impact, with instantaneous accumulation of elastic energy as shown in Fig. 4.13, is related to the falling of the second jet. In Fig. 4.16 is displayed the simulation at $t \cong 2.30$ s, an instant of time prior the impact. The last frame in Fig. 4.16 shows the fluid mass at $t \cong 3.93$ s, where, even if kinetic energy due to fluid motion is still present, most of the mechanical energy is already transferred into internal one.

In Fig. 4.14 is shown the conservation of the total energy of the system, where the mechanical energy evolution is exactly balanced by the internal energy (heat dissipated by the viscosity). This result shows that the SPH model remains very accurately con-

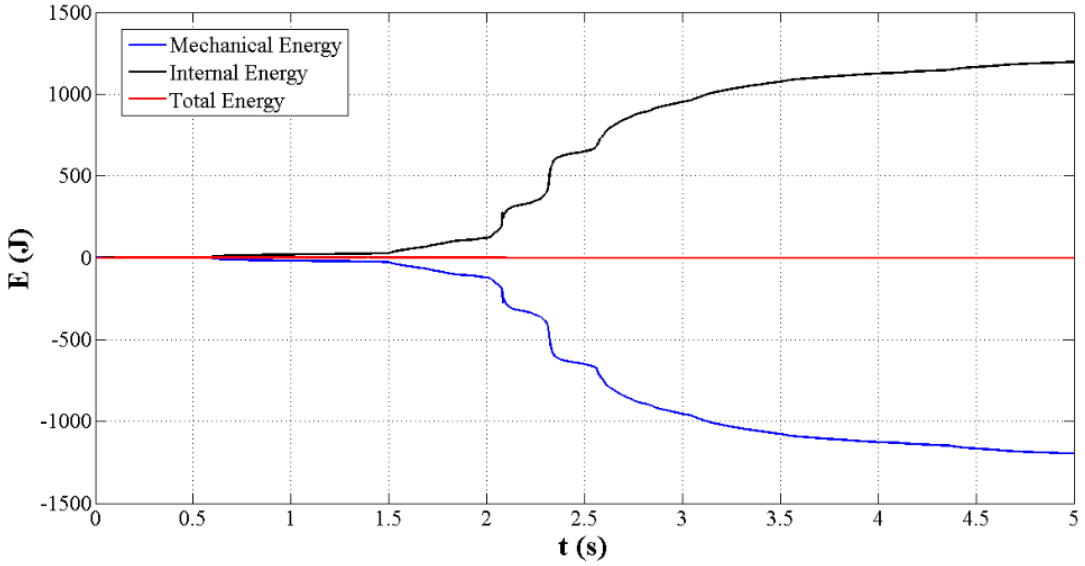

Figure 4.14: *Internal energy and mechanical energy evolutions. The total energy is conserved in time.*

servative. This fact has been also shown by Le Touzé et al. [81], for cases characterized by different dynamics and by varying the spatial resolutions.

It is important to notice that the energies variations, related in this case to the physics of the problem, are of 10^5 order of magnitude higher than that encountered in the previous analysis for the still water tank, only related to the numerical issues of SPH.

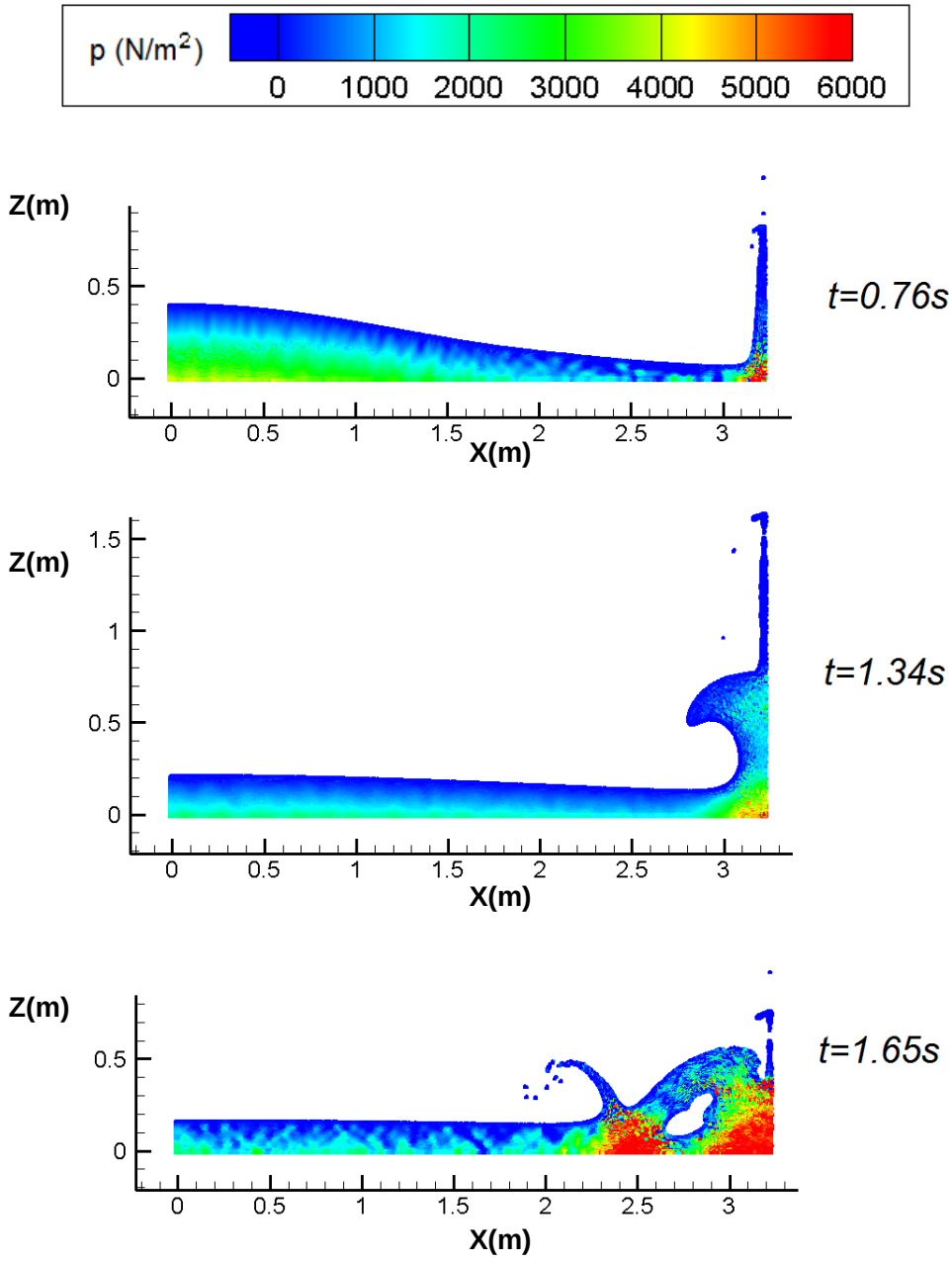

Figure 4.15: *Frames of the evolution of the pressure field. The time instants shown are those represented in Fig. 4.13 where the different forms of energy are shown.*

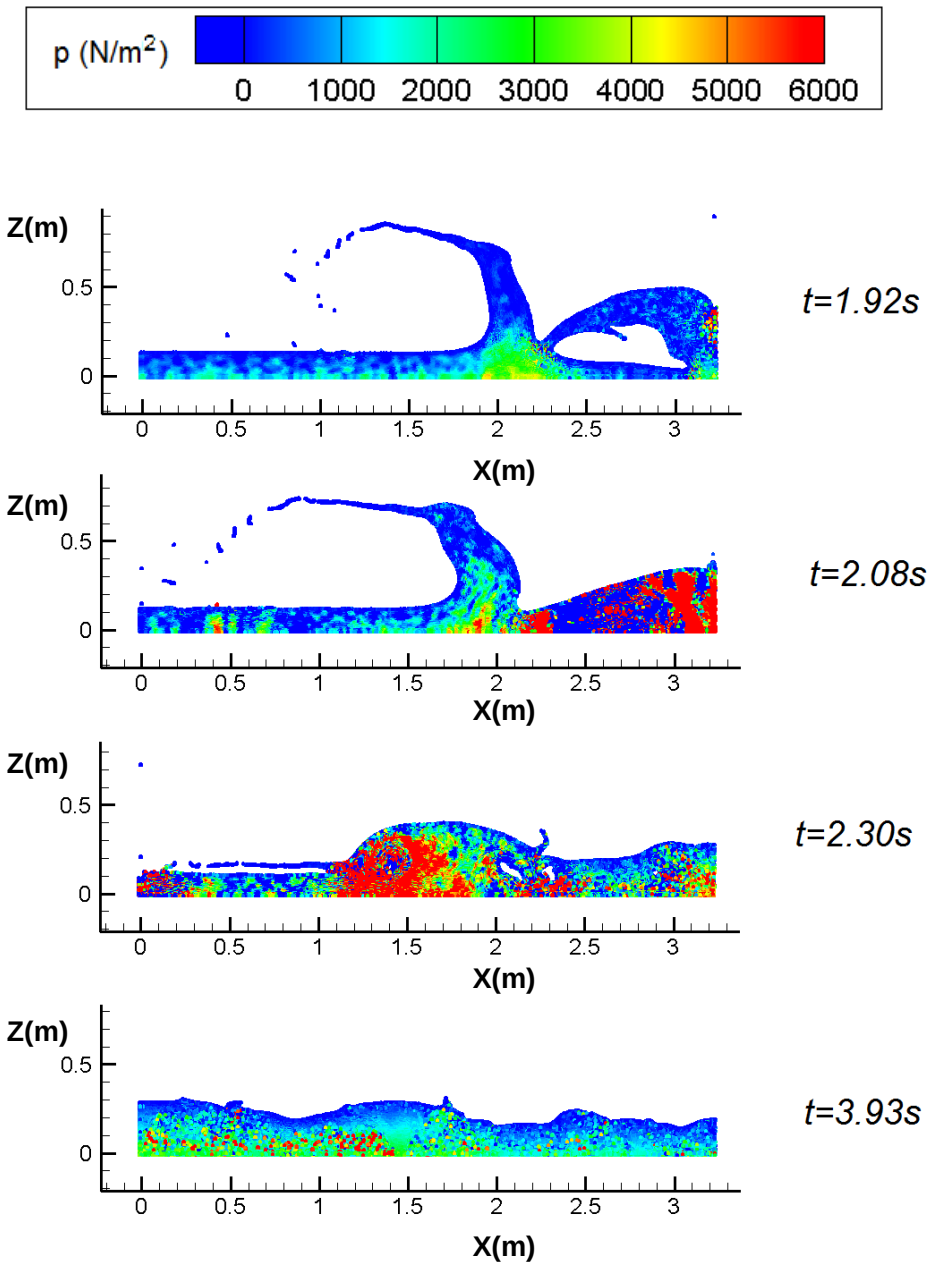

Figure 4.16: *Frames of the evolution of the pressure field. The time instants shown are those represented in Fig. 4.13 where the different forms of energy are shown.*

4.3.2 Dam-break impacting an obstacle

In this section the simulation of a dam break impacting on a rectangular rigid obstacle placed at the bottom is presented. For this case, the problem is solved with the governing equations of System 2.71. Fixed ghost particles are implemented for the modeling of the solid boundary. The problem is solved with a modified Verlet integration scheme, while the artificial viscosity is tuned with a coefficient $\alpha = 0.01$.

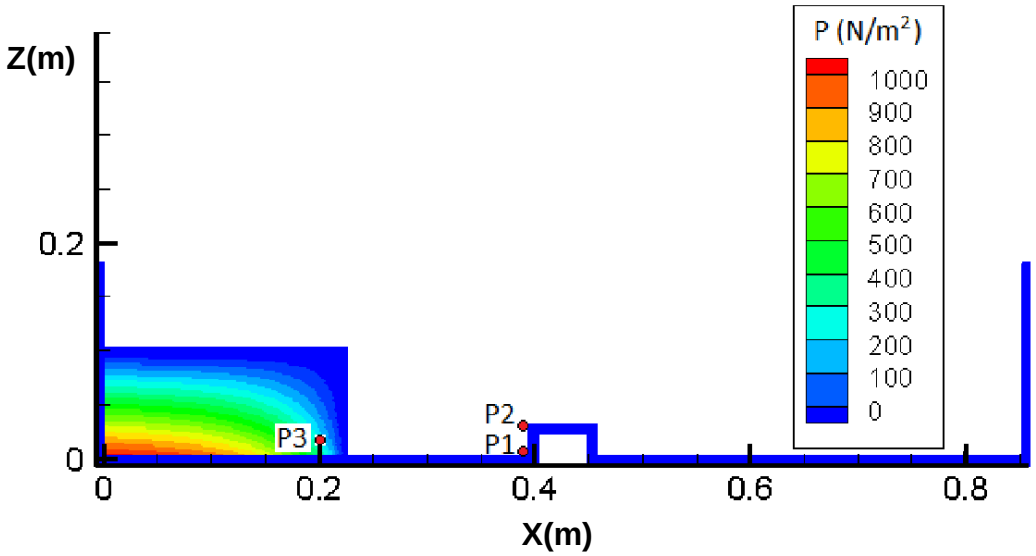

Figure 4.17: *Initial configuration with pressure distribution of the dam-break impacting on a obstacle. Points P1, P2 and P3 represents the numerical gauges where the pressure is evaluated.*

The initial setting of the particles with pressure distribution and the geometry of the computational domain are presented in Fig. 4.17. In particular the water height is $H = 0.1$ m, while the length of the water mass is $L = 0.225$ m. The obstacle is set at a distance $L_o = 0.395$ m from the left wall of the domain. The obstacle height is $h_o = 0.03$ m, while its length is $l_o = 0.06$ m.

In Fig. 4.18 SPH simulation of the dam-break evolution are presented for different significant time instants, in comparison with the experimental results and with another SPH solver. Different diffusive formulations are taken into account for the simulation of the problem. In particular, a first analysis is carried out without diffusive correction (standard-SPH), followed by simulations using the Groenenboom and Cartwright [68] and the δ-SPH [6] diffusive models. Two resolutions, $\Delta x1 = 0.0035$ m and $\Delta x2 = 0.0018$ m, and two values of the diffusive coefficient, $\delta = 0.1$ and $\delta = 0.2$, are taken into account. The results, obtained for the pressure gauges at points P1, P2 and P3 shown in Fig. 4.17, are displayed in Fig. 4.19.

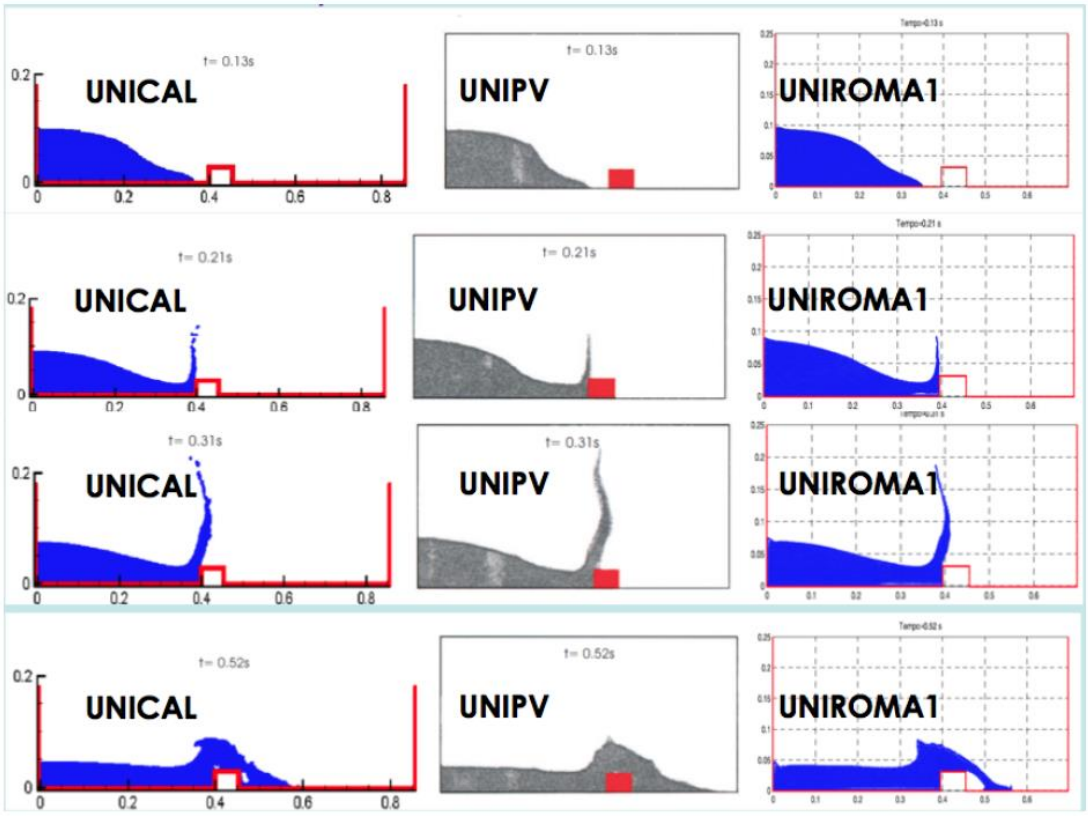

Figure 4.18: *Frame of dam-break flow evolution: the first column is obtained with the present SPH solver, the second column is an experimental study while the third is the result of another SPH solver [133].*

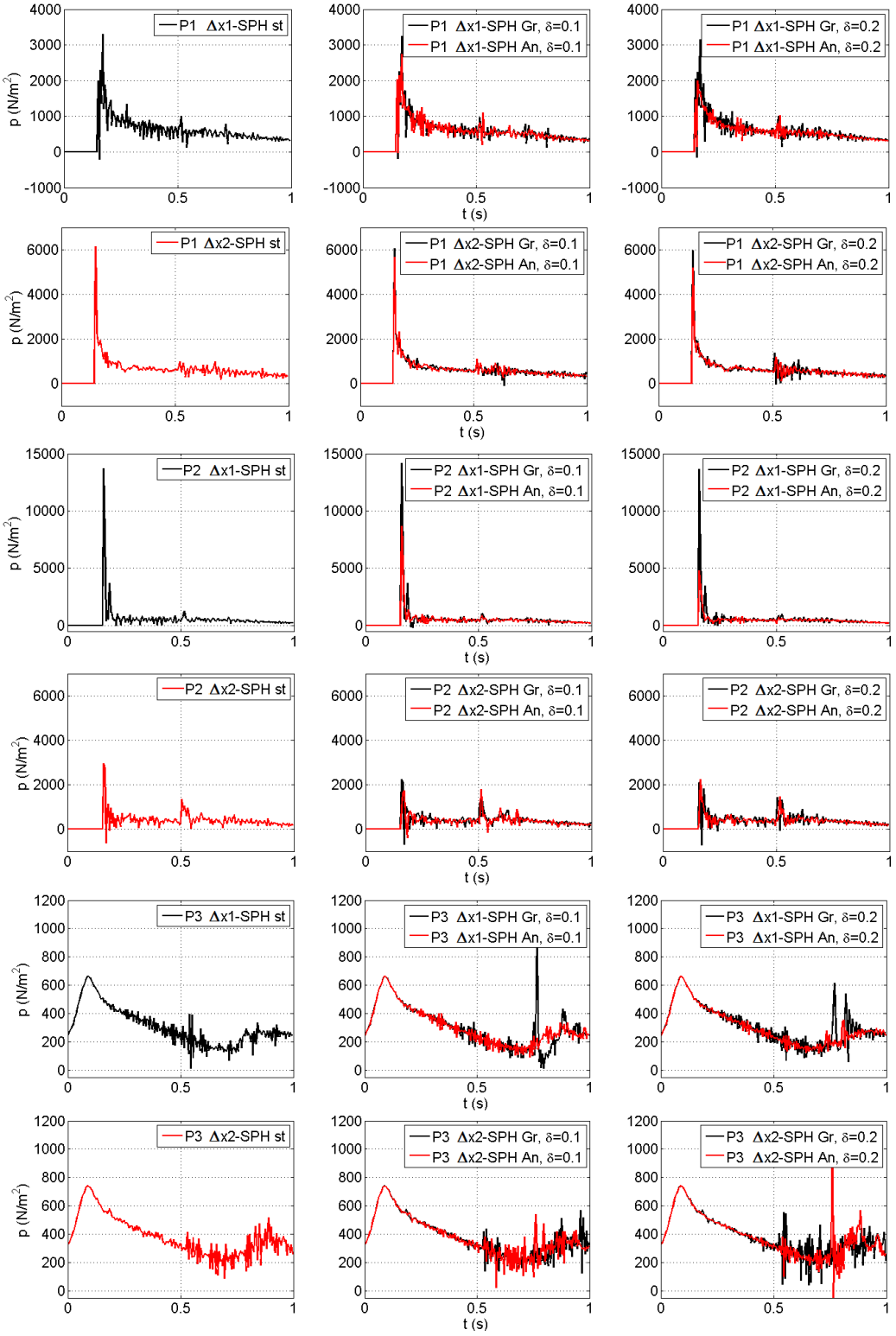

Figure 4.19: *Time variations pressure evolution at gauges P1, P2 and P3. The results are obtained without diffusive corrections (SPH st) and with diffusive formulations of [68] (SPH Gr) and [6] (SPH An).*

4.4 Multi-node fixed ghost particles validation

In this section, the proposed SPH modeling of solid boundaries using multi-node fixed ghost particles is firstly tested for a still water tank with two different levels, concerning the conservation in time of the hydrostatic solution. A second test case in hydrodynamic conditions, dealing with the wave impact on a thin horizontal deck, modeled with multi-node fixed ghost particles is then performed, comparing the time instants of the wave interaction with the results obtained from the SPH model of Gómez-Gesteira et al. [65] in terms of particle positions, velocity and pressure fields.

4.4.1 Hydrostatic test case

The hydrostatic test involves a double tank in still water conditions, containing liquid at different levels and divided by a thin solid separation. In this case, System 2.72 for the governing equations is taken into account, considering a Runge-Kutta 3.34 integration scheme, with a coefficient for the artificial viscosity equal to $\alpha = 0.01$ and without diffusive correction. Regarding the geometries of the domain, the length of each tank is $L_t = 0.5$ m, the water level in the left tank is $d_1 = 0.4$ m, while in the right tank is $d_2 = d_1/4$. The adopted resolution is $\Delta x = 0.0045$ m.
The separation wall is firstly modeled with four lines of canonical fixed ghost particles and only one node is associated to them (specifically located in the left tank). As can be seen in Fig. 4.20, the fluid particles in the right tank interact with the central solid boundary whose quantities are interpolated in the left side. As a result, a positive pressure gradient due to the difference in water height between the two tanks generates an unphysical shock wave in the right tank with a consequent appearance of a relevant velocity field. A similar problem will be encountered if the interpolation nodes are located only in the right side. In this case, a negative pressure disturbance will be induced in the fluid particles contained in the left tank, resulting again in an incorrect solution.

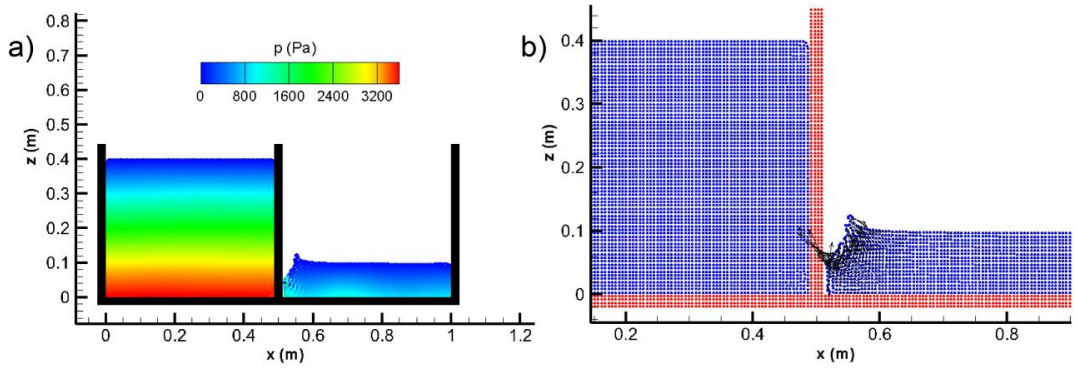

Figure 4.20: *Frame of the SPH simulation using one-node fixed ghost particles at t = 0.1 s; a) pressure field; b) fluid particles (blue) with associate velocity vectors and solid particles (red).*

When the partition wall of the tanks is modeled with a multi-node approach, the solution proves to be correct. In this case, as illustrated in Fig. 4.21, the computational

domain is subdivided into two regions Ω_a and Ω_b with the corresponding a-node and b-node associated with the central wall by the proposed technique. The external walls and the bottom tanks are instead modeled by classical fixed ghost particles.

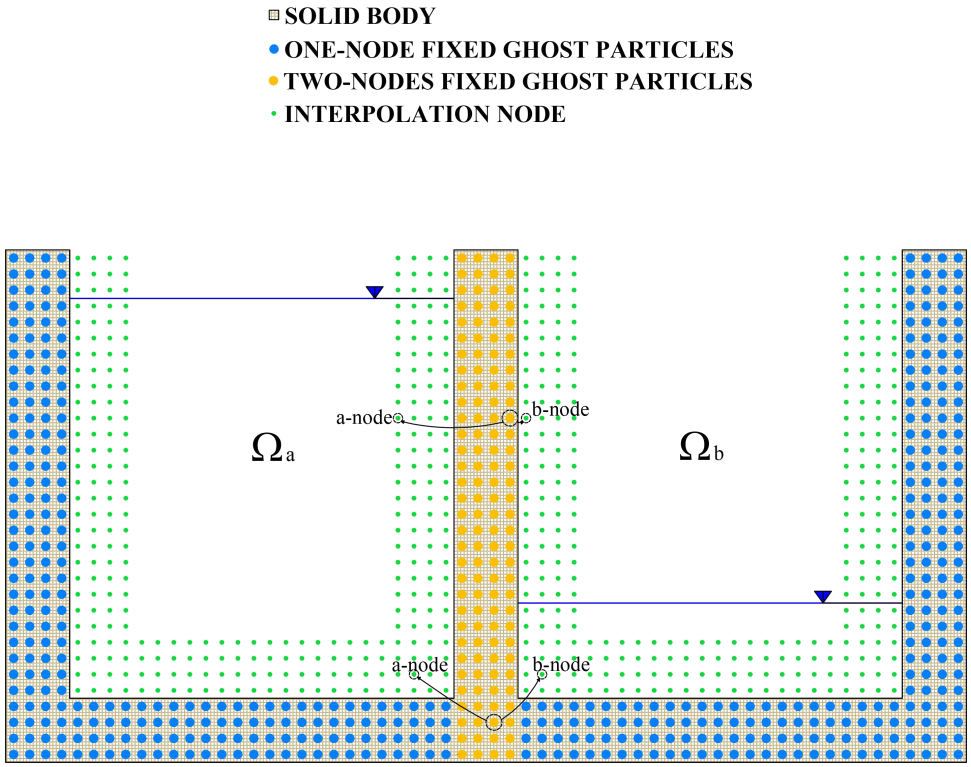

Figure 4.21: *Sketch of solid boundary conditions modeled by a combination of single-node and multi-nodes fixed ghost particles and corresponding interpolation nodes for the hydrostatic test case.*

Fig. 4.22 shows the results of the simulation obtained with the multi-node enforcement, in which the preservation of the hydrostatic solution remains stable in time for the considered two tanks. In this case, the interpolation nodes furnish correct values of pressure for the interacting fluid particles, avoiding the occurrence of spurious hydrodynamic phenomena.

4.4.2 Hydrodynamic test case

The hydrodynamic test refers to a horizontal deck placed above the SWL and subjected to water waves. The analysis here is principally addressed to check the performances of the proposed multi-node fixed ghost particles to model thin solid bodies in hydrodynamic conditions. As for the previous case, the adopted governing equations are those of System 2.72, while a Runge-Kutta integration scheme is taken into account. SPH simulations are conducted using $\alpha = 0.05$ and $\epsilon_X = 0.5$, as calibrated by Gómez-Gesteira et al. [65], for a successive comparison of numerical results.

As shown in Fig. 4.23, the adopted computation domain is characterized by a length of the wave flume $L_c = 9$ m, a water depth $d = 0.65$ m and a distance between wave paddle and leading edge of the deck $x_d = 2$ m. Following the experimental investigation by Cox and Ortega [34], the length of the horizontal deck is $L_d = 0.61$ m and its height is $H_d = 0.0115$ m, while the distance of its upper part from the SWL is

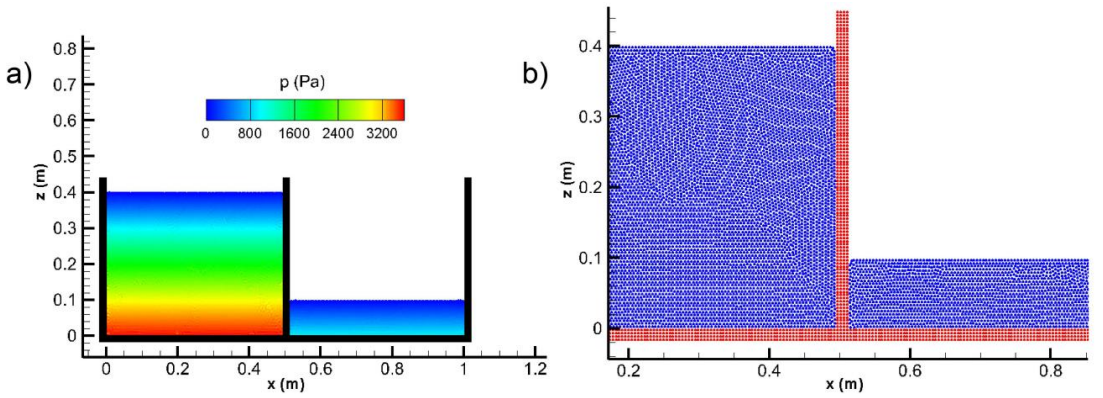

Figure 4.22: *Frame of the SPH simulation using multi-node fixed ghost particles at t = 10 s; a) pressure field; b) fluid particles (blue) with associate velocity vectors and solid particles (red).*

$h_d = 0.0525$ m. The deck is modeled by a combination of single and multi-node fixed ghost particles with corresponding interpolation nodes. The left wall of the channel is modeled by moving fixed ghost particles and implemented with the sinusoidal time law in order to simulate a piston-type wavemaker for wave generation (see Eq. 3.23). As in the case of the hydrostatic test (see Fig. 4.21), the other solid boundaries are enforced using one-node fixed ghost particles.

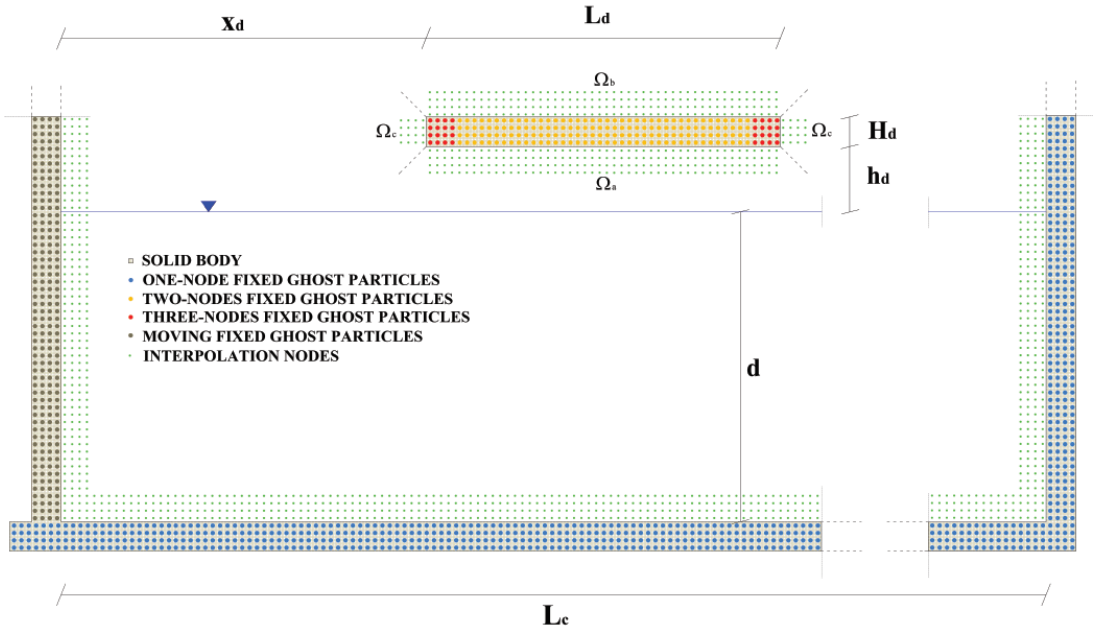

Figure 4.23: *Sketch of solid boundary conditions modeled by a combination of single-node and multi-node fixed ghost particles and corresponding interpolation nodes for the case of the horizontal deck.*

The adopted spatial resolution for the multi-node fixed particles is driven by the small height of the plate, so that $\Delta x = H_d/4 = 0.002875$ m. Second-order Stokes waves are generated in the channel by imposing an amplitude of the stroke equal to $S_0/2 = 0.25$ m and a wave period $T = 2$ s to a piston-type wavemaker, as simulated by

Gomez et al. [65]. To avoid an improper numerical damping during wave propagation along the channel, the condition $A/\Delta x > 2$ have to be satisfied [5], where A is the wave amplitude. In this case, this condition results as largely satisfied being the ratio equal to about 87. For the test cases dealing with wave-perforated breakwater interaction, analyzed in chapter 5, the above constraint will always be satisfied for the considered wave conditions and spatial resolution.

In order to test the proposed boundary technique, the numerical results deduced from the present SPH model are compared with the SPH model developed by Gómez-Gesteira et al. [65]. These authors proposed an ad-hoc test case dealing with the wave-deck interaction and the associated processes of overtopping and jet formation, on the basis of the initial experimental layout proposed by Cox and Ortega [34]. In order to model solid boundaries, Gómez-Gesteira et al. [65] applied *quasi* fluid particles which follow only the continuity equation and the state equation in a fixed position (*e.g.* [36]). A less refined spatial resolution $\Delta x = 0.025$ m with respect to the present SPH simulation was adopted in [65].

With reference to five significant time instants of the wave impact at the deck ($t = 3.15$ s, 3.27 s, 3.39 s, 3.45 s and 3.53 s), Fig. 4.24 shows the particle positions (left panel) and the associated horizontal velocity field and streamlines (right panel) simulated through the proposed SPH solver, while Fig. 4.25 illustrates the particle positions (left panel) and the associated velocity vectors (right panel) simulated through the SPH model by [65]. In the first selected time instant ($t = 3.15$ s), the incoming wave reaches about the front face of the deck and a portion of the flow arrives at about the half of the lower zone of the deck, as observed by [65]. The largest velocities appear at the wave crest and, due to the presence of the deck, in its lower zone. In the second frame ($t = 3.27$ s), the wave crest overcomes the upper part of the deck with an increase in its steepness while the flow under the deck reaches its rear part where relevant velocities appear. For $t = 3.39$ s, the wave over the deck arrives at the rear of the deck while beyond it a breaking wave process induced by the flow past under the deck is noticed. A forward shift of the above mentioned physical processes are highlighted in the successive time window ($t = 3.45$ s) in which the water completely surrounds the involved horizontal structure. The formation of a vertical jet as a result of the interaction between the flows propagating upper and lower the deck is evident at the successive considered time $t = 3.53$ s.

The comparisons between the present SPH and that developed by [65] are also performed in terms of time variation of pressure acting on the rear of the deck, as described in Fig. 4.26 for a significant time window ranging from 3.15 s to 3.53 s. In [65] the above quantity was calculated by a spatial average of the pressure at the two last solid particles of the deck, while it is determined here by averaging the pressures interpolated in the Ω_c sub-area of the rear of the deck by the three-nodes fixed ghost particles (red particles in Fig. 4.23). In this case, the diffusive term by Molteni and Colagrossi [104], with $\delta = 0.1$, is adopted to model the pressure field due to its better smoothing effect when a violent fluid-solid interaction occurs. Regarding the pressure field, only the dynamic contribution is present since the deck has been placed above the SWL. Although the spatial resolution and the evaluation of the pressure at the rear of the deck using the SPH based-models is quite different, a general agreement on the behavior of the pressure can be observed. This is particularly evident for the peak value which appears

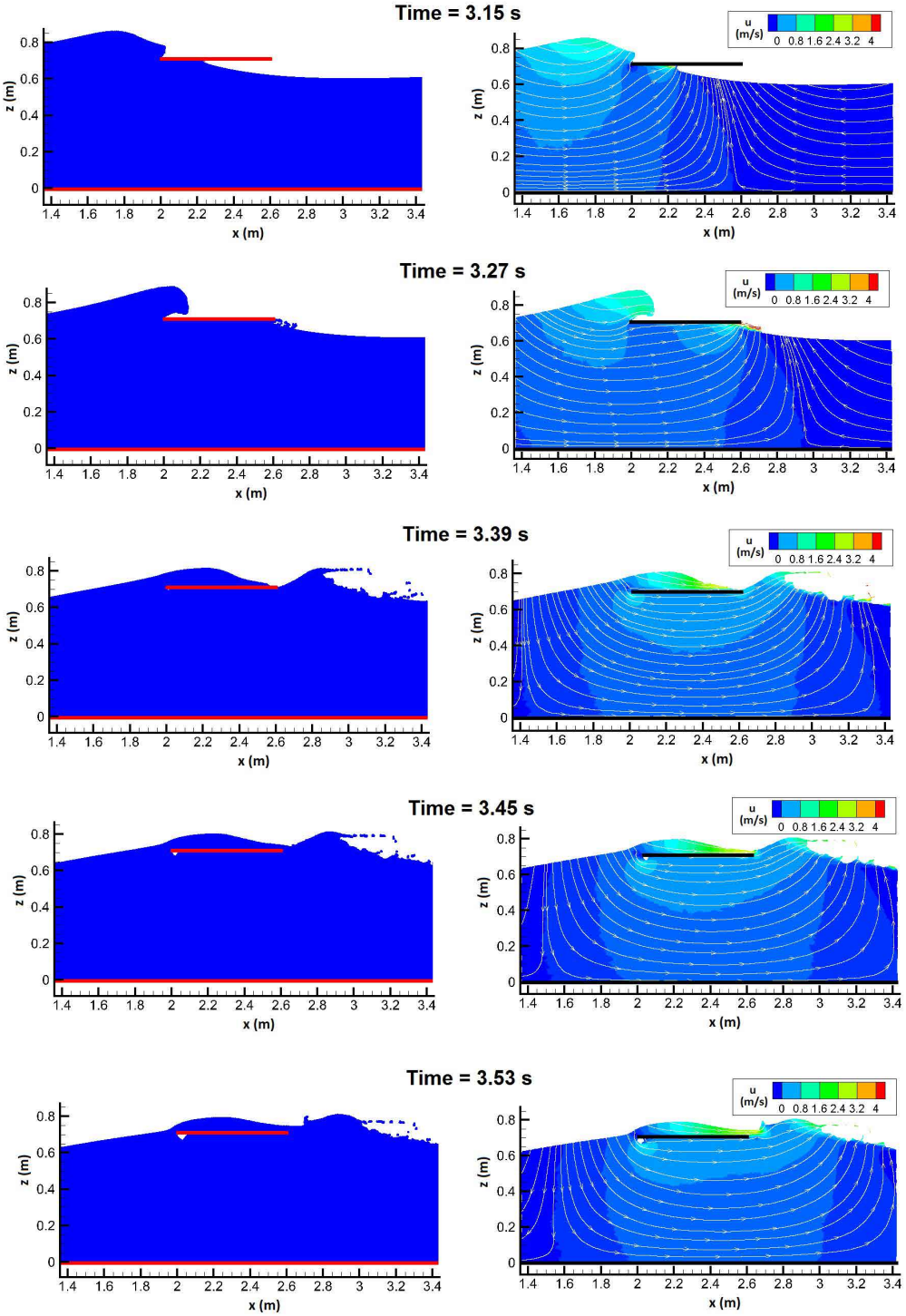

Figure 4.24: *Particle positions (left panel) and associate horizontal velocity field and streamlines (right panel) simulated through the present SPH model at $t = 3.15$ s, 3.27 s, 3.39 s, 3.45 s and 3.53 s.*

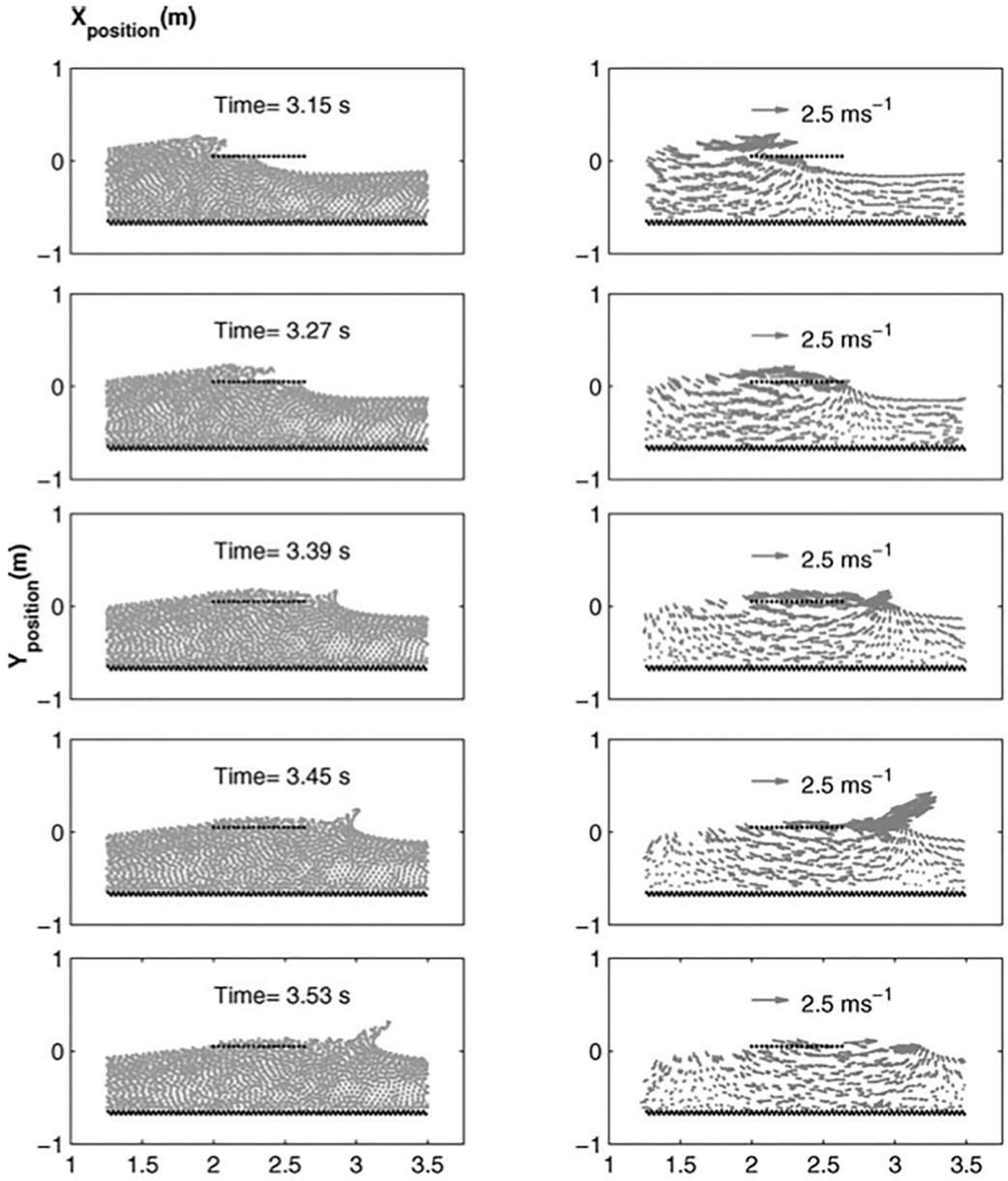

Figure 4.25: *Particle positions (left panel) and associate velocity vectors (right panel) simulated through the SPH model by Gómez-Gesteira et al. [65] at t = 3.15 s, 3.27 s, 3.39 s, 3.45 s and 3.53 s.*

close to the significant time instant $t = 3.27$ s where the flow starts to interact with the rear of the deck. After the maximum value of the pressure, a secondary peak simulated by the present SPH model proves to be forward shifted compared to that simulated by [65] as well as the values of relative minimum of the pressure. It can be noticed that non-linear effects deduced from the adopted SPH solver could be associated to the more refined resolution adopted in the space-time domain compared to that performed by [65]. Additional information on the physical processes induced by the wave-deck interaction can be found in [34] and [65].

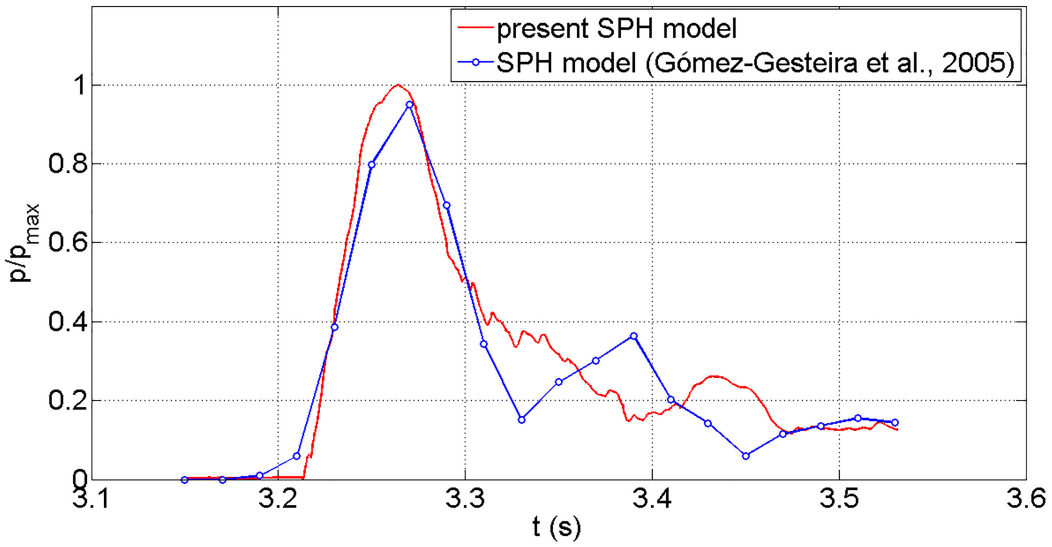

Figure 4.26: *Time variation of pressure at the rear of the deck: comparison between present SPH model and that referred to Gómez-Gesteira et al. [65].*

CHAPTER 5

Wave interaction with perforated breakwaters

5.1 Overview on perforated breakwaters

Perforated breakwaters are maritime structures widely used in harbors with the aim to guarantee safe navigation during sea storms. The main purpose of these structures is thus to minimize the reflection of the incoming waves, limiting in this way wide free-surface oscillations related with interferences between incoming and reflected wave. As pointed out by Huang et al. [72], the advantages of these coastal structures with respect to the traditional vertical or rubble mound breakwaters are the saving in construction cost in finite water conditions and less disturbance to coastal water environments.

The most simple configuration of breakwaters consists in a perforated front wall and a solid vertical back wall, so that the wave damping occurs in the chambers located between the two walls. The first scientific studies of these structures refer to the works of Wiegel [156] and Jarlan [74]. Afterward, several modification and more complex configurations were proposed in order to increase the performance of the caisson, like introducing multiple walls, a top cover between the walls or considering perforated caisson with a rock core. A review of these perforated breakwater is presented in Huang et al. [72].

The performance of a perforated breakwater can be seen under a structural stability point of view, concerning the analysis of wave forces, and under an hydraulic point of view, concerning the analysis of water dynamics at the caisson and the wave reflection properties. In literature the analysis of wave reflection has been more investigated than the analysis of the pressures acting on the caissons (see *e.g.* [72]). Regarding the pressure spatial distribution at perforated breakwaters, empirical formulation are commonly adopted. In this case, wave design forces are converted into quasi-static load diagrams which are taken into account for the analysis of global stability of these structures. An empirical (and widespread) model of the spatial wave pressures distribution has been

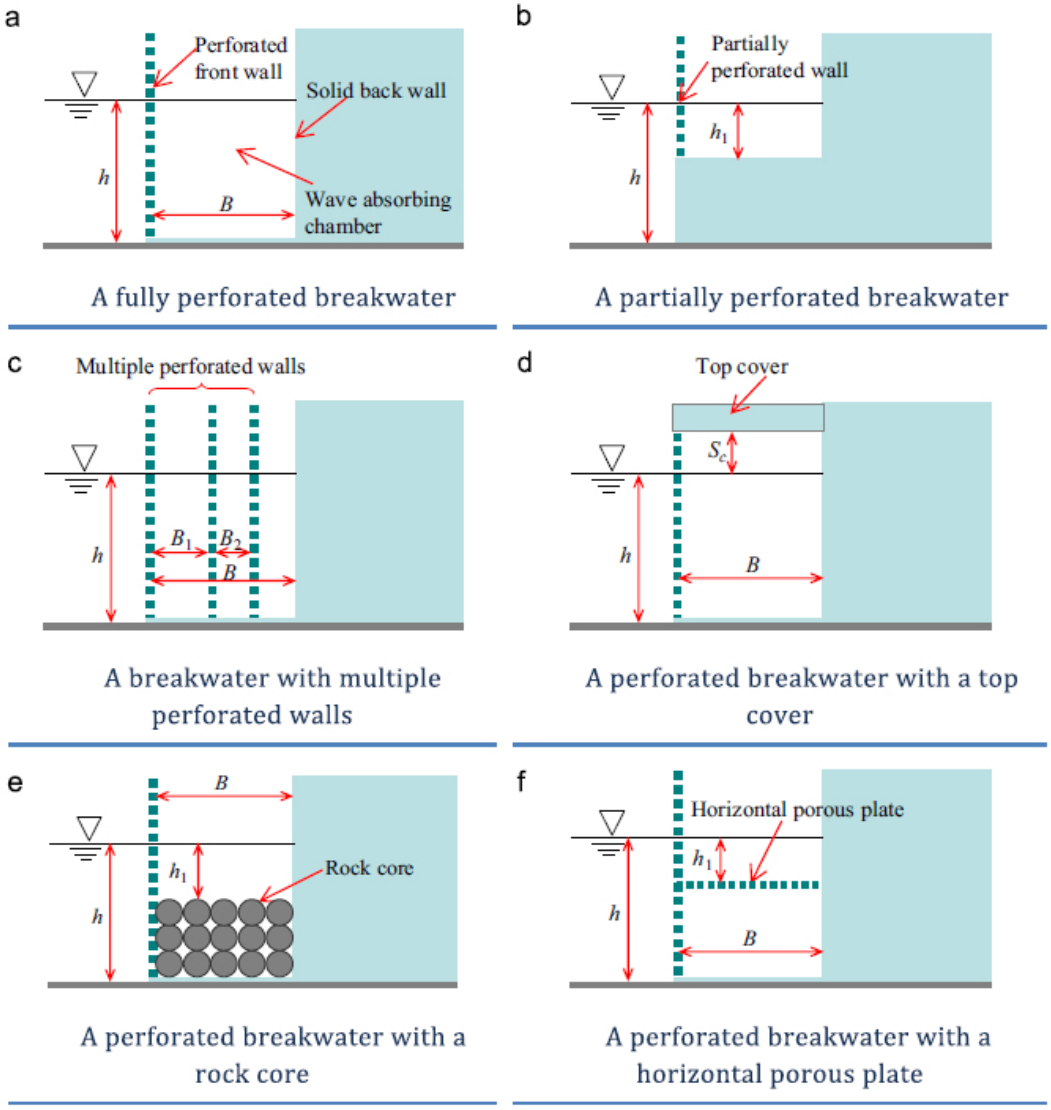

Figure 5.1: *Sketch of different schemes of perforated wall breakwaters (Huang et al. [72]).*

proposed by Goda [62] for a vertical wall and, successively, extended by Takahashi and Shimosako [148] to the case of slotted structures. In this model, the dynamic pressure is assumed to be linear from the bottom to the SWL and from the SWL to the maximum wave run-up. The parameters influencing the pressure values are the wave characteristics, the water depth and the geometrical shape of the breakwater. Takahashi and Shimosako [148] noted that peak pressures occur at different walls for different time instants as a function of the width of the chamber, as shown in Fig. 5.2. Moreover,

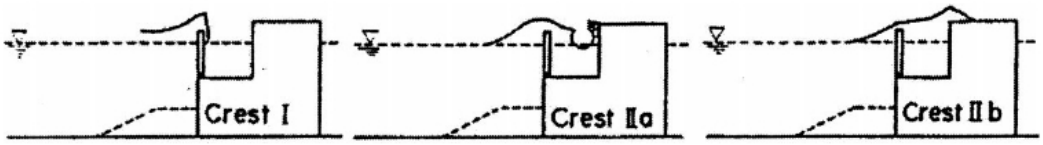

Figure 5.2: *Wave evolution at a caisson breakwater (Takahashi and Shimosako [148]).*

these authors pointed out that the determination of the maximum forces acting on the walls requires a good knowledge of the water dynamics inside the caisson. If this information is not accurate it may be difficult to calculate the total force for the three configurations. To overcome this limitation, Tabet-Aoul and Lambert [146] proposed a new formulation for the wave forces, taking into account for the phase shift among the pressure peaks between the solid and the slotted walls. In fact, referring to Fig. 5.2, classical models lead to an underestimation of loads for the Crest I case and an overestimation for the Crest IIa and IIb cases. The [146] method is based on [148] formula, in which some modification factors are introduced. In particular, a dimensionless parameter accounts for the phase delay, avoid the choice between the three cases of maximal force instants shown in Fig. 5.2. In general, as noticed by [146], the maximum total force occurs between these cases, and its appearance time is strongly linked to B/L, being B the chamber width and L the wave length. From the model of [148] some coefficients are introduced to evaluate wave loads:

$$\alpha_1 = 0.6 + 0.5 \left[\frac{2kh}{\sinh(2kh)} \right]^2 \tag{5.1}$$

$$\alpha_2 = \min \left\{ \left[1 - \frac{d}{3h_b} \left(\frac{H_D}{d} \right)^2 \right], \quad \frac{2h}{H_D} \right\} \tag{5.2}$$

$$\alpha_3 = 1 - \frac{h'}{h} \left[1 - \frac{1}{\cosh(kh)} \right] \tag{5.3}$$

$$\alpha_4 = 1 - \frac{1}{\eta^*} \min \{ h_e, \quad \eta^* \} \tag{5.4}$$

in which k is the wave number, d is the water depth in front of the caisson, h_b is the offshore water depth at a distance five times the significant wave height, H_D is the wave height applied to calculate design wave forces as expressed in Goda [63], h' is the water depth including the armor layer on the berm, h_e is the emerged height of the caisson. In [146] the pressure parameters are the same as those given by [148] formula, but are based on a different definition of the wave run-up parameter, η^*. For the perforated wall it is:

$$\eta^* = -0.32(1 + \cos\beta) H_D, \tag{5.5}$$

while for the rear wall:

$$\eta^* = -0.75(1 + \cos\beta)(0.7 - B/L)^2 H_D, \tag{5.6}$$

in which β is, in this context, the incidence wave direction. The pressures for the perforated wall are then calculated as follows:

$$P_{p1} = (1 + \cos\beta)\left[0.21\alpha_1 + (B/4L)(1 + \alpha^*)\cos^2\beta\right]\rho g H_D, \tag{5.7}$$
$$P_{p3} = \alpha_3 P_{p1}, \tag{5.8}$$
$$P_{p4} = \alpha_4 P_{p1}, \tag{5.9}$$

where, as shown in Fig. 5.3, P_{p1}, P_{p3} and P_{p4} are the resulting pressures on the SWL, on the bottom, and on the top of the perforated wall, respectively. In Eq. 5.7 $\alpha^* = \max\{\alpha_1, \alpha_2\}$. In the case of the rear wall, the pressures are calculated as follows:

$$P_{r1} = 0.5(1 + \cos\beta)\left[F_1\alpha_1 + +F_2(1 + \alpha^*)\cos^2\beta\right]\rho g H_D, \tag{5.10}$$
$$P_{r3} = \alpha_3 P_{r1}, \tag{5.11}$$
$$P_{r4} = \alpha_4 P_{r1}, \tag{5.12}$$

in which the values P_{r1}, P_{r3} and P_{r4} are the resulting pressures on the SWL, on the bottom, and on the top of the rear wall, respectively, as shown in Fig. 5.3. In Eq. 5.10, $F_1 = (0.7 - B/L)^2$ and $F_2 = (0.43 - B/L)$.

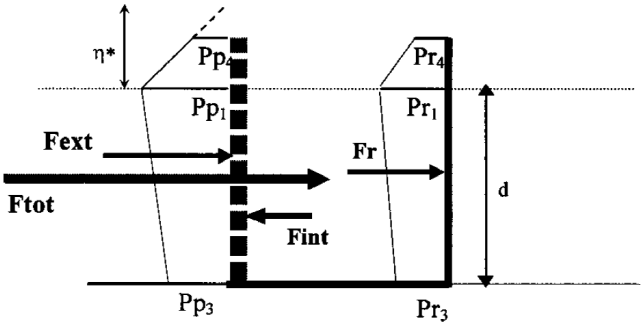

Figure 5.3: *Peak pressure diagrams and resultant forces on the caisson (Tabet-Aoul and Lambert [146]).*

Kirca and Kabdasli [78] provided an experimental investigation on a new type of perforated caisson, characterized with a heavier structure and greater inner stability compared with a fully perforated caisson. In addition, this proposed caisson shows a different mechanism of dissipation resulting in a reduction of the wave loads compared to a purely vertical caisson. The geometry of the caisson consists in two parallel chambers divided by an impermeable plate settled just on the SWL. In this case, when there is no wave motion the lower chamber of the caisson is completely filled with water, while no water in present in the upper chamber.

Another important contribution to study wave loads acting on perforated breakwaters comes from the numerical modeling. Chen et al. [20] determined the wave pressure acting on a perforated breakwaters and the arm of the wave force on them, through an Eulerian numerical model developed by Wang [154]. The results obtained from the numerical simulations are validated through laboratory experimental data. Chen et al. [21]

analyzed the same model extended to a perforated caissons with a top cover. In this case the authors studied the wave forces acting on the front wall and on the back walls, in case of non-overtopping and non-breaking waves. The resulting pressures acting on the caissons depend, apart of the wave characteristics, on the geometry of the caisson, that can be summarized in the width of the chamber, on the height from the water level to the top of the inside chamber as well as from the porosity, μ, defined as the ratio between the section of the holes and the total area of the front wall.

Other aspects to take into account when designing perforated breakwater are their hydraulic properties. In particular, an important aspects is related with the energy dissipation mechanisms, occurring when the waves pass through the slotted wall. The analysis of this kind of problem is approached assuming that the motion is irrotational and therefore introducing a velocity potential, so that $\boldsymbol{u} = \nabla\Phi$. The fluid motion in correspondence of the holes results to be highly turbulent, so that a relevant loss of energy appears in this part of the caisson. In literature, different models aimed to predict the energy drop. These approaches can be divided in models in which the porous wall is considered to be a thin wall with orifices, and models in which the wall is considered as a porous medium. Mei et al. [102], under the hypothesis of thin wall compared with the wave length, derived a model that in its simplest form reads:

$$p(x_-, z, t) - p(x_+, z, t) = \frac{C_f}{2} u(x_+, z, t)|u(x_+, z, t)| + L_g \frac{\partial u(x_+, z, t)}{\partial t} \tag{5.13}$$

in which the coordinates x_- and x_+ are located immediately up-wave and down-wave of the slotted wall, so that the loss of energy is evaluated by applying the conservation principle in correspondence of the crossing of the wall, L_g is an empirical length scale of the problem and C_f is a quadratic loss coefficient. (see Fig. 5.4).

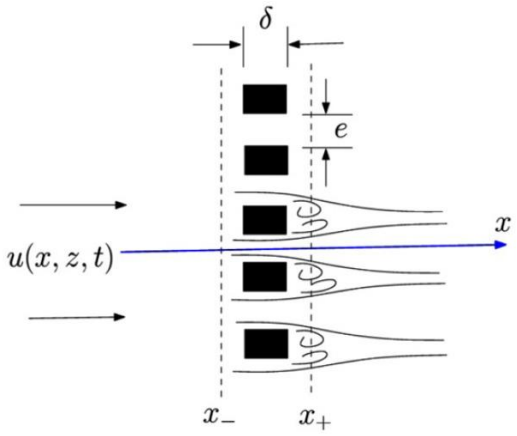

Figure 5.4: *Scheme of the flow passing through a slotted wall (Huang et al. [72]).*

Regarding the evaluation of the reflection coefficient, K_R, different approaches have been presented over the years. In general, these methods are based on the idea of dividing the resultant free-surface surface elevation in incident and reflected waves. The resulting elevation can be indeed written as a superposition of these two components:

$$\begin{cases} \eta_I = a_I \cos(kx - \omega t + \phi_I) \\ \eta_R = a_R \cos(kx - \omega t + \phi_R) \end{cases} \tag{5.14}$$

The indexes I and R stand for incident and reflected, respectively. In order to find a method capable of resolving the incident and reflected wave spectra, Goda and Suzuki [64] developed a method based on the Fast Fourier Transform (FFT) technique. In this method, the incident and reflected wave amplitudes a_I and a_R are estimated through a harmonic analysis. The wave elevation have to be recorded at two locations $x = x_1$ and $x = x_2 = x_1 + \Delta l$, with Δl the separation distance. From the surface elevation measured at these gauges, the method allows to determine the energy associated to the incident and reflected waves. As sketched in Fig. 5.5 the upper, f_{max}, and lower, f_{min}, limits of the effective frequency range used in the calculation have to be chosen in order to be in the range away from the values $k\Delta l = n\pi$, with $n \in \mathbb{N}$ $k = 2\pi/L$ the wave number in which the method diverges. The energy of the incident, E_I, and reflected,

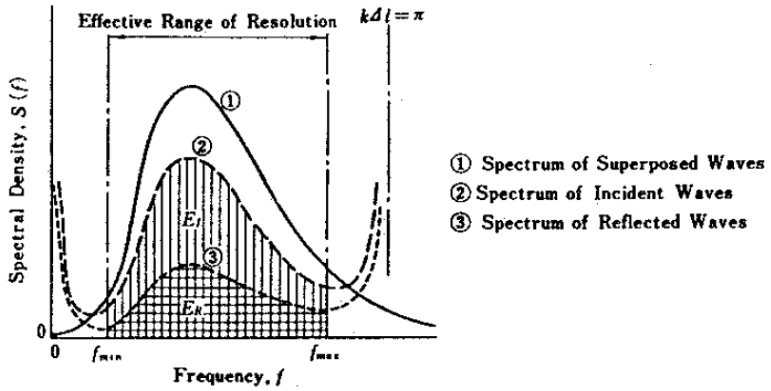

Figure 5.5: *Illustration of spectral resolution of incident and reflect waves (Goda and Suzuki [64]).*

E_R, waves within the range f_{min} to f_{max} are therefore obtained as:

$$\begin{cases} E_I = \displaystyle\int_{f_{min}}^{f_{max}} S_I(f)df = \frac{\Delta t}{2t_0}\sum_{f_{min}}^{f_{max}} I_I \\ E_R = \displaystyle\int_{f_{min}}^{f_{max}} S_R(f)df = \frac{\Delta t}{2t_0}\sum_{f_{min}}^{f_{max}} I_R \end{cases} \tag{5.15}$$

From these expressions comes the definition of K_R. Since the wave energy is a function of the square of the wave height, the reflection coefficient, defined as the ratio between heights, is obtained as:

$$K_R = \sqrt{\frac{E_R}{E_I}} \tag{5.16}$$

In the case of a fully perforated Jarlan-type structure, Sahoo et al. [134] presented an explicit expression for K_R, based on the potential theory and assuming normal incident plane waves:

$$K_R = \left|\frac{1 - G(1 - i\cot(kB))}{1 + G(1 + i\cot(kB))}\right|, \qquad G = \frac{\mu}{ks(f - ip)} \tag{5.17}$$

in which i is the imaginary unit number, G is the porous-effect parameter of the perforated wall, expressed in Chwang [25]. Since p is a parameter related to the wall inertial

effect, G assumes real values only when $p = 0$ (case of rigid structure), while becomes complex for $p \neq 0$ (case of flexible structure). The term s is the front wall thickness, while the dimensionless parameter f is a linear porous resistance coefficient. An interesting result of this formula is that, when G is considered real, the reflection coefficient takes its minimum values at $B/L = 0.25 + 0.5n$, with $n \in \mathbb{N}$. Due to the limitation in chamber width, only the fundamental resonant mode, $n = 0$, is of engineering interest when designing Jarlan-type structures (Huang et al. [72]).

As pointed out by Fugazza and Natale [58], when the reflection coefficient assumes a minimum the incident waves pass through the front perforated wall without changing its wave phase, while the waves reflected by the solid back-wall and the incident waves at the front wall have opposite phases. In this situation also it is also encountered the largest horizontal wave force at the wall, being the surface elevations on both sides of the front plate at the largest difference. As observed by Yip and Chwang [158], the reflection coefficient response with B/L is opposite to that of wave force acting on the front wall.

Often, in practical applications, the perforated wall breakwaters are constructed with a partially perforated caissons, in order to increase their structural stability. In these cases the water depth inside the chamber is smaller than outside. This particular configuration affect the variation of reflection coefficient, according with the difference in water depth inside and outside the chamber. In any case, the accurate definition of the flow field (kinematics, flow discharge through the holes of the caisson and estimation of the energy loss coefficients, reflection coefficients, dynamic pressures, etc.) requires detailed investigations. The main aim is to reduce the wave reflection induced by the fluid-structure interaction and, simultaneously, the hydrodynamic loads in order to give a better level of global stability of these kind of structures. The use of an advanced numerical tool has been rarely adopted to support the design of perforated breakwaters, in which it would furnishes useful and practical guidelines for their design. In the following sections breakwaters performances are investigated through the SPH model.

5.2 Analysis of wave pressures at breakwaters

In this section SPH simulations of wave pressures for the cases of a vertical breakwater and two types of perforated breakwaters subjected to regular waves propagating along a plane channel in intermediate water conditions are presented. The capabilities of the hybrid formulation, expressed by Eq. 3.12, are compared with the diffusive models proposed by Molteni and Colagrossi [104] and Antuono et al. [6], against laboratory experimental data by Kirca and Kabdasli [78] and Chen et al. [21]. In order to optimize the numerical results, the SPH parameters α and ϵ_X have been set equal to 0.01 and 0.25, respectively. For the vertical breakwater and the perforated ones, the spatial resolutions are $d/\Delta x$ = 75 and 115, respectively. The problems are solved with the governing equations expressed by System 2.72, while fixed ghost particles are implemented for the modeling of the solid boundary. The integration scheme adopted in this case is the Runge-Kutta with frozen diffusive approach.

5.2.1 Vertical breakwater

The first test case deals with the interaction between a regular wave train and a simple vertical breakwater. The incident waves are 3rd order Stokes waves, characterized by a wave height H = 0.1 m and a wave period T = 0.8 s. The value of water dept, d, is constant and fixed to 0.54 m. The length of the wave flume is L_c = 4 m. In Fig. 5.6 the time instant when the first wave reach the right wall is presented, where the vertical and horizontal velocities fields are shown. Different diffusive formulations are considered for the simulations. In the specific, the Molteni and Colagrossi model [104], the δ-SPH [6] and the hybrid (coupled) formulation, presented in 3.12, are taken into account. The hybrid formulation is a function of the position of the fluid particles in the domain. Only in a region adjacent the right wall with width equal to the support kernel, $3h$, the [104] model is enforced (fluid-solid interaction), while in the remaining part of the domain, since no violent dynamics occurs, the [6] model is enforced. The transition (hybrid) zone between the two formulations also occurs in a width equal to $3h$. In the following simulations, the same coefficient for the diffusive term (δ = 0.1) is imposed.

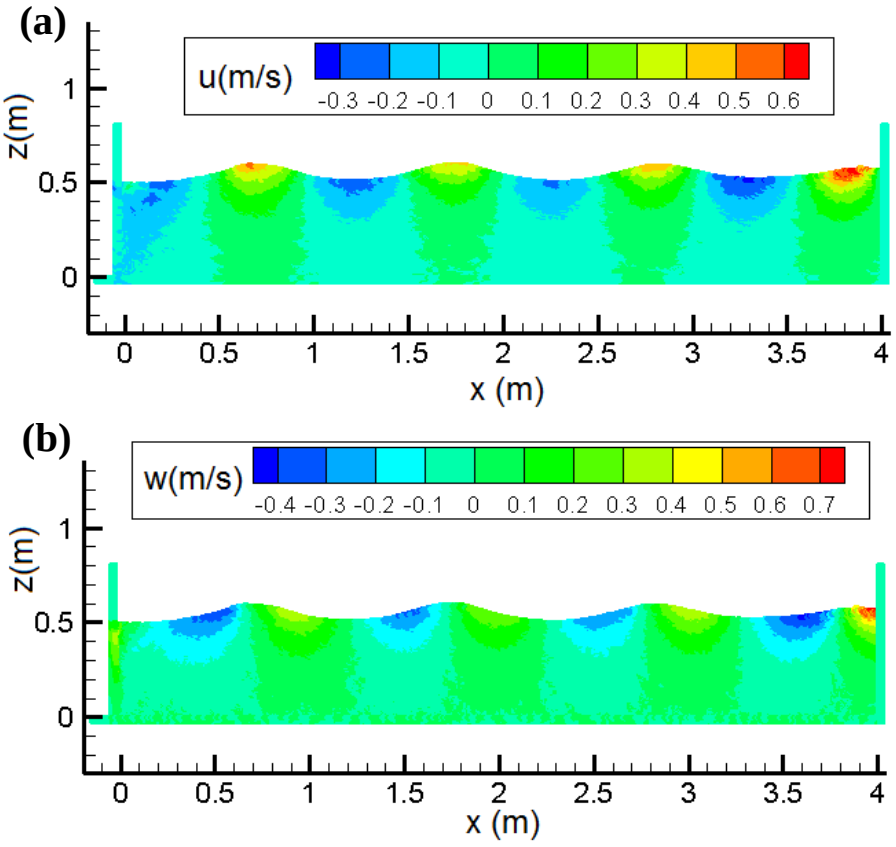

Figure 5.6: *Time instant of wave impact at the right wall. In (a) is the horizontal velocity field, while in (b) the vertical velocity field.*

The results are compared with the experimental data obtained by Kirca and Kabdasli [78] in terms of dynamic pressures acting on the vertical body profile, evaluated

through the use of Eq. 3.38, for some specific points located below and above the SWL. Fig. 5.7 shows the time variations of dynamic pressures, respectively, at z/d = 0.79, 0.93 and 1.07, where z/d = 1 corresponds to the SWL. Since non-breaking waves are taken into account, the resulting shape is characterized by the occurrence of standing wave pressures (see *e.g.* [147]) with temporal scale equal to the wave period. For the considered points of the body profile, a good agreement between all diffusive models and the experimental data can be observed in terms of amplitude and wave shifts of Δp.

It is worth nothing that the reference experimental data of dynamic pressures exhibit spiky values of positive peaks and non-physical negative values acting above the SWL related to the inaccuracy of the experimental instruments, as shown in Fig. 5.7 (c).

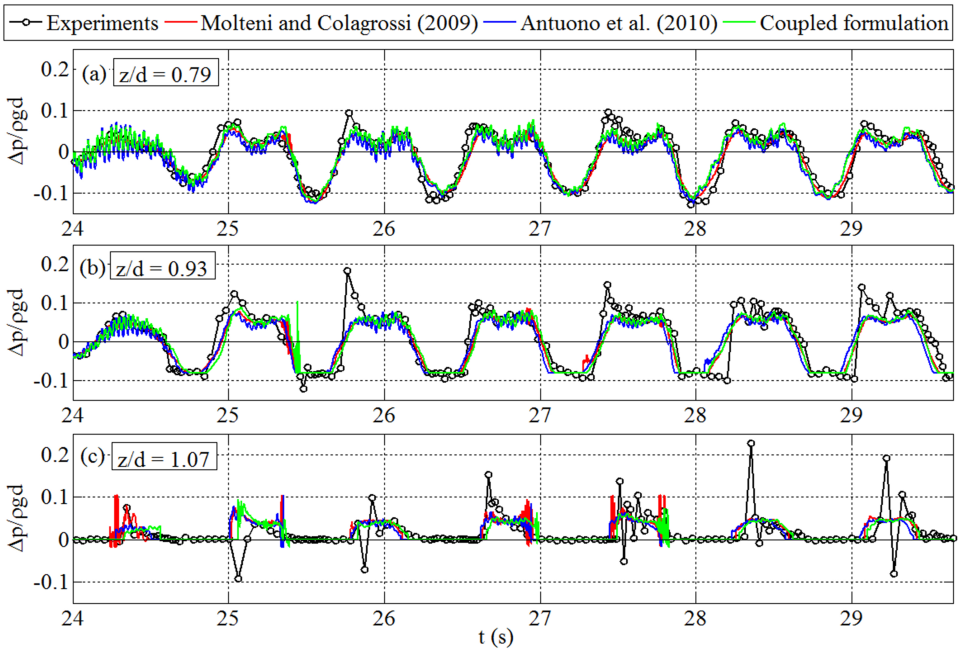

Figure 5.7: *Comparisons of time variation of wave pressures acting on the vertical breakwater at z/d = 0.79, 0.93 and 1.07 using the adopted diffusive SPH schemes, with experimental data of Kirca and Kabdasli [78].*

The difference in the results of the diffusive SPH models refers to their different magnitude of high-frequency oscillations. This feature is here exploited through a spectral analysis, allowing the dynamic pressure signals to be analyzed in frequency domain. For the same three locations mentioned above, the dynamic pressure power spectra, $S_{\Delta p}$, are highlighted in Fig. 5.8, where the vertical black lines are inserted to separate the energy contents linked to the Stokes waves and the acoustic oscillations occurring at a frequency greater than the wave harmonics. It can be observed that the occurrence of significant high-frequency noise appear in a range greater than the wave harmonics (in the considered waves, $f/f_p > 3 \div 4$, where f is here the frequency and f_p is the fundamental peak frequency). The greater spurious energetic contents are associated to the model of Molteni and Colagrossi [104]. For the spectrum of $S_{\Delta p}$ referred to the point above the SWL, shown in Fig. 5.8 (c), high-frequency energetic levels are distributed almost uniformly for values greater that the physical wave harmonics.

The level of high-frequency noise appearing in the oscillatory feature of $S_{\Delta p}$ is ana-

lyzed by evaluating the ratio between the zero-order moment of high-frequency noise in the power spectrum, m_{0hf}, and the total zero-order moment of the power spectrum, m_0, as follows:

$$\frac{m_{0hf}}{m_0} = \frac{\int_{(n+0.5)f_p}^{f_{max}} S_{\Delta p}(f)df}{\int_{f_{min}}^{f_{max}} S_{\Delta p}(f)df} \tag{5.18}$$

where n is here the number of wave harmonics occurring in the dynamic pressure wave spectrum, and f_{min} and f_{max} are the minimum and the maximum computed wave frequencies.

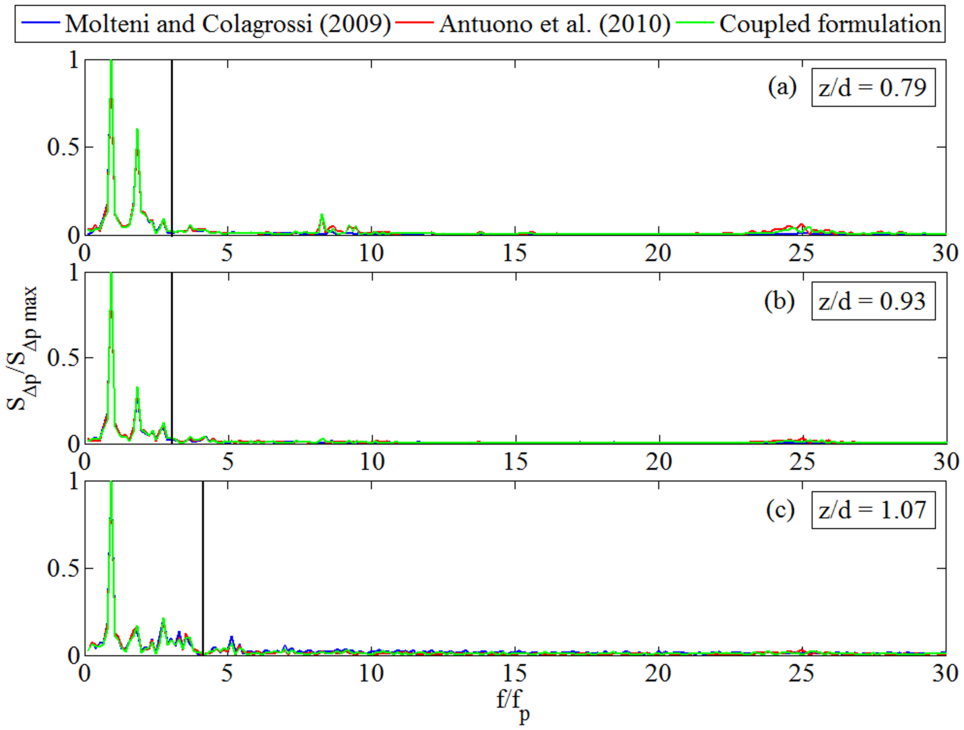

Figure 5.8: *Dynamic pressure power spectra at z/d = 0.79, 0.93 and 1.07 using the adopted diffusive SPH schemes.*

Fig. 5.9 describes the variation of the ratio m_{0hf}/m_0 along the vertical wall (from the bottom to the maximum wave run-up, η_{max}). The magnitude of high-frequency wave pressures furnishes the capabilities of the considered diffusive terms to smooth the numerical noise. For points located far from the SWL ($0 < z/d < 0.85$) the diffusive model by Molteni and Colagrossi [104] induces lowest values of m_{0hf}/m_0 resulting in the smoothest effect of the dynamic pressure, while the model by Antuono et al. [6] shows highest values of spurious numerical noise. The vertical range corresponds to measuring points located in the underwater part of the breakwater, *i.e.* below the maximum run-down, η_{min}.

The hybrid approach furnishes, as expected, intermediate values of m_{0hf}/m_0 between the other formulations. Across the SWL ($z/d > 0.85$) limited by the maximum run-up and run-down, the hybrid formulation and the model by Antuono et al. [6] furnish lower values of high-frequency wave pressures than the model by Molteni and Colagrossi [104]. This last model shows highest energy associated with the numerical

noise due to the lack of the renormalized density gradients which conversely act to regularize the free surface and, consequently, the spatial distribution of fluid particles near the gauge point. It is important to notice, however, that the area of the spectrum associated to the Stokes harmonics may also be characterized by the presence of pressure noise, leading to an incorrect identification of the effective acoustic noise. The role of the acoustic noise in the analytical frequency range is however further investigated in chapter 6.

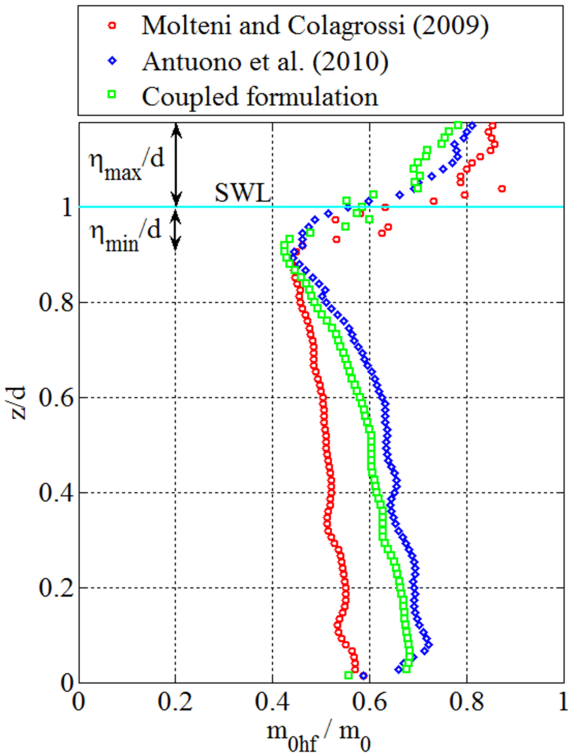

Figure 5.9: *Level of high-frequency noise occurring in the zero-order moment of the power spectrum of dynamic pressure using the adopted diffusive SPH schemes.*

5.2.2 Perforated breakwaters

In this first application of SPH to perforated breakwaters, two different geometries of caisson are considered, as presented by Chen et al. [21]. Both caissons present a top cover plate over the free surface and one internal chamber. The front wall of the first breakwater is perforated by two rectangular holes, while the back wall is solid. It is characterized by a porosity $\mu = 20\ \%$, a width of the chamber $B = 0.2$ m, a vertical base $d' = 0.2$ m, and a height of top cover above SWL $s = 0.08$ m. The second one is perforated by three holes, adopting $\mu = 20\ \%$, $B = 0.15$ m, $d' = 0.2$ m and $s = 0.16$ m. In a plane channel 0.4 m deep, second-order incident waves are characterized by $H = 0.08$ m and $T = 1.2$ s for the breakwater no. 1 and by $H = 0.1$ m and $T = 1$ s for the breakwater no. 2.

The diffusive terms of Molteni and Colagrossi [104], Antuono et al. [6] and the hybrid formulation expressed in Eq. 3.12 are taken into account. In this last case the δ-SPH is enforced in the area near the walls of the caisson, on a area fixed heuristically

to the length of the adopted kernel support, $3h$. Away from the walls, where fluid-structure interaction does not occur, the [104] formulation is enforced. In this case the transition between the two models is introduced also inside the chamber of the caisson where the three vertical walls (external front, internal front and rear) are considered in the analysis of the wave pressures for calculating the horizontal loads, as displayed in Fig. 5.10 for the geometry no. 2.

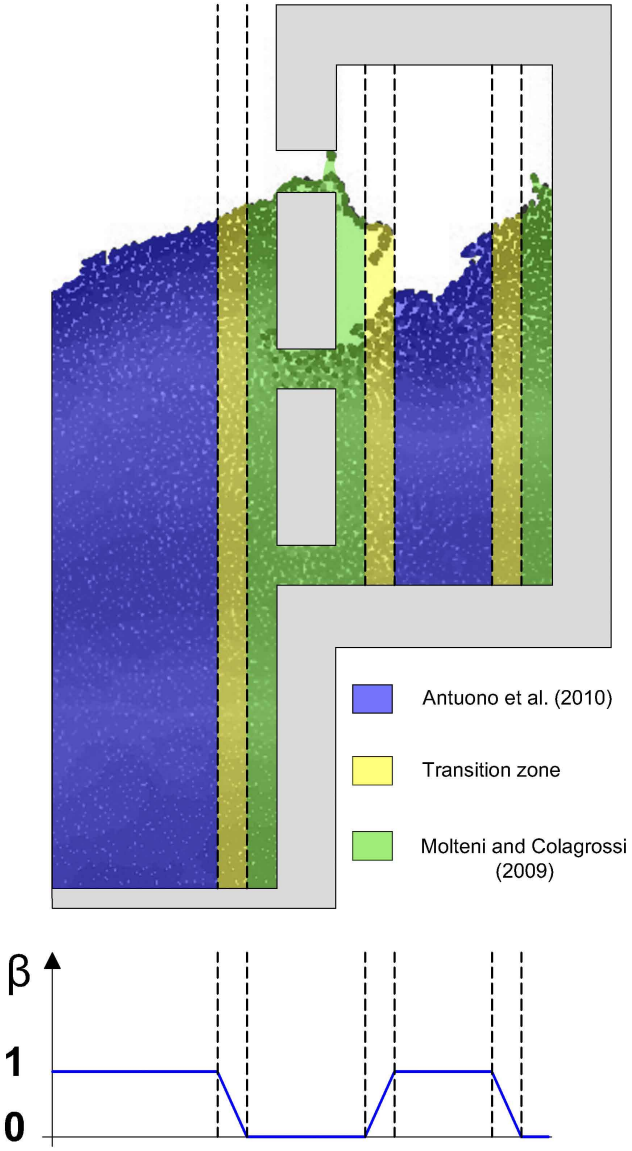

Figure 5.10: *Domain subdivision of the hybrid model in the case of a perforated breakwater no. 2, with the corresponding spatial variation of the parameter β (colored areas of the fluid domain are associated to the involved diffusive formulations).*

Figs. 5.11 and 5.12 the frame of the simulations with pressure field and velocity vectors are shown for the case of the breakwater no. 1 and no. 2, respectively. The first time instant, presented Figs. 5.11 (a) and 5.12 (a), refers to the wave crest impacts at the front walls, in which a considerable flow discharge inwards the chamber is encountered.

The second time instant, presented Figs. 5.11 (b) and 5.12 (b), refers to the wave trough at the front wall, with considerable flow flux outwards the chamber.

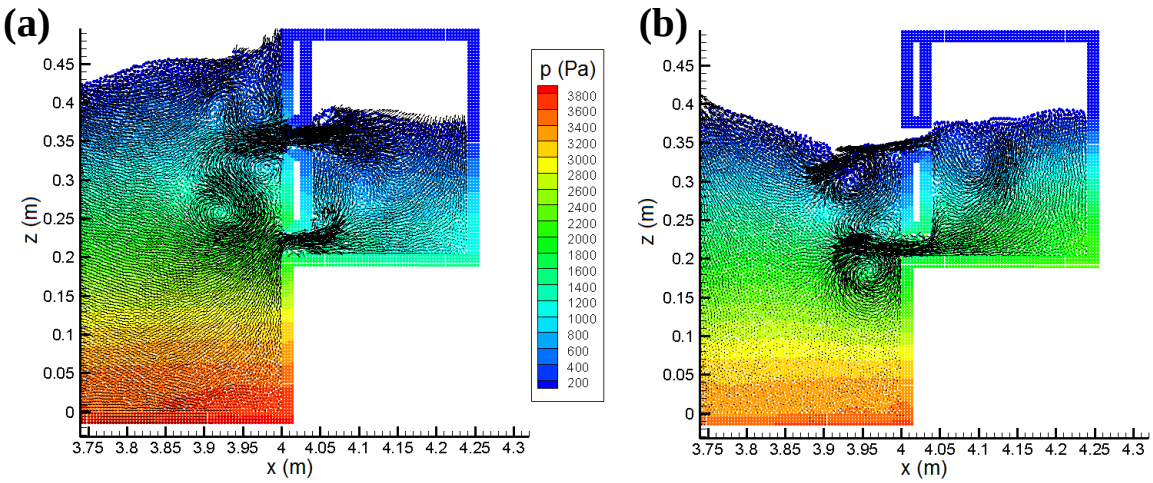

Figure 5.11: *Frames of the simulation with pressure distribution and velocity vectors for the breakwater geometry no. 1. In (a) wave crest at the front wall, while in (b) wave trough at the front wall.*

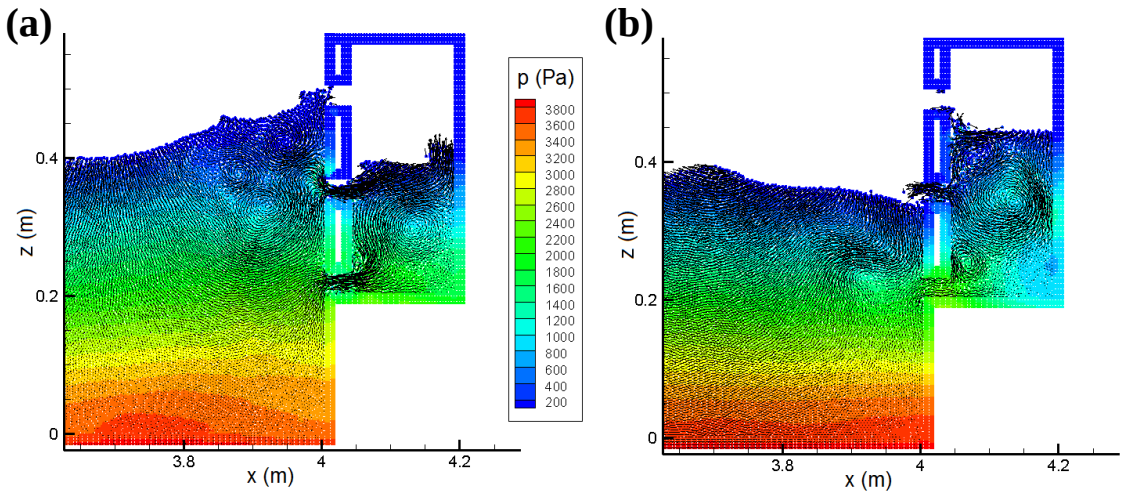

Figure 5.12: *Frames of the simulation with pressure distribution and velocity vectors for the breakwater geometry no. 2. In (a) wave crest at the front wall, while in (b) wave trough at the front wall.*

The spatial distributions of dynamic pressures at the front wall and at the internal walls of the chamber, are analyzed when the maximum pressure induced by the wave crest within the regular wave train appears in correspondence to the SWL. Positive dynamic pressures are displayed on the external side of the walls and negative ones on their internal side. Is noticed that the pressure peaks at the three reference walls appear at different time instants. Their phase shift is dependent on the wave celerity and the width of the chamber. In Figs. 5.13 and 5.14 SPH results obtained with the hybrid formulation and the models by Molteni and Colagrossi [104] and Antuono et al. [6] with a coefficient $\delta = 0.2$ are compared with the experimental data by Chen et al. [21],

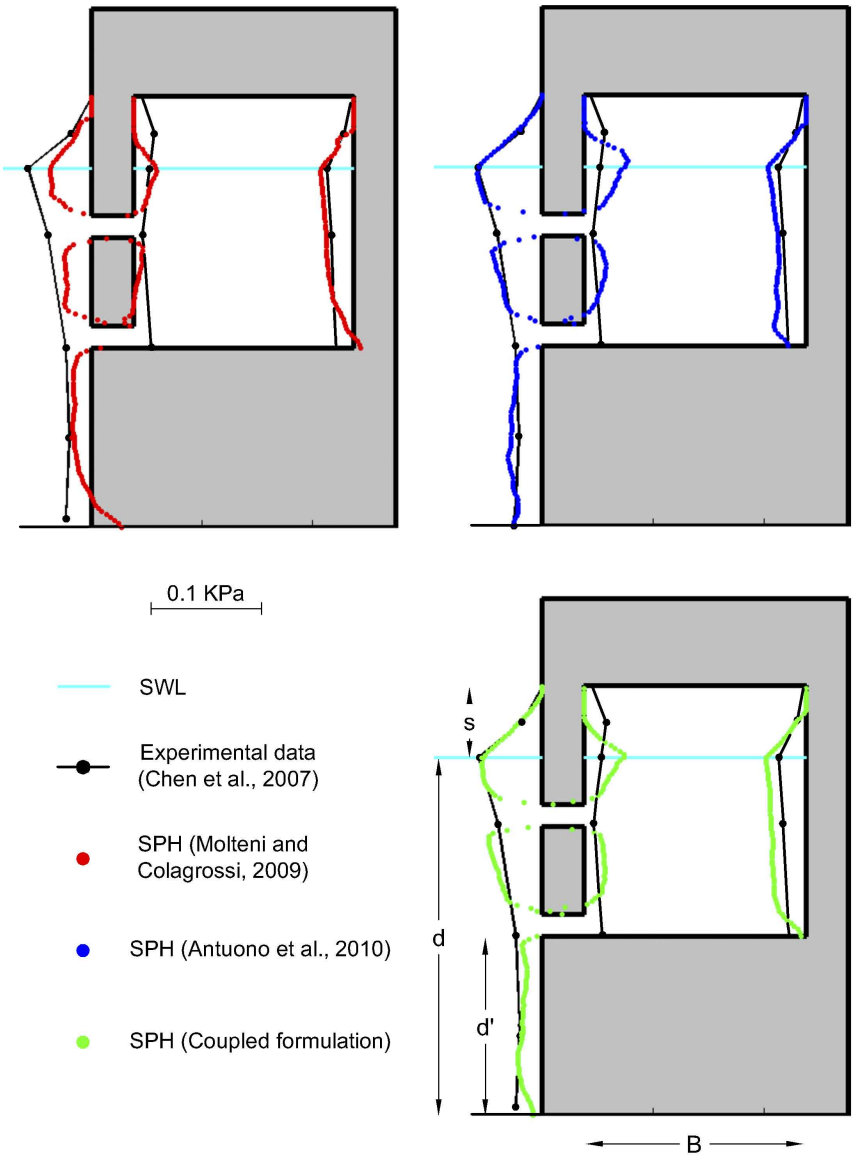

Figure 5.13: *Spatial distribution of wave pressures at perforated breakwater no. 1 using the adopted diffusive SPH schemes.*

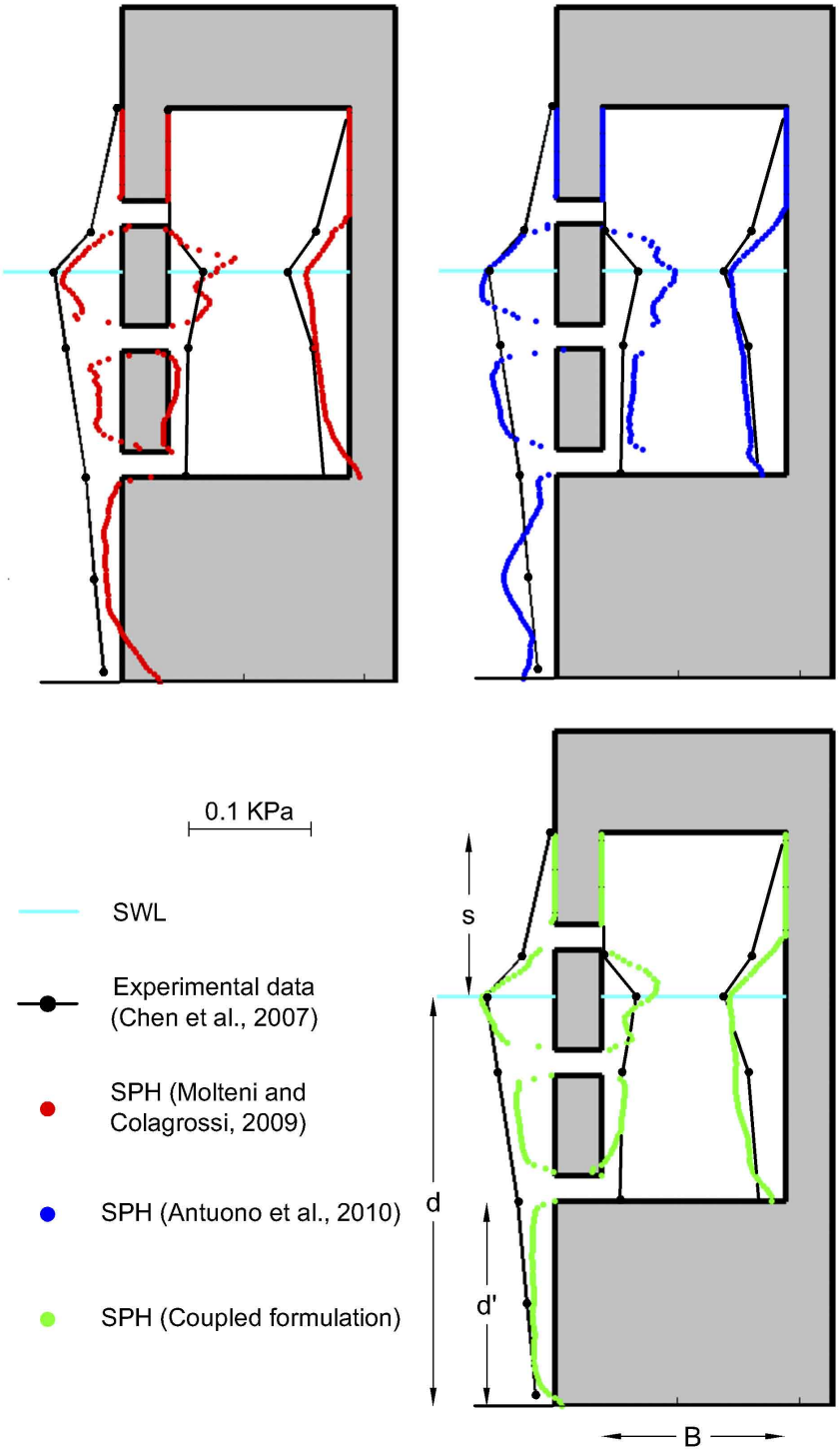

Figure 5.14: *Spatial distribution of wave pressures at perforated breakwater no. 2 using the adopted diffusive SPH schemes.*

showing an overall agreement on the front wall and the right internal wall.

The magnitude of Δp along the depth is greater for the front wall and lower for the internal walls due the wave dissipation generated by the presence of perforations, as also observed by Takahashi [147]. A general underestimation of the dynamic pressures is observed when the formulation of Molteni and Colagrossi [104] is applied. Since the hydrostatic solution is not preserved in the mentioned model, unphysical negative values of Δp appear near the lower horizontal parts of the caisson and the maximum dynamic pressure at the SWL is underestimated with respect to the laboratory data. Conversely, the use of the present hybrid formulation and the one developed by Antuono et al. [6] lead to a better assessment of load diagrams along the depth, where a general compressive strain state occurs at the walls due to the preservation of the hydrostatic pressure, as expected. A substantial difference between SPH and experiments in evaluating Δp can be observed near the holes where the results obtained by the three diffusive models highlight lower dynamic pressures than the experimental ones.

Near these geometrical singularities, the reference experimental measurements are missing because of constructional constraints induced by the difficulty to place the pressure sensors near the edges of a structure. This result suggests the need to assess load diagrams on distinct elements of the perforated breakwaters and, however this aspect it will be further investigated in the next section.

An application example of a diffusive SPH model is given in Fig. 5.15, where the dynamic pressure distribution at the perforated breakwater no. 1 is illustrated when the maximum wave crest arrives on the front wall. Strong variations in the values of Δp

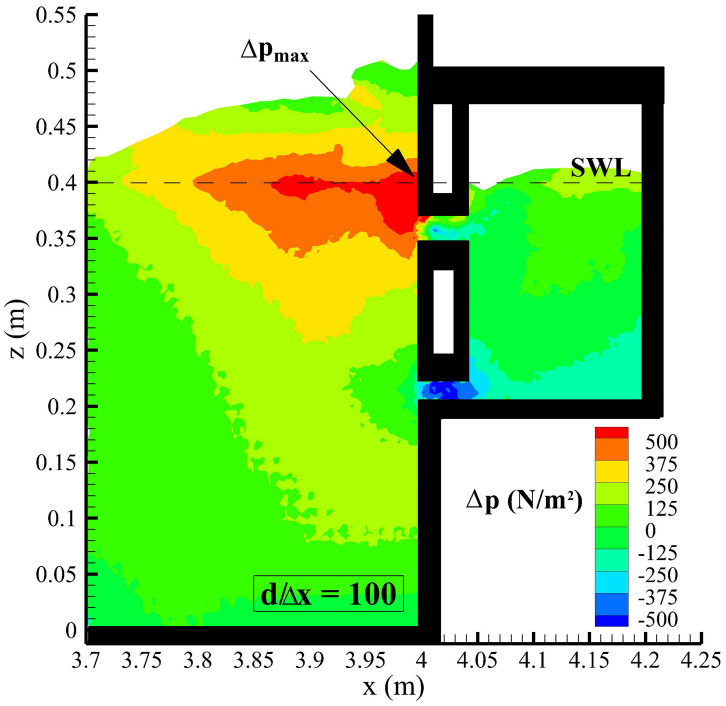

Figure 5.15: *Dynamic pressure for a diffusive SPH formulation at a perforated breakwater no. 1 when the crest within the regular wave train impacts on the front wall.*

are evident across the holes of the structure due to the loss of wave energy. In this case, negative dynamic pressure can occur during the passage of the water flux. The pressure

drops are related to the strong horizontal velocity gradients occurring at the geometrical singularities, as expressed by the canonical Bernoulli's theorem (see *e.g.* [72]).

In order to assess the capabilities of the involved diffusive SPH forms in simulating the experimental values of wave pressures on the three faces of the caissons [21], Fig. 5.16 shows the root mean square errors, e_{RMS}, as a function of the magnitude of the diffusive parameter δ. In all cases the value of e_{RMS} is lower than 30 N/m^2 and, particularly for the second breakwater, the use of the hybrid formulation gives lowest errors.

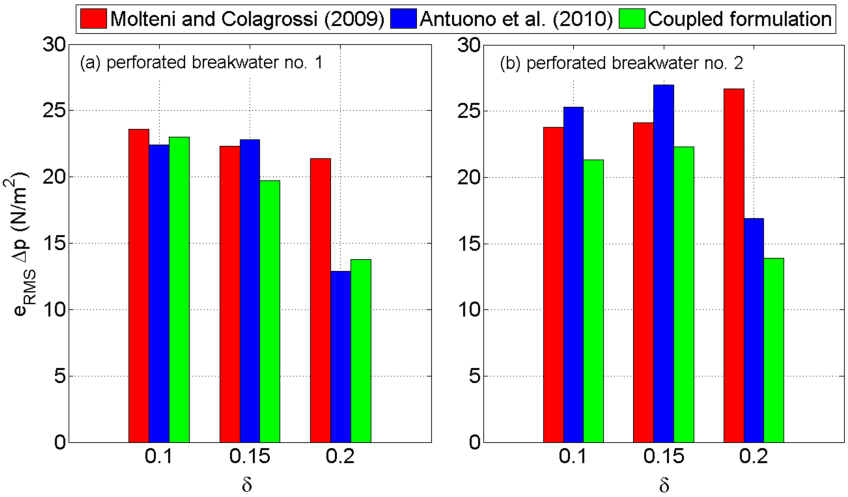

Figure 5.16: *Root mean square errors on Δp vs. parameter δ.*

5.3 Analysis of thin front wall breakwaters

In this section SPH is applied to study the performances of perforated wall-caisson breakwaters, characterized by a thin solid front wall, under the action of regular waves. The governing equations adopted are expressed by System 2.72, while fixed ghost particles are implemented for the modeling of the solid boundary. For the modeling of the thin front wall the multi-node treatment is employed. The integration scheme adopted in this case is the Runge-Kutta with frozen diffusive approach, while the SPH parameters α and ϵ_X have been calibrated and fixed to 0.01 and 0.25, respectively.

The first analysis concerns the dynamic pressures acting at the walls of a fully perforated breakwater. The numerical results, in terms of spatial distribution of wave pressures, are compared with the empirical model by Tabet-Aoul and Lambert [146], presented in section 5.1. Two diffusive formulations and different weighting functions are taken into account to assess the dynamic pressures acting on the body profiles of the breakwater. The second SPH analysis deals with the hydraulic properties of a partially perforated breakwater, regarding the reflection of the incoming waves and its level of efficiency in terms of wave energy dissipation. The numerical results referred to the reflection coefficient are calculated through the frequency domain method of Goda and Suzuki [64], also presented in section 5.1, on the basis of the time series of surface elevations at different spatial locations and compared with experimental data by Chen et al. [19].

5.3.1 Wave pressures at a fully perforated breakwater

The results in terms of dynamic pressures acting on a perforated breakwater are shown in this section. Specifically, SPH simulations are performed for the case of a fully perforated breakwater subjected to regular waves propagating along a plane channel. Concerning the geometry of the computational domain, a schematic representation is shown in Fig. 5.17, where L_c = 4 m, d = 0.4 m and the chamber width is B = 0.54 m. For 2D problems, the adopted porosity of the slotted wall of the breakwater is μ = $d2/(d1+d2)$ = 0.25, where $d2$ is the height of the hole and $d1$ is the height of the solid part (see Fig. 5.18). The height and the period of the incident waves are respectively H = 0.08 m and T = 1.03 s, resulting in 2nd order Stokes wave trains at intermediate water depth conditions. As a result, the considered non-breaking regular waves lead to the occurrence of standing dynamic pressures at the perforated breakwater (see Takahashi [147]).

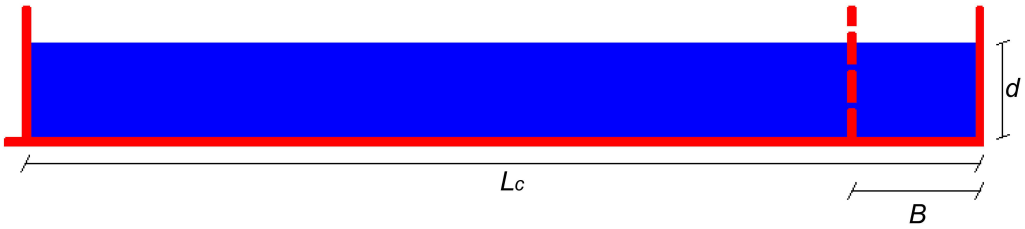

Figure 5.17: *Representation of the computational domain with characteristic dimensions adopted for the simulations.*

The adopted combination of wave characteristics and chamber width ensures to remain within the limits of applicability of the empirical model developed by Tabet-Aoul and Lambert [146] for successive comparisons with SPH simulations. To model the thin perforated wall of the caisson, multi-node fixed ghost particles are employed with the related interpolation nodes, as described in Fig. 5.18. Ghost particles with two or three nodes are adopted as a function of their position along the perforated wall.

The spatial resolution used for the multi-node fixed ghost particles simulations has been driven by the width of the slotted wall, s, resulting in Δx = s/4 = 0.0045 m. The simulation of 10 s takes a CPU time of about 9 h using a single 3.4 GHz Intel(R) i7-3770 core with 8GB RAM. Conversely, the use of classical fixed ghost particles requires a spatial resolution equal to Δx = s/8 = 0.00225 m, as described in Fig. 3.4, resulting in a total CPU time equal to 44 h with the same computational strategies and machine. The number of total particles required by the fixed ghost particle method, in our specific 2D problem, is about four times the proposed approach. The simulation with multi-node fixed ghost particles gives a reduction of the CPU time of about 79.5% with respect to the application of one-node fixed ghost particles. It is worth noting that in the standard implementation the spatial resolution is only driven by the modeling of the thin wall and it does not lead to an effective improvement in the accuracy of the numerical results. In order to provide a more detailed examination of the computational demand, two simulations performed with classical and multi-node fixed ghost particles at the identical spatial resolution were performed. In this case, the CPU time for the multi-node simulation resulted to be about 2% longer than that with classical fixed

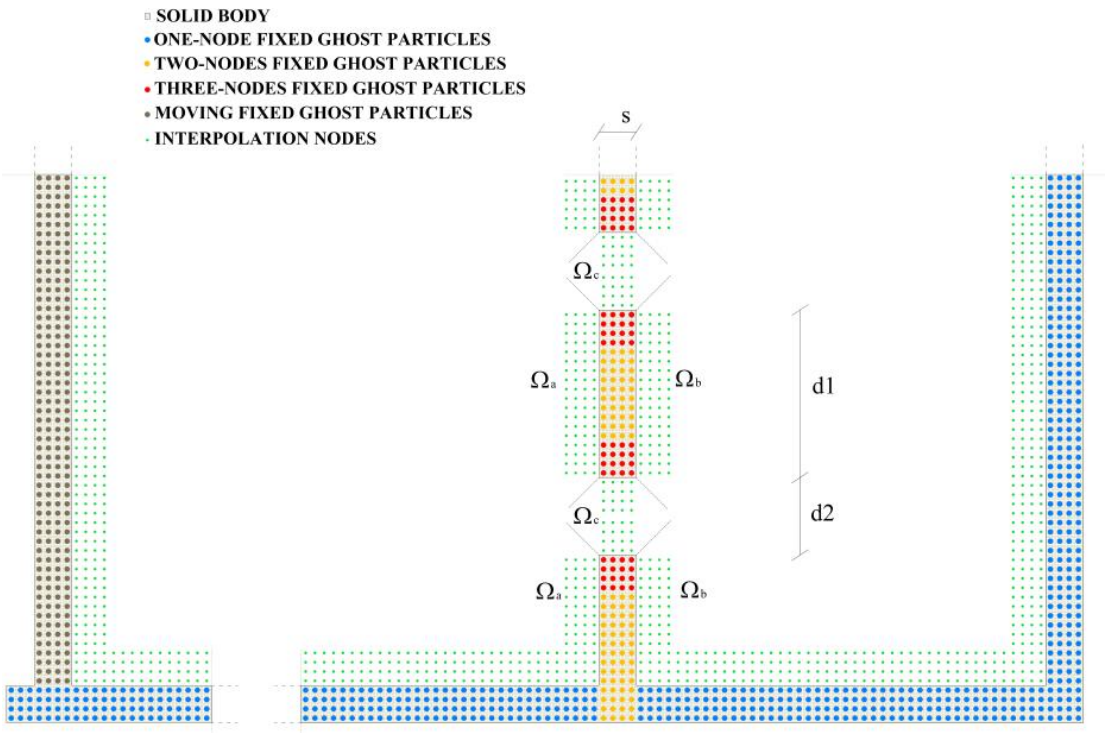

Figure 5.18: *Sketch of solid boundary conditions modeled by a combination of single-node and multi-node fixed ghost particles and corresponding interpolation nodes for the case of the fully perforated breakwater (the width of the front wall is s = 0.018 m, the height of the solid parts is $d1$ = 0.12 m and the height of the holes is $d2$ = 0.04 m).*

ghost particles. This slight difference is due to the fact that the multi-node treatment requires a half number of solid particles to model the thin wall and supplementary switches to compute the field values, resulting in a really small influence on the CPU time. In any case, this result is referred to this specific application, the difference in the computational demand being dependent on the number of total particles and on the number of multi-node fixed ghost particles.

SPH simulations considering the diffusive formulations by Molteni and Colagrossi [104] and the δ-SPH model [6] are performed in order to evaluate the dynamic pressures at the perforated breakwater. The diffusive terms are tested also considering the influence of the magnitude of the diffusive coefficient (δ = 0.1 and 0.2). Moreover, to understand the influence of the interpolating function for the measurements of dynamic pressures at the body profiles, different shapes are taken into account. In particular, the renormalized Gaussian and Wendland kernels, with supporting radius area of $2h$ and $3h$, presented in section 2.2.2, are compared. Hereinafter, the adopted kernels are named as follows: RG2 = Renormalized Gaussian $2h$, W2 = Wendland $2h$, RG3 = Renormalized Gaussian $3h$ and W3 = Wendland $3h$. In Figs. 5.19, 5.20 and 5.21 three significant time instants of SPH simulations in which a wave interacts with the fully

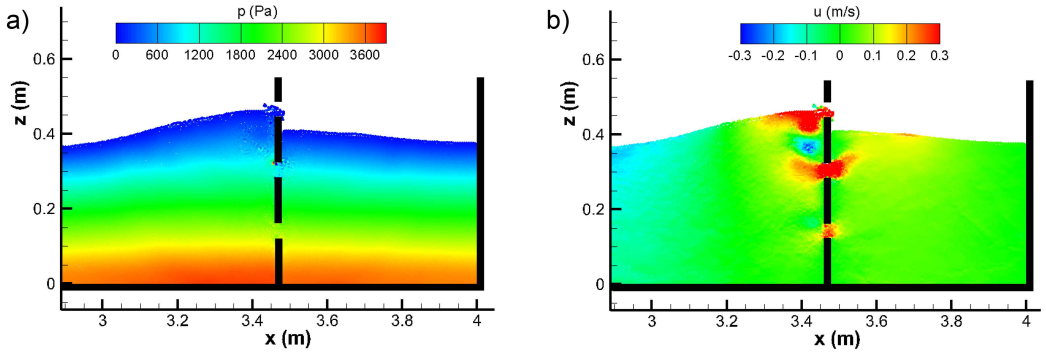

Figure 5.19: *Frame of the SPH simulation in which the maximum dynamic pressure is encountered at the front face in correspondence to the SWL; (a) pressure field; (b) horizontal velocity field.*

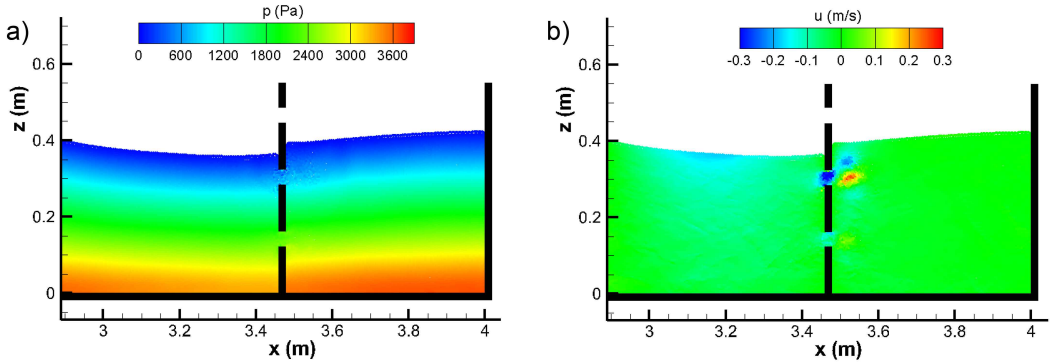

Figure 5.20: *Frame of the SPH simulation in which the maximum dynamic pressure is encountered at the rear face in correspondence to the SWL; (a) pressure field; (b) horizontal velocity field.*

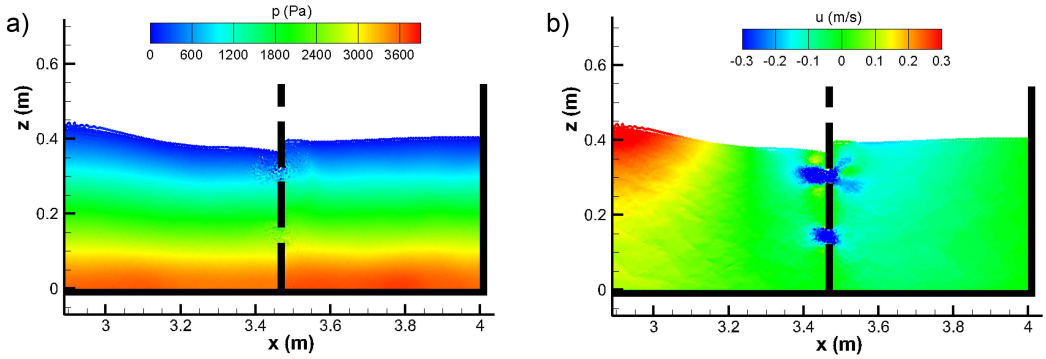

Figure 5.21: *Frame of the SPH simulation in which the wave trough is passing on the front face; (a) pressure field; (b) horizontal velocity field.*

perforated breakwater are displayed. In these characteristic frames (obtained by the diffusive model of [104] with $\delta = 0.1$), pressure and horizontal velocity fields are shown. The first two instants correspond to the maximum dynamic pressure occurring at the SWL for the front and rear faces, respectively. These conditions assume a relevant role in evaluating the load diagrams to be adopted in the stability analysis of perforated breakwaters (see Takahashi [147]). The last instant refers to the occurrence of the wave trough at the perforated front wall. Indeed, the wave initial impact on the front wall and successively to the back wall occurs within a half wave cycle or, in other words, before the passage of the wave trough in correspondence with the perforated front wall. These simulation frames highlight that spurious flow processes do not appear near the slotted front wall, allowing verification of the stability of the proposed multi-node approach to model thin solid bodies in dynamic conditions. The physical insights deduced from the SPH simulations will be discussed later in order to support the features of the numerical load diagrams represented by the spatial distributions of dynamic pressures.

The maximum dynamic pressures at the walls appear during the first wave cycle, obtained after the transition phase induced by the initial ramp. As shown in Fig. 5.22, the dynamic pressure peaks at the front and rear faces in correspondence of the SWL clearly occur at different time instants. It is interesting to notice that the maximum dynamic pressure at the front face is slightly back-shifted compared to the passage of the wave crest. This time shift is not encountered for the rear face in which the instant of the maximum pressure at SWL corresponds to the occurrence of the wave crest. In any case, the time interval between the occurrences of maximum dynamic pressures and wave crests at the two reference walls is influenced by the presence of the slotted wall. The above time window is greater than that referring to undisturbed wave conditions (without the perforated front wall), which is conversely given by the ratio between the sum of the width of the front wall and the chamber (s+B) and the wave celerity, c_w. Moreover, the maximum wave pressure at the rear wall occurs before the appearance of the wave trough at the front wall (see Fig. 5.22). Indeed, the time interval between the occurrences of maximum wave pressure at the two reference walls is lower than a half wave period. It can be noticed that the above mentioned hydrodynamic processes on the occurrence of maximum wave pressures at the walls of the caisson in comparison to the free-surface oscillations were highlighted in the reference experiments by Tabet-Aoul

and Lambert also for different values of B/L.

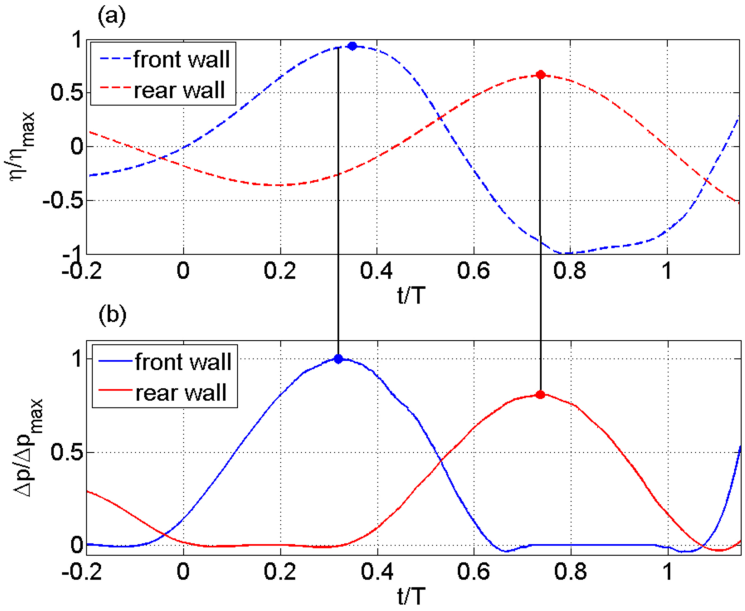

Figure 5.22: *(a) Time variation of surface elevation within the considered wave cycle for the front and the rear walls of the breakwater. (b) Time variation of corresponding dynamic pressure at the SWL for the front and the rear walls of the breakwater.*

Figs. 5.23 and 5.24 highlight the results in terms of spatial distribution of dynamic pressures along the reference walls obtained by the diffusive models of [104] and of [6], respectively, and by adopting two diffusive coefficients and different weighting functions (RG2, RG3, W2 and W3). The numerical results obtained from the SPH model are compared with the empirical formulation of [146]. Positive dynamic pressures are displayed on the external side of the walls and negative ones on their internal side. A good agreement between numerical and experimental results is obtained at the rear wall and at the front wall away from the holes. As expected, the wave loads acting on the rear wall result to be smaller than on the front wall, due to wave energy dissipation induced by the slotted part of the breakwater (see Tabet-Aoul and Lambert [146]).

The numerical simulations have shown detailed properties of the flow dynamics through the perforated breakwaters and some limitations of the current formulas adopted for their structural stability design. In particular, since the commonly adopted empirical formulations (see *e.g.* [147], [146]) do not take into account the local effects induced by the presence of the holes on the perforated wall, result in an approximate assessment of the total loads acting on the slotted part of the breakwater. In these cases, the maximum dynamic pressure is determined at the SWL, at the channel bottom and in correspondence with the maximum water level reached at the structure above the SWL. Then, a linear variation is considered between these points, without considering the actual position of the holes on the perforated structure. Indeed, as shown in Figs. 5.19 and 5.21, during a wave cycle, positive values of horizontal velocity appear at the passage of the wave crest close to the perforations, while relevant negative values occur in correspondence of the wave trough. Due to the loss of wave energy, these velocity gradients affect the pressure field leading to pressure drops near the holes of the slot-

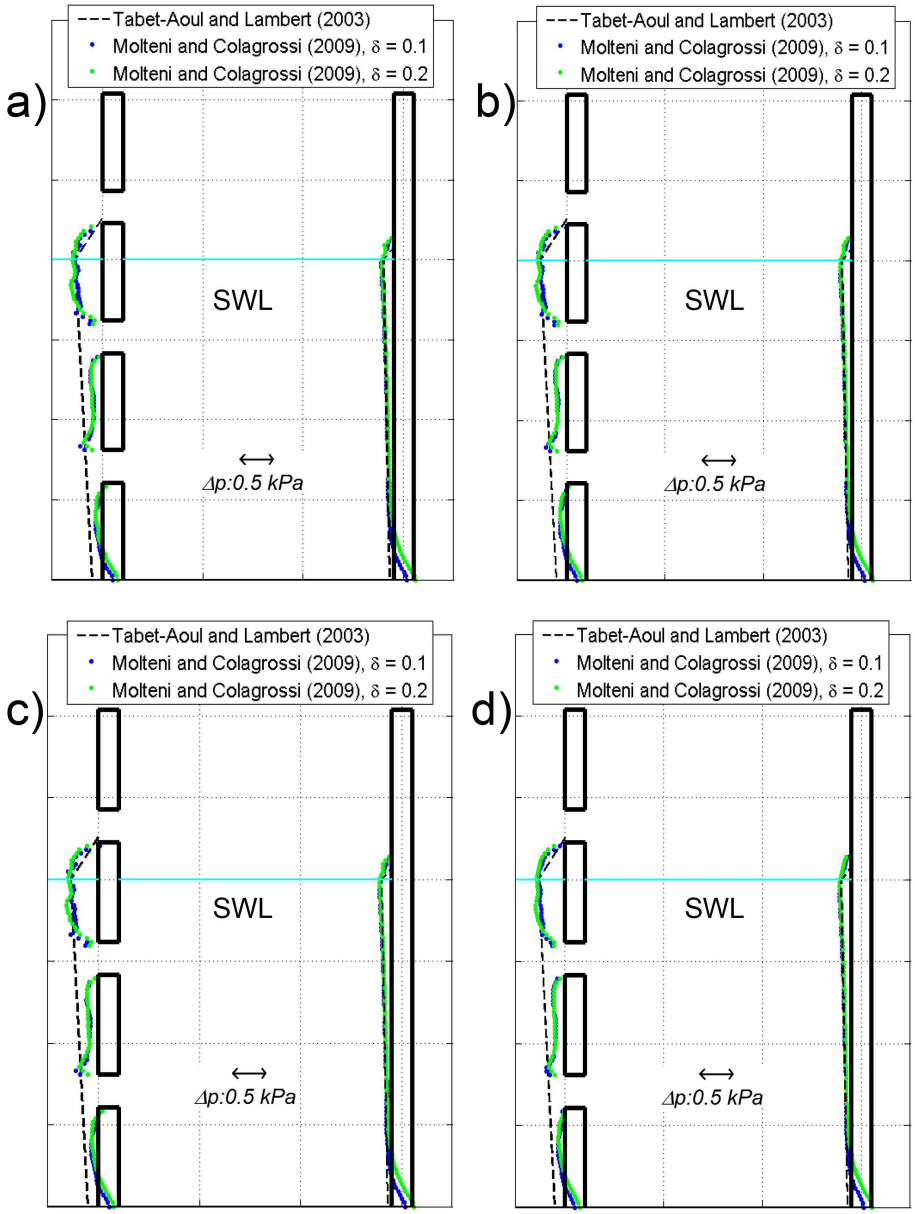

Figure 5.23: *Spatial distribution of wave pressures at perforated breakwaters obtained using the diffusive formulation of [104]. a) RG2, b) RG3, c) W2, d) W3.*

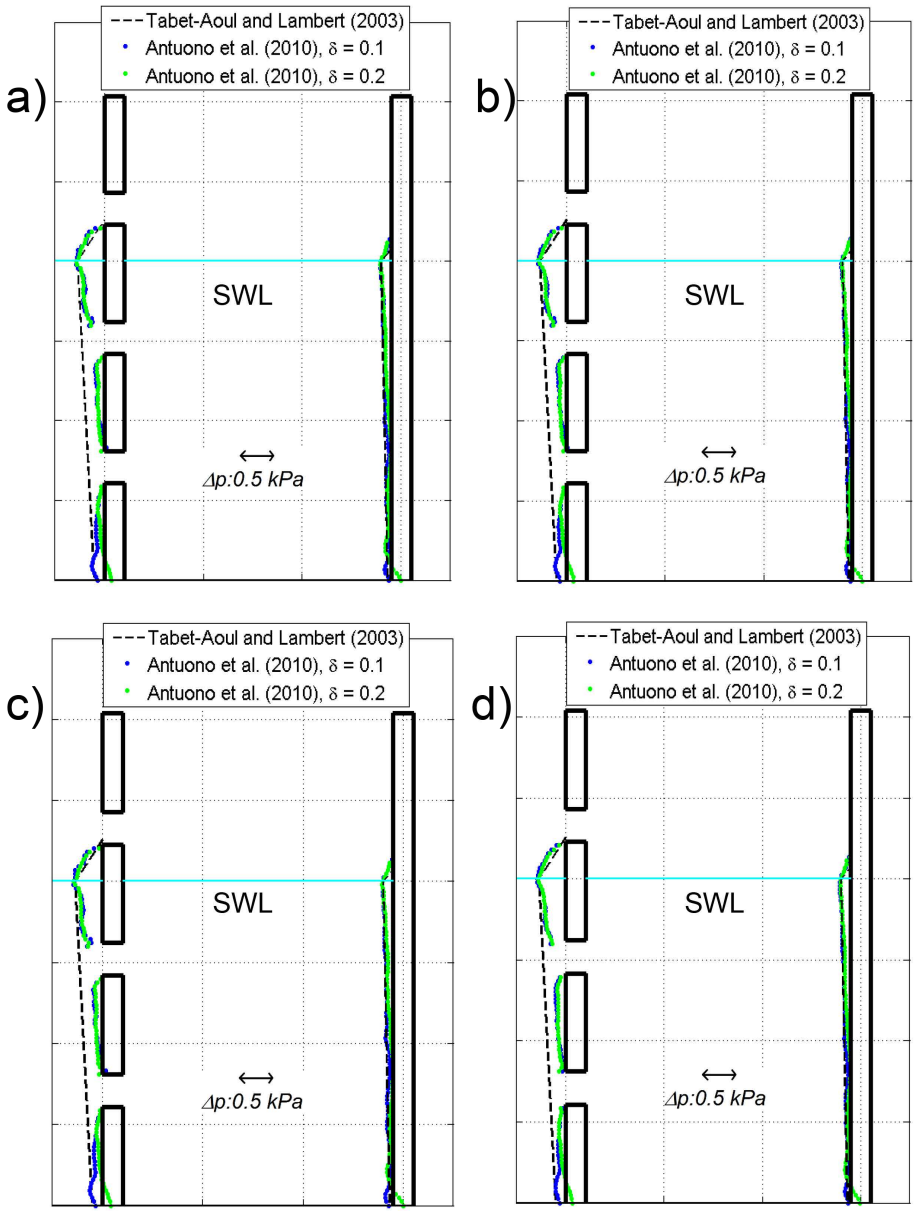

Figure 5.24: *Spatial distribution of wave pressures at perforated breakwaters obtained using the diffusive formulation of [6]. a) RG2, b) RG3, c) W2, d) W3.*

ted structure, as also expressed by Bernoulli's theorem for slotted walls (see Huang et al. [72]). It can be noticed that in the experimental set-up used by [146], the pressure gauges were placed only at the center of the solid parts of the perforated face due to the logistical difficulties in positioning these instruments near the edges. The dynamic pressure measured at these points results as being only minimally affected by the pressure drops induced by the velocity field around the holes. Conversely, the problem in measuring dynamic pressures close to the edges of solid bodies does not represent any difficulty when advanced numerical simulations are adopted.

On the basis of the above considerations, in the numerical simulations a certain part of the error can be linked to SPH inaccuracy, while another part can be attributed to the effects of pressure drops. In order to define the level of accuracy of the simulated dynamic pressures, the Mean Square Error Percent (MSEP) between SPH and the experimental solution of Tabet-Aoul and Lambert is performed.

The error analysis is carried out for all measurements with the prescribed spatial distance Δx for the slotted and solid wall. As illustrated in Figs. 5.25 and 5.26, the values of MSEP are evaluated separately for the front and rear walls in order to quantify the error due to the occurrence of pressure drops close to the perforations. In this way, the error obtained for the rear wall is only due to the potential inaccuracy of the SPH model, since no perforations are present on it, while the error is a combination of model inaccuracy and actual physical effects for the perforated wall. As it is possible to notice in Figs. 5.25 and 5.26, the errors on the front face are always greater than the errors on the rear one.

Concerning the Molteni and Colagrossi diffusive term, being characterized by the loss of the hydrostatic solution, it results in an underestimation of the pressure acting on the walls close to the channel bottom and, particularly, at the rear wall (see Fig. 5.23). This behavior is more evident when the higher value of the diffusive coefficient, δ = 0.2, is assumed. These results are highlighted by the analysis of the errors, in which, for the rear face, lower MSEP values are obtained with the δ-SPH model which remain in the order of 2% for δ = 0.1 and increase to around 4% for δ = 0.2 for all adopted interpolating functions. For the Molteni and Colagrossi model, the errors at the rear face result to be around 4% for δ = 0.1, while increase to around 12% when δ = 0.2. Considering the errors obtained on the front face, the formulation by Molteni and Colagrossi gives lower errors. In any case, the errors are around 20% using δ = 0.1 and around 25% using δ = 0.2 using the adopted diffusive terms. According to the Molteni and Colagrossi formulation, the difference between the errors evaluated for the front and the rear walls is equal to around 15%, while for Antuono et al. the errors are approximately 20%. Even if the Molteni and Colagrossi formulation has a drawback in the progressive decay of the potential energy, the lower approximation of the diffusive term provides a better agreement with the reference empirical relationships compared to the Antuono et al. model, as it was also observed in the case of a dam-break flow impacting on a vertical wall (see Antuono et al. [4]).

With reference to the results obtained by the different shape functions used for the interpolation of dynamic pressures, small differences in the spatial pressure distribution are encountered, as noticeable in Figs. 5.23 and 5.24 and for the analysis of errors in Figs. 5.25 and 5.26. In particular, referring to the values of MSEP evaluated with a specific kernel, the lowest overall error is encountered for the Wendland with support

$3h$ (12.56%). For the cases of kernels W2, G2 and G3, the overall MSEP error result to be equal to 14.65%, 13.86% and 13.89%, respectively. As noticeable in Fig. 2.1, the kernel W3 gives a more regular weight over the support area than the other interpolation functions.

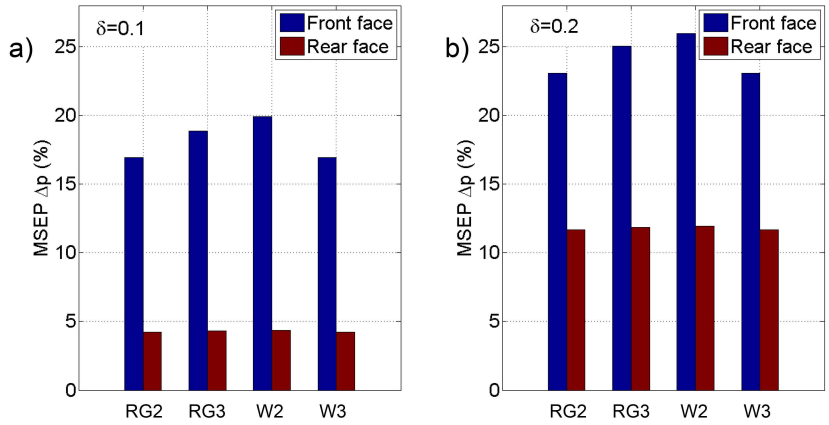

Figure 5.25: *Mean Square Error Percent (MSEP) on Δp for the front and the rear faces, obtained by the formulation of Molteni and Colagrossi [104]; a) $\delta = 0.1$; b) $\delta = 0.2$.*

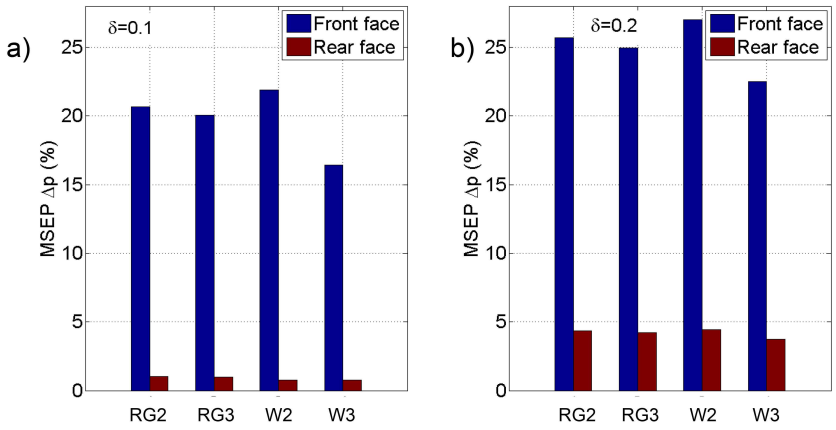

Figure 5.26: *Mean Square Error Percent (MSEP) on Δp for the front and the rear faces, obtained by the formulation of Antuono et al. [6]; a) $\delta = 0.1$; b) $\delta = 0.2$.*

In this context the capabilities of the automatic hybrid formulation presented in section 3.1.2 are examined. In the specific Fig. 5.27 shows the differences between the already presented diffusive formulations, with the hybrid (coupled) diffusive term in which the threshold values $\Delta\rho_A = 0.3\%\rho_0$ and $\Delta\rho_M = 0.6\%\rho_0$ have been taken into account.

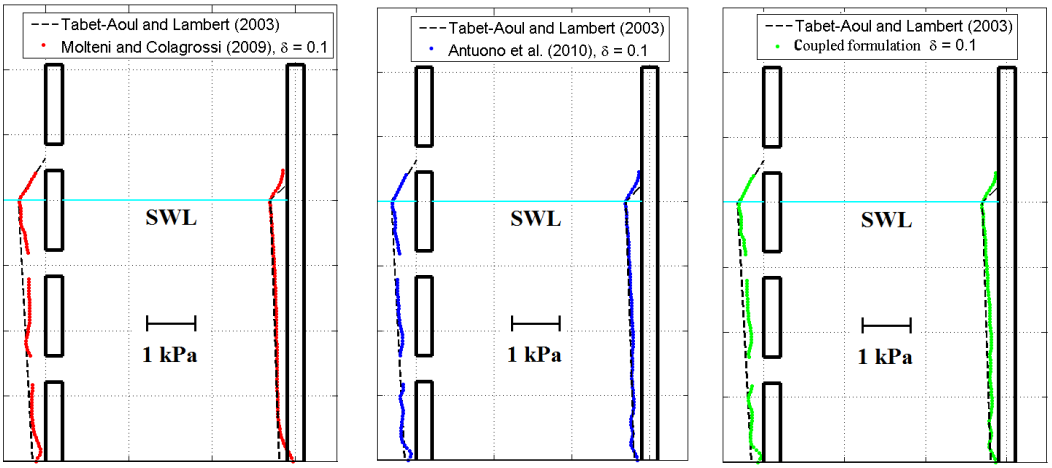

Figure 5.27: *Comparison of spatial pressure distribution between the diffusive models of [104] and [6] with the automatic hybrid (coupled) formulation.*

5.3.2 Wave reflection at a partially perforated breakwater

The adopted SPH model was applied here to investigate the wave reflection induced by the interaction between regular wave trains and a partially perforated breakwater, where the water depth within the chamber, h_c, is lower than outside. This kind of perforated breakwater provides an additional weight to the lower part of the caisson, resulting in an improvement in its structural stability in comparison with a fully perforated one (see Suh et al. [145]).

The dimensions of the computational domain are reported in Fig. 5.28, in which d = 0.4 m, h_c = 0.2 m and L_c = 6 m. The chamber width, B, is changed in a range of values for the SPH simulations in order to optimize the perforated caisson in terms of reduction of the wave reflection in front of it. The porosity of the slotted wall is μ = 0.2. The solid structure of the partially perforated breakwater is modeled with a combination of one-node and multi-node fixed ghost particles, as similarly illustrated in the representative sketch in Fig. 5.18 for the case of the fully perforated breakwater. The height of the solid elements of the slotted wall is $d1$ = 0.112 m, while the height of the holes is $d2$ = 0.028 m.

Also in this case, the initial spatial resolution has been driven by the presence of the thin perforated wall, characterized by width s = 0.016 m, so that $\Delta x = s/4$ = 0.004 m. The computational time for 12 s is equal to 26.3 h, adopting a single 3.4 GHz Intel(R) i7-3770 core with 8GB RAM. The same simulation performed by one-node fixed ghost particles implies a value of $\Delta x = s/8$ = 0.002 m and a computational time equal to 118.2 h. In this context, the use of multi-node fixed ghost particles gives a reduction in the computational time equal to about 77.7%.

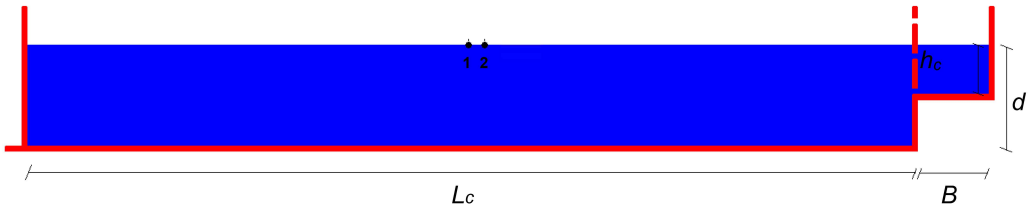

Figure 5.28: *Computational domain with characteristic dimensions adopted for the simulations (the numbers 1 and 2 refer to the position of the wave gauges adopted to perform the analysis of wave reflection)*

The physical process dealing with the energy dissipation effect induced by the interaction between incoming waves and perforated-type breakwaters is usually quantified by the evaluation of the reflection coefficient, K_r. This parameter, as expressed in section 5.1, is defined as the square root of the ratio between reflected and incident wave energy (see Goda [63]). The time series of η are calculated with SPH at different spatial locations along the wave flume through wave gauges and are considered for the calculation of the values of K_r. Specifically, the diffusive term by [6] is implemented for these SPH simulations due to its ability to accurately model the free-surface oscillations because of the presence of the renormalized density gradients which act to regularize the wave profile, as also verified by the same authors (Antuono et al. [5]) in simulating the propagation of linear and non-linear waves. Therefore, the simulated time series of η are used to perform a separation between incident and reflected waves.

The channel length is here chosen to be greater than the previous test case in order to determine a sufficient number of waves and assess the wave reflection processes of the considered breakwater. Here, the SPH simulations are carried out using small waves with T = 1 s and varying the value of the chamber width. Attention is paid to remove the unphysical re-reflected waves at the section of the considered numerical gauges in the analysis. Through a sensitivity analysis, a minimum number of about 10 waves has been considered sufficient for applying a wave reflection method in order to calculate the values of K_r. However, for a more accurate analysis of wave reflection at a perforated breakwater with SPH, an active absorption system (in SPH context, see *e.g.* Liu et al. [88]) proves to be necessary to simulate the involved physical process in a larger range of wave conditions and for a longer time than that adopted in the present SPH model. Even if an active absorption wavemaker in several SPH models is lacking, it is, however, possible to note the ability of the involved Lagrangian approach in simulating wave-structure interaction processes (see Altomare et al. [1]).

The frequency domain method by Goda and Suzuki [64] is taken into account to evaluate the reflection coefficient since the reference laboratory experiments by Chen et al. [19] considered the same wave reflection method. In order to obtain reliable results on the assessment of K_r using the adopted wave reflection approach, the general recommendations provided in Goda [63] suggest that the numerical wave gauges should be placed at a distance of more than one wavelength from both the model structure and the wave paddle (see section 5.1). In particular, the suitable application of the method by Goda and Suzuki implies that the ratio between the distance between gauges 1 and 2, λ_{12}, and the wavelength should be chosen so that the upper and lower bounds of

wave frequencies range from 0.05 Hz to 0.45 Hz, and $\lambda_{12} \neq nL/2$, where n = 0, 1, 2,..., to avoid divergences in the wave spectra. On the basis of the above restrictions, we consider λ_{12} = 0.15 m (see Fig. 5.28). As a consequence, the distance between the wavemaker and the first wave gauge is equal to 3 m and the distance between the second wave gauge and the caisson is equal to 2.85 m.

The evaluation of the reflection coefficient is carried out as a function of the relative wave chamber width B/L. This ratio represents the main dimensionless parameter which influences the degree of efficiency of all perforated-type breakwater in terms of energy dissipation of incident waves (*e.g.* Fugazza and Natale [58]). The values of K_r obtained by the present SPH model are compared with experimental data deduced from laboratory tests by Chen et al. [19] adopting 3rd-order Stokes waves, defined by the following pairs of values of height and period: H = 0.08 m and T = 1 s, H = 0.1 m and T = 1 s, and H = 0.12 m and T = 1 s, with corresponding values of B/L = 0.1, 0.133 and 0.2. Moreover, the SPH model is used to perform additional numerical simulations to find a more accurate feature of K_r as a function of B/L. Indeed, with regards to the reference experimental data [19], the optimal feature of the reflection coefficient was not illustrated for the considered partially perforated breakwater in the above wave conditions. In the SPH simulations, changing the chamber width of the caisson with a spatial step equal to 0.01 m, a more refined dependence of K_r on B/L was found with reference to the experimental range 0.1 < B/L < 0.2 [19]. This range is of practical interest in the engineering applications due to the constructional limits in the chamber width of a perforated caisson [72].

Fig. 5.29 shows the comparisons on the reflection coefficient, K_r, as a function of B/L, between laboratory experiments of Chen te al. [19] and SPH simulations deduced from the application of the method by Goda and Suzuki [64]. An overestimation of K_r obtained by SPH can be observed for B/L = 0.133. The variation of wave characteris-

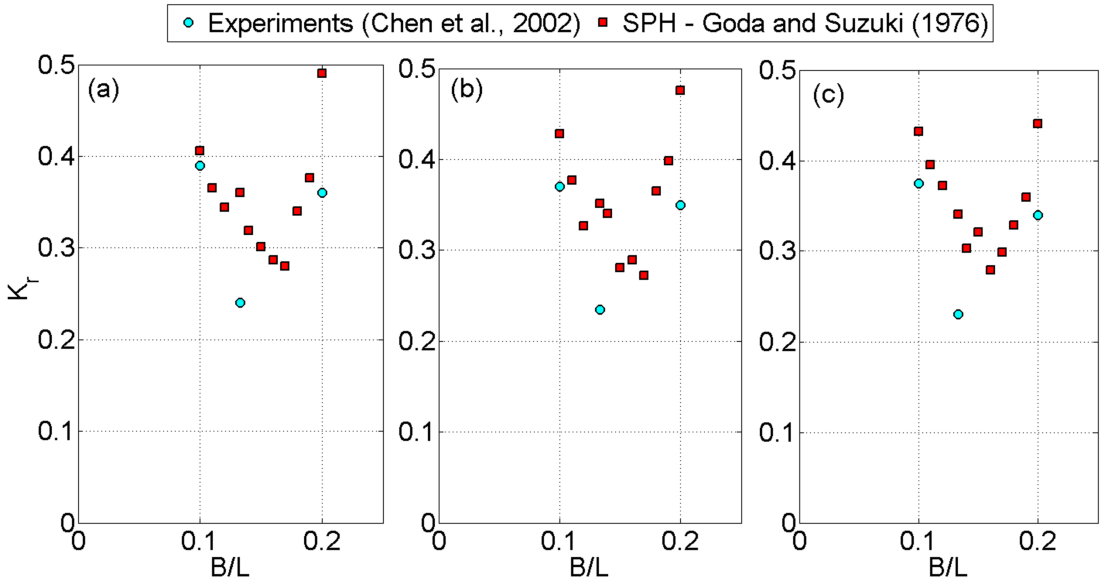

Figure 5.29: *Reflection coefficient, K_r, vs. B/L: comparison between laboratory experiments (Chen et al. [19]) and SPH through the method by [64]. (a) H = 0.08 m, T = 1 s, (b) H = 0.1 m, T = 1 s, (c) H = 0.12 m, T = 1 s.*

tics through the change of the incident wave height, represented by an increase in wave steepness, H/L, does not seem to provide a significant variation in the values of K_r, as also noticeable in the reference laboratory data [19]. Through the additional SPH simulations, it is possible to observe a general decrease of K_r within the experimental range of B/L. The minimum values of reflection coefficient occur between B/L = 0.16 and 0.17. On the basis of the simulated values of K_r in the range $0.1 < B/L < 0.2$, a quadratic relationship between K_r as a function of the main parameter influencing its variation, B/L, can be obtained:

$$K_r = 56.71 \left(\frac{B}{L}\right)^2 - 16.97 \left(\frac{B}{L}\right) + 1.57 \tag{5.19}$$

where the correlation coefficient R^2 = 0.857.

SPH results referred to the evaluation of the minimum reflection coefficient occurring at $B/L = 0.16 \div 0.17$ for $h_c/d = 0.5$ prove to be in agreement with the experimental and numerical results obtained by Suh et al. [145]. In the latter case, the authors adopted a partially perforated breakwater characterized by a composite mound and vertical slots in its front face and they determined that the value of K_r was minimized at $B/L = 0.177$ for $h_c/d = 0.65$. For a partially perforated breakwater with a chamber filled with a submerged rock core, the numerical results by Liu et al. [89] found that the minimum value of K_r corresponds to $B/L = 0.15$ for $h_c/d = 0.5$. For the adopted wave conditions (H = 0.08 m and T = 1 s, H = 0.1 m and T = 1 s, H = 0.12 m and T = 1 s), the values of Mean Square Error Percent between SPH and the experiments by [19] are equal to about 2% for $B/L = 0.1$, 12% for $B/L = 0.2$ and 23 % for $B/L = 0.133$.

The incident and reflected wave spectra deduced from the application of the method by Goda and Suzuki on the basis of the time series of surface elevations simulated by SPH are described in Fig. 5.30 for a representative test case characterized by H = 0.1 m, T = 1 s and $B/L = 0.133$. As noticeable, the spectral density of the incident wave

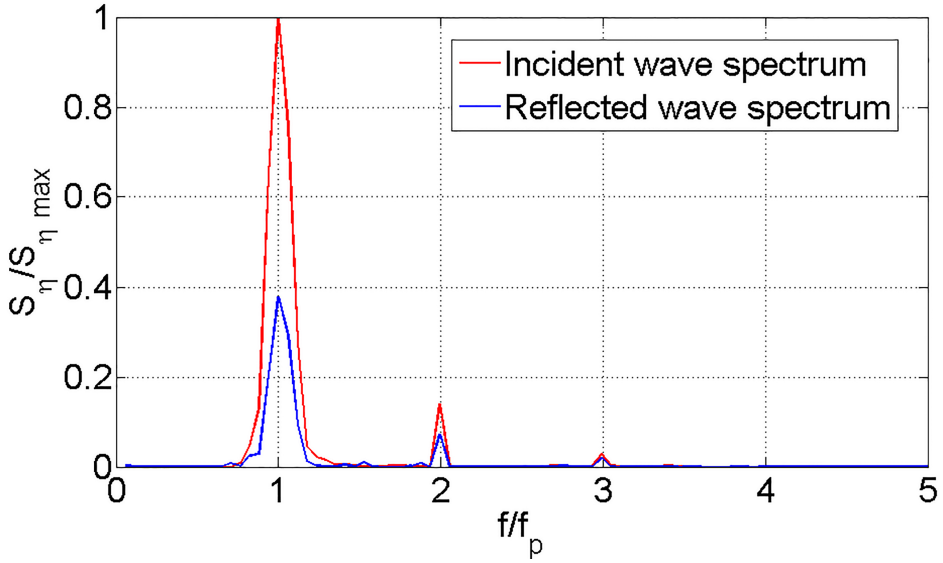

Figure 5.30: *Incident and reflected wave spectrum simulated by SPH using the method by [64] (H = 0.1 m, T = 1 s and $B/L = 0.133$)*

spectrum shows two additional wave harmonics which are, respectively, two and three times the fundamental peak frequency, f_p. The number of wave harmonics are linked to the degree of non-linearity of the surface waves generated by the wavemaker, confirming that third-order Stokes waves are generated in the numerical wave flume. The reflected wave spectrum is characterized by the presence of a reduction in the spectral energy for the fundamental and the secondary wave harmonics. It can be observed that wave reflection methods, based on the use of three wave gauges (*e.g.* Mansard and Funke [94]), could improve the results obtained from experimental and numerical data since they are less sensitive to non-linear wave interaction processes.

CHAPTER 6

Filtering acoustic component in weakly-compressible SPH

6.1 Frequency analysis tools

To disclose the features of a pressure signal obtained from a weakly-compressible SPH simulation, an extremely efficient instrument is furnished by the wavelet analysis. The nature of the problems usually investigated in fluid mechanics context, such as wave impacts, dam breaks, or fluid-structures interaction problems, contains unsteady, impulsive and irregular characteristics that makes the classical Fourier analysis unfruitful for these purposes. In this context, the wavelet analysis represents a capable instrument for the filtering of the acoustic noise of the weakly-compressible solution. In this section, an overview on the most important steps that brought from the Fourier to the wavelet analysis and a description of the main features of wavelets is presented.

6.1.1 From Fourier to wavelets

The Fourier analysis is a well known mathematical tool that allows for the decomposition of a signal into sinusoidal components of different frequencies. This technique proves to be fundamental for the characterization of the energy content in the frequencies domain, by transforming the analyzed function from a time-based point of view to a frequency-based one. The Fourier Transform (FT) of a function $f(t)$ is defined as:

$$\mathcal{T}_F(\omega) = \int_{\Re} f(t) e^{-i\omega t} dt. \tag{6.1}$$

In recent years, investigations from researchers in different field of study and with different backgrounds have been addressed to determine a different way for decomposing a generic function in the frequency domain. The necessity of exploring this frontier

has been essentially motivated because of the difficulty in the Fourier space to analyze signals with certain characteristics. Indeed, since the constitutive elements of the FT are trigonometric functions, the result is that the Fourier analysis is non local, due to their space-filling nature. In other words the FT is suitable only for analyzing stationary signals, *i.e.* signals whose properties do not change with time. The FT is therefore a powerful tool for processing signal that can be expressed as a sum of sines and cosines, but becomes less useful when the signal is non-stationary. Moreover when transforming to the frequency domain with the FT, time information is lost and it is impossible to know the instant when a particular event appears.

A first attempt to overcome these limitations has been presented in 1946 by Gabor [59], by adapting the Fourier Transform only to a small section of the signal time by time, introducing a technique known as Short-Time Fourier Transform (STFT). With this "windowing" approach the signal is represented into a two-dimensional function of time and frequency. The STFT hence yields information about both frequency and time, allowing for the identification of when and at which frequency a specific event occurs. In the STFT, however, the size of the considered window for the Fourier Transform is the same for all the frequencies, constraining therefore the analysis of both high and low frequencies to the same time interval. The successive step has been the adoption of a flexible time windowing, by adapting the window size to the analyzed frequency: for low frequencies larger time windows, while for high frequencies smaller ones. This mathematical framework is today known as wavelet analysis.

The concept of wavelet has been first introduced in the early 1980s by Jean Morlet, a geophysicist working on seismic data analysis, by directly translating from french the word *ondelette*, small wave (see *e.g.* [116], [117]). The successive collaboration between Grossmann and Morlet [69] led to the mathematical foundation of the wavelet transforms with their possible applications. Only a year later it became clear that the Morlet and Grossmann's work rediscovered the same concepts obtained some decades before by Calderon [18] in the harmonic analysis, a pure theoretical field apparently disjointed from the Fourier analysis. Since then the interest of the scientific community towards this new subject have had an increasing interest with remarkable contributions. A detailed presentation of the mathematics of wavelets can be found in the works of Daubechies [38], Chui [24] and Mallat [93].

6.1.2 Wavelet Transform

In the wavelet framework the basic functions present a limited spatial support, allowing for a local analysis of the signal. The localized functions used for the transform are obtained by scaling and shifting a basic function, called *mother wavelet*, ψ:

$$\psi_{ab}(t) = \frac{1}{\sqrt{a}}\psi\left(\frac{t-b}{a}\right), \tag{6.2}$$

where $a \in \Re^+$ is the parameter to scale in frequency the wavelet, while $b \in \Re$ is the parameter to shift in time the wavelet. The Wavelet Transform (WT) of a function $f(t)$ is thus defined as:

$$\mathcal{T}_W(a,b) = \frac{1}{\sqrt{a}}\int_{\Re} f(t)\psi\left(\frac{t-b}{a}\right)dt. \tag{6.3}$$

A mother wavelet can be adopted for the integral wavelet transform only if it presents an inversion formula. This property is expressed by the *admissibility condition*:

$$C_\psi = \int_{\Re} |\mathcal{T}_F(\psi)|^2 \frac{d\omega}{|\omega|} < \infty, \tag{6.4}$$

where $\mathcal{T}_F(\psi)$ represents the FT of the mother wavelet. The finiteness of the constant C_ψ limits in the class of $L^2(\Re)$ the functions that can be adopted as basic wavelets in the definition of the WT. From Eq. 6.4 follows that the condition necessary for C_ψ not to diverge is $\mathcal{T}_F(\psi(0)) = 0$, that is the mean value of the wavelet has to be equal to zero:

$$\int_{\Re} \psi(t)dt = 0. \tag{6.5}$$

The time localization property is mathematically expressed by the fact that the mother wavelet function has to belong to $L^1(\Re)$, meaning that:

$$\int_{\Re} |\psi(t)|\, dt < \infty. \tag{6.6}$$

Differently from Fourier, in the wavelet analysis there exist many different families of mother wavelets that can be adopted for the signal decomposition, *i.e.* wavelets functions that satisfies the conditions expressed by Eqs. 6.5 and 6.6. In this framework, the choice of the mother wavelet is therefore case-dependent and also varies on the specificity of the analyzed problem. The criterion of the choice of a wavelet function is generally obtained as the wavelet shape that better approximates the original signal.

In fluid dynamic context the wavelets analysis has been widely applied to study coherent structures in turbulence fields. After the reference work presented in 1992 by Farge [53], many improvements and analyses on this subject have been developed regarding the extraction of coherent vortexes (see *e.g.* [132], [136]). Wavelet analysis of turbulent flows is particularly useful because is able to identify localized regions of energy concentration and the distribution of energy at the scales of observations. As pointed out by Farge [53], the choice of the mother wavelet has to be performed on the basis of the mathematical structure that better resembles the coherent structures of the vortexes, but the problem that still persists in turbulence theory is that the typical objects that compose a turbulent field have not yet clearly identified. Upon this premise, among the broad possibility of options of wavelet functions, Farge [53] adopted the Morlet wavelet for the analysis of turbulence. As the same author expressed, a "naive" reason for this choice is due to the fact that the Morlet wavelet recalls the shape of Tennekes and Lumley's eddy [149] proposed to model turbulence, and of some coherent structures whose existence had been conjectured by other scientists. The Morlet wavelet is represented by a plane wave modulated with a Gaussian function:

$$\psi(t) = e^{\left(-t^2/2\right)} e^{(ik_M t)} \tag{6.7}$$

The shape of Morlet wavelet is represented in Fig. 6.2 (a), where $k_M = 4$. Another wavelet function often used in fluid dynamic context is the Marr wavelet, also known for its shape as Mexican hat, mathematically expressed by the negative Laplacian of a Gaussian function:

$$\psi(t) = (1 - t^2) e^{\left(-t^2/2\right)} \tag{6.8}$$

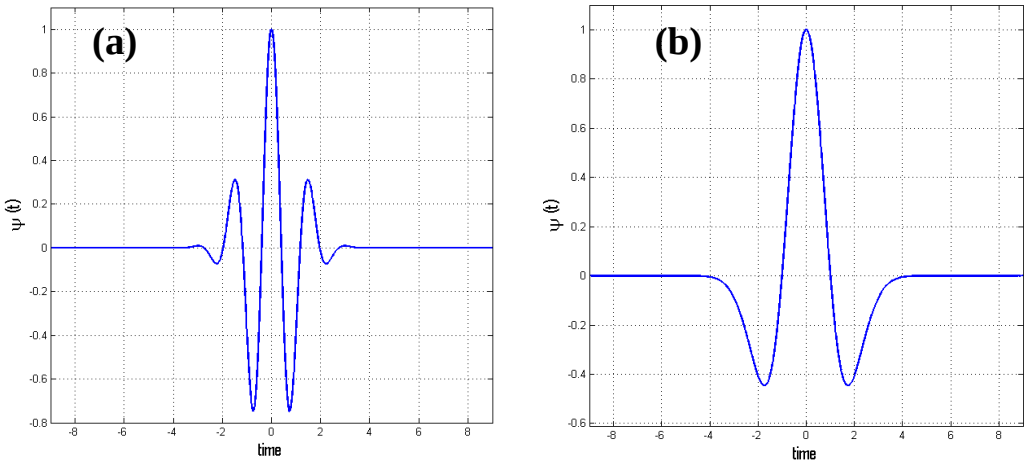

Figure 6.1: *Presentation of wavelet shapes: (a) Morlet with k_M=4; (b) Mexican hat. This last mother wavelet is adopted for the successive analysis.*

The shape of Mexican hat wavelet is represented in Fig. 6.2 (b).

Wavelets have been used for analysis in different fluid dynamic contexts, such as atmospheric sciences (see *e.g.* [46]), computational fluid mechanics (see *e.g.* [135]), analysis of the tsunami properties (see *e.g.* [123]) and random free surface wave trains (see *e.g.* [84]). Regarding the investigation about pressures and forces, Wang et al. [153] used the Wavelet Transform to analyze time-variant features of flow-induced forces in the time frequency domain occurring at the flow interference between two side-by-side stationary cylinders. In the present analysis the attention is focused on the pressure signals obtained from weakly-compressible SPH simulations. Both Morlet and Mexican hat wavelet have been tested in this context, resulting for the latter to be more appropriate in representing the time variation of pressure usually encountered in fluid mechanics context, especially when rapid changes in the fluid dynamic occur. For this reason the Mexican hat wavelet has been chosen for the successive analysis.

6.2 The acoustic problem

For a deeper understanding of the pressure noise issue in the weakly-compressible SPH solution the hydrodynamic/acoustic splitting method offers a diverse perspective. As it has been shown by different authors (see *e.g.* [142], [121], [137]) in the limit of $\mathrm{Ma} \to 0$ the flow variables for the weakly-compressible solution can be written as sum of an incompressible solution and an acoustic perturbation:

The physical superposition of these two components is at the core of the following analysis. The pressure signal is analyzed in the wavelet domain in which the frequencies of the acoustic pressure perturbation are identified. The WT therefore allows to

filter these quantities in order to obtain the incompressible solution from the original weakly-compressible one.

In this section it is firstly shown how the instantaneous total flow variables are decomposed into incompressible and perturbed compressible variables and then how these acoustic perturbations affect the weakly-compressible solution. For this purpose, the quantities of interest for the considered problem are split as:

$$\rho(\boldsymbol{r},t) = \rho_0 + \rho'(\boldsymbol{r},t) \tag{6.9}$$

$$\boldsymbol{u}(\boldsymbol{r},t) = \boldsymbol{U}(\boldsymbol{r},t) + \boldsymbol{u}'(\boldsymbol{r},t) \tag{6.10}$$

$$p(\boldsymbol{r},t) = P(\boldsymbol{r},t) + p'(\boldsymbol{r},t) \tag{6.11}$$

in which the terms ρ_0, $\boldsymbol{U}$ and P denote the incompressible components, while ρ', $\boldsymbol{u}'$ and p' the acoustic perturbations. Introducing the decompositions expressed by Eqs. 6.9, 6.10 and 6.11 into the continuity and momentum Eqs. 2.1, results in:

$$\begin{cases} \dfrac{\partial \rho'}{\partial t} + (\boldsymbol{U}\cdot\nabla)\,\rho' + \rho_0 \nabla\cdot\boldsymbol{u}' = 0 \\ \\ \dfrac{\partial \boldsymbol{u}'}{\partial t} + (\boldsymbol{U}\cdot\nabla)\,\boldsymbol{u}' + (\boldsymbol{u}'\cdot\nabla)\,\boldsymbol{U} + \dfrac{1}{\rho_0}\nabla p' = 0 \end{cases} \tag{6.12}$$

in which no viscous effects and external forces, $\boldsymbol{g}$, are taken into account. Eqs. 6.12 are obtained after rewriting the total derivative as $D/Dt = \partial/\partial t + \boldsymbol{u}\cdot\nabla$, and neglecting non-linear terms, such as $\boldsymbol{u}'\cdot\nabla\boldsymbol{u}'$.
As shown by Seo and Moon [137], it is possible to rewrite:

$$(\boldsymbol{U}\cdot\nabla)\,\boldsymbol{u}' + (\boldsymbol{u}'\cdot\nabla)\,\boldsymbol{U} = \nabla\,(\boldsymbol{u}'\cdot\boldsymbol{U}) + \boldsymbol{\Omega}\times\boldsymbol{u}' + \boldsymbol{\omega}\times\boldsymbol{U} \tag{6.13}$$

where $\boldsymbol{\Omega} = \nabla\times\boldsymbol{U}$ and $\boldsymbol{\omega} = \nabla\times\boldsymbol{u}'$. The last two terms in the right side of Eq. 6.13 are not responsible for sound generation at low Mach numbers and thereby can be neglected to avoid the generation of perturbed vorticity. Eqs. 6.12, considering Eq. 6.13 and neglecting the vorticity terms, becomes:

$$\begin{cases} \dfrac{\partial \rho'}{\partial t} + (\boldsymbol{U}\cdot\nabla)\,\rho' + \rho_0 \nabla\cdot\boldsymbol{u}' = 0 \\ \\ \dfrac{\partial \boldsymbol{u}'}{\partial t} + \nabla\,(\boldsymbol{u}'\cdot\boldsymbol{U}) + \dfrac{1}{\rho_0}\nabla p' = 0 \end{cases} \tag{6.14}$$

Eqs. 6.14 represent the *linearized perturbed compressible Navier-Stokes equations* and have to be considered along with the state equation, $p' = c^2\rho'$. In order to calculate the acoustics, the incompressible components are subtracted from Eqs. 6.14, obtaining thus:

$$\begin{cases} \dfrac{\partial \rho'}{\partial t} + \rho_0 \nabla\cdot\boldsymbol{u}' = 0 \\ \\ \dfrac{\partial \boldsymbol{u}'}{\partial t} + \dfrac{1}{\rho_0}\nabla p' = 0 \\ \\ p' = c^2\rho' \end{cases} \tag{6.15}$$

Taking the divergence from the second equation in System 6.15, and introducing the first equation into that, is possible to obtain:

$$\frac{\partial}{\partial t}\left[-\frac{1}{\rho_0}\frac{\partial \rho'}{\partial t}\right] + \frac{1}{\rho_0}\nabla^2 p' = 0 \tag{6.16}$$

simplifying ρ_0 and using the state equation, Eq. 6.16 becomes:

$$\Delta p' - \frac{1}{c^2}\frac{\partial^2 p'}{\partial t^2} = 0 \tag{6.17}$$

Eq. 6.17 is the canonical D'Alembert equation for the propagation of waves. Therefore in the compressible Navier-Stokes formulation, acoustic (pressure) waves are contained and the following analysis aims to further study this particular aspect.

In this context the oscillating drop subjected to a central force field, presented in section 4.2 is analyzed as a benchmark case for the acoustic and incompressible decomposition. In this case indeed the analytic (incompressible) solution is well known and the acoustic perturbations are studied through analytical and numerical approaches. In particular, the acoustic of two geometrical configurations assumed during the drop evolution are analyzed, respectively the circular and elliptical shapes. These results are compared with the acoustic noise encountered in the SPH simulation of the drop measured at the center of the domain.

6.2.1 Circular and elliptical patches

The simplest case in which the results from analytical and numerical approaches can be tested is to consider a circular domain, whit radius $R = 1$. In this case, the problem is firstly studied analytically by solving Eq. 6.17, in which null pressure is imposed at the boundary of the domain. Considering a polar coordinates system, $x = r\cos\theta$ and $y = r\sin\theta$, the D'Alembert equation becomes:

$$\begin{cases} \dfrac{\partial^2 p'}{\partial r^2} + \dfrac{1}{r}\dfrac{\partial p'}{\partial r} + \dfrac{1}{r^2}\dfrac{\partial^2 p'}{\partial \theta^2} = \dfrac{1}{c^2}\dfrac{\partial^2 p'}{\partial t^2} \\ \\ p' = 0, \qquad \forall\, r = R \end{cases} \tag{6.18}$$

Since the problem is radially symmetric, the solution does not depend on the angle, θ, therefore the third term on the left side of the Eq. 6.18 can be neglected. The solution of Eq. 6.18 can be found considering separated variables, $p'(r,t) = q(t)P(r)$, in which $q(t)$ is a function only of time, while $P(r)$ is a function only of the spatial position. Substituting this quantity and dividing for $q(t)P(r)$, Eq. 6.18 becomes:

$$\frac{1}{P(r)}\left[\frac{\partial^2 P(r)}{\partial r^2} + \frac{1}{r}\frac{\partial P(r)}{\partial r}\right] = \frac{1}{c^2 q(t)}\frac{\partial^2 q(t)}{\partial t^2} \tag{6.19}$$

Since the left side of Eq. 6.19 depends only on r, while the right side depends only on t, both sides have to be equal to the same constant k, obtaining thus:

$$\frac{d^2 q(t)}{dt^2} = kc^2 q(t) \tag{6.20}$$

$$\frac{d^2 P(r)}{dr^2} + \frac{1}{r}\frac{dP(r)}{dr} = kP(r) \tag{6.21}$$

The solution for Eq. 6.20 is:

$$q(t) = q_0 e^{\lambda c t} \tag{6.22}$$

where q_0 is a constant, while $\lambda = \sqrt{-k}$.

The solution for Eq. 6.21 is instead obtained, as a linear combination of *Bessel functions* of zeroth-order, resulting in:

$$P(r) = p_1 J_0(kr) + p_2 Y_0(kr) \tag{6.23}$$

in which the Bessel function Y_0 is singular for $r = 0$, resulting in this case in an unphysical solution. The constant p_2, therefore has to be equal to zero, while the first constant is assumed to be unitary, $p_1 = 1$. This quantity is therefore incorporated in the constant q_0 and only defines the magnitude of the vibrations. Imposing the boundary condition to Eq. 6.23, it is possible to obtain:

$$P(r = 1) = J_0(k) = 0 \tag{6.24}$$

The solution to this equation is furnished by the roots of the Bessel function J_0. In particular, there exist infinite solutions for the Bessel function, given by the eigenvalues of the differential problem, that correspond to the vibration modes of an elastic circular domain. For the case of interest J_0, the first roots are given in Table 6.1.

k_{01}	2.405
k_{02}	5.520
k_{03}	8.654
k_{04}	11.792
k_{05}	14.931
k_{06}	18.071
k_{07}	21.212
k_{08}	24.352
k_{09}	27.496
k_{010}	30.636

Table 6.1: *First vibration modes of the circular domain, i.e. first roots k_{0n} of the Bessel function, J_0.*

The solution to the problem is therefore obtained as the product of Eq. 6.22 with Eq. 6.23:

$$p'(r,t) = \sum_{n \in \mathbb{N}} q_0 \, e^{\lambda_n c t} J_0(k_{0n}, r) \tag{6.25}$$

in which $\lambda_n = \sqrt{-k_{0n}}$. The vibration modes presented in Table 6.1 are related to the vibration frequencies of the circular domain through the speed of sound adopted, as $f_n = k_{0n} c / 2\pi$.

It is noticed that in a problem in which no radial symmetry is encountered, the third term in Eq. 6.18 has to be taken into account. The solution to this problem is given by a combination of m-th orders Bessel functions, $J_{m,n}$, in which $m, n \in \mathbb{N}$. Bessel functions with $m > 0$ corresponds, in fact, to non-symmetrical radial vibration of the circular domain.

The considered problem is now studied by means of the numerical method. In this case a circular domain is initialized with a uniform null pressure field and only the center of the domain is excited with a Dirac pressure impulse:

$$p_0 = a \, \delta(0,0) \qquad \text{for } t = 0, \tag{6.26}$$

in which a defines the magnitude of the perturbation. The pressure perturbation propagates in the circular domain, as it can be seen in Fig. 6.2, in which the pressure field is presented for a generic time instant. The pressure evolution is evaluated at the center of

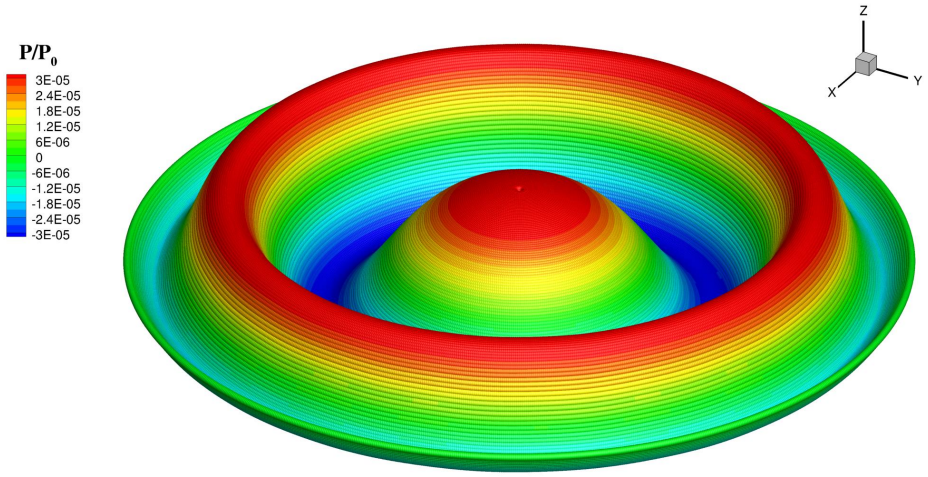

Figure 6.2: *Simulation of pressure field at a generic time instant, for the considered circular patch, after the pressure impulse is given at the center of the domain.*

the circle and is studied in the frequency domain. Specifically, Fig. 6.3 shows the FT of the signal, in which are also highlighted, in dashed vertical lines, the frequencies of vibration of the circular domain found analytically, related to the roots, k_{0n}, of the Bessel function, J_0. As it is possible to see the frequencies of the peaks found numerically correspond to the frequencies found analytically, confirming that the pressure oscillations are indeed acoustic perturbations. The different height of the peaks, occurring for different frequencies, is dependent instead on the specific initial perturbation used to excite the problem.

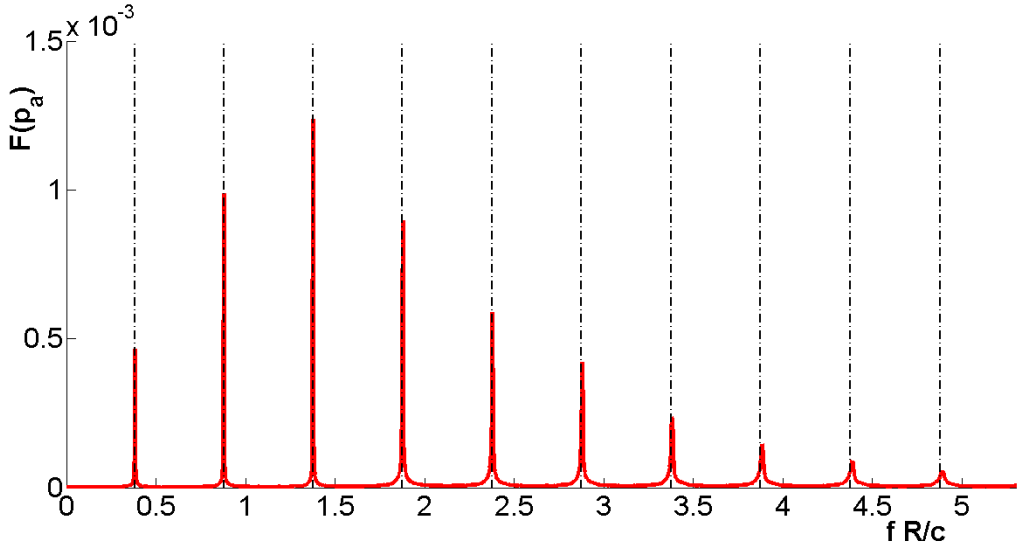

Figure 6.3: *FT of the pressure signal measured at the center of the circle. The vertical dashed lines represent the frequencies related to the roots of the Bessel function, k_{0n}, shown in Table 6.1.*

The analysis of the vibration modes is carried out also for an elliptic domain. Differently from the circular patch problem, in this case it is not straightforward to write the explicit analytical solution for the Eq. 6.17. For this reason the problem is only studied numerically. The geometry of the ellipse is chosen as the configuration related to the maximum elongation of the oscillating drop, as presented in Fig. 4.9. As for the previous case, the domain is initialized with a uniform null pressure field and a Dirac impulse, Eq. 6.26, is given at the center of the elliptic patch. Fig. 6.4 shows the pressure perturbation propagating in the elliptic domain in a generic time instant.

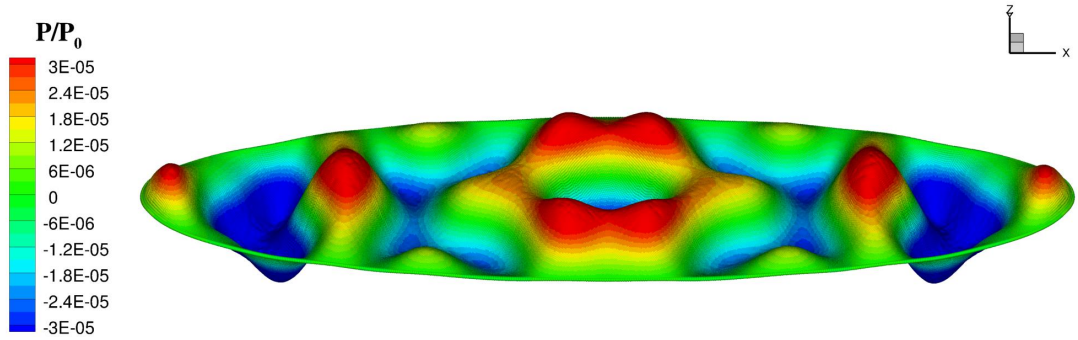

Figure 6.4: *Simulation of pressure field at a generic time instant for the considered elliptic patch, after an initial pressure impulse is given at the center of the domain.*

The energy contents in frequency domain related to the pressure evolution at the center of the ellipse, are displayed in Fig. 6.5. The frequencies where the energy peaks appear correspond to the vibration modes, k_n, of the elliptic domain and are represented in Table 6.2. Due to the non symmetrical configuration of the elliptical patch, the energy peaks occur at frequencies which are not equispaced with respect to the circular case.

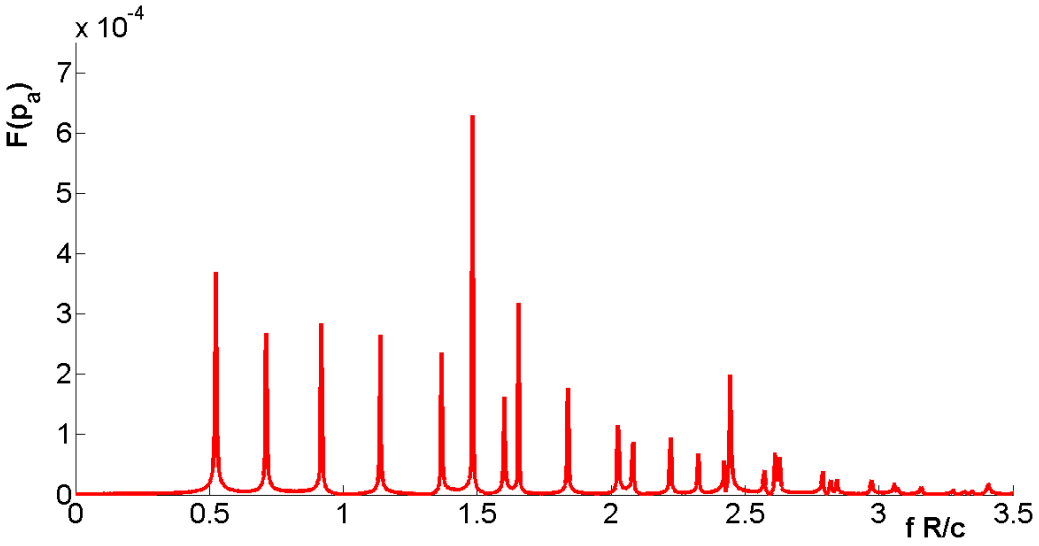

Figure 6.5: *FT of the pressure signal evaluated at the center of the ellipse.*

k_{01}	3.299
k_{02}	4.476
k_{03}	5.765
k_{04}	7.147
k_{05}	8.592
k_{06}	9.315
k_{07}	10.053
k_{08}	10.398
k_{09}	12.723
k_{10}	13.084

Table 6.2: *First vibration modes, k_n, for the elliptic domain found numerically.*

6.2.2 Oscillating drop

In this section the wavelet filtering of the acoustic component for the problem of the oscillating drop subjected to a central force field, shown in section 4.2.2, is presented. Fig. 6.6 shows the wavelet transform of the analytic solution of the time variation of pressure at the center of the drop, presented in Fig. 4.10. The result is shown only

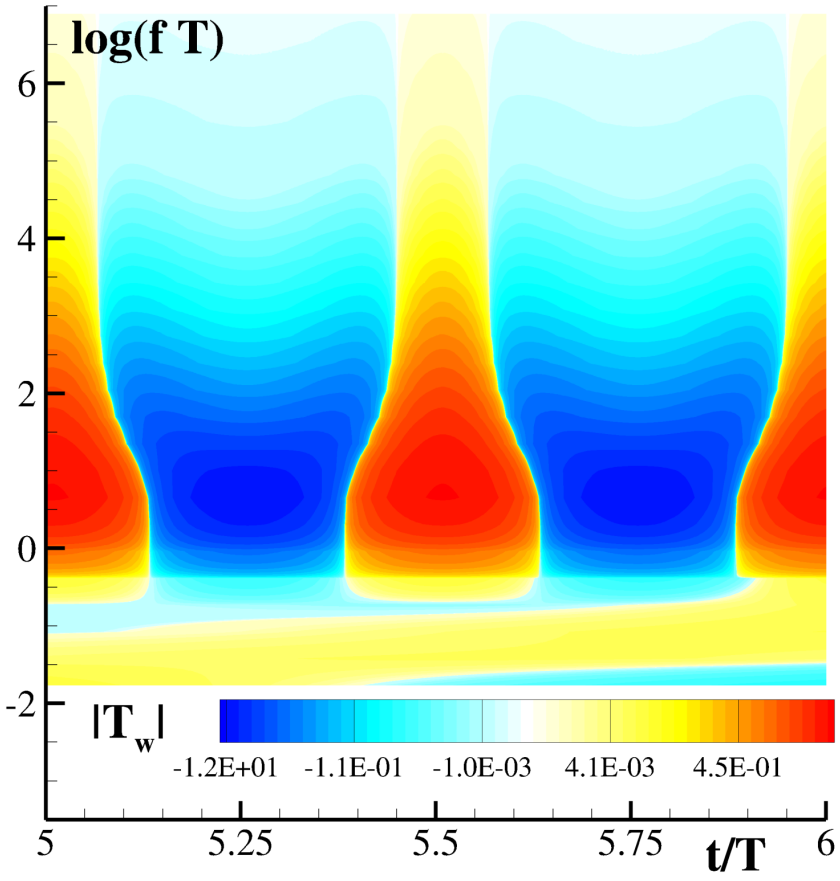

Figure 6.6: *Wavelet transform of the analytic solution for pressure evolution at the center of the oscillating drop, presented in Fig. 4.10, for one period of the evolution.*

for one period of the oscillations. High positive values for the wavelet coefficients means high correlation between the analytic signal and the wavelet that oscillates at the considered frequency. Conversely, high negative wavelet coefficients means that the analytic signal is highly uncorrelated with the wavelet function, *i.e.* the signal and the wavelet are in antiphase. Null coefficients are instead encountered when there is no correlation between the wavelet and the signal, meaning that the signal does not contain energy at the corresponding frequency. On the basis of these considerations, it is possible to see in Fig. 6.6 that the analytic solution is contained at a low frequency range, while the energy content for high frequencies is almost zero being the residual essentially due to numerical issues of the discrete wavelet transform.

The wavelet transform is applied to the SPH numerical result. The standard SPH, with $R/\Delta x = 200$, shown in Fig. 4.10 (a), is taken into account. Fig. 6.7 shows the wavelet transform of the pressure oscillation obtained from SPH, for the same time window presented for the analytical solution. As it is possible to see, the acoustic noise of the SPH solution is encountered in the range of high frequencies. In this case in fact, to proceed with the wavelet filtering, a threshold frequency, f^*, is identified

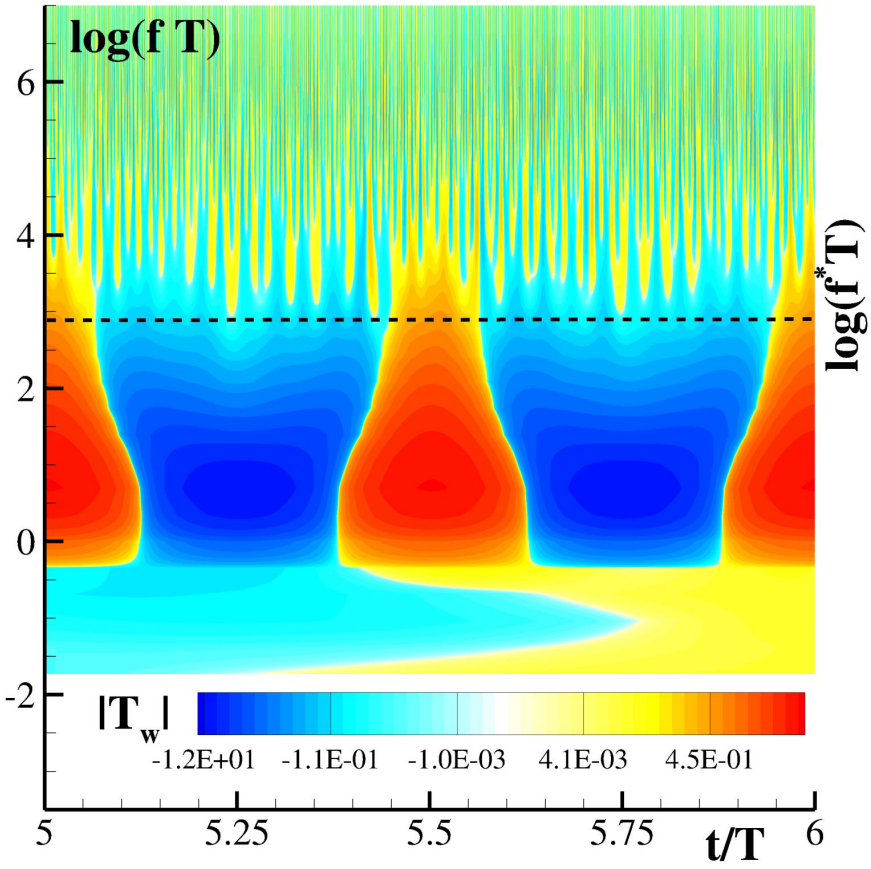

Figure 6.7: *Wavelet transform the pressure evolution at the center of the oscillating drop obtained by standard SPH solution with $R/\Delta x$=200, presented in Fig. 4.10 (a). The horizontal dashed line corresponds to the cut-off frequency, f^*.*

in the wavelet plane. This threshold frequency corresponds to a value higher than the frequencies related with the analytic solution but lower than those in which the acoustic perturbations arise in the numerical solution.

In the wavelet analysis the energy content related with frequencies higher than f^* are therefore cut and the inverse wavelet transform is used to reconstruct the signal without these acoustic contributions. In particular, Fig. 6.8 shows the superposition of the original SPH signal with the one filtered of the high frequencies through the wavelet transform. As it is possible to see, the filtered numerical signal perfectly fits the analytical solution.

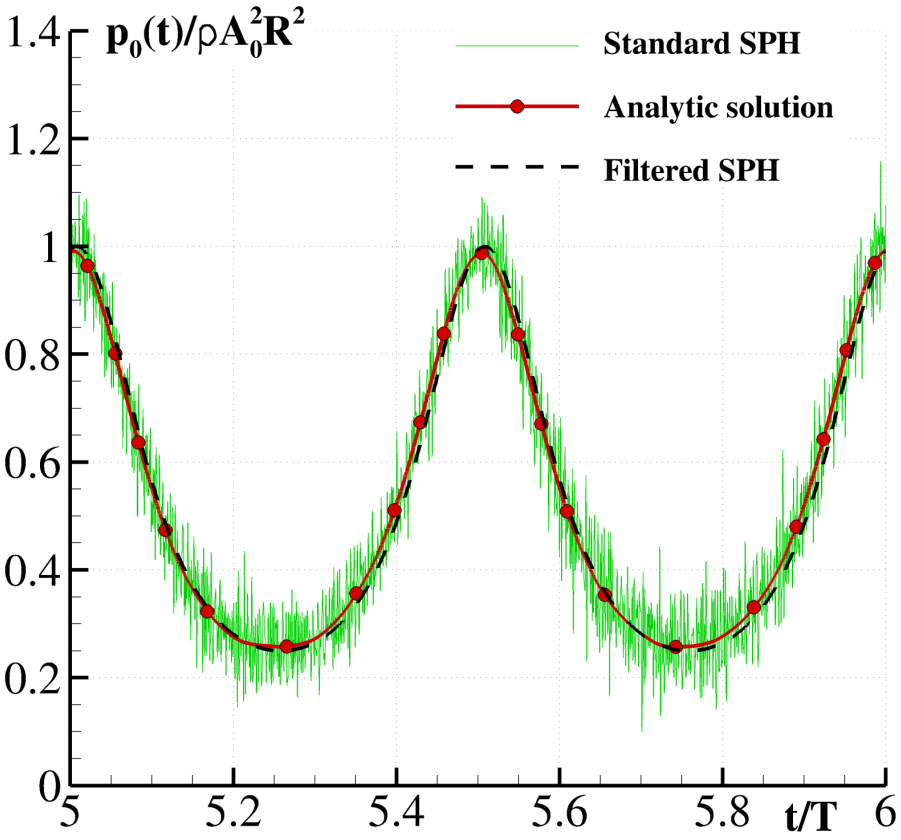

Figure 6.8: *Comparison of the standard SPH signal, analytic solution and inverse wavelet transform in which energy contents related to the acoustic components, $f > f^*$, are cut.*

To better understand the role of the acoustic perturbations in the case of the oscillating drop, a comparison with the results previously obtained for the circular and elliptical domains is presented. Differently from the latter cases, in which the fluid domain does not undergo deformations, the problem of the oscillating drop is characterized by a periodic evolution of the fluid domain from a circular shape, into ellipses with different eccentricities. The result is that, for each of the, theoretically, infinite configurations of the drop, the vibration modes associated to it are excited and combined in the resultant acoustic solution. This insight is shown in Fig. 6.9, in which the FT of the acoustic

part of the weakly-compressible solution, obtained as the difference between the original SPH signal and the same one filtered with the WT in correspondence of f^*, is presented. As it is possible to see, the acoustic perturbations present a continuous spectrum instead of localized peaks as in the case of a fixed domain. Considerable energy is encountered in correspondence of the frequency associated to the first vibration mode of the circular domain, $f_{1\,\mathrm{cr}}$, that progressively decreases to the frequency associated to the first vibration mode of the ellipse domain at his maximum elongation, $f_{1\,\mathrm{el}}$. It can be also observed that the value of the cut-off frequency, f^*, chosen for the wavelet transform, results to be effectively lower than the acoustic frequencies. Moreover, the

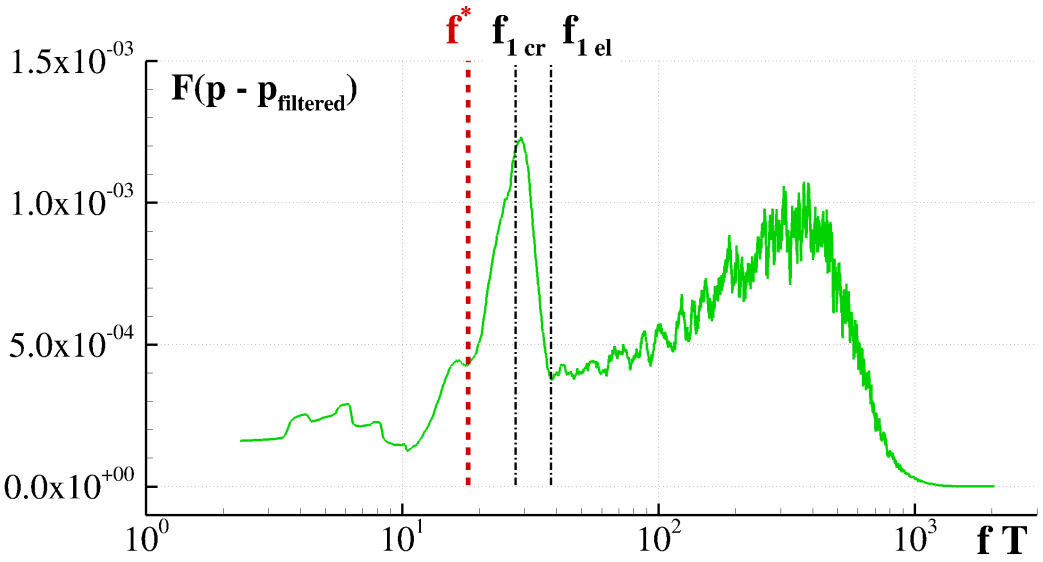

Figure 6.9: *FT of the acoustic component for the pressure at the center of the drop. The dashed vertical lines f_{1cr} and f_{1el} are the frequencies corresponding, respectively, to the first vibration modes of the circular domain and the elliptic domain at its maximum elongation, while f^* is the cut-off frequency adopted.*

fact that the filtering process allowed for a optimal elimination of the acoustic noise is possible because the incompressible (analytical) solution entirely lays in the range of frequencies lower than the cut-off frequency. The incompressible and acoustic components are therefore decoupled and the presented filtering procedure furnishes very good results. In the cases instead of fluid impacts or more impulsive dynamics, the frequencies of the incompressible and acoustic components might belong to the same range, resulting in this case in the impossibility of an effective filtering. These cases are analyzed in the following part of the thesis.

6.3 Water impacts

In this section the wavelet filtering of the acoustic component is applied to pressure signals obtained from water impact problems. The first considered test is a prototype problem introduced in order to reproduce the impact of a water wedge on a vertical wall. In this context, cases characterized by different degrees of impulsiveness are taken into account. The same problem is successively studied with the SPH. In this case the effects

of the spatial resolution on the SPH pressure signal are investigated and the results are compared with the similarity solution by Dobrovol'skaya [45]. The successive analysis regards the pressure signal measured at a wall of a water tank subjected to a sloshing process, in which breaking waves dynamic occur. Also in this case the effect of the spatial resolution is investigated.

6.3.1 Prototype problem

A prototype problem for a wedge impacting a vertical wall is here introduced. As in the case of the oscillating drop prototype (see section 4.2), also the following test is used to highlight specific aspect of the problem. In particular, the aim of this analysis is to examine the capabilities of the wavelet transform in filtering the acoustic part of a pressure signal characterized by different degrees of impulsiveness.

The water wedge considered for the analysis is supposed to be of trapezoidal shape, as shown in Fig. 6.10. The features of the interaction of the wedge with a vertical wall are defined by the horizontal velocity of the fluid mass, U, and by the deadrise angle, α. Specifically, for high values of α the interaction is smooth, while for small values of α the dynamics becomes more impulsive. In the limit $\alpha \to 0$ the impact becomes flat, resulting in a singular condition.

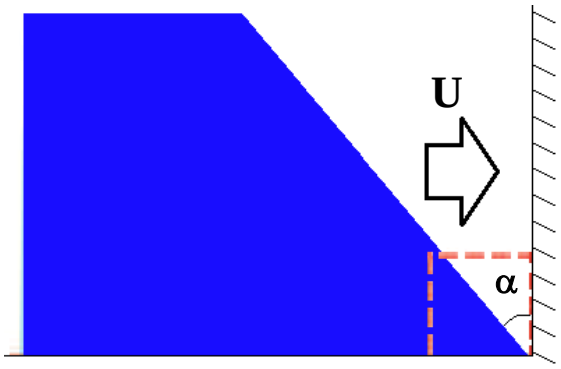

Figure 6.10: *Sketch of the prototype problem: a water wedge impacts a vertical wall with horizontal velocity U and deadrise angle α.*

In this framework, the analysis is carried out for the pressure evolution at a point, P_1, of the vertical wall hit by the trapezoidal water mass. In the specific, the pressure signal is obtained as a superposition of an artificial analytic pressure evolution and an acoustic perturbation. Regarding the analytical component, it is here considered zero for $t < t_0$, and an exponential decay, $P_I(t)/P_{\text{Max}} = e^{-(t-t_0)/\varepsilon} + 0.1$, for $t \geq t_0$. This expression is represented in Fig. 6.11 in which different values for the parameter ε are taken into account. The parameter ε can be seen in this context as a direct measure of the deadrise angle for a considered wedge configuration. Indeed, decreasing the value of ε increases the impulsiveness of the phenomenon, resulting in a a progressive sharpness of the pressure peak, followed by a fast time decay.

The pressure noise is furnished, in this framework, by analyzing the acoustics of a trapezoidal domain, representative of the water wedge configuration after the impact with the vertical wall. As in the previous cases, the vibration modes of the considered geometry are numerically solved by exciting the acoustic waves through a Dirac

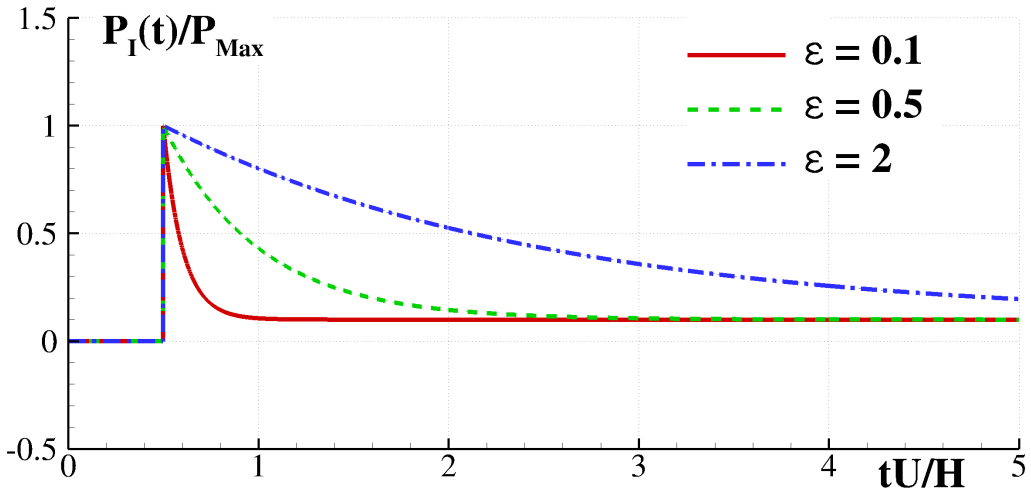

Figure 6.11: *Theoretical pressure peaks and decays for the prototype test case for different values of ε.*

impulse. In Fig. 6.12 is presented the configuration of the analyzed wedge patch, in which the pressure impulse is given at the point P_1. The vibration modes analysis is also performed for the same point of the domain, P_1, and the results are shown in Fig. 6.13, in which the frequencies are referred to a speed of sound adopted for the simulation $c = 25U$.

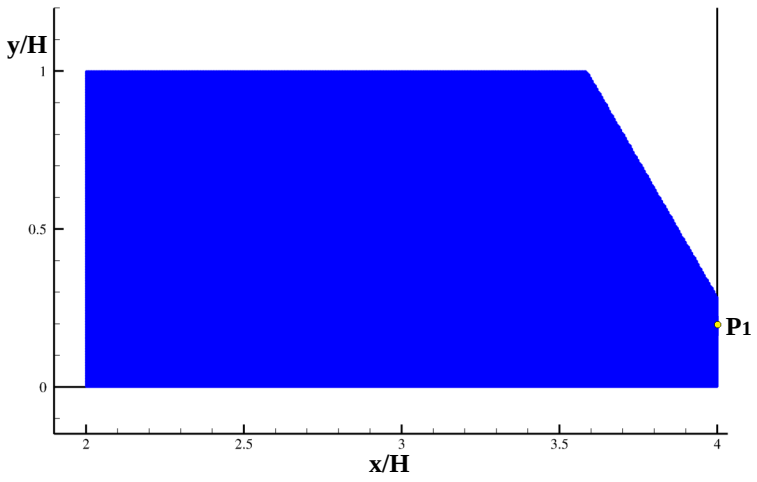

Figure 6.12: *Domain of analysis for the acoustic components for the prototype problem. The pressure impulse and the frequency analysis are performed at the point P_1, in which $y(P_1)$=0.192H.*

The acoustic component is therefore generated as a sum of sinusoidal functions in which the i-th amplitude b_i, frequency f_i and phase ϕ_i are given from the vibration modes analyzed for the point P_1. It is noticed that the amplitudes of the sinusoidal functions are multiplied for the same constant in order to scale the acoustic on the same order of magnitude of the analytical solution. The resulting prototype signal is therefore

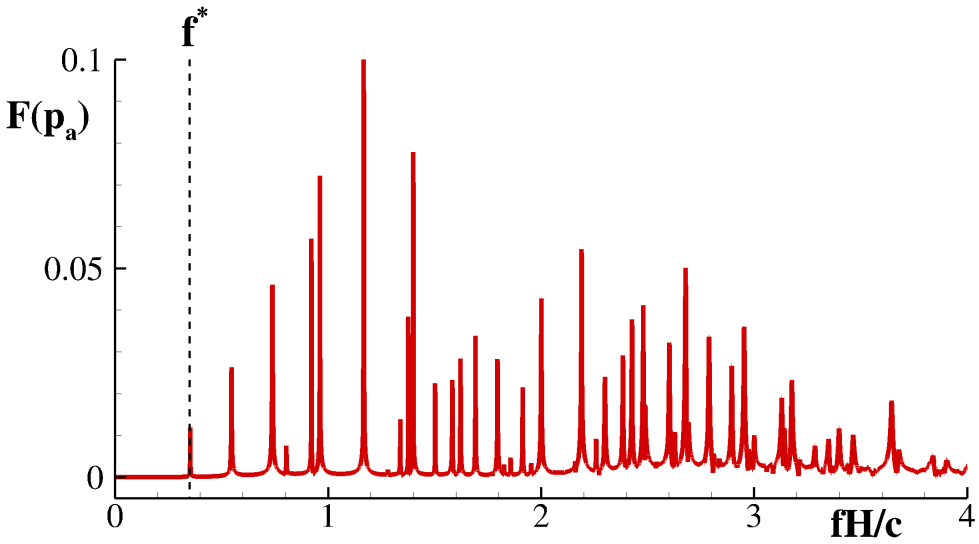

Figure 6.13: *Fourier coefficients of the frequency analysis related to the point P_1. The value of f^* refers to the cut-off frequency adopted for the wavelet filtering.*

obtained as a sum of the analytic expression and the acoustic perturbation:

$$P(t)/P_{\text{Max}} = P_I(t)/P_{\text{Max}} + \sum_i b_i \sin(2\pi f_i t + \phi_i) \tag{6.27}$$

This result is presented, for the considered values of ε, in Fig. 6.14.

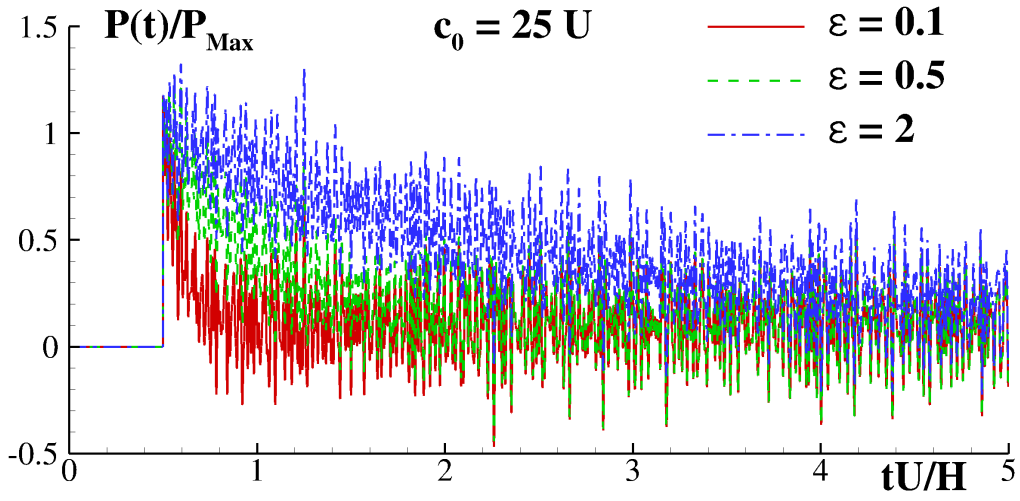

Figure 6.14: *Prototype signal, obtained as a sum of the analytical solution and the acoustic perturbation.*

These results are analyzed in the wavelet domain. In Fig. 6.15 the wavelet transform of the analytic signals shown in Fig. 6.11 are plotted for the cases $\varepsilon = 2.0$ and 0.1. As the dynamics become more impulsive, the energy content goes to higher frequencies. This behavior is highlighted by the dashed line that delineate the area on the wavelet

plan in which the highest energy content is encountered. In Fig. 6.16 is presented the wavelet transform of the prototype problem, presented in Fig. 6.14. In this case it is possible to observe the presence of energy content related with the acoustics in the high frequency regions. As it is shown in Fig. 6.13, the cut-off frequency of the

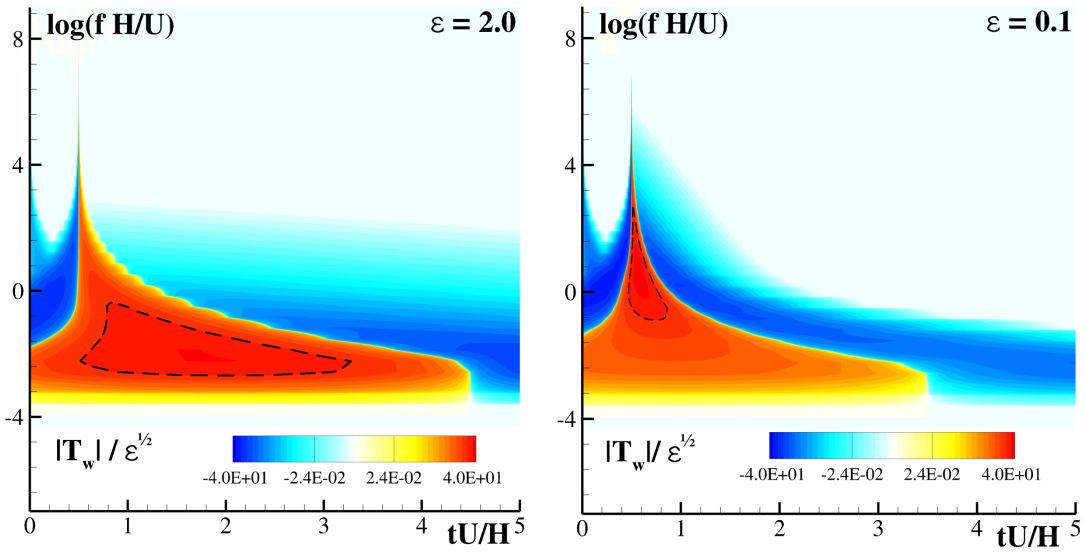

Figure 6.15: *Wavelet coefficients obtained for the analytical solution presented in Fig. 6.15 for the cases* $\varepsilon = 2.0$ *and* 0.1.

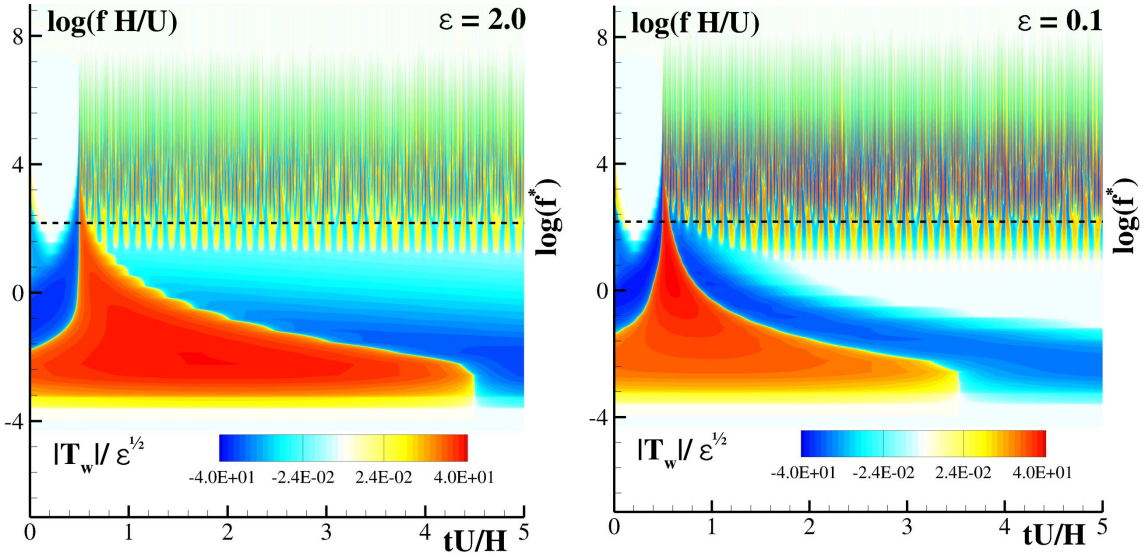

Figure 6.16: *Wavelet coefficients obtained for the prototype problem for the cases* $\varepsilon = 0.1$ *and* 2.0. *The dashed line corresponds to* f^*, *representing the cut-off frequency adopted for the filtering.*

acoustic component for all the analyzed cases is set equal to the frequency associated to the first vibration mode of the trapezoidal domain $f^* = f_{1\,\mathrm{tr}}$. From Fig. 6.16 it is

possible to observe, however, that some energy content of the acoustic component is also present in a range of frequencies lower than the value f^*. This effect is due to the wavelet transform. The use of an operator based on a mother wavelet approximation (with a Mexican hat shape in this case) results in a "diffusion" effect for a signal that is oscillating at a given frequency. This feature presents however practically negligible effects when filtering at the frequency f^*, allowing for a entire removal of frequencies higher than the considered cut-off.

The results presented in Figs. 6.15 and 6.16 clearly show the differences between smooth ($\varepsilon = 2.0$) and impulsive ($\varepsilon = 0.1$) dynamics. In the case of $\varepsilon = 2.0$ the highest energy contents of the analytical solution occur in a frequency range lower than the cut-off frequency. When filtering the perturbed signal at f^* the result allows to accurately recover the analytical solution, as shown in Fig. 6.17. A different situation is encountered when $\varepsilon = 0.1$. In this case considerable energy content associated with the analytic solution of the water impact goes in the acoustic frequency range. The incompressible and acoustic solution live therefore in the same frequency range, resulting in the impossibility to efficiently decouple the problem. As it is possible to see in Fig. 6.17, the result is that the filtered signal for $\varepsilon = 0.1$ results to be also considerably filtered of the analytical component.

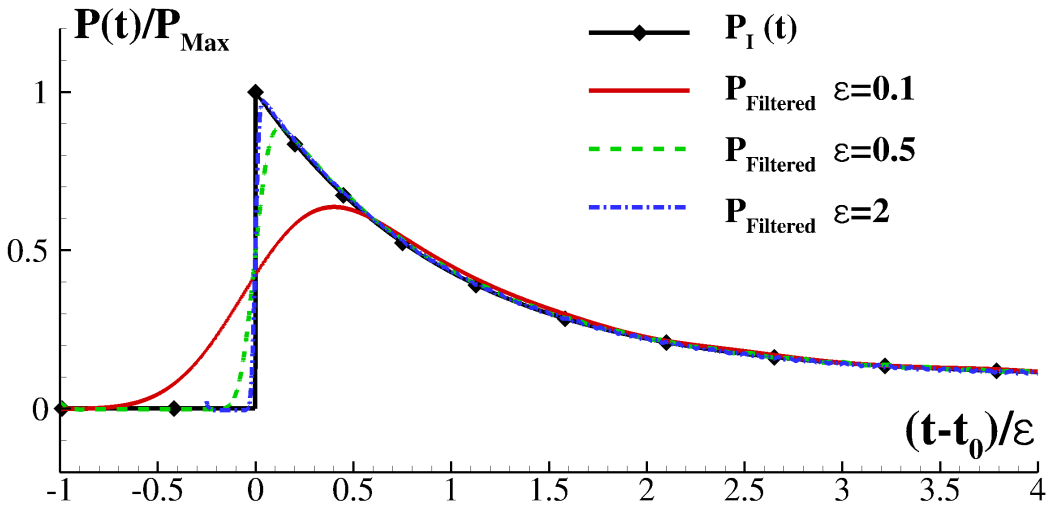

Figure 6.17: *Signals presented in Fig. 6.14 filtered of the frequencies higher than f^*, in comparison with the analytical solution.*

Table 6.3 shows the relative errors estimated for the pressure impulse, E_{Imp}, and for the pressure peak, E_{Pmx}, for the considered values of ε. As it is possible to see, the errors made in the wavelet filtering for small values of ε essentially affect the pressure peaks. Conversely, the wavelet filtering proves to be conservative with respects of the pressure impulse, in which even small ε lead to small errors.

A possible solution for a better decoupling of the acoustic components in impulsive pressure peaks could be to rise the value of the adopted speed of sound c. In this case in fact the acoustic part goes to a higher frequency range and the problem results to be decoupled again getting closer to the real speed of sound in water. As pointed out by

ε	2.0	0.5	0.1
E_{Imp} (%)	0.048	0.093	0.126
E_{Pmx} (%)	2.896	11.182	36.382

Table 6.3: *Relative errors for pressure impulse and pressure peak for the considered values of ε.*

Le Touzé et al. [81], giving the flow a weaker and weaker compressibility through the speed of sound, does not only shift the spectrum of these spurious oscillations towards higher frequencies but also increases their magnitude. The effect of the speed of sound on the pressure peaks encountered in impacts requires therefore further studies.

6.3.2 Wedge slamming

The results of SPH simulations of a water wedge impacting a vertical solid wall are here analyzed. The physics of slamming processes has been investigated by different authors, starting with the studies of Wagner [152]. Zhao and Faltinsen [159] developed a numerical model based on a nonlinear boundary element method with a jet flow approximation. In their formulation the water is assumed to be incompressible and the flow irrotational. This means that the impact velocity and the deadrise angle have to be in a range in which compressibility effects are negligible during the fluid-structure interaction process. Moreover it is assumed that no air pocket are captured at the interface fluid-solid during the impact. This hypothesis allows to model problems in which $\alpha > 4^\circ$. More recently Wu [157] has established a relationship between the free surface shape and the pressure distribution for the impact of a triangular liquid column onto a vertical wall. An interesting modeling of the dynamics of wedge impacts is given by the self-similarity solution presented by Dobrovol'skaya [45]. In this formulation the solution is furnished in terms of non-dimensional space and time coordinates, meaning that the pressure evolution for every point located along the vertical wall follows the same evolution in appropriate normalized coordinates. This last analytic solution is taken into account for comparisons with the SPH results.

The involved test case refer to a water wedge, with height H and characterized by $\alpha = 30^\circ$, impacting a vertical wall are analyzed. The problem is solved by SPH, using the governing equations expressed by System 2.72, while fixed ghost particles are implemented to model the bottom and the vertical wall. The Runge-Kutta integration scheme with δ-SPH diffusive correction is taken into account, while for the artificial viscosity a value of $\alpha = 0.01$ is enforced. Fig. 6.18 shows three significant time instants of the flow evolution, with pressure field, obtained from SPH. In this context, the evolution of the flow dynamics is characterized by a vertical jet rising progressively the wall. The jet is created at the intersection between the free surface wedge and the vertical wall. The velocity of the induced vertical jet is dependent on the value of the deadrise angle.

In Fig. 6.19 shown the time variation of the pressure at the point P_1 for the results obtained from simulations with five different spatial resolutions ($H/\Delta x = 100$, 200, 400, 800, 1600). As it is possible to notice, the increasing of the resolution gives a decreasing in the acoustic pressure oscillations and a defined tendency to reach asymptotic values for the pressure solution. This situation highlights the effects of refinement to the acoustic solution of the SPH. As already noticed by Le Touzé et al. [81], physical

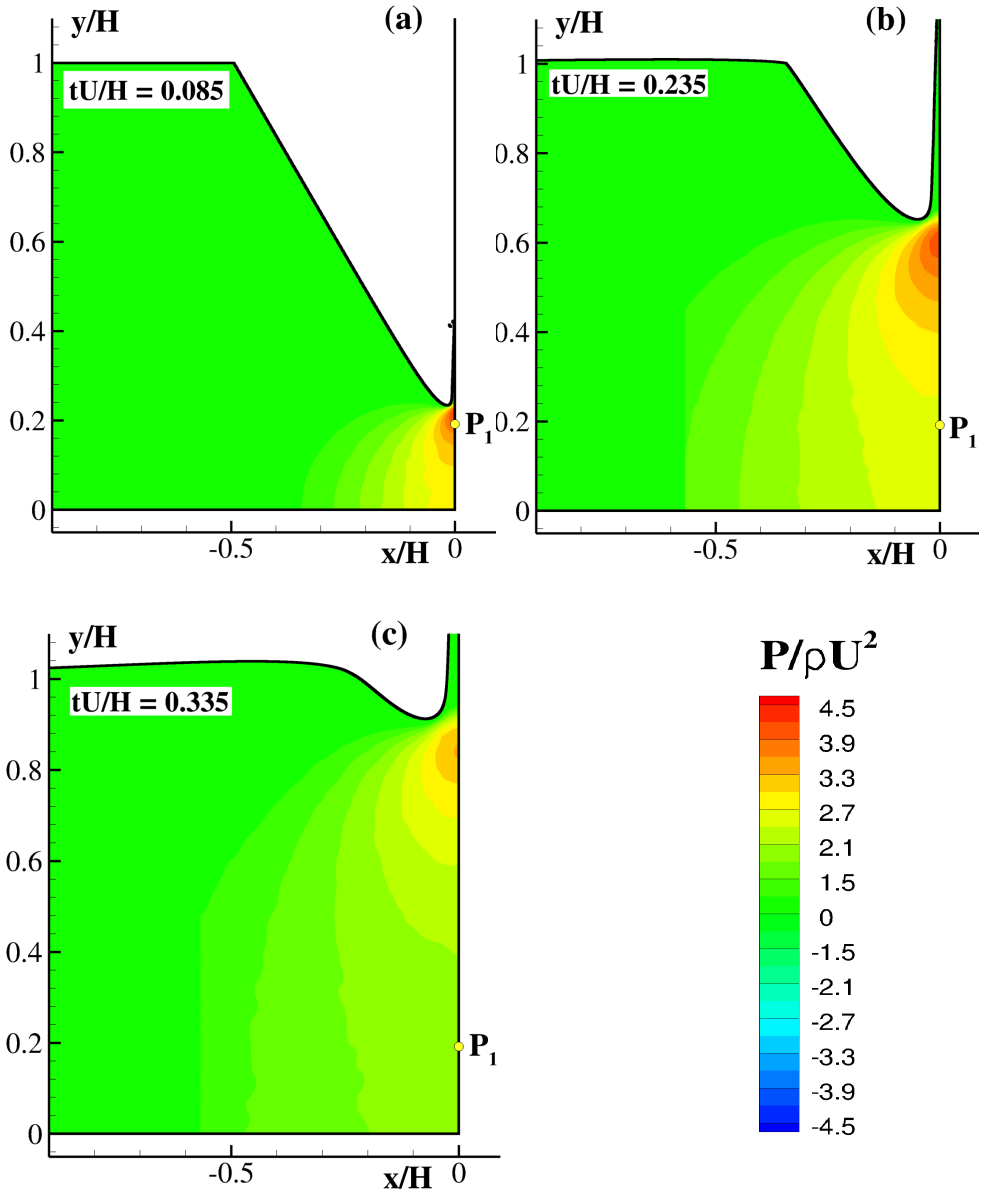

Figure 6.18: *Dynamic of the water wedge impacting a vertical wall. The time instant in which the wedge arrives ate the wall is $t = 0$. In (a) is the time instant in which the maximum pressure is on P_1. In (b) and (c) are shown two successive time instant in which the maximum spatial pressure progressively moves upwards and the pressure measured in P_1 decreases.*

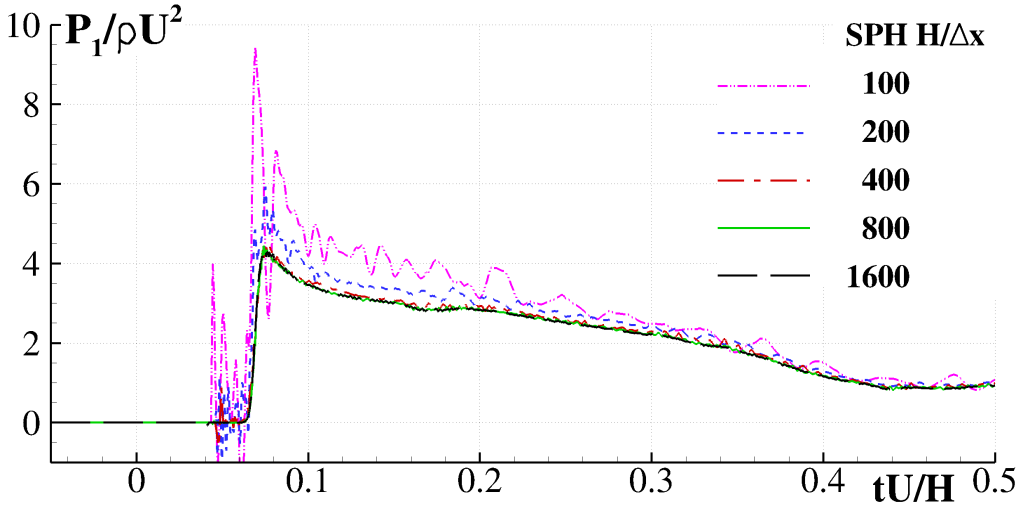

Figure 6.19: *SPH results for the pressure evolution at P_1 for different resolutions.*

processes not characterized by singular impacts, such as flat impacts cases mentioned in the section 1.1 of the thesis, present a decreasing of the energy content related with a low range acoustic frequency, when increasing resolution. In Fig. 6.20 is shown a comparison between the highest adopted SPH resolution and the Dobrovol'skaya [45] solution. As it is possible to see, when a high resolution is chosen for the SPH simulation the result converges to the analytical solution.

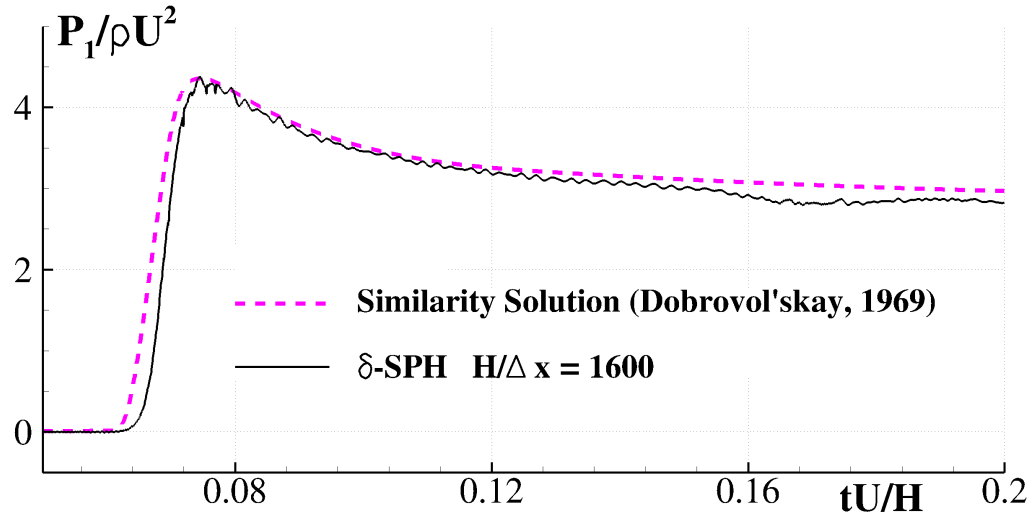

Figure 6.20: *Comparison of the higher adopted SPH resolution $H/\Delta x = 1600$ and the analytic solution of Dobrovol'skaya [45] at point P_1.*

The results are now studied through the wavelet transform. Fig. 6.21 shows the wavelet coefficients obtained for the analytical solution of Dobrovol'skaya [45], while Fig. 6.22 the results for the SPH solution with two different resolutions. In this context, for the mentioned reasons, the adopted cut-off frequency changes according with the

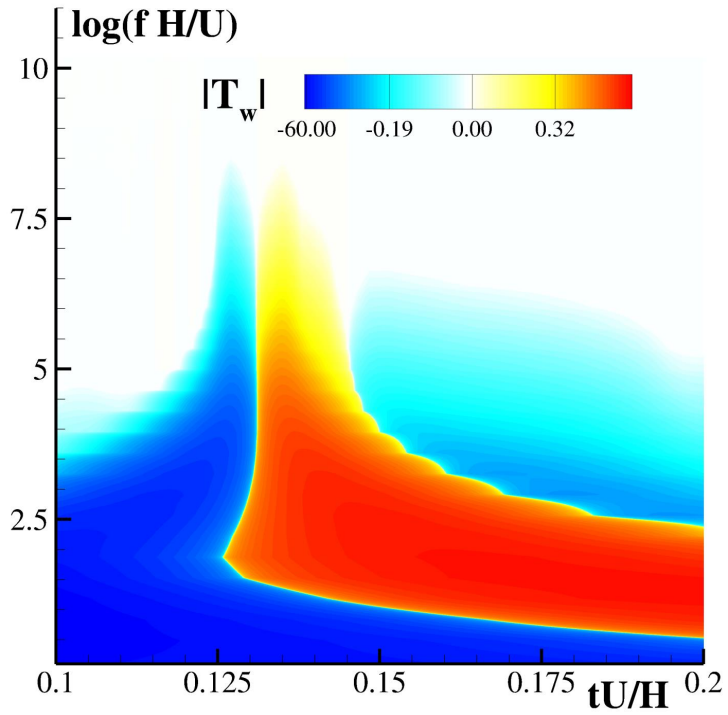

Figure 6.21: *Wavelet coefficients obtained for the analytical solution of Dobrovol'skaya [45] for the point* P_1.

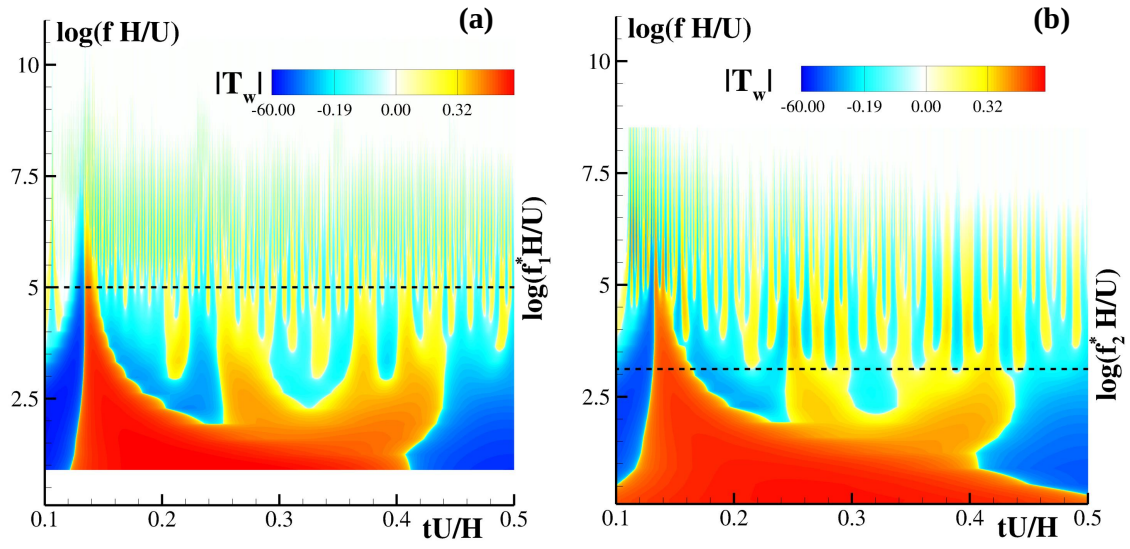

Figure 6.22: *Wavelet coefficients obtained for the pressure signals of the SPH solution at the point* P_1. *The horizontal dashed lines indicate the considered cut-off frequencies. In (a) is* $H/\Delta x = 1600$, *while in (b) is* $H/\Delta x = 200$.

analyzed resolution. The individuation of an accurate cut-off frequency is furnished in this context by the wavelet coefficients. As it is possible to see in Fig. 6.22, the values f_1^* and f_2^*, respectively adopted for the high and low resolutions, are fixed where the energy content related to the acoustic perturbations rises in the wavelet domain.

Fig. 6.23 shows the results of the wavelet filtering in which a comparison between a low resolution ($H/x = 200$) considering original and filtered SPH signals and the highest filtered resolution ($H/x = 1600$). In Fig. 6.24 is shown the comparison between the highest adopted resolution with the analytical one. In this last case, the acoustic component represents indeed only a minor issue of the SPH solution since no relevant differences appear in the time history of original and filtered SPH pressures

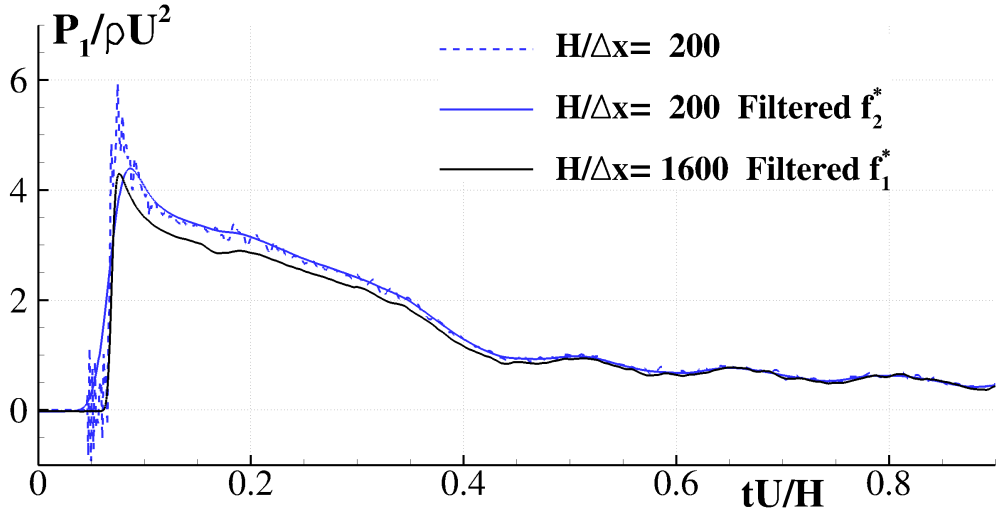

Figure 6.23: *Comparison between the original and filtered SPH solution at $H/\Delta x = 200$, and the filtered SPH solution at $H/\Delta x = 1600$, for the point P_1.*

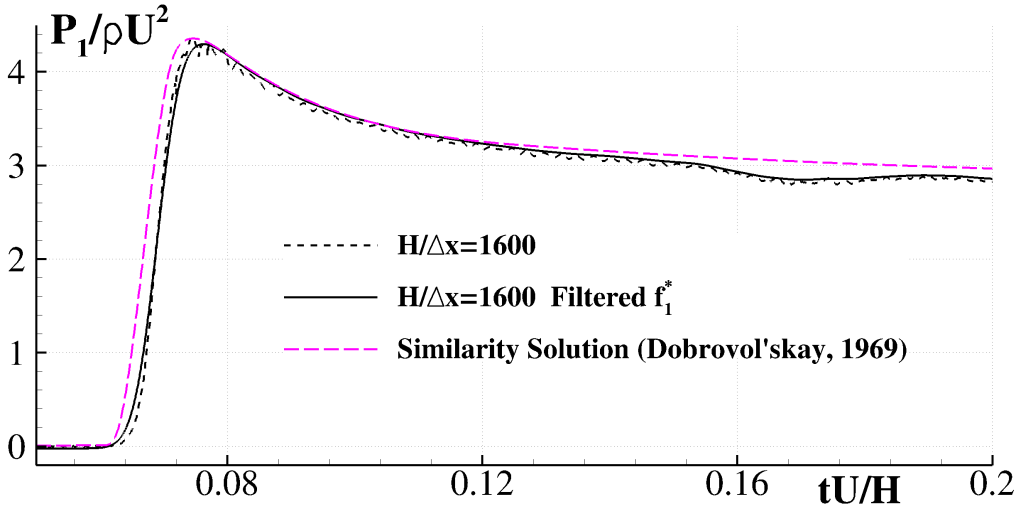

Figure 6.24: *Comparison between the original and filtered SPH solution at $H/\Delta x = 1600$, and the analytical solution, for the point P_1.*

6.3.3 Sloshing

The results of SPH simulations of a sloshing dynamic are here analyzed. Sloshing is a dynamic phenomenon occurring in partially filled tanks when subjected to external forces. In the case of shallow water conditions, the forcing frequencies in proximity of the lowest natural frequency for the fluid motion inside the tank lead to violent surface wave response. In this case, even if a tank oscillates with small amplitude, it is easy to observe the occurrence of breaking waves. Different theoretical approaches have been presented to model sloshing dynamics. In particular, the multi-modal method, developed by Faltinsen et al. [50] and successively by Faltinsen and Timokha [51], has been widely validated. This approach is based on an asymptotic theory to truncate the equation system in which the tank forcing is assumed to be small. Sloshing dynamic is also studied through experimental analyses. In Fig. 6.25 is presented the result of an experiment of a water tank subjected to sloshing dynamics during one period of the oscillations. This result highlights also the symmetric spatial configuration appearing during one cycle evolution.

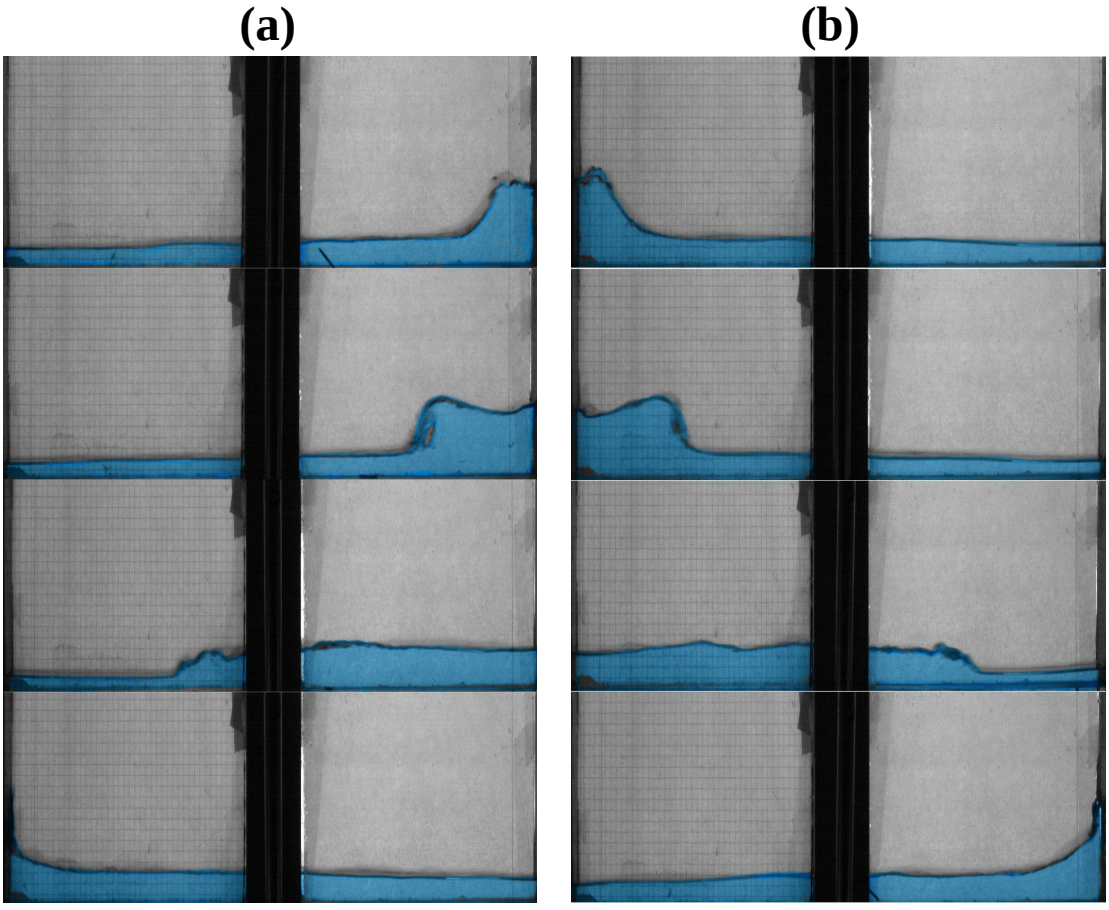

Figure 6.25: *Experimental results of a water tank subjected to sloshing dynamics, in which a breaking wave traveling, from right to left sides (a) and from left to right sides (b) is presented.*

In this context, the SPH simulations of a sloshing dynamics, characterized by water depth H and tank length L, are analyzed. The SPH computational strategies are the same of those adopted for the case dealing with the wedge slamming.

Fig. 6.26 presents the SPH results in terms of pressure field for the evolution of the breaking waves encountered during the analyzed sloshing process. A good agreement with the experimental observation in Fig. 6.25 is observed. In the result, the acoustic wave traveling in the fluid domain after the impact on the left wall of the tank is highlighted. In this case moreover, the pressure field result to be perturbed by the impacts consequent the closure of the cavities formed during the breaking of the waves. To properly model these phenomena indeed, a two phase model offers a more accurate physical description, being the breaking process characterized by water-air phases mixture. For the present one-phase SPH model, these acoustic perturbation effects due to these processes are more significant and, for this reason, the analysis of this problem is crucial to evaluate the capabilities of the wavelet filtering.

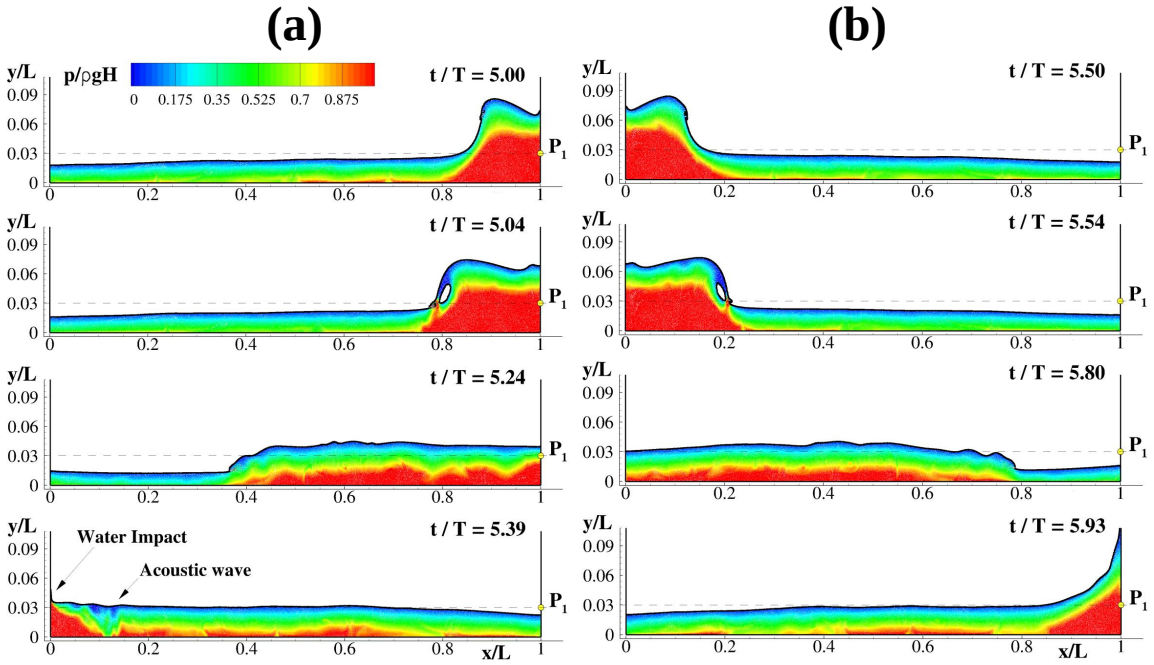

Figure 6.26: *SPH results of one period of the evolution of a sloshing dynamic, obtained with* $H/\Delta x = 50$*. The frames in (a) and (b) refers to the same time instants presented experimentally in Fig. 6.25.*

Fig. 6.27 presents the SPH result for the pressure evolution, at the point P_1 of the right wall located above the still water level, shown in Fig. 6.26. As it is possible to see, increasing the spatial resolution leads to a decreasing of the pressure peak encountered at the impact. Moreover, the adoption of a higher resolution offers, as also seen in the previous section, a reduction of the acoustic pressure noise. This fact is highlighted in the wavelet transform of these signals, presented in Figs. 6.28, 6.29 and 6.30, for $H/\Delta x = 25, 50, 100$, respectively. As it is possible to see the acoustic noise appear in the wavelet domain at a lower frequency for lower resolutions. The appearance of these high energy content indicates also where the cut-off frequency for the wavelet filtering has to be fixed. Indeed, the value of the cut-off frequency adopted for $H/\Delta x = 50$

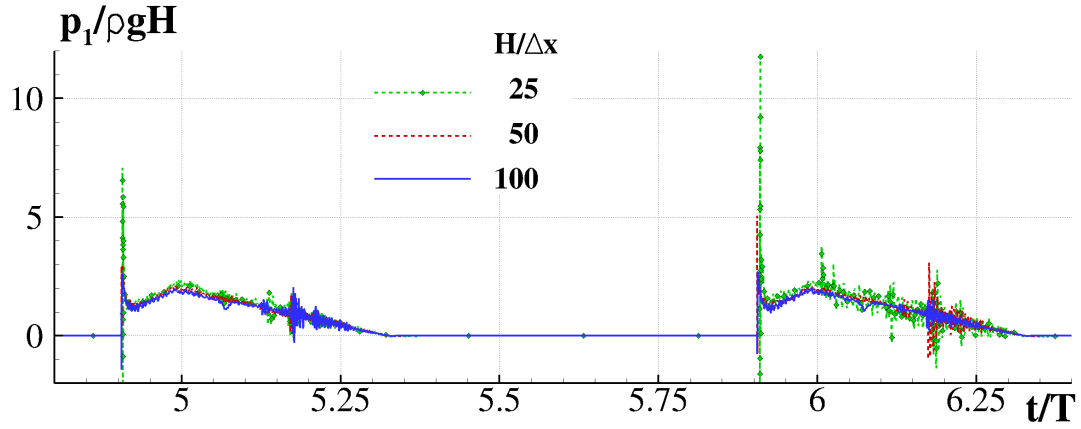

Figure 6.27: *Comparison of the pressure evaluated at the point P_1 for two periods of the evolution considering three different SPH resolutions.*

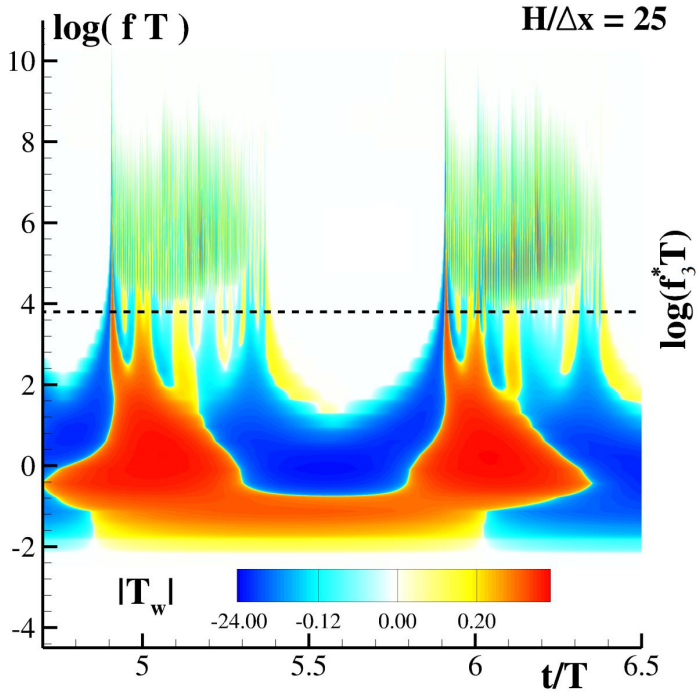

Figure 6.28: *Wavelet coefficients obtained for the pressure signal of the SPH solution at the point P_1 for $H/\Delta x = 25$, with the considered cut-off frequency.*

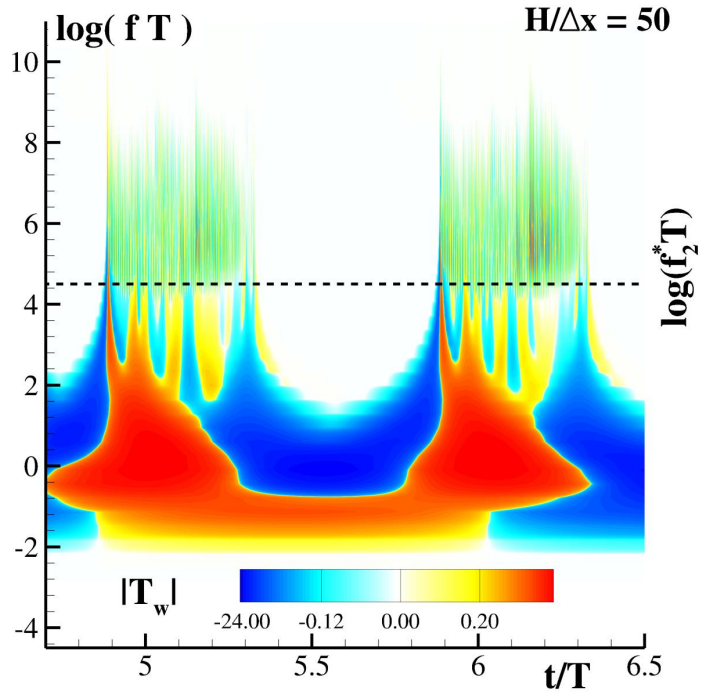

Figure 6.29: *Wavelet coefficients obtained for the pressure signal of the SPH solution at the point P_1 for $H/\Delta x = 50$, with the considered cut-off frequency.*

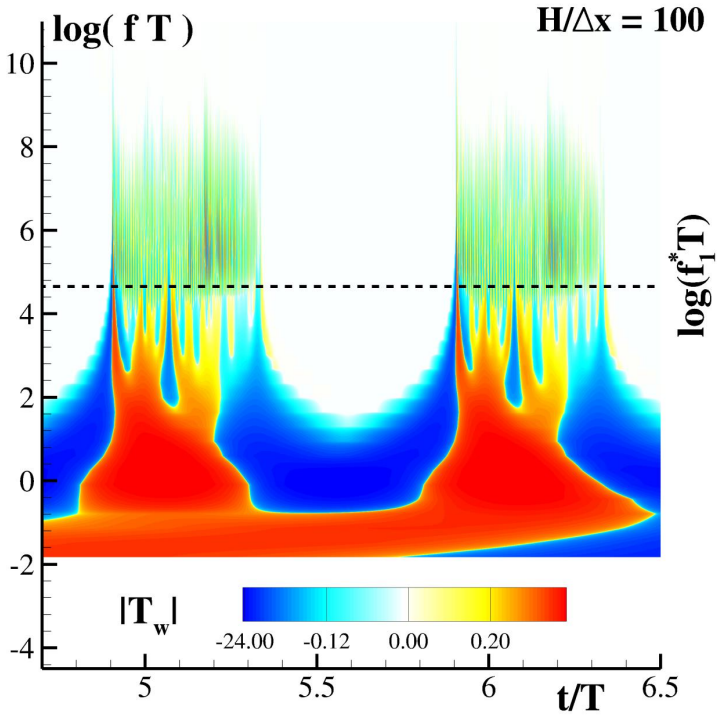

Figure 6.30: *Wavelet coefficients obtained for the pressure signal of the SPH solution at the point P_1 for $H/\Delta x = 100$, with the considered cut-off frequency.*

($f_2^*T = 90$) is twice the value adopted for $H/\Delta x = 25$ ($f_3^*T = 45$). When passing to the resolution $H/\Delta x = 100$ the cut-off frequency results to be only slightly increased ($f_1^*T = 105$), meaning that in this case a saturation for the accuracy linked to the spatial refinement as been reached. However, these cut-off values refer to a intermediate case between the frequency related to the horizontal width of the tank, $f = c/2L \cong 5$ Hz, and that related to the water depth, $f = c/2H \cong 170$ Hz, being c the speed of sound of the numerical simulation. Fig. 6.31 shows the results of filtered pressure signals for the three analyzed resolutions. As it is possible to observe, the filtered signals result

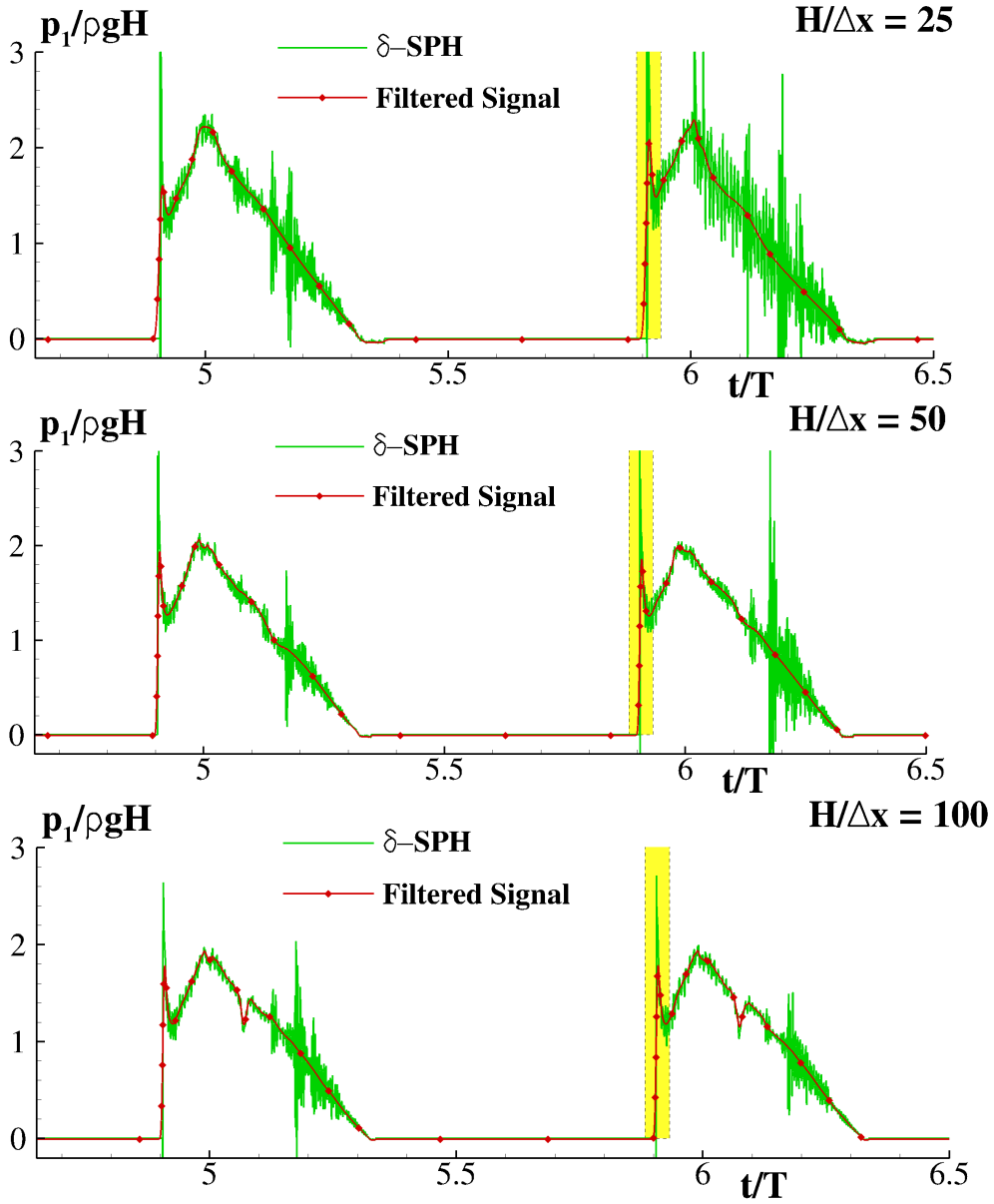

Figure 6.31: *Comparison between the original and filtered SPH solution, for the point P_1, for the three adopted resolution. Yellow areas are zoomed in Fig. 6.32.*

indeed appropriately removed by the acoustic component.

When a zoom is applied to the time window in which the analyzed impact occurs, as

shown in Fig. 6.32, is possible to observe more in details the behavior of the numerical solution. In this case, the numerical pressure peak is indeed associated with the artificial acoustic wave generated after the impact and highlighted in Fig. 6.33 (b). In these results it is shown how the pressure peak decreases when increasing the resolution as a function of the Mach number. For the coarser resolution, a value $P_{\max} = 60\%\, \rho c U$ is encountered, that decreases to $P_{\max} = 13\%\, \rho c U$, for the higher resolution.

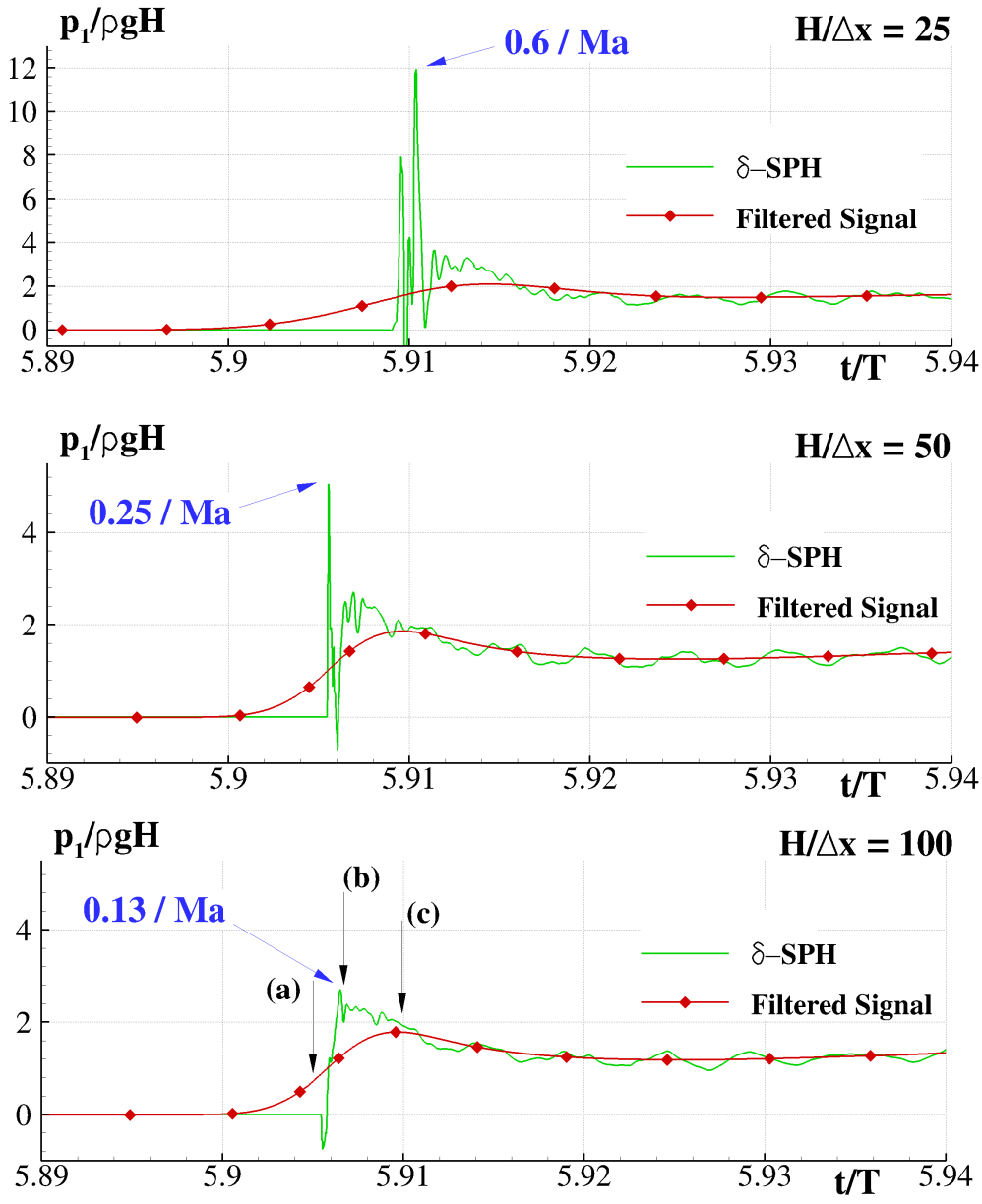

Figure 6.32: *Comparison between the original and filtered SPH solution for the time interval in which the impact occurs, as highlighted in yellow in Fig. 6.31.*

In Fig. 6.34 a comparison between the filtered pressure evolution for the three resolution is presented, showing the convergence of the filtering methodology towards a asymptotic solution.

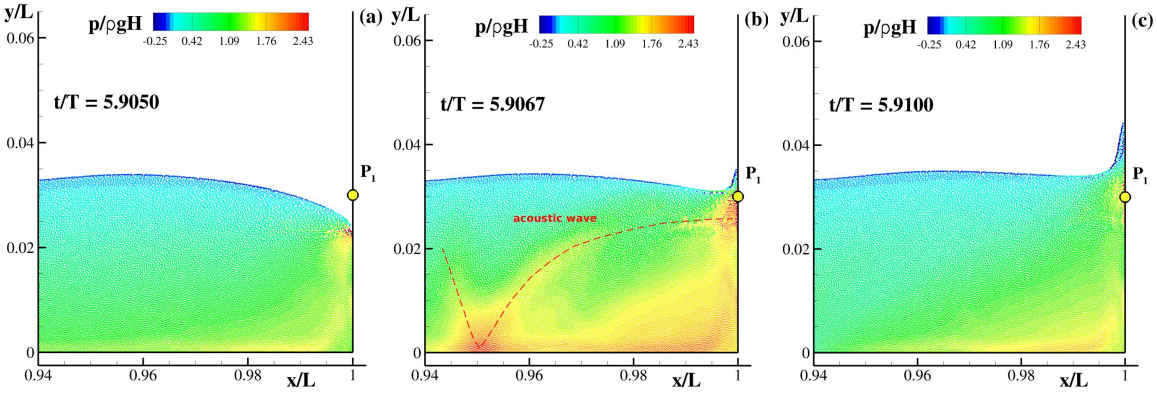

Figure 6.33: *Frames of the water impact at the point P_1, referred to Fig. 6.32 for $H/\Delta x = 100$. In (a) the water is approaching the gauge P_1, in (b) the fluid mass invested the numerical gauge and the simultaneous passage of the acoustic wave is highlighted, while in (c) the gauge is completely submerged and a vertical water jet is created.*

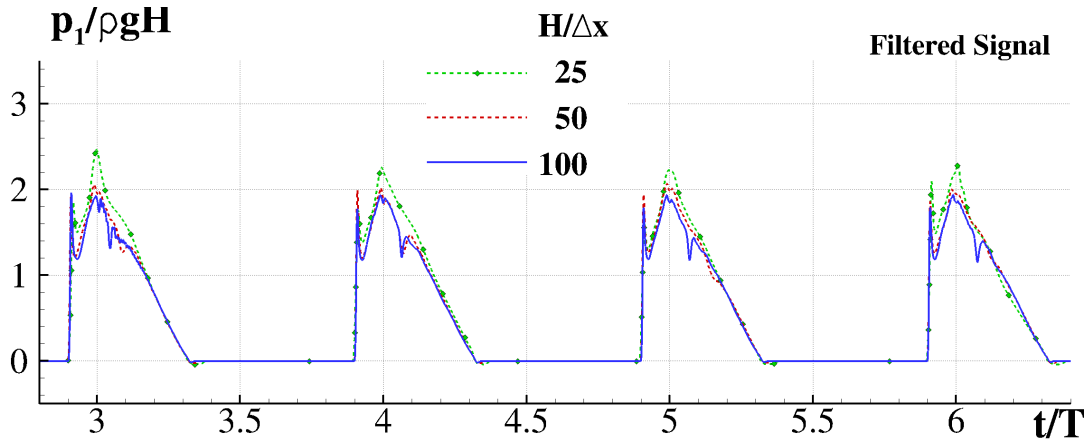

Figure 6.34: *Comparison between the filtered SPH solutions at the three different spatial resolutions.*

Conclusions

THE thesis presented the numerical modeling of fluid-structure interaction problems through the Lagrangian weakly-compressible Smoothed Particles Hydrodynamics (SPH) method. Several investigations on computational aspects of the weakly-compressible SPH solver have been carried out in order to improve the applicability of the involved numerical method in problems dealing with water interaction with solid structures. The capabilities of the proposed modeling have been initially tested through some preliminary test cases. In particular, these tests referred to the conservation of the flow field and the energy properties of SPH in static and dynamic conditions, with particular attention to the features of the weakly-compressible assumption.

An improvement in modeling solid boundaries in the fixed ghost particles framework has been developed. The enhancement consists of the adoption of more interpolation nodes for each considered solid particle in order to model thin structures surrounded by a fluid mass. Since the spatial resolution to model the involved structures is driven by the presence of thin solid boundaries, the use of multi-node fixed ghost particles allows to avoid long, often redundant, simulations related to the standard implementation. Indeed, the one-node fixed ghost particle approach yields numerical models characterized by a number of particles which is, in 2D problems, about four times that resulting from the proposed multi-node technique. In the present study, the time saving was respectively about 79.5% and 77.7%, for two investigated cases. It is noticed that in the case of an extension to 3D applications, the present modeling of thin solid bodies could lead to a higher computational time saving than the 2D cases investigated.

The proposed solid boundary treatment has been applied to the investigation of different aspects of the interaction of waves with perforated breakwaters. In this context, the research has been addressed to overcome the limitations in the breakwaters design, particularly when different fluid dynamics occur. Phenomena characterized by the occurrence of slow dynamics, as in the case of the wave propagation, and fast dynamics, as in the case of the fluid interaction with breakwaters, have required an accurate treatment of the pressure field. In these conditions, a hybrid formulation based on the use of the diffusive terms proposed by Molteni and Colagrossi [104] and Antuono et al. [6] has been introduced, representing a different formulation from the classical diffusive

approaches.

The improved SPH model has been then adopted to investigate the spatial distribution of wave pressures and wave reflection at perforated breakwaters. For the analysis of wave pressures, SPH simulations have described the occurrence of pressure drops near the holes of the slotted wall, showing that literature formulas furnish a poor assessment of the load diagrams. Analysis of the reflection coefficient, based on a free-surface elevation method, for different values of the ratio between the chamber width and the wave length has been carried out. SPH simulations have also allowed for the determination of the minimum values of the reflection coefficient in a range of practical interest for engineering applications.

A post-processing algorithm based on the wavelet transform to filter the acoustic pressure perturbations in the weakly-compressible SPH solution has been presented. The capabilities of the method proved to be outstanding for cases characterized by slow dynamics. In these cases the incompressible and the acoustic components result to be decoupled, allowing for an effective filtering of the acoustic part of the solution. A different situation is encountered when the dynamic become more impulsive, as in the case of impacts. In this case, the result is that the incompressible and the acoustic components are coupled, resulting in the difficulty for a proper filtering of the acoustic part without wiping out the analytical component. This situation have been tested for different flow evolutions, characterized by different degrees of impulsiveness.

As regards the engineering aspects, further developments will be addressed to better quantify the wave loads due to the pressure drops effects near the holes of the structure through experiences from ad-hoc laboratory tests using pressure gauges with refined spatial resolution. Moreover, an active absorption wavemaker will be implemented for detailed studies of the hydraulic performances of perforated-type breakwaters.

Concerning the analysis of the acoustic component in a weakly-compressible SPH model, successive analyses will regard phenomena characterized by higher level of impulsiveness in which, however, the presence of air does not play an important role in evaluating the pressure peaks. In these situations, an one-phase approach results to be suitable to model these cases, in which a solution to decouple the incompressible and the acoustic components could be, at a first glance, the adoption of a higher speed of sound for the simulations. Increasing the speed of sound, indeed, allows to shift the acoustic perturbations to higher frequencies, allowing for a decoupling of the problem. However, giving the fluid a weaker and weaker compressibility through an increasing of the speed of sound, does not only shift the spectrum of these spurious oscillations towards higher frequencies but also increases their magnitude. These cases have to be further investigated in successive analysis, studying the effects of the speed of sound in relation to the adopted spatial resolution, to the cut-off frequency for the wavelet filtering. In the limit case of a flat impact, to correctly model the pressure field, it will be necessary to take into account for the presence of the air at the interface of the impact, overcoming the difficulties to model accurately these events through a one-phase approach.

For a comprehensive analysis of water-structure interaction problems, a comparison between the involved spurious frequencies with the natural frequencies of vibration of the structure will be performed to ensure that spurious oscillations will not affect the structural response of the considered structure.

Associated Publications

- D.D. Meringolo, F. Aristodemo, P. Groenenboom, A. Lo Schiavo, P. Veltri, M. Veltri, "SPH modeling of wave pressures at vertical and perforated breakwaters". *9th international SPHERIC workshop*, Paris, France, June, 03-05 2014.
- D.D. Meringolo, F. Aristodemo, G. Viccione, P. Groenenboom, P. Veltri, "Diffusive WCSPH modeling of wave impact on structures". *XXXIV Convegno nazionale di Idraulica e Costruzioni Idrauliche*, Bari, 8-10 Settembre 2014.
- F. Aristodemo, P. Veltri, D.D. Meringolo, A. Lo Schiavo, "On the interaction between waves and perforated breakwaters with Smoothed Particle Hydrodynamics". *XXXIV Convegno nazionale di Idraulica e Costruzioni Idrauliche*, Bari, 8-10 Settembre 2014.
- F. Aristodemo, D.D. Meringolo, P. Groenenboom, A. Lo Schiavo, P. Veltri, M. Veltri, "Assessment of dynamic pressures at vertical and perforated breakwaters through diffusive SPH schemes". *Mathematical Problems in Engineering*, Article ID 305028, vol. 10 pages, 2015.
- D.D. Meringolo, F. Aristodemo, P. Veltri, "SPH numerical modeling of wave-perforated breakwater interaction", *Coastal Engineering* vol. 101 pgs. 48-68, 2015.
- D.D. Meringolo, F. Aristodemo, P. Groenenboom, P. Veltri, "Multi-nodes fixed ghost particles for SPH simulations". *10th International SPHERIC workshop*, Parma, Italy, June 16-18 2015.
- D.D. Meringolo, A. Colagrossi, S. Marrone, F. Aristodemo, P. Veltri, "An improved post-processing filtering algorithm of acoustic components in weakly compressible SPH simulations". *In preparation*.

Bibliography

[1] Altomare, C., Crespo, A.J.C., Domínguez, J.M., Gómez-Gesteira, M., Suzuki, T., Verwaest, T. Applicability of Smoothed Particle Hydrodynamics for estimation of sea wave impact on coastal structures. *Coastal Engineering*, 96:1–12, 2015.

[2] Altomare, C., Crespo, A.J.C., Rogers, B.D., Domínguez, J.M., Gironella, X., Gómez-Gesteira, M. Numerical modelling of armour block sea breakwater with Smoothed Particle Hydrodynamics. *Computer and Structures*, 130:34–45, 2014.

[3] Antuono, M., Bouscasse, B., Colagrossi, A., Marrone, S. A measure of spatial disorder in particle methods. *Computer Physics Communications*, 185:2609–2621, 2014.

[4] Antuono, M., Colagrossi, A., Marrone, S. Numerical diffusive terms in weakly-compressible SPH schemes. *Computer Physics Communications*, 183:2570–2580, 2012.

[5] Antuono, M., Colagrossi, A., Marrone, S., Lugni, C. Propagation of gravity waves through an SPH scheme with numerical diffusive terms. *Computer Physics Communications*, 182(4):866–877, 2011.

[6] Antuono, M., Colagrossi, A., Marrone, S., Molteni, D. Free-surface flows solved by means of SPH schemes with numerical diffusive terms. *Computer Physics Communications*, 181:532–549, 2010.

[7] Antuono, M., Marrone, S., Colagrossi, A., Bouscasse, B. Energy balance in the δ-SPH scheme. *Computer Meth. in Appl. Mech. and Eng.*, 289:209–226, 2015.

[8] Atluri, S.N., Zhu, T. New concepts in meshless methods. *Internat. J. Numer. Methods Engrg.*, 47:537–556, 2000.

[9] Batchelor, G.K. An introduction to fluid dynamics. *Cambridge University Press*, 1967.

[10] Belytschko, T., Krongauz, Y., Organ, D., Fleming, M., Krysl, P. Meshless methods: an overview and recent developments. *Comp. Meth. Appl. Mech. Engng.*, 139:3–47, 1996.

[11] Belytschko, T., Lu, Y.Y., Gu, L. Element-free Galerkin Methods. *Internat. J. Numer. Methods Engrg.*, 37:229–256, 1994.

[12] Bennett, G.S., Mc Iverband, P., Smallman, J.V. A mathematical model of a slotted wavescreen breakwater. *Coast. Eng.*, 18:231–249, 1992.

[13] Benz, W. *Smoothed Particles Hydrodynamic: A Review*. Kluwer Academic Publishers, 1990.

[14] Blackmorpe, A., Hewsonp, J. Experiments on full-scale wave impact pressures. *Coastal Engng.*, 8:331–346, 1984.

[15] Bonet, J., Kulasegaram, S. Correction and stabilization of Smoothed Particle Hydrodynamics methods with applications in metal forming simulations. *Internat. J. Numer. Methods Engrg.*, 47:1189–1214, 2000.

[16] Bouscasse, B., Antuono, M., Colagrossi, A., Lugni, C. Numerical and experimental investigation of nonlinear shallow water sloshing. *Int. J. Nonlinear Sci. Numer. Simul.*, 14(2):123–138, 2013.

[17] Bouscasse, B., Colagrossi, A., Marrone, S., Antuono, M. Nonlinear water wave interaction with floating bodies in SPH. *Journal of Fluids and Structures*, 42:112–129, 2013.

[18] Calderon, A. P. Intermediate spaces and interpolation, the complex method. *Stud. Math.*, 24:113–90, 1964.

[19] Chen, X., Li, Y., Sun, D., Chen, R. Experimental study of reflection coefficient and wave forces acting on perforated caisson. *Acta Oceanol. Sin.*, 21(3):451–460, 2002.

[20] Chen, X., Li, Y., Sun, D., Teng, B. Wave action on perforated caisson breakwater. *Proc. Of the 13th Int. Offshore and Polar Eng. Conf.*, pages 647–652, 2003.

[21] Chen, X.F., Li, Y.C., Ma, B.L., Jiang, J.J., Lu, G.R. Numerical and simplified methods for the calculation of the total horizontal wave force on a perforated caisson with a top cover. *Coastal Engineering*, 54:67–75, 2007.

[22] Cherfils, J.M., Pinon, G., Rivoalen, E. JOSEPHINE: A parallel SPH code for free-surface flows. *Computer Physics Communications*, 183(7):1468–1480, 2012.

[23] Chorin, A.J. A numerical method for solving incompressible viscous flow problems. *J. Comput. Phys.*, 2:12–26, 1967.

[24] Chui, C.K. *An introduction to wavelet*. Academic Press, 1992.

[25] Chwang, A.T. A porous-wavemaker theory. *Journal of Fluid Mechanics*, 132:395–406, 1983.

[26] Colagrossi, A. *A meshless Lagrangian method for free-surface and interface flows with fragmentation*. PhD Thesis, Università di Roma La Sapienza, 2005.

[27] Colagrossi, A., Antuono, M., Le Touzé, D. Theoretical considerations on the free surface role in the SPH model. *Phys. Rev. E*, 79(5):1–13, 2009.

[28] Colagrossi, A., Antuono, M., Souto-Iglesias, A., Le Touzé, D. Theoretical analysis and numerical verification of the consistency of viscous Smoothed Particle Hydrodynamics formulations in simulating free-surface flows. *Phys. Rev. E*, 84(026705), 2011.

[29] Colagrossi, A., Bouscasse, B., Antuono, M., Marrone, S. Particle packing algorithm for SPH schemes. *Computer Physics Communications*, 183(8):1641–1653, 2012.

[30] Colagrossi, A., Landrini, M. Numerical simulation of interfacial flows by Smoothed Particle Hydrodynamics. *Journal of Computational Physics*, 191:448–475, 2003.

[31] Colagrossi, A., Souto-Iglesias, A. Enforcing incompressibility in sph: Weakly compressible or not weakly compressible, this is the question. *SPHERIC 2015 Discussion Panel Presentations, 10 th international SPHERIC workshop, Parma, Italy, June, 16-18 2015*, 2015.

[32] Cooker, M., Peregrine, D.H. Pressure-impulse theory for liquid impact problems. *Journal of Fluid Mech.*, 297:193–214, 1995.

[33] Cottet, G.H., Koumoutsakos, P.D. *Vortex methods: theory and practice*. Cambridge University Press, 2000.

[34] Cox, D.T., Ortega, J.A. Laboratory observations of green water overtopping a fixed deck. *Ocean Engineering*, 29:1827–1840, 2002.

[35] Cummins, S.J., Rudman, M. An SPH projection method. *J. Comp. Phys.*, 152(2):584–607, 1999.

[36] Dalrymple, R.A., Knio, O., Cox, D.T., Gómez-Gesteira, M., Zou, S. Using a Lagrangian particle method for deck overtopping. *Proc. of Waves, San Francisco*, pages 1082–1091, 2001.

[37] Dalrymple, R.A., Rogers, B.D. Numerical modeling of water waves with the SPH method. *Coastal Engineering*, 53:141–147, 2006.

[38] Daubechies, I. Ten Lectures on Wavelets. *CBMS-NSF Regional conference series in applied mathematics*, 1992.

[39] De Chowdhury, S., Sannasiraj, S.A. SPH simulation of shallow water wave propagation. *Ocean Engineering*, 60:41–52, 2013.

[40] De Chowdhury, S., Sannasiraj, S.A. Numerical simulation of 2D sloshing waves using SPH with diffusive terms. *Applied Ocean Research*, 47:219–240, 2014.

[41] De Girolamo, P. Dispense del corso di costruzioni marittime. *Università degli Studi La Sapienza di Roma (in italian)*.

[42] De Leffe, M., Le Touzé, D., Alessandrini, B. A modified no-slip condition in weakly-compressible SPH. *Proc. of 6th International Spheric SPH Workshop, Hamburg*, pages 291–297, 2011.

[43] Di Lisio, R., Grenier, E., Pulvirenti, M. The convergence of the SPH method. *Comp. Math. Appl.*, 35:95–102, 1998.

[44] Dilts, G. Moving-Least-Squares-Particle Hydrodynamics - I. Consistency and stability. *Int. J. for Numerical Methods in Engineering*, 44(8):1115–1155, 1999.

[45] Dobrovol'skaya, Z.N. On some problems of similarity flow of fluid with a free surface. *Journal Fluid Mechanics*, 36:805–829, 1969.

[46] Domingues, M.O., Mendes, O., Mendes da Costa, A. On wavelet techniques in atmospheric sciences. *Advances in Space Research*, 35:831–842, 2005.

[47] Domínguez, J.M., Crespo, A.J.C., Gómez-Gesteira, M. Optimization strategies for CPU and GPU implementations of a Smoothed Particle Hydrodynamics method. *Computer Physics Communications*, 184(3):617–627, 2013.

[48] Domínguez, J.M., Crespo, A.J.C., Valdez-Balderas, D., Rogers, B.D., Gómez-Gesteira, M. New multi-GPU implementation for smoothed particle hydrodynamics on heterogeneous clusters. *Computer Physics Communications*, 184(4):1848–1860, 2013.

[49] Ellero, M., Serrano, M., Espanol, P. Incompressible Smoothed Particle Hydrodynamics. *J. Comp. Phys.*, 226:1731–1752, 2007.

[50] Faltinsen, O., Lukovskyand, O.R.I., Timokha, A. Multidimensional modal analysis of nonlinear sloshing in a rectangular tank with finite water depth. *J. Fluid Mech.*, 407:201–234, 2000.

[51] Faltinsen, O., Timokha, A. Asymptotic modal approximation of nonlinear resonant sloshing in a rectangular tank with small fluid depth. *J. Fluid Mech.*, 470:319–357, 2002.

[52] Faraci, C., Scandura, P., Foti, E. Reflection of sea waves by combined caissons. *J. Waterw. Port Coast. Ocean Eng.*, 141(2), 2015.

[53] Farge, M. Wavelet transforms and their application to turbulence. *Annu. Rev. Fluid Mech.*, 24:395–457, 1992.

[54] Federico, I., Marrone, S., Colagrossi, A., Aristodemo, F., Antuono, M. Simulating 2D open-channel flows through an SPH model. *Eur. J. Mech. B/Fluids*, 34:35–46, 2012.

[55] Federico, I., Marrone, S., Colagrossi, A., Aristodemo, F., Veltri, P. Simulating free surface channel flows through SPH. *Proc. of 5th International Spheric SPH Workshop, Manchester*, pages 90–97, 2010.

[56] Ferrari, A., Dumbser, M., Toro, E.F., Armanini, A. A new 3D parallel SPH scheme for free-surface flows. *Computer and Fluids*, 38:1203–1217, 2009.

[57] Fries, T.P., Matthies, H.G. Classification and overview of meshfree methods. *Technical University Braunschweig, Informatikbericht*, page 122, 2004.

[58] Fugazza, M., Natale, L. Hydraulic design of perforated breakwaters. *Journal of Waterway, Port, Coastal and Ocean Engineering*, 118(1):1–14, 1992.

[59] Gabor, D. Theory of communication. *Journal of the Institute of Electrical Engineers*, 93:429–457, 1946.

[60] Gao, R., Ren, B.,Wang, G.,Wang, Y. Numerical modelling of regular wave slamming on subface of open-piled structures with the corrected SPH method. *Appl. Ocean Res.*, 34:173–186, 2012.

[61] Gingold, R., Monaghan, J.J. Smoothed Particle Hydrodynamics: theory and application to non spherical stars. *Mon. Not. Roy. Astron. Soc.*, 181:375–389, 1977.

[62] Goda, Y. New wave pressure formula for composite breakwaters. *Proc. 14th Int. Conf. Coast. Engrg.*, pages 1702–1720, 1974.

[63] Goda, Y. Random seas and design of maritime structures. *World Scientific*, pages 1–443, 2000.

[64] Goda, Y., Suzuki, Y. Estimation of incident and reflected waves in random wave experiments. *Proc. of 15th International Coastal Engineering Conference, Honolulu*, pages 828–845, 1976.

[65] Gómez-Gesteira, M., Cerqueiro, D., Crespo, C., Dalrymple, R.A. Green water overtopping analyzed with a SPH model. *Ocean Engineering*, 32:223–238, 2005.

[66] Grenier, N., LeTouzé, D., Colagrossi, A., Antuono, M., Colicchio, G. Viscous bubbly flows simulation with an interface SPH model. *Ocean Engineering*, 69:88–102, 2013.

[67] Groenenboom, P., Cartwright, B. Hydrodynamics and fluid-structure interaction by coupled SPH-FE method. *Journal of Hydraulic Research*, 48:61–73, 2010.

[68] Groenenboom, P., Cartwright, B. Pressure-corrected SPH with innovative particle regularization algorithms and non-uniform, initial particle distribution. *Proc. of 8th International Spheric SPH Workshop, Trondheim*, 2013.

[69] Grossmann, A., Morlet, J. Decomposition of hardy functions into square integrable wavelets of constant shape. *SIAM Journal of Analysis*, 15:723–736, 1984.

[70] Harlow, F. The Particle-In-Cell Method for Fluid Dynamics. *Methods in Computational Physics*, 3, 1964.

[71] Hou, Q., Kruisbrink, A.C.H., Pearce, F.R., Tijsseling, A.S., Yue, T. Smoothed Particle Hydrodynamics simulations of flow separation at bends. *Computational Fluids*, 90:138–146, 2014.

[72] Huang, Z., Li, Y., Liu, Y. Hydraulic performance and wave loadings of perforated/slotted coastal structures: A review. *Ocean Engineering*, 38:1031–1053, 2011.

[73] Jamenson, A., Schmidth, W., Turkel,E. Numerical solution of the Euler equations by finite volume methods using Runge-Kutta time-stepping schemes. *AIAA 14th Fluid and Plasma Dynamics Conference, Palo Alto, CA, June 23-25*, 1981.

[74] Jarlan, G.E. A perforated vertical wall breakwaters. *Dock and Harbour Authority XII*, 486:394–398, 1961.

[75] Jensen, T.G. Artificial retardation of barotropic waves in layered ocean models. *Mon. Weather Rev.*, 124(6):1272–1283, 1996.

[76] Jiang, F., Tang, X., Jin, Z., Zhang, L., Chen, H. Numerical method for wave forces acting on partially perforated caisson. *China Ocean Eng.*, 29:197–208, 2015.

[77] Kamoulakos, A., Groenenboom, P., Vlachoutsis, S., Ramos, J. Realistic Simulation of Tsunami induced Flooding and associated Fluid-Structure Interaction using the ESI Group VPS suite of codes. *Proceedings of XXII International ISOPE Conference, Rhodes*, 2012.

[78] Kirca V. S., Kabdasli, M. S. Reduction of non-breaking wave loads on caisson type breakwaters using a modified perforated configuration. *Ocean Engrg.*, 36:1316–1331, 2009.

[79] Landrini, M., Colagrossi, A., Greco, M., Tulin, M. P. Gridless simulation of splashing processes and near-shore bore propagation. *J. Fluid Mech.*, 591:183–213, 2007.

[80] Landrini, M., Colagrossi, A., Greco, M., Tulin, M.P. The fluid mechanics of splashing bow waves on ships: A hybrid BEM - SPH analysis. *Ocean Engineering*, 53:111–127, 2012.

[81] Le Touzé, D., Colagrossi, A., Colicchio, G., Greco, M. A critical investigation of Smoothed Particle Hydrodynamics applied to problems with free-surfaces. *Int. J. Numer. Meth. Fluids*, 73:660–691, 2013.

[82] Lee, E.S., Moulinec, C., Xu, R., Violeau, D., Laurence, D., Stansby, P. Comparisons of weakly compressible and truly incompressible algorithms for the SPH mesh free particle method. *Journal of Computational Physics*, 227(18):8417–8436, 2008.

[83] Li, J., Liu, H., Gonga, G., Tanb, A.K., Shao, S.D. SPH modeling of solitary wave fissions over uneven bottoms. *Coastal Engineering*, 60:261–275, 2012.

[84] Li, J., Yang, J., Liu, S., Ji, X. Wave groupiness analysis of the process of 2D freak wave generation in random wave trains. *Ocean Engrg.*, 104:480–488, 2015.

[85] Libersky, L.D., Petschek, A.G., Carney, T.C., Hipp, J.R., Allahdadi,F.A. High strain Lagrangian hydrodynamics a threedimensional SPH code for dynamic material response. *J. Comp. Phys*, 109(1):67–75, 1993.

[86] Lind, S.J., Xu, R., Stansby, P.K., Rogers, B.D. Incompressible Smoothed Particle Hydrodynamics for free-surface flows: A generalised diffusion-based algorithm

for stability and validations for impulsive flows and propagating waves. *J. Comp. Phys*, 231:1499–1523, 2012.

[87] Liu, G.R., Liu, M.B. *Smoothed Particle Hydrodyndmics. A meshfree particle method*. World Scientific Publishing Co. Pte. Ltd., 2003.

[88] Liu, X., Lin, P., Shao, S. ISPH wave simulation by using an internal wave maker. *Coastal Engrg.*, 95:160–170, 2015.

[89] Liu, Y., Li, Y.C., Teng, B., Ma, B.L. Reflection of regular and irregular waves from a partially-perforated caisson breakwater with a rock-filled core. *Acta Oceanologica Sinica*, 26(3):129–141, 2007.

[90] Lu, X.Z., Cherfils, J.M., Pinon, G., Rivoalen, E., Brossard, J. SPH numerical computations of wave impact onto a vertical wall. *Proc. 9-th international SPHERIC workshop, Paris, France, June 2-5*, 2014.

[91] Lucy, L. A numerical approach to the testing of fission hypothesis. *Astronomical Journal*, 82(12):1013–1024, 1977.

[92] Madsen, P.A., Schäffer, H.A. A discussion of artificial compressibility. *Coastal Engrg.*, 53:93–98, 2006.

[93] Mallat, S. A wavelet tour of signal processing. *Coastal Engrg.*, 2009.

[94] Mansard, E.P.D., Funke, E.R. The measurements of incident and reflected wave spectra using a least square method. *Proc. of 17th International Coastal Engineering Conference, Sydney*, pages 154–172, 1980.

[95] Marrone, S. *Enhanced SPH modeling of free-surface flows with large deformations*. PhD Thesis, Università di Roma La Sapienza, 2011.

[96] Marrone, S., Antuono, M., Colagrossi, A., Colicchio, G., Le Touzé. δ-SPH model for simulating violent impact flows. *Computer Methods in Applied Mechanics and Engineering*, 200:1526–1542, 2011.

[97] Marrone, S., Bouscasse, B., Colagrossi, A., Antuono, M. Study of ship wave breaking patterns using 3D parallel SPH simulations. *Computers and Fluids*, 69:54–66, 2012.

[98] Marrone, S., Colagrossi, A., Antuono, M., Colicchio, G., Graziani, G. An accurate SPH modeling of viscous flow around bodies at low and moderate Reynolds numbers. *J. Comput. Phys.*, 245:456–475, 2013.

[99] Marrone, S., Colagrossi, A., Antuono, M., Lugni, C., Tulin, M.P. A 2D+t SPH model to study the breaking wave pattern generated by fast ships. *J. Fluids Struct.*, 27(8):199–1215, 2011.

[100] Marrone, S., Colagrossi, A., Di Mascio, A., LeTouzé, D. Prediction of energy losses in water impacts using incompressible and weakly compressible models. *Journal of Fluids and Structures*, 54:802–822, 2015.

[101] Marsh, A.P., Prakash, M., Semercigil, S.E., Turan, O.F. A shallow-depth sloshing absorber for structural control. *J. Fluid. Struct.*, 26:780–792, 2010.

[102] Mei, C.C., Liu, P.L. Ippen, A.T. Quadratic loss and scattering of long waves. *Journ. Of Waterway, Harbours and Coastal Engineering Division*, 100:217–239, 1974.

[103] Merkle, C.L., Athavale, M. Time-accurate unsteady incompressible flow algorithms based on artificial compressibility. *AIAA J.*, 87:1137–1147, 1987.

[104] Molteni, D., Colagrossi, A. A simple procedure to improve the pressure evaluation in hydrodynamic context using the SPH. *Computer Physics Communications*, 180:861–872, 2009.

[105] Monaghan, J.J. An introduction to SPH. *Comp. Phys. Comm.*, pages 89–96, 1988.

[106] Monaghan, J.J. Simulating free surface flows with SPH. *Journal of Computational Physics*, 110:399–406, 1994.

[107] Monaghan, J.J. SPH without a tensile instability. *Journal of Computational Physics*, 159:290–311, 2000.

[108] Monaghan, J.J. Smoothed Particle Hydrodynamics. *Reports on Progress in Physics*, 68:1703–1759, 2005.

[109] Monaghan, J.J. Time stepping algorithms for SPH. *Proceedings of 1st International Spheric SPH Workshop, Rome*, pages 1–13, 2006.

[110] Monaghan, J.J. Smoothed Particle Hydrodynamics and Its Diverse Applications. *Annual Review of Fluid Mechanics*, 44:323–346, 2012.

[111] Monaghan, J.J., Ashkan Rafiee. A simple SPH algorithm for multi-fluid flow with high density ratios. *Int. J. Numer. Meth. Fluids*, 71:537–561, 2013.

[112] Monaghan, J.J., Gingold, R.A. Shock simulation by the particle method SPH. *Journal of Computational Physics*, 52:374–389, 1983.

[113] Monaghan, J.J., Kajtar, J.B. SPH particle boundary forces for arbitrary boundaries. *Computer Physics Communications*, 180:1811–1820, 2009.

[114] Monaghan, J.J., Kos, A. Solitary waves on a Cretan beach. *J. Waterw. Port Coast. Ocean Eng.*, 125(3):145–154, 1999.

[115] Monaghan, J.J., Kos, A. Scott Russell's wave generator. *Phys. of Fluids*, 12(3):622–630, 2000.

[116] Morlet, J. Sampling theory and wave propagation. *Proc. 51st Annu. Meet. Soc. Explor. Geophys., Los Angeles*, 1981.

[117] Morlet, J., Arens, G. Fourgeau, E., Giard, D. Wave propagation and sampling theory, Part1: Complex signal land scattering in multilayer media. *Journal of Geophysics*, 47:201–221, 1982.

[118] Morris, J.P. *Analysis of smoothed particle hydrodynamics with applications*. PhD thesis, Dept. Math. Monash University, 1996.

[119] Morris, J.P., Fox, J., Zhu, Y. Modeling Low Reynolds Number Incompressible Flows Using SPH. *J. Comp. Phys.*, 136:214–226, 1997.

[120] Moussa, B.B., Lanson, N., Vila, J.P. Convergence of meshless methods for conservations laws: applications to Euler equations. *Int. Ser. Numer. Math.*, 129:31–40, 1999.

[121] Munz, C.-D., Roller, S., Klein, R., Geratz, K.J. The extension of incompressible flow solvers to the weakly compressible regime. *Computers and Fluids*, 32(2):173–196, 2003.

[122] Nayroles, B., Touzot, G., Villon, P. Generalizing the Finite Element Method: Diffuse Approximation and Diffuse Elements. *Comp. Mech.*, 10:307–318, 1992.

[123] Panizzo, A., Bellotti, G., De Girolamo, P. Application of wavelet transform analysis to landslide generated waves. *Coastal engineering*, 44:321–338, 2002.

[124] Peregrine, D.H. Water-wave impact on walls. *Annual review of fluid mechanics*, 35(1):23–43, 2003.

[125] Peyret, R., Taylor, T.D. *Computational Methods for Fluid Flow*. Springer-Verlag Inc., New York, 1983.

[126] Quinlan, N.J., Basa, M., Lastiwka, M. Truncation error in mesh-free particle methods. *Internat. J. Numer. Methods Engrg.*, 66:2064–2085, 2006.

[127] Rasio, F.A. Particle methods in astrophysical fluid dynamics. *Progr. Theor. Phys. Suppl.*, 138:609–621, 2000.

[128] Ren, B., Wen, H., Dong P., Wang, Y. Numerical simulation of wave interaction with porous structures using an improved Smoothed Particle Hydrodynamic method. *Coastal Engineering*, 88:88–100, 2014.

[129] Rodriguez-Paz, M., Bonet, J. A corrected smooth particle hydrodynamics formulation of the shallow-water equations. *Computers and Structures*, 83:1396–1410, 2005.

[130] Rogers, B.D., Dalrymple, R.A., Stansby, P.K.X. Simulation of caisson breakwater movement using 2-D SPH. *Journal of Hydraulic Research*, 48(EI):135–141, 2010.

[131] Rogers,J.,Szymczak,W. Computations of violent surface motions: comparisons with theory and experiment. *Philosophical Transactions of the Royal Society of London*, 355(A):649–663, 1997.

[132] Roussel, O., Schneider, K., Farge, M. Coherent vortex extraction in 3D homogeneous turbulence: comparison between orthogonal and biorthogonal wavelet decompositions. *Journal of Turbulence*, 6(11):1–15, 2005.

[133] Rufo, A. Approccio lagrangiano sph per la modellazione numerica di problemi in idraulica marittima. *Tesi di Laurea, Università di Roma Tre (in italian)*, 2004.

[134] Sahoo, T., Lee, M.M., Chwang, A.T. Trapping and generation of waves by vertical porous structures. *Journal of Engineering Mechanics-ASCE*, 126(10):1074–1082, 2000.

[135] Schneider, K., Vasilyev, O.V. Wavelet methods in computational fluid dynamics. *Annu. Rev. Fluid Mech.*, 42:473–503, 2010.

[136] Seena, A., Sung, H.J. Wavelet spatial scaling for educing dynamic structures in turbulent open cavity flows. *Journal of Fluids and Structures*, 27:962–975, 2011.

[137] Seo, J.H., Moon, Y.J. Linearized perturbed compressible equations for low Mach number aeroacoustics. *Journal of Computational Physics*, 218:702–719, 2006.

[138] Shao, S., Edmond, Y.M.L. Incompressible SPH method for simulating Newtonian and non-Newtonian flows with a free surface. *Adv. Water Res.*, 26:787–800, 2003.

[139] Shao, S.D. Incompressible SPH simulation of wave breaking and overtopping with turbulence modelling. *Int. J. Numer. Meth. Fluids*, 50:597–621, 2006.

[140] Shao, S.D., Ji, C.M., Graham, D.I., Reeve, D.E., James, P.W., Chadwick, A.J. Simulation of wave overtopping by an incompressible SPH model. *Coastal Engineering*, 53(9):723–735, 2006.

[141] Shepard, D. A two dimensional interpolation function for irregular spaced data. *In Proc. of 23rd A.C.M. Nat. Conf.*, pages 517–524, 1968.

[142] Slimon, S.A., Soteriou, M.C., Davis, D.W. Computational aeroacoustics simulation using the expansion about incompressible flow approach. *AIAA Journal*, 37(4), 2000.

[143] Souto-Inglesias, A., Delorme, L., Perez-Rojas, L., Abril-Perez, S. Smoothed particle hydrodynamics simulation of a tuned liquid damper (tld) with angular motion. *Ocean Eng.*, 33:1462–1484, 2006.

[144] Souto-Inglesias, A., Rojas, L.P., Rodriguez, R.Z. Simulation of anti-roll tanks and sloshing type problems with smoothed particle hydrodynamics. *Ocean Eng.*, 31:1169–1192, 2004.

[145] Suh, K.D., Park, J.K., Park, W.S. Wave reflection from partially perforated-wall caisson breakwater. *Ocean Engineering*, 33:264–280, 2006.

[146] Tabet-Aoul, E. H., Lambert, E. Tentative new formula for maximum horizontal wave forces acting on perforated caisson. *Journ. Of Waterway, Port, Coastal and Ocean Engineering*, 129(1), 2003.

[147] Takahashi, S. Design of vertical breakwaters. *Lecture note at 28th Int. Conf. on Coast. Engrg., Cardiff*, pages 1–105, 2002.

[148] Takahashi, S., Shimosako, K. Wave pressure on a perforated wall caisson. *Proc. Int. Conf. Hydro-tech. Eng. Port and Harbor Const. (HYDRO-PORT '94)*, pages 747–764, 1994.

[149] Tennekes, H., Lumley, J.L. *A First Course in Turbulence*. Cambridge: MIT Press, 1972.

[150] Vacondio, R., Rogers, B.D., Stansby, P.K., Mignosa, P., Feldman, J. Variable resolution for SPH: A dynamic particle coalescing and splitting scheme. *Computer Methods in Applied Mechanics and Engineering*, 256:132–148, 2013.

[151] Veen, D., Gourlay, T. A combined strip theory and Smoothed Particle Hydrodynamics approach for estimating slamming loads on a ship in head seas. *Ocean Engineering*, 43:64–71, 2012.

[152] Wagner, H. Über stoss- und gleitvergänge an der oberfläche von flüssigkeiten. *Z. Angew. Math. Mech. (in German)*, 12(4):192–235, 1932.

[153] Wang, X.Q., So, R.M.C., Xie, W.-C. Features of flow-induced forces deduced from wavelet analysis. *Journal of Fluids and Structures*, 23:249–268, 2007.

[154] Wang, Y.X. Numerical wave channel with absorbing wavemaker. *Journal of Hydrodynamics (in Chinese)*, 9(2):205–214, 1994.

[155] Wendland, H. Piecewise polynomial, positive definite and compactly supported radial functions of minimal degree. *Advances in Computational Mathematics*, 4(1):389–396, 1995.

[156] Wiegel, R.L. Trasmission of waves past a rigid vertical thin barrier. *Journal of Waterway, Harbour, Division ASCE*, 86(1):1–12, 1960.

[157] Wu, G.X. Fluid impact on a solid boundary. *Journal of Fluids and Structures*, 23:755–765, 2007.

[158] Yip, T.L., Chwang, A.T. Perforated wall breakwater with internal horizontal plate. *Journal of Engineering MechanicsâASCE*, 126(5):533–538, 2000.

[159] Zhao, R., Faltinsen, O. Water entry of two-dimensional bodies. *J. Fluid Mech.*, 246:593–612, 1993.